ISSN 1349-0087
SPring-8 Document D2012-005

SPring-8
Research Frontiers

2011

SPring-8
Research Frontiers
2011

CONTENTS
2011

Note: The principal publication(s) concerning each article is indicated with all author's names in italics in the list of references.

PREFACE

SPring-8 has been enjoying one of its most successful years in terms of achieving scientific accomplishments, that have been celebrated both abroad and at home.

Internationally, the journal *Science* selected two scientific achievements using SPring-8 facilities among the top ten 2011 Breakthroughs of the Year. One is the HAYABUSA asteroid sample analysis by Professor Tsuchiyama (Kyoto University) and the other is the crystal structure determination of a membrane-protein complex, Photosystem II, led by Professor Shen (Okayama University) and Professor Kamiya (Osaka City University).

Domestically, the Japan Academy conferred the Imperial Prize and the Japan Academy Prize upon two prominent scientists using SPring-8 in two consecutive years. In 2011, Professor Hirose (Tokyo Institute of Technology) was awarded the Japan Academy Prize for his remarkable discovery of the structure of the Earth's deep interior, and in 2012, Professor Namba (Osaka University) was awarded both the Imperial Prize and the Japan Academy Prize for his invaluable contribution to the crystal structure analysis of a macromolecular complex. These prizes are highly esteemed because the award ceremony is graced by the presence of His Majesty the Emperor and Her Majesty the Empress of Japan.

These scientific and technological achievements at SPring-8 were also acknowledged by JIAC 2011 (JASRI International Advisory Committee), the report of which is summarized in Research Frontiers 2011 along with its valuable recommendations.

SACLA (SPring-8 Angstrom Compact free electron LAser) started its user operation in March 2012, and we are very much looking forward to witnessing world-class research outcomes from SACLA in the very near future, which will hopefully be reported in Research Frontiers 2012.

As I announced in the last year's Preface, the former editor-in-chief, Prof. Kikuta, has retired, and we would like to welcome the new editor-in-chief, Dr. Ohno, who was the former executive managing director of JASRI.

白川哲久

Tetsuhisa Shirakawa
President
SPring-8 / JASRI

EDITOR'S NOTE

SPring-8 Research Frontiers 2011 covers advances achieved during the last two consecutive research periods, the second half of 2010 (2010B) and the first half of 2011 (2011A). Extraordinary scientific achievements at SPring-8 in various fields of basic and applied science, including industrial applications, are described, as well as the development of accelerators, beamlines and experimental apparatus, and the present status of the SPring-8 facility. In addition, the activities using NewSUBARU, which forms an integral part of the research complex, are introduced.

SACLA (the SPring-8 Angstrom Compact free electron Laser) was built jointly by RIKEN and JASRI as one of the Key Technologies of National Importance designated in 2006. Electron beam commissioning began in February 2011 and we accomplished "lasing" with SACLA on June 7, 2011. The SACLA facility opened to both domestic and international public users on March 7, 2012.

Two papers using SPring-8 facilities were included in the top ten groundbreaking scientific achievements from 2011 by the journal *Science*. These two papers concerned research led by Japanese researchers. In both cases, analyses at SPring-8 contributed greatly to breakthroughs. One paper was on the Hayabusa Mission led by Prof. Akira Tuchiyama (Kyoto Univ.). The analyses of dust particles from the Itokawa asteroid revealed that dust from Itokawa matched the composition of the most abundant type of meteorite, ordinary chondrites. The other paper reported the detection of a photosynthetic protein. The Structure of Oxygen-Evolving Photosystem II (PS II) has been revealed by a research group led by Prof. Jian-Ren Shen (Okayama Univ.) and Prof. Nobuo Kamiya (Osaka City Univ.). The research advanced another step in the bid to understand the natural catalyst for splitting water into oxygen and hydrogen using solar energy and progressed toward the realization of artificial photosynthesis, which could be a key to solving clean energy environmental and food issues.

In the layout of Research Frontiers, photographs of flowers grown at the SPring-8 campus and the Harima Science Garden City have been inserted. Photographs taken by Mr. M. Sugiura, Mr. M. Kida, Ms. T. Masaki, and Mr. T. Ozaki, are greatly appreciated.

Copies of SPring-8 Research Frontiers will be sent on request. The full text is also available on the SPring-8 website (http://www.spring8.or.jp/). For the list of publications produced by SPring-8 users and staff, please visit the publication database at http://www.spring8.or.jp/en/science/publication_database/ .

We extend our appreciation to those who have recommended excellent research results suitable for publication in SPring-8 Research Frontiers. We would also like to express our sincere gratitude to the users and staff of SPring-8 for contributing their reports to this issue.

EDITORIAL BOARD

Scientific Frontiers

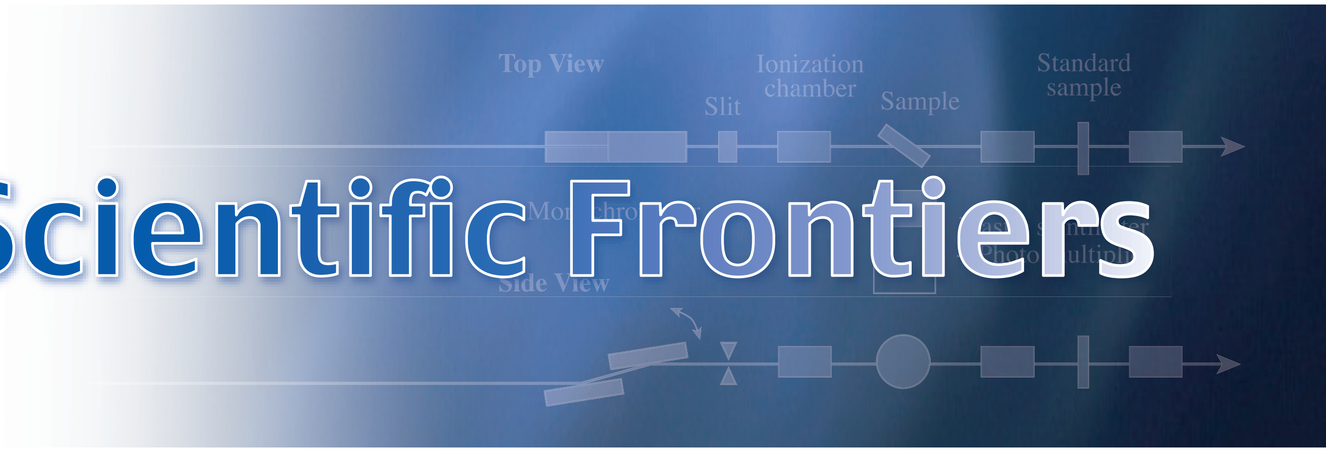

A Place in the "X-ray" Sun

2011 Breakthrough of the Year

In the "best of 2011" list of "*Science*" Magazine, two breakthroughs related to SPring-8 were compiled [1]. One is about the dust sample of the asteroid Itokawa, which was probed by Japan's Hayabusa after a long voyage full of misfortunes and troubles. Investigation of samples via SPring-8 helped to settle the mystery about asteroids and the earth. The other is the crystal structure determination of Photosystem II after many years of research using SPring-8. The finding shall provide a range of insights into photosynthesis to produce energy.

Other path-breaking stories, which are the development of energy saving vehicle tires via an advanced industry application and the first challenge application of nonlinear X-ray optics, were unveiled.

[1] Breakthrough of the Year: Science **334** (2011) 1630.

Synchrotron Radiation SkyGazers

Akira Tsuchiyama, professor of Kyoto University, has carried out years of investigation about "Pebble in the Universe" at SPring-8 in collaboration with JAXA (Japan Aerospace Exploration Agency) and NASA (National Aeronautics and Space Administration). In 2006, NASA Stardust spacecraft safely returned to Earth with cometary dust from Comet Wild2 captured in silica aerogel collectors [2]. The particles and impact tracks left in the aerogel have been analyzed by scientists all over the world. Via SR at Diamond Light Source, UK scientists found minerals, such as chondrule-like and CAI-like particles, in dust and proved the existence of an unexpected high-temperature, chemical process in the comet formation region. Tsuchiyama has further investigated various 3D structures and elemental distributions of impact tracks by microtomography and XRF and determined the quantitative proportion of high-temperature crystalline particles as approximately 6 vol.% with Tomoki Nakamura, a professor of Tohoku University [3]. Their research results provided fundamental parameters to model closely a scenario comet formation and evolving process.

Asteroid 25143 Itokawa became their next research target in order to uncover the real features of asteroids as well as the solar system formation by the Hayabusa mission of JAXA [4]. The story about the long return trip of Hayabusa after overcoming various technical troubles is all too famous to describe the incredible voyage (Fig. 1). In the returned sample box, only

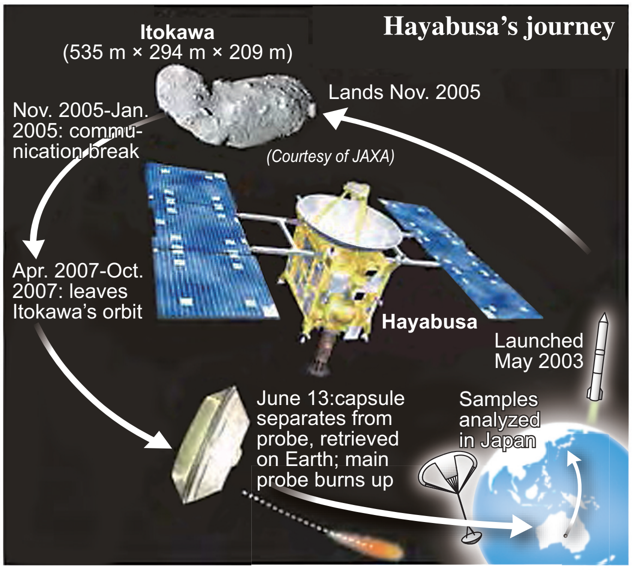

Fig. 1. Hayabusa's journey.

micron-size particles were observed. The first question was whether those particles were really collected from Itokawa or not. Consequently, X-ray microbeam analysis using Synchrotron Radiation conclusively identified the samples as LL chondrite from Itokawa (Fig. 2). Tsuchiyama and Nakamura (Fig. 3) have further challenged an investigation of mineral and element abundances, size distribution, 3D shape distribution as well as textures related to asteroid crash impact. The obtained results allow an improvement in the prediction of the Asteroid Itokawa formation. Their findings from "Pebble in the Universe" at SPring-8 shall draw up a scenario of the solar system history and evolution in the future.

[2] D. Brownlee *et al*.: Science **314** (2006) 1711.
[3] T. Nakamua *et al*.: Science **321** (2008) 1664.
[4] T. Nakamua *et al*.: Science **333** (2011) 1113;
A. Tsuchiyama *et al*.: Science **333** (2011) 1125.

Fig. 2 . Sample from Itokawa at SPring-8.

Fig. 3. Tsuchiyama and Nakamura with Hayabusa box.

Unravel the Mystery in the Heart of Plant Life

Jian-Ren Shen, a professor of Okayama University, has long wanted to unravel the mystery lying in the heart of plant life, which is the structure and function of photosystem II (PSII). PSII is a protein complex performing the initial reaction of photosynthesis by using sunlight to split water into molecular oxygen that we breathe. This reaction leads to the conversion of light energy into biologically useful chemical energy that sustains almost all life on the earth. The light-induced water-splitting reaction is also important in terms of efficient harvesting and utilization of sunlight to produce virtually unlimited clean energy, in order to overcome the increasing energy and environmental problems that we face. Thus, studies to unravel the mystery of the natural water-splitting reaction of PSII has been competitive over the last several decades. However, since PSII is a membrane-protein complex consisting of 19-20 different subunits with a total molecular weight of 350 kDa, it has been a major challenge to obtain crystals of PSII that diffract to an atomic resolution.

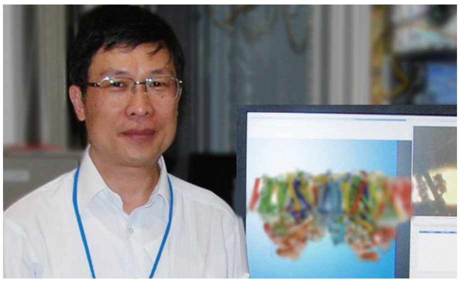

Jian-Ren Shen

Through a long-term and extensive search for the right conditions of crystallization, Shen and his colleagues eventually succeeded in analyzing the dimeric structure of the 19-subunit PSII complex at 1.9 Å resolution, using the beamlines BL41XU, BL44XU, and BL38B1 at SPring-8 [5]. They revealed for the first time the clear structure of the catalytic center of the water-splitting reaction, which is a Mn_4CaO_5 core organized in a distorted chair form, harbored by a number of amino acid residues and water molecules in a specific environment within PSII. The structure determination of the largest membrane-protein complex PSII provides a blueprint for the design of artificial catalysts capable of utilizing visible light to split water into oxygen and hydrogen, that is, a key technology that may lead to an unlimited source of clean energy.

[5] Crystal structure of oxygen-evolving photosystem II at a resolution of 1.9 Å: Nature **473** (2011) 55.

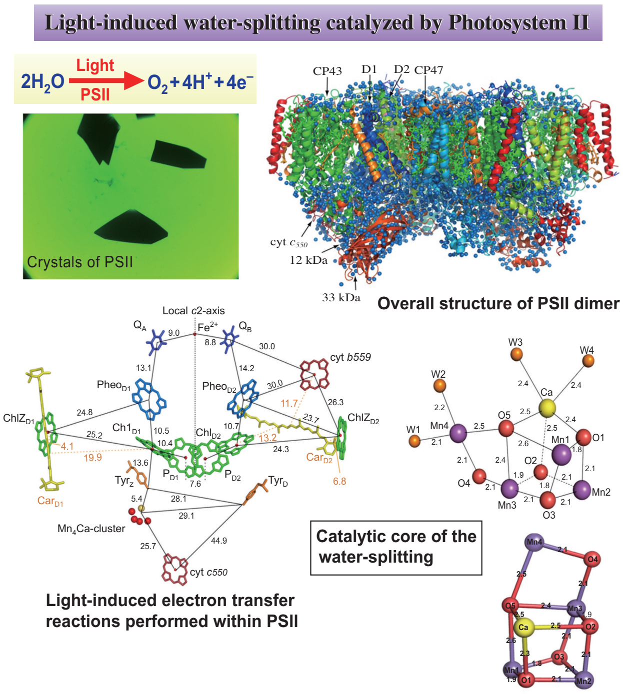

Light-induced water-splitting catalyzed by Photosystem II.

Vanguard of the X-ray Nonlinear Optics

The most exciting developments of photon science will sit at the intersection between the Synchrotron Radiation of SPring-8 and the X-ray Free-Electron Laser of SACLA. It is an intersection that shall break the novel research ground of X-ray science application. Kenji Tamasaku of RIKEN Harima and his research group succeeded in visualizing how the electrons in diamonds respond to the light (λ=203 Å) with an unprecedented resolving power of λ/380 (0.54-Å resolution) far beyond the wavelength limit [6] using an X-ray nonlinear optical phenomenon, which *detaches the resolution from the probing wavelength*. No one has imagined that she or he can see the scene of electrons responding to the light in the material. This is the angstrom version of the saying "A picture is worth a thousand words". Tamasaku stated that his microscopic optical probe with X-ray resolution crosses the bonds of the research on the optical response of materials and the related charge dynamics, opening a new window into the optical properties of solids. Now, scientists can see which part of the unit cell is responsible for the optical response of interest and use the knowledge for the better understanding of the optical property and to enhance the optical functions of materials.

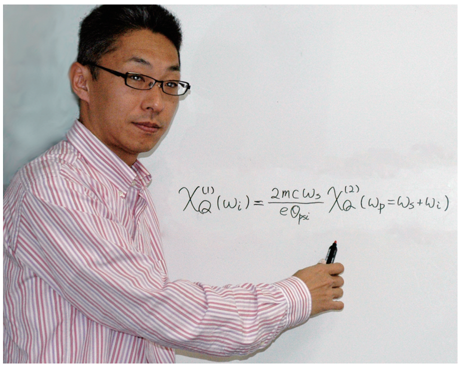

Kenji Tamasaku

Using SPring-8, he has been creating a firm vision for the essence of X-ray nonlinear optics (XNLO). Needless to say, nonlinear optics is one of the most important fields in modern science. In spite of extensive research over half a century, the X-ray region is still not explored and remains as a frontier. Tamasaku emphasized that XNLO is not a simple X-ray analogue of nonlinear optics, and that XNLO is important as it is, because the nonlinear interaction

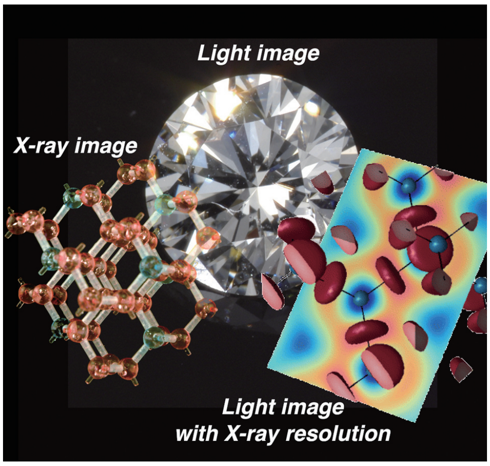

Visualized image via each light probe.

between radiation and electrons is completely different from those in the optical region. His article highlights one side of this unique feature and builds a bridgehead to explore other sides, which should open up novel applications in multidisciplinary scientific fields, such as laser physics, chemistry, solid-state physics, and material science.

The present achievement is an unprecedented application of the X-ray nonlinear optical processes. Remembering the successful history of nonlinear optics in the visible region from the invention of lasers in 1961, his success stimulated many scientists in various fields related to the nonlinear optics. He is now challenging XNLO using an X-ray free electron laser at SACLA.

[6] Tamasaku *et al*.: Nature Physics **7** (2011) 705.

Industrial Innovations from SPring-8

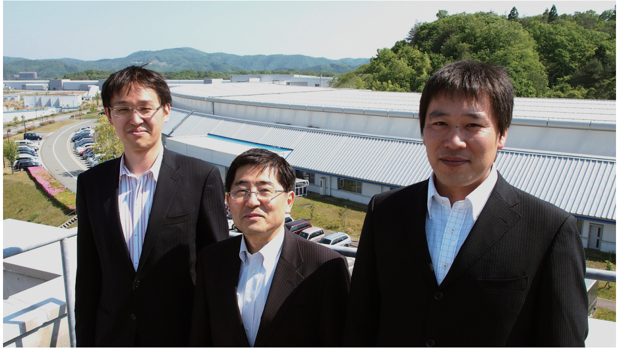

Yuya Shinohara and Yoshiyuki Amemiya (the University of Tokyo) with Hiroyuki Kishimoto (Sumitomo Rubber Industries, Ltd.)

Industry Application of SPring-8 has been one of the most valued activities from the viewpoints of social demands. Testing of various materials and product assurance were successfully carried out as a result of appropriate promotion based on marketing of attainment targets since early years. However, according to the progress in the performance of industry utilization, further demand for SR application has increased and enhanced the new firm collaborative relationship with academy. Such movements lead to the new beamline constructions based on the strategic project, such as the Catalytic Reaction Dynamics for Fuel Cells beamline BL36XU, Advanced Basic Science for Battery Innovation beamline BL28XU and Advanced Soft-material Beamline BL03XU.

Sumitomo Rubber Industries, Ltd. has developed a new material development technology named 4D NANO DESIGN using the SR application of SPring-8 and the supercomputer Earth Simulator, and successfully created high-performance tires to meet both environment protection and safety requirements in collaboration with Yoshiyuki Amemiya and Yuya Shinohara, professors of the University of Tokyo and National Institute of Advanced Industrial Science and Technology (AIST).

The key for the material design of rubber materials has been to mix-and-match the molecular structure and the compound characteristics to confer excellent performance to tires. The 4D NANO DESIGN allows us to enhance tire performance and control tire materials at the nano level by combining 4 separate technologies focusing on (1) the investigation, (2) estimation, (3) Producing, and (4) drawing of characteristics. Among them, the investigation conducted by Hiroyuki Kishimoto of Sumitomo Rubber Industries, Ltd. minutely visualized the nanoparticle construction inside rubber, which has a major impact on tire performance, by 2D-USAXS experiment at SPring-8 and Reverse Monte Carlo (RMC) simulation analysis using Earth Simulator. It allows us to simulate the characteristics of rubber materials more accurately at the molecular level. Their research is described in detail in their report. The results were applied to the simulation and molecular design by multi scale simulation in the estimation. Then, the optimization of a material process in order to draw such performance out of materials at maximum was achieved by drawing the characteristics, resulting in the drawing of the potential performance out of tire rubber materials. ENASAVE PREMIUM, which will be sold beginning February 2012, achieved a 6% improvement in fuel efficiency and is the first innovative product that adopts the 4D NANO DESIGN.

Various advanced approaches for product development are now emerging from the industry-academy utilization at SPring-8 and shall drive technological innovations.

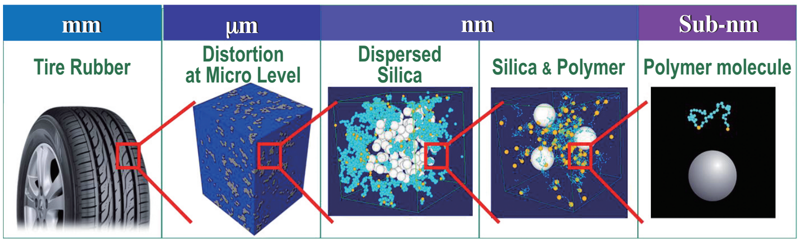

Multi-scale materials design of tire.

by Masaki Takata

LIFE SCIENCE:


"Nadeshiko"- *Fringed Pink*

Synchrotron radiation is a fundamental technology in macromolecular crystallography which reveals three-dimensional structures of biomolecules at atomic and molecular levels. Because of this importance, a national structural biology research project started five years ago, the 'Target Protein Research Program' (TPRP) has totally supported structural biology research in the aspects of scientific research and infrastructure development, and has produced many fruitful results. Although this project terminated at the end of the 2011 fiscal year, as the successor to the part of infrastructure development in the project, the 'Platform for Drug Design, Discovery and Development' will start in the 2012 fiscal year. This is a response to the expanding need and importance of the analytical technologies for innovative research including drug discovery. This concept is similar to the 'Instruct' program started in the European Union: "Instruct is the dynamic hub of structural biology providing an integrated infrastructure of cutting edge technology, scientific expertise and pioneering training." In the next five years, the user support system for the structural analyses and upgrading beamlines will be established.

Again this year, many outstanding results have been reported, particularly in the research field of bioenergy and membrane protein. We briefly introduce each article.

Photosynthesis is the greatest energy source for biological activity and produces organic compounds including sugar from water and carbon dioxide with light energy of the sun. Oxygenic photosynthesis causes charge separation of water by light reaction, resulting in the production of molecular oxygen, protons and electrons. The proton gradient, produced by this reaction and successive electron transport chain, enables the synthesis of ATP, a major and common biological energy currency, utilized for organic compound production in cyanobacteria and plants. Umena *et al*. revealed the high resolution structure of photosystem II and the secret of the reaction center for the charge separation reaction.

Oxygen evolution by the photosynthesis reaction maintains an aerobic condition in the atmosphere. Heterotrophic organisms, which depend on complex organic substances including sugar for nutrition, produce ATP by oxidizing the organic substances. For the oxidizing reaction, cellular respiration, i.e. the use of oxygen uptaken by breathing, is essential and it is coupled with the reduction of molecular oxygen obtained from atmosphere. However, in an ancient era where atmospheric oxygen was rarefied before the photosynthesis machinery was established, anaerobic respiration, where an electron acceptor other than oxygen is used, was rather common. Shiro *et al*. determined two anaerobic respiratory enzymes and discussed their evolutionary processes.

STRUCTURAL BIOLOGY

The recycling of oxygen and carbon is a closed loop because of the existence of plants and heterotrophs in an aerobic environment. On the other hand, the recovery of electron acceptors is crucial in anaerobes. Hydrogenases directly catalyze the reversible oxidation involving molecular hydrogen and water with electron acceptors including biological cofactors of NAD and quinones. This enzyme is also of interest in the synthesis of molecular hydrogen useful in power fuel cells. However, the enzymes produced by anaerobes are generally ineffective in an aerobic environment. Shomura *et al*. revealed a hydrogenase structure that is effective even in an aerobic environment.

A membrane is the border between self and the outer world, where membrane proteins play an important role as gates. The exporting of protein from inside of the cell, i.e., secretion, is an essential activity in the modification of the outer world by a living organism. However, unlike smaller molecules such as sugar, protein is too large to permeate the cell border. Tsukazaki *et al*. determined the protein secretion machinery and revealed its dynamical structure.

Protein export is also necessary for an extracellular structure such as a flagellum used for bacterial swimming. This biological machinery penetrates membranes and tightly connected to the flagellar motor protein. Thus the export apparatus for flagella should be assembled in concert with the flagellar motor protein. Imada *et al*. determined the flagellar export apparatus and compared it with another bacterial protein export apparatus, injectors of virulence factors in pathogenic bacteria.

As described above, structures of membrane proteins clarify the fundamentals of many biological functions. However, due to their amphipathic character, the preparation of purified specimens is often laborious work. Wada *et al*. successfully utilize an effective protein production system, a cell-free system, to produce a membrane protein, marine alga rhodopsin. Its structure is also of interest in the proton pumping mechanism driven by light energy.

Cellular motility is a biological kinematic process and related to essential biological processes of cell division for example. Cytoplasmic dynein can walk on a microtubule, that is, a cellular skeleton, and carries large cargo such as organelles and chromosomes. This dynamical action is supported by its ATP-dependent motor action. Kon *et al*. determined the functional full-length motor domain of dynein.

Flowering, a successor process to fruition, is a key step also in agricultural applications. This process is known to be regulated by the hormonal protein ‘florigen’, whose protein family is distributed in a wide variety of organisms, but its functional detail has not been known. Ohki *et al*. determined the ternary complex of florigen with a transcription factor and scaffold protein and clearly depicted the activation mechanism of the flowering signal.

The centromere is the attachment site of spindle fibers for cell division and the part of a chromosome that links sister chromatids, which is another copy of the chromosome resulting from DNA replication earlier in the cell cycle. To reveal the unique DNA packaging structure at the centromere, Kurumizaka *et al*. determined the structure of centromere specific histone CENP-A complexed with DNA.

A wire shows various topological structures such twisting and winding. The long strand that stores genetic information, DNA, also exihibits topological changes. The wound form of DNA is useful to compactly package DNA, but conversely, the unwound form is essential for DNA transactions including replication and transcription. The enzymes of DNA topoisomerase/gyrase contribute to the regulation of the dynamics of DNA topology. Wu *et al*. determined the complex structure of topoisomerase, TOP2, using inhibitory drugs.

Takashi Kumasaka

Structure of photosystem II oxygen-evolving complex at 1.9 Å resolution

The process of photosynthesis is composed of two reactions, the light and dark reactions. In the light reaction, solar energy is utilized to synthesize the cellular energy source, adenosine triphosphate (ATP), and the cellular reducing reagent, nicotinamide adenine dinucleotide phosphate (NADPH). In the dark reaction, carbon dioxide (CO_2) is fixed and converted to carbohydrates with the consumption of ATP and NADPH. The first light reaction is catalyzed by photosystem II (PSII) embedded in the thylakoid membrane. PSII catalyzes photoinduced water oxidation leading to the production of protons, electrons, and molecular oxygen. The former two products are utilized by ATPase and NADP reductase in the light reaction, respectively, and the third product is indispensable for sustaining oxygenic life on the earth. Cyanobacterial PSII contains 17 membrane-spanning subunits and 3 membrane-extrinsic subunits in each monomer. The catalytic center of the oxygen-evolving complex (OEC) is located in the lumenal surface of PSII. Upon light-induced charge separation at the PSII reaction center, electrons are abstracted from the OEC via a redox-active tyrosine, D1-Y161 (Yz). The OEC is composed of 4 Mn atoms and 1 Ca atom forming a Mn_4Ca cluster. In the last decade, the structures of PSII have been reported at resolutions in the range of 3.8-2.9 Å [1-4], from two closely related thermophilic cyanobacteria, *Thermosynchococcus elongatus* and *T. vulcanus*. These structural studies provided the arrangement of the protein subunits, the location of the cofactor molecules; however, these resolutions were inadequate to solve the detailed structure of the Mn_4Ca cluster as well as the precise arrangement of the amino acid residues and cofactors. In addition, no water molecules, which are important as substrates and ligands, have been found in these structures. In order to uncover the mechanism of light-induced water oxidation, it is essential to solve the detailed structure of the Mn_4Ca cluster as well as to locate the water molecules.

In this study, we prepared PSII dimers from *T. vulcanus*, and improved their purity and homogeneity by introducing a recrystallization step. PSII crystals were then obtained and their quality was improved by post-crystallization dehydration treatments, which yielded crystals diffracted to a resolution of 1.9 Å. Here, we report the PSII structure at 1.9 Å resolution (PDB code: 3ARC) [5] using diffraction data collected at beamline **BL44XU**.

The overall PSII dimer structure is shown in Fig. 1. Each PSII monomer contained 19 subunits, among which the small membrane-spanning subunit, psbY, was not found. The superposition of our PSII dimer with the dimeric structure composed of two monomers (PDB code: 3BZ1 and 3BZ2), which were reported at 2.9 Å resolution from *T. elongatus* [4], yielded a root mean square deviation of 0.78 Å, indicating that our structure from *T. vulcanus* is similar as the structure from *T. elongatus*. In addition to the protein subunits, there were 81 or 82 cofactors: 35 chlorophylls, two pheophytins, 11 β-carotenes, 20 lipids, two plastoquinones, two haems, one non-haem iron, one bicarbonate, one magnesium ion, three chloride ions, two or three calcium ions, and one Mn_4Ca cluster, in each PSII monomer. We found about 2,800 water molecules in PSII dimer, for the first time. The water molecules were organized into two layers located in the stromal and lumenal regions, with the latter having

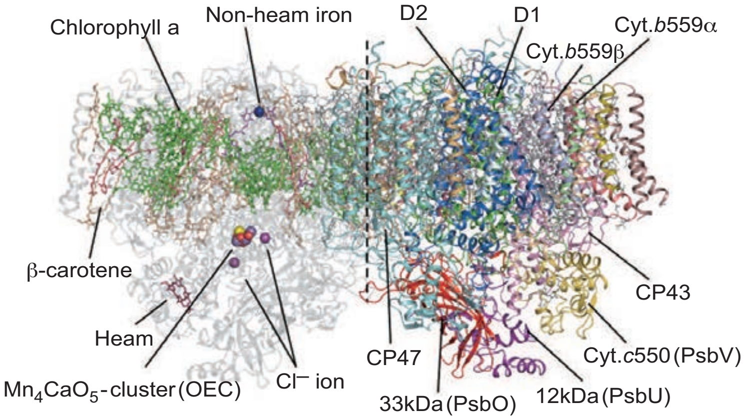

Fig. 1. Overall structure of PSII dimer from *T. vulcanus* and the location of the Mn_4CaO_5 cluster. The protein subunits on the right-hand side were colored individually and the locations of the cofactors are illustrated on the left-hand side. The central broken line is the non-crystallographic pseudo-C2 axis relating the two monomers.

four-folds more water molecules than the former. Some water molecules were found within the membrane region, most of which served as ligands to chlorophylls, and four water molecules were found to be associated with the Mn_4Ca cluster, two of which were associated with Mn_4 (W1 and W2) and the other two with Ca atoms (W3 and W4) (Fig. 2). Some water molecules participated in the hydrogen-bond network linking the OEC to bulk solvent region, and filled some channels from the bulk solvent to the OEC. They may therefore serve as channels for the transport of products (proton and dioxygen) and substrates (water) from and to the OEC.

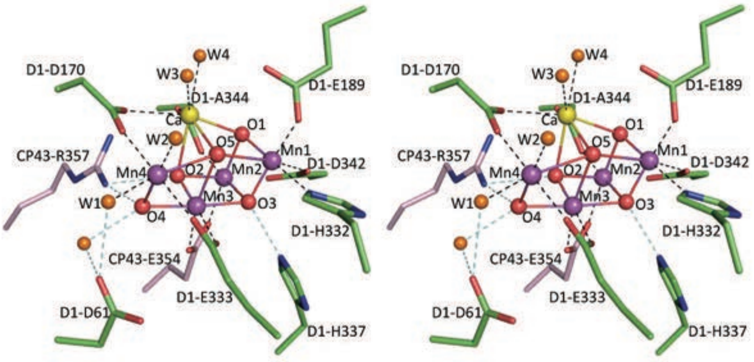

Fig. 3. Stereoview of the Mn_4CaO_5 cluster and its ligand environment. The hydrogen bonds are indicated by cyan broken lines, and the coordinating bonds are indicated by black broken lines. Water molecules are indicated by orange dots [5].

We determined unambiguously the positions of the metal atoms in the Mn_4Ca cluster using the electron density map corresponding to each of the five metal atoms. Five oxygen atoms, which linked each metal atom with oxo-bridges, were also clearly observed with the omitted difference Fourier map (Fig. 2). We therefore determined the Mn_4Ca cluster to be a Mn_4CaO_5 cluster, for the first time.

There are six carboxylate ligands and one histidine ligand for the Mn_4CaO_5 cluster, among which, D1-D170, D1-E333, D1-D342, D1-A344, and CP43-E354 served as bidentate ligands and D1-189 and D1-H332 served as monodentate ligands (Fig. 3). Three oxygen atoms in the cluster, O2, O3, and O4, were hydrogen-bonded by CP43-R357, D1-H337, and CP43-R357, respectively, and two of the oxygen atoms, O1 and O4, were linked to water networks by the hydrogen-bond, but one of the oxygen, O5, was located in the hydrophobic environment surrounded by D1-V185. These hydrogen bonds to the oxygen atoms may stabilize the structure of the cluster (Fig. 3). The cluster structure determined had a distorted chair form. The distortion was caused by the differences in the bond distances between Mn-O and Ca-O. While most of the Mn-O distances are within the range of 1.9-2.1 Å, the distances between one oxygen atom (O5) and 3 Mn atoms (Mn1, Mn3, and Mn4) are in the range of 2.4-2.6 Å, and Ca-O distances are in the range of 2.3-2.5 Å, which are longer than the normal Mn-O distances except for the Mn-O5 distance. Thus, the bond distances between O5 and metal atoms were considerably long. This is a significant feature of the cluster, and may suggest a higher reactivity of O5 compared with other oxo-atoms. Interestingly, two water ligands, W2 and W3, which are bonded to Mn4 and Ca atoms, respectively, are within the range of the hydrogen bond of O5. This suggests that W2, W3, and O5 constitute the site for the water oxidation that reaction leads to the generation of molecular oxygen.

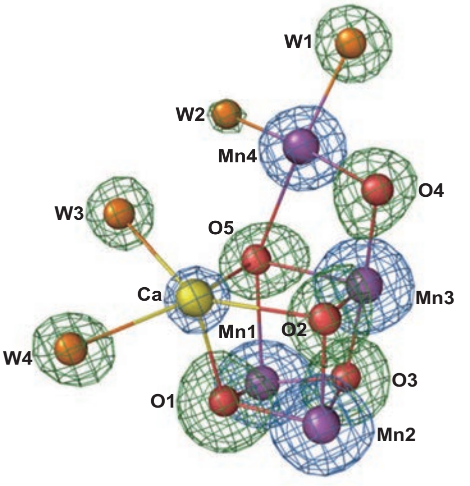

Fig. 2. Determination of individual atoms associated with the Mn_4CaO_5 cluster. The structure of the Mn_4CaO_5 cluster was superposed with the $2F_O$-F_C map (blue) contoured at 5σ for manganese and calcium atoms, and the omitted F_O-F_C map contoured at 7σ for oxygen atoms and water molecules. The cluster formed resembled a distorted chair.

Y. Umena[a,b,*], K. Kawakami[a], J.-R. Shen[c] and N. Kamiya[a,d]

[a] The OCU Advanced Research Institute for Natural Science and Technology (OCARINA), Osaka City Univ.
[b] PRESTO, Japan Science and Technology Agency (JST)
[c] Graduate School of Natural Science and Technology, Okayama University
[d] Graduate School of Science, Osaka City University

*E-mail: umena@ocarina.osaka-cu.ac.jp

References

[1] A. Zouni *et al*.: Nature **409** (2001) 739.
[2] N. Kamiya and J.-R. Shen: Proc. Natl. Acad. Sci. USA **100** (2003) 98.
[3] K.N. Ferreira *et al*.: Science **303** (2004) 1831.
[4] A. Guskov *et al*.: Nat. Struct. Mol. Biol. **16** (2009) 334.
[5] *Y. Umena, K. Kawakamia, J.-R. Shen and N. Kamiya: Nature* ***473*** *(2011) 55.*

Nitric oxide reductase; a key enzyme in understanding structural and functional conversion of respiratory enzymes in their molecular evolution

Respiration is a physiological process to gain the biological energy, ATP, coupled with a reduction of a terminal electron acceptor with electrons e^- and protons H^+. In aerobic respiration, cytochrome oxidase COX pumps H^+ from the inside to the outside of cells, coupled with the reduction of molecular oxygen O_2 ($O_2 + 4e^- + 4H^+ \rightarrow 2H_2O$). The generated proton gradient across the cellular membrane can be utilized for the ATP biosynthesis by ATP synthase. The corresponding enzyme in anaerobic respiration of a microorganism has been considered to be nitric oxide reductase NOR, which is also a membrane-integrated protein catalyzing reduction of NO ($2NO + 2e^- + 2H^+ \rightarrow N_2O + H_2O$: eq.1), but does not exhibit the proton pumping ability. Three billion years ago, photosynthesis by cyanobacteria began, producing O_2 by water oxidation, and the emergence of O_2 on the earth caused a drastic change in the respiration of living systems from anaerobic to aerobic respiration. We determined crystal structures of two bacterial NORs, gram-negative *Pseudomonas aeruginosa* cNOR and gram-positive *Geobacillus stearothermophilus* qNOR, whose diffraction data were collected at beamlines **BL44B2** and **BL41XU** [1,2]. The analysis enabled us to compare structural and functional features of NOR and COX at a molecular level, and provided novel insight into the molecular evolution of respiratory enzymes.

cNOR, which is observed only in denitrifying bacteria, is a cytochrome *c*-dependent enzyme consisting of two subunits, NorB and NorC, whereas qNOR is a related single-peptide and quinol-dependent enzyme that is observed in non-denitrifying pathogenic bacteria as well as in denitrifying bacteria and archaea. The overall structural characteristics of these two NORs, i.e., the configuration of transmembrane (TM) helices as well as the folding of the hydrophilic domain, are almost identical to one another (Fig. 1). A high level of structural similarity of the TM region is found in NORs and COXs, in good consistency with the previous idea that these anaerobic and aerobic respiratory enzymes share the same ancestor protein in their molecular evolution.

On the other hand, the active-site structure of two NORs is somewhat different from that of COX, in which heme iron and copper Cu_B are present, and the His-Tyr linkage in one of the Cu_B ligands is characteristic. In the case of NOR, the catalytic binuclear center is constructed of heme and non-heme irons (Fig. 2). As ligands, the heme b_3 iron has one His, and the non-heme iron Fe_B has three His and one Glu, but His-Tyr is absent. Such differences observed in the active-site structure should be responsible for the difference in the catalytic activities of NOR and COX. In combination with the time-resolved spectroscopic results [3], we proposed a possible mechanism of NO reduction by NOR, in which two NO molecules are shared by ferrous heme b_3 and Fe_B, supporting the so-called trans-mechanism [4].

In the NO reduction reaction catalyzed by NOR (eq. 1), two H^+ are required. The highly conserved Glu ligand of Fe_B of NOR has been suggested to be a terminal donor of protons utilized in the catalytic reaction. The H^+ can be transferred from bulk water to Glu carboxylate through a channel consisting of the hydrogen-bonding network and/or the water chain.

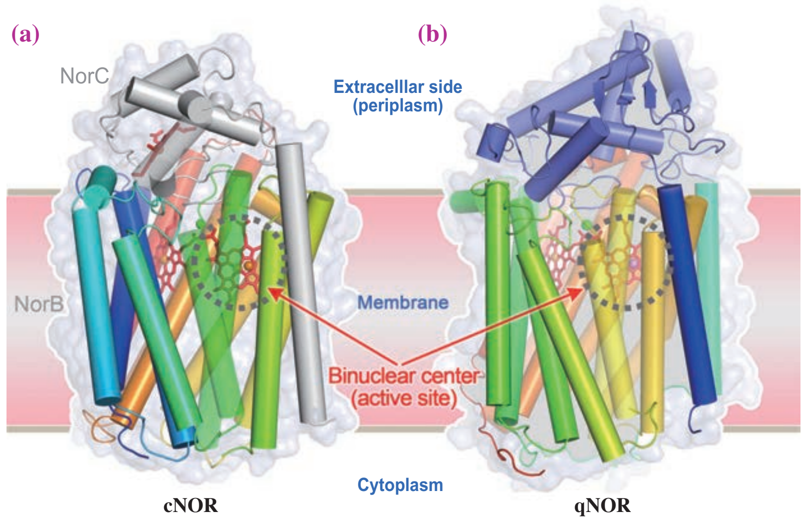

Fig. 1. Overall structures of NORs. **(a)** Crystal structure of *Pseudomonas aeruginosa* cNOR. The helices are represented by cylinders. NorB subunit (colored in rainbow, starting from blue for the N-terminus and ending with red at the C-terminus) contains 12 transmembrane helices with heme *b* and binuclear center (heme b_3 and Fe_B). NorC subunit (gray) contains one transmembrane helix in its N-terminus and cytochrome *c* domain in the periplasmic side. **(b)** Crystal structure of *Geobacillus stearothermophilus* qNOR in a single peptide is shown. The hydrophilic domain in the extracellular side (light blue) shows cytochorme *c*-like fold but lacks heme *c* and its binding motif.

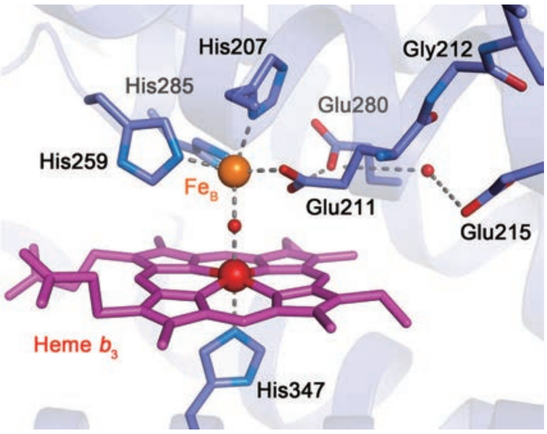

Fig. 2. Binuclear center of *Pseudomonas aeruginosa* cNOR. Heme b_3 is shown by red stick model. The ligands for the non-heme metal Fe_B (orange sphere) shows a distorted trigonal-bipyramidal geometry with three His and one Glu.

In cNOR, there are many water molecules and polar residues in the periplasmic side near the binuclear center, but no hydrophilic region in the cytoplasmic region (Fig. 3(a)). The structural observation suggests that the catalytic proton can be delivered from the periplasmic side, consistent with the previous proposal based on electrometric measurement combined with flow-flash methods. On the other hand, in qNOR, we found the water channel connecting the binuclear center with the cytoplasmic side, while there is no channel in the extracelluar (periplasmic) side (Fig. 3(b)). A molecular dynamic simulation based on these two NOR structures supports the suggestion; i.e., although both NORs exhibit the same NO reduction capability, the proton utilized in the catalytic reaction could be supplied in a different way between cNOR and qNOR. It is also interesting to find that the water channel found in qNOR is located in the same region of the "K-channel" of COX, which can act as the catalytic and pumped protons pathway (Fig. 3(c)). The water channel observed in qNOR might be a prototype of the proton-pumping pathway in O_2 reduction respiration.

Through denitrification, a kind of anaerobic respiration, NOR, of microorganisms in soil and ocean produces a large amount of nitrous oxide N_2O, which is an ozone-depleting and greenhouse gas 310 times more potent than carbon dioxide CO_2. It has been predicted that the amount of N_2O will increase yearly in the 21st century [5]. On the other hand, NOR in pathogenic bacteria can detoxify NO for survival, which is produced by macrophages as a chemical weapon against infection agents. Our NOR structures could contribute to a variety of fields including not only biology and chemistry, but also environmental and physiological sciences.

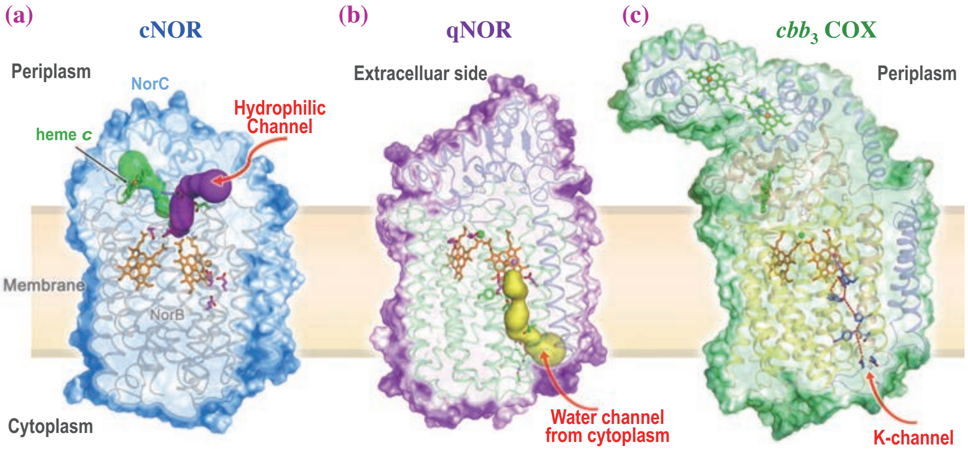

Fig. 3. Possible proton transfer pathways of respiratory enzymes. **(a)** Periplasmic hydrophilic channels observed in crystal structure of cNOR. **(b)** Water channel observed in crystal structure of qNOR. **(c)** K-pathway in cbb_3 cytochrome oxidase connecting the cytoplasmic surface with the active site of oxygen reduction.

Yoshitsugu Shiro

SPring-8/RIKEN

E-mail: yshiro@riken.jp

References

[1] *T. Hino, Y. Matsumoto, S. Nagano, H. Sugimoto, Y. Fukumori, T. Murata, S. Iwata, Y. Shiro: Science* ***330*** *(2010) 1666.*
[2] *Y. Matsumoto, T. Tosha, A.V. Pisliakov, T. Hino, H. Sugimoto, S. Nagano, Y. Sugita, Y. Shiro: Nat. Struct. Mol. Biol.* ***19*** *(2012) 238.*
[3] H. Kumita *et al.*: J. Biol. Chem. **279** (2004) 55247.
[4] T. Hino: Biochim. Biophys. Acta - Bioenergetics (2012) - in press.
[5] A.R. Ravishankara *et al.*: Science **326** (2009) 123.

Crystal structure of O_2-tolerant [NiFe] hydrogenase reveals the mechanism of O_2-tolerance attributable to a redox-dependent conformational change of [4Fe-3S] cluster

Hydrogenases are metalloenzymes that catalyze the reversible oxidation of dihydrogen, and have been considered to be a potential catalyst for biofuel cells and biosensors or an attractive model for bio-mimetic chemical catalysts. [NiFe] hydrogenases have four metal centers: the Ni-Fe active site for catalytic reaction and three iron-sulfur clusters for electron transfer. The Ni-Fe active site is composed of two metals, Ni and Fe, which are supported by four cysteines in the protein molecule [1]. Fe has three additional intrinsic non-protein diatomic ligands [1]. One of the serious weak points in the application of hydrogenases to biocatalysts is their sensitivity to O_2. [NiFe] hydrogenases are reversibly inactivated by O_2, producing two inactive forms, Ni-A and Ni-B. Ni-A is a strong inactive form with a dioxygen species between two metals and requires a prolonged reactivation time, whereas Ni-B has a monoxygen ligand which can be immediately liberated to become an active form upon reduction with H_2 [1]. This kind of well-studied O_2-sensitive [NiFe] hydrogenase is referred to as the "standard" enzymes. Generally, standard [NiFe] hydrogenases do not display the catalytic activity even in the presence of small amounts of O_2. Some H_2-oxidizing bacteria, however, have O_2-tolerant [NiFe] hydrogenases that form only Ni-B after exposure to O_2 and are rapidly reactivated by H_2 to show catalytic activity even at ambient O_2 concentration. Therefore, it has been considered that the prevention of the active site from producing Ni-A upon oxidation is associated with the O_2-tolerance of [NiFe] hydrogenases [2]. In order to elucidate the mechanism underlying the O_2-tolerance of the enzyme, we have carried out diffraction experiments at **BL41XU** and **BL44XU** beamlines, and solved the crystal structures of membrane-bound O_2-tolerant [NiFe] hydrogenase (MBH) from *Hydrogenovibrio marinus* in the reduced and ferricyanide-oxidized forms at 1.18 and 1.32 Å resolution, respectively [3].

MBH is composed of two (large and small) subunits, and the complex with cytochrome *b* catalyses the oxidation of H_2 and the reduction of quinones in its energy metabolism. Standard enzymes are usually crystallized as a heterodimeric unit, whereas MBH is crystallized as a dimer of the heterodimer in the crystal. The overall structure of the heterodimeric unit of MBH and relative disposition of the four metal centers are similar to those of the standard enzymes (Figs. 1(a) and 1(b)). The notable difference is that the Fe-S cluster proximal to the active site of MBH is not a [4Fe-4S] type as in the standard enzyme, but a [4Fe-3S] type. In the H_2-reduced MBH, one of the corner sulfides (S4), which binds to Fe1, Fe2, and Fe4 in the usual [4Fe-4S] cubane cluster (Fig. 2(a)), is replaced by a nearby cysteinyl sulfur (Cys25) and another cysteinyl sulfur (Cys126) coordinate Fe4 (Fig. 2(b)). One bond, Fe4-S4, in the cubane [4Fe-4S] cluster is missing, but all four iron atoms are coordinated by four ligands. Despite the difference of the coordination features, the whole shape of the cluster including the coordinating cysteinyl sulfur atoms is very similar to that of the standard

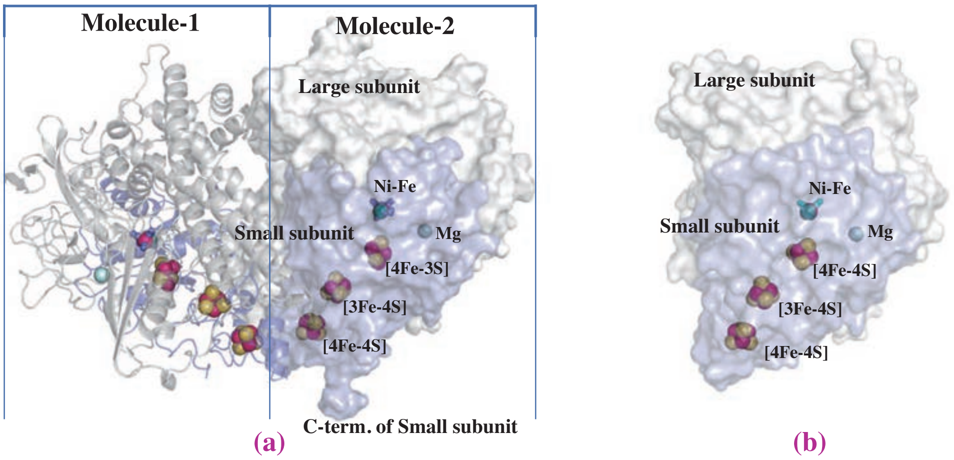

Fig. 1. Overall structures of [NiFe] hydrogenases. [NiFe] hydrogenases are composed of large (gray) and small (light blue) subunits. **(a)** Membrane-bound O_2-tolerant (MBH) enzyme from *H. marinus* in a dimeric form in this study. **(b)** Standard enzyme from *D. vulgaris* Miyazaki. Protein folding is schematically depicted in ribbon and/or surface models, whereas metal centers are shown in spheres. Ni, Fe, Mg, and S atoms are colored green, red, cyan, and yellow, respectively.

enzyme. The proximal Fe-S cluster revealed redox-dependent structural changes when the enzyme was exposed to an oxidant. In the ferricyanide-oxidized condition, deprotonated amide nitrogen of Cys26 replaced the S3 ligand of Fe2 (Fig. 2(c)). This ferricyanide-oxidized form of the cluster was recovered upon re-reduction with H_2 or titanium(III) citrate, indicating that this redox-dependent structural change is reversible.

EPR redox titration of MBHs from *R. eutropha* H16 and *A. aeolicus* showed four distinct one-electron transitions attributable to three iron-sulfur clusters [4,5]. Three of four mid-potentials were consistently assigned to three clusters. The metal center with the remaining highest potential had some interactions on both Ni in the active site and the medial [3Fe-4S], suggesting that this high-potential species should be assigned to the proximal cluster. Namely, the proximal cluster was proposed to have two midpoint potentials (dual redox character). These results are astonishingly consistent with our findings described above. The net charge of the [4Fe-3S]-6Cys in MBH established in this study is equal to that of [4Fe-4S]-4Cys in the standard enzymes, assuming that the oxidation states of the iron atoms are identical. The redox transition of 4+/3+ (corresponding to 2+/1+ for cubane [4Fe-4S] cluster) is most probable for the proximal [4Fe-3S] cluster during the H_2-oxidation catalytic cycle. The superoxidation of the proximal cluster to $[4Fe\text{-}3S]^{5+}$ should require the conformational change and concomitant donation of an additional negative charge to the Ni-Fe active site. In this superoxidized structure, an additional negative charge of the deprotonated amide nitrogen, which coordinates Fe2, should stabilize a higher oxidation state of the iron atoms. Two previously proposed single-electron transitions of the proximal cluster in MBH (that is, $[4Fe\text{-}3S]^{5+/4+/3+}$) can thus be reasonably explained by the redox-dependent conformational change observed in this study. In standard enzymes, Ni-A is considered to be produced by the oxidation of the active site with O_2 under electron-deficient conditions, whereas Ni-B is formed under electron-rich conditions [2]. Therefore, having a higher redox potential and a two-electron donation property in the proximal cluster are advantageous in preventing the formation of Ni-A. Our results provide a structural basis that underlies the unprecedented function of the [4Fe-3S] cluster in the O_2 tolerance of MBH, which acquires a superoxidized state to supply two electrons and one proton for the reduction of O_2 through a redox-dependent conformational change.

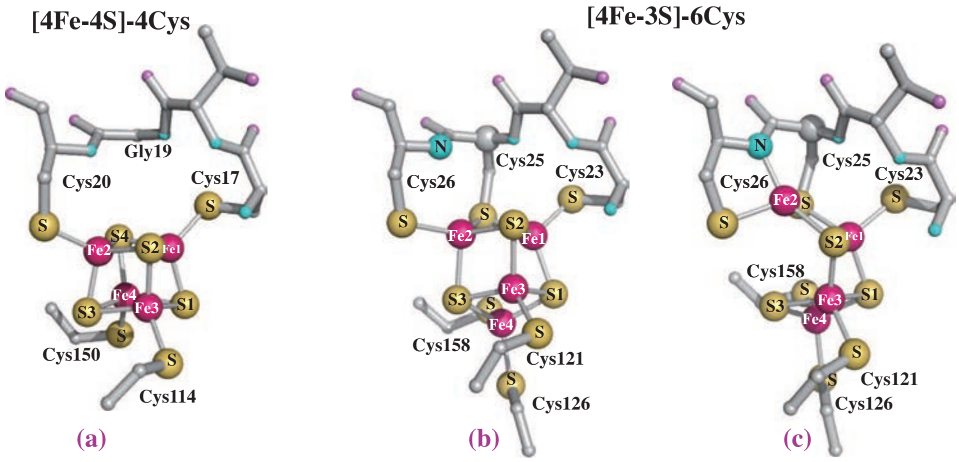

Fig. 2. [4Fe-4S] and [4Fe-3S] clusters. Cubane-type [4Fe-4S] cluster **(a)** in standard enzymes is coordinated by four cysteines, whereas [4Fe-3S] cluster in H_2-reduced **(b)** and ferricyanide-oxidized **(c)** forms found in this study are coordinated by six cysteines. Fe and S atoms in the inorganic part are labeled by element symbols with numbers, whereas S atoms belong to cysteine residues, and the amide N atom participating in the coordination to Fe2 are without numbers. Fe, S, N, O, and C atoms are colored red, yellow, cyan, pink, and gray, respectively.

Yasuhito Shomura and Yoshiki Higuchi*

Department of Life Science, University of Hyogo

*E-mail: hig@sci.u-hyogo.ac.jp

References

[1] H. Ogata *et al.*: Dalton Trans. (2009) 7577.
[2] J.A. Cracknell *et al.*: Proc.Natl Acad. Sci. USA **106** (2009) 20681.
[3] *Y. Shomura, K. Yoon, H. Nishihara and Y. Higuchi: Nature **479** (2011) 253.*
[4] M.E. Pandelia *et al.*: Proc. Natl Acad. Sci. USA **108** (2011) 6097.
[5] T. Goris *et al.*: Nature Chem. Biol. **7** (2011) 310.

Crystal structure of SecDF, a Sec translocon-associated membrane protein

Most proteins synthesized in the cytoplasm are secreted across membranes. The bacterial Sec Translocon, consisting of three membrane proteins, SecY, SecE, and SecG, provides a channel-like pathway for protein translocation. SecA ATPase drives the protein movement across the membrane (Fig. 1(a)), which is facilitated by the proton motive force (PMF) and a membrane-integrated Sec component, SecDF [1,2]. However, the structure and function of SecDF have remained unclear. We reported the first crystal structure of SecDF and elucidated the mechanism of SecDF-driven protein translocation through a structure-based functional analysis [3,4].

The functional importance of SecDF was previously shown *in vivo* and *in vitro*. For instance, a SecDF-deficient *Escherichia coli* strain is severely defective in protein export, exhibiting cold sensitivity for growth. Despite the vital importance of SecDF *in vivo*, the mechanism of protein transport enhancement by SecDF has not been defined. To clarify how SecDF is involved in protein translocation in detail, we started structural biological analysis of SecDF in 2004. In 2006, we obtained an initial electron density map of SecDF at ~4.0 Å resolution by the single-wavelength anomalous dispersion method using selenomethionine-labelled crystals. However, the low quality of the initial map hampered the model building. To address this problem, we separately determined the higher resolution structures of periplasmic domains, P1 and P4, by X-ray crystallography and NMR, respectively. These periplasmic structures enabled us to correctly build the SecDF model. In 2010, we finally refined the structure of full-length *T. thermophilus* SecDF, consisting of 735 residues, at 3.3 Å resolution (Fig. 1(b)). The X-ray diffraction data sets for full-length SecDF were collected at beamline **BL41XU**.

As shown in Fig. 1(b), transmembranes (TM) 1-6 and TM7-12 are assembled in a pseudo-symmetrical manner. The periplasmic surface of the TM regions is covered by the P1 and P4 domains. The P1 domain is composed of head and base subdomains. The head domain protrudes into the periplasmic space, while the two connecting loops between the head and base subdomains form a constricted region.

A comparison of the crystal structure of full-length SecDF (called the F form; Fig. 2(a)) with the model of the full-length I form, which was built by docking the base subdomain of the isolated P1 structure onto that of the full-length SecDF (Fig. 2(b)), revealed a significant difference in the head-to-base orientation of the P1 domain. This conformational transition is due to the ~120° rigid-body rotation of the head domain. *In vivo* and *in vitro* analyses using *E. coli* SecDF suggested that conformational flexibility of the essential P1 domain is required for effective protein translocation. In addition, biochemical experiments revealed that the flexible P1 domain directly interacts with unfolded proteins, such as preproteins.

The TM arrangement of SecDF is similar to that of multidrug efflux transporter AcrB [5]. Homotrimeric AcrB extrudes a variety of drugs by utilizing the proton gradient across the membrane, whereas SecDF functions as a monomer associated with the Sec translocon. We propose that the conserved Asp and Arg residues at the transmembrane interface between the TM1-6 and TM7-12 bundles (Fig. 1(b)), in a similar manner to the conserved charged residues of AcrB, play essential roles in the movements of protons and preproteins. The mutants in which the

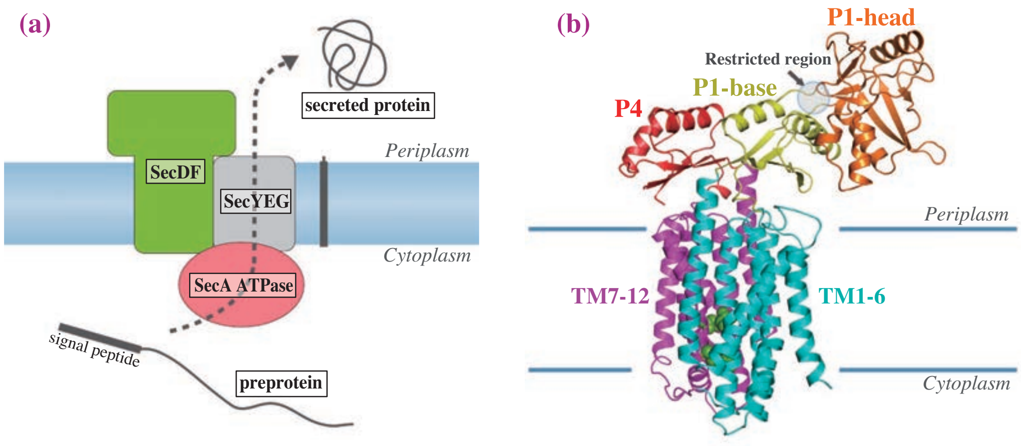

Fig. 1. **(a)** Protein translocation *via* Sec machinery. **(b)** Crystal structure of SecDF.

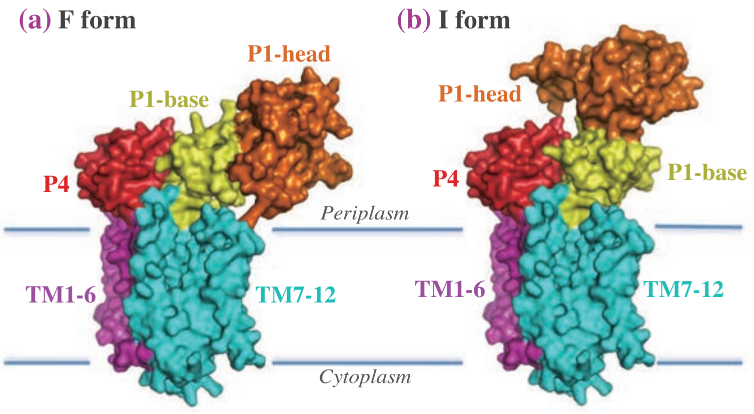

Fig. 2. Conformational transition of SecDF. **(a)** F form, **(b)** I form.

charged residues in *E. coli* SecDF were replaced by uncharged residues lacked the SecDF activity. This observation is consistent with the hypothesis that the charged residues in the TM region of SecDF participate in proton transport. The highly conserved SecDF regions are clustered from the center of the TM to the periplasmic base region underneath the head. The hinge motion of the P1 domain is likely to be functionally related to the proton flow through the TM region of SecDF.

Taken all together, we proposed the working model of SecDF-enhanced protein translocation (Fig. 3). The Sec translocon could be just underneath the protruding P1 head domain, enabling it to interact with a translocating preprotein *via* the Sec translocon. The preprotein-capturing F form could transform to the I form, preventing the backward movement of the preprotein, which leads to acceleration of protein transport. Then, the preprotein-releasing I form could convert to the F form. By repeating this conformational transition cycle coupled with proton flow, SecDF can facilitate protein transport. Here, we did not describe functional analysis of Vibrio SecDF or the electrophysiological analyses of SecDF, as mentioned in the original paper [3], owing to space limitations. Indeed, all of our data is consistent with the idea that SecDF utilizes the proton gradient across the membrane for protein translocation. We finally propose that SecDF functions as a dynamic, membrane-integrated chaperone, which is possibly powered by the proton-motive force, to actively complete Sec translocon-mediated protein translocation. Although the crystal structural information for all of the Sec proteins, Sec translocon, SecA ATPase, and SecDF is now available, it is unclear how the Sec proteins interact with each other and form the Sec translocon complex. To fully understand the SecA-dependent protein translocation, we are still attempting to obtain much more information about the Sec translocon machinery.

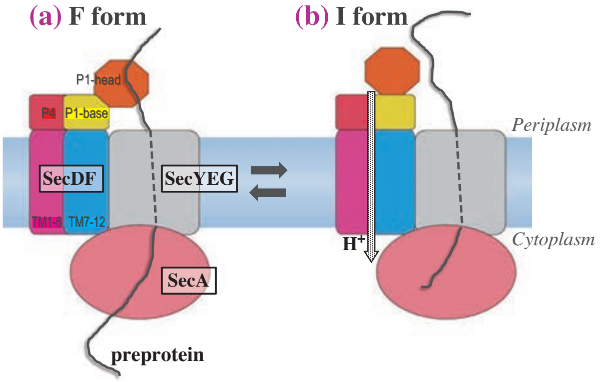

Fig. 3. Working model of PMF-driven protein translocation by SecDF. **(a)** F form, preprotein-capturing state. **(b)** I form, preprotein-releasing state.

Tomoya Tsukazaki* and Osamu Nureki

Graduate School of Science, The University of Tokyo

*E-mail: ttsukaza@biochem.s.u-tokyo.ac.jp

References

[1] E. Park, T.A. Rapoport: Annu. Rev. Biophys. (2012) - in press.
[2] T. Tsukazaki *et al*.: Nature **455** (2008) 988.
[3] *T. Tsukazaki, H. Mori, Y. Echizen, R. Ishitani, S. Fukai, T. Tanaka, A. Perederina, D.G. Vassylyev, T. Kohno, A. Matsurana, K. Ito, O. Nureki: Nature* ***474*** *(2011) 235.*
[4] *Y. Echizen, T. Tsukazaki, N. Dohmae, R. Ishitani, O. Nureki: Acta. Crystallogr. F* ***67*** *(2011) 1367.*
[5] S. Murakami *et al*.: Nature **443** (2006) 173.

The flagellar type III protein export apparatus and F/V type ATPases share a common architecture

Bacteria swim in liquid environment using a helical filamentous organelle called the flagellum, which is composed of a rotary motor and an axial tubular structure. The flagellum is a large macromolecular assembly made of tens of thousands of almost 30 different protein molecules, most of which are exported to the distal end of the growing flagellum for self-assembly. The axial component proteins and the proteins that help flagellar assembly are efficiently translocated from the cytoplasm into the 2 nm central channel of the growing flagellum by the flagellar protein export apparatus [1]. The proteins involved in the flagellar protein export is highly homologous to those of the type III secretion system of pathogenic bacteria, which injects virulence effectors directly into their eukaryotic host cells for invasion. Thus the understanding of flagellar protein export will provide useful information for unveiling the mechanism of the virulence type III secretion system.

The flagellar export apparatus consists of the export gate made of six integral membrane proteins and three soluble proteins, FliH, FliI and FliJ [2]. These soluble components assemble onto and disassemble from the gate during the export cycle (Fig. 1). FliI is an ATPase that facilitates the flagellar protein export process, and FliH regulates the ATPase activity of FliI. FliI shows an extensive structural similarity to the α/β subunits of F_oF_1-ATP synthase [3]. FliI forms a homo hexamer ring just like the one formed by three α/β hetero dimers, which is the core part of F_1-ATPase. FliH was identified to have a sequence homology with the b and δ subunits of F_1-ATPase, which form the peripheral stalk connecting F_1 with F_o to function as the stator. FliJ is essential for efficient protein export but its function remains obscure. FliJ seems to regulate the entire export process through the dynamic interactions with its binding partners, because it interacts with various flagellar proteins. To elucidate the molecular mechanism of the flagellar protein export and the role of FliJ in the export process, we carried out the structural analysis of FliJ from *Salmonella enterica* serovar Typhimurium [4].

FliJ is a 17 kDa protein consisting of 147 residues. FliJ tends to form insoluble aggregates, but the addition of three residues, Gly-Ser-His, to its N-terminus as a His-tag stub prevented it from aggregation. This allowed us to crystallize FliJ for structure determination. The FliJ structure was solved at 2.1 Å resolution by using anomalous X-ray diffraction data from a mercury derivative crystal collected at beamline **BL41XU**.

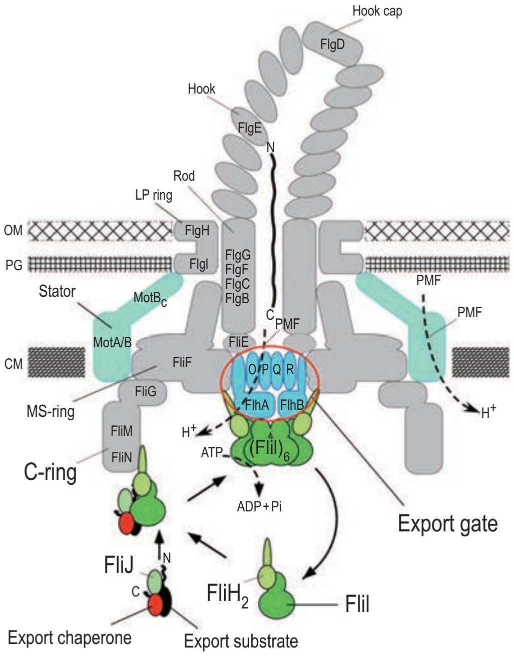

Fig. 1. Schematic diagram of the bacterial flagellar type III protein export apparatus. FlhA, FlhB, FliO, FliP, FliQ and FliR are integral membrane components and FliH, FliI and FliJ are cytoplasmic components. FliI forms a hetero-trimer with the FliH dimer in the cytoplasm and assembles into a hexamer upon docking to the gate with FliH and FliJ.

FliJ consists of two long α-helices that form an anti-parallel coiled-coil structure. This structure is remarkably similar to the coiled-coil region formed by the N- and C-terminal α-helices of the γ subunit of F_1-ATPase (Fig. 2). Although FliJ and the γ subunit have no apparent sequence similarity, structure-based sequence alignment revealed a conserved region between them. The conserved residues are localized on the surface where the ε subunit interacts with the γ subunit in F_1-ATPase, suggesting that FliJ may interact with a protein corresponding to the ε subunit in the export apparatus (Fig. 2).

The structural similarities between FliJ and the γ subunit and between FliI and the α/β subunits imply that FliJ and FliI may form a complex similar to F_1-ATPase. In fact, when FliI and FliJ were mixed at a molar ratio of 6:1 with Mg^{2+}-ADP-AlF_4, the FliI ring formation was much enhanced, suggesting that FliJ interacts with the FliI ring and facilitates the ring formation. The FliI and FliI-FliJ ring complexes,

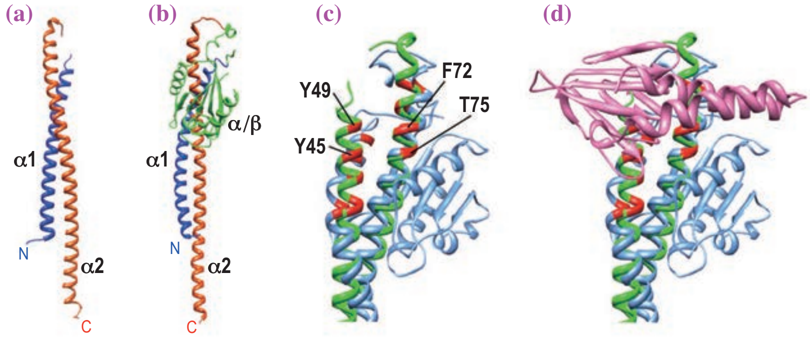

Fig. 2. Structural comparison of FliJ and the γ subunit of F_1-ATPase. Cα ribbon representation of **(a)** FliJ and **(b)** the γ subunit of F_1-ATPase. The α1 and α2 helices and the α/β domain of the γ subunit are colored blue, red and green, respectively. **(c) (d)** Close-up view of the conserved region between FliJ and the γ subunit. FliJ (green) is superimposed to the γ subunit (light blue). Residues conserved among FliJ homologs and γ subunits are shown in red. **(d)** The ε subunit (pink) is indicated with FliJ and the γ subunit. [4]

however, were not stable enough for crystallization work. We therefore analyzed the structures of the complexes by electron cryomicroscopy. Because the orientation of the ring particles embedded in vitreous ice was strongly biased to end-on views, we constructed 2D averaged images of the complexes and compared them. The averaged image of the FliI ring showed a hexameric ring structure with a central hole of 2 nm in diameter. On the contrary, the mixture of FliI and FliJ showed the same hexameric ring as the FliI ring but an extra density was identified in the central hole. These observations indicate that FliJ penetrates into the central hole of the FliI hexamer ring just like the γ subunit of F_1-ATPase (Fig. 3).

On the basis of these structures we proposed a model of the export apparatus (Fig. 4). The structural similarities found in this study suggest a similar mechanism and an evolutionary relationship between the type III protein export system and F- and V-type ATPases, despite that these two biological nanomachines have been thought to be totally unrelated to each other.

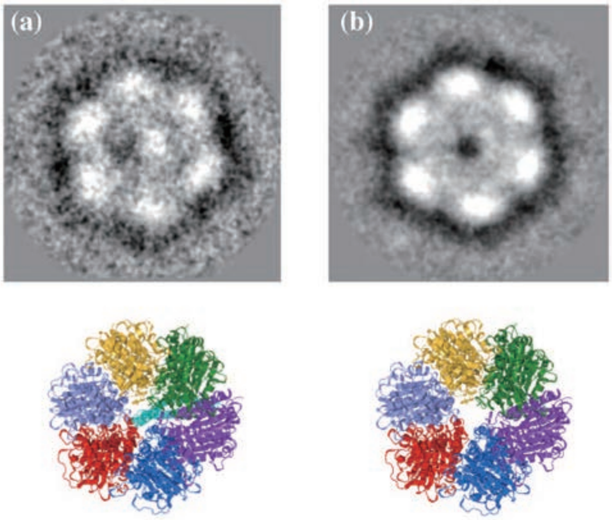

Fig. 3. Averaged cryoEM images of the FliI-FliJ **(a)** and FliI **(b)** ring complexes. Plausible ribbon models are indicated below each EM image.

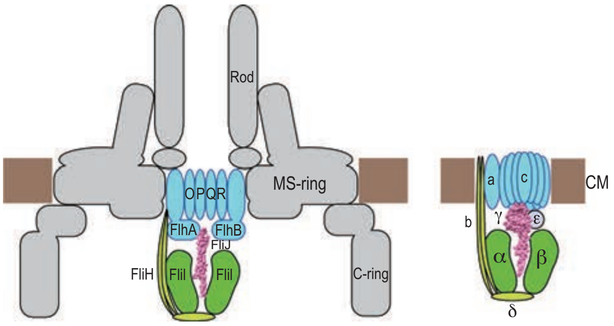

Fig. 4. Schematic diagram of a plausible model of the FliH-FliI-FliJ complex attached to the export gate. F_oF_1-ATP synthase is shown in the right panel as a reference. The flagellar basal body is colored gray. CM is the cytoplasmic membrane. [4]

Katsumi Imada[a,*], Tohru Minamino[b] and Keiichi Namba[b]

[a] Dept. of Macromolecular Science, Osaka University
[b] Dept. of Frontier Biosciences, Osaka University

*E-mail: kimada@chem.sci.osaka-u.ac.jp

References

[1] T. Minamino *et al.*: Mol. Biosyst. **4** (2008) 1105.
[2] T. Minamino and R.M. Macnab: J. Bacteriol. **181** (1999) 1388.
[3] K. Imada *et al.*: Proc. Natl. Acad. Sci. USA **104** (2007) 485.
[4] *T. Ibuki, K. Imada, T. Minamino, T. Kato, T. Miyata and K. Namba: Nat. Struct. Mol. Biol.* ***18*** *(2011) 277.*

Crystal structure of the proton pumping rhodopsin ARII from marine alga *Acetabularia acetabulum*

The membrane protein rhodopsins, consisting of opsin with seven helices and a retinal chromophore, can be classified in three types according to their electrical properties: 1) ion pump, including the proton pump of bacteriorhodopsin (BR) from the archaeon *Halobacterium salinarium* and the chloride pump of *Natronomonas* halorhodopsin (NpHR); 2) channel rhodopsin, such as the cation channels from *Chlamydomonas* (ChR1,2); and 3) electrically neutral rhodopsin, such as the visible photoreceptor in the human retina and *Anabaena* sensory rhodopsin (ASR). The best-studied rhodopsin is BR, in terms of its proton transport mechanism. BR at the ground state, and the intermediates K, L, M, N and O during the photocycle, have been analyzed by spectroscopic methods and X-ray crystallography. Proton pumping rhodopsins have been widely found in not only archaea, but also bacteria and eukarya. The first proton pumping rhodopsin discovered in a green plant was the rhodopsin from the marine alga *Acetabularia acetabulum*. Recently, some algal rhodopsins have been applied in neurosciences. Neuron spiking in nerve cells expressing chloride and proton pumps, including NpHR and *Acetabularia* rhodopsin (AR), and the channel rhodopsins, including ChR2, can be controlled by laser light, even in the mouse brain. Furthermore, a modified NpHR, engineered for high level expression in neurons, was used for ultrafast optogenetics.

We now describe the crystal structure and the function of a newly identified AR, ARII [1]. ARII was synthesized by a cell-free protein synthesis system with detergent/lipid [2], and was crystallized by the *in meso* method, using monoolein. Many reddish-purple, plate-like crystals (Fig. 1) grew to sizes of 100×100×10 μm^3 at 20°C in two weeks. The ARII crystal was picked from the lipidic mesophase and flash-cooled in a nitrogen stream at –180°C, as soon as the seal of the glass plate was opened. Data collection was performed using a 10 μm-size microbeam at **BL41XU** beamline. The crystals were unstable under the open air conditions, and were easily damaged during handling with the micro tool. Thus, the crystal-picking and diffraction check were performed repeatedly, until diffraction pattern images that could be indexed were obtained. The crystal structure of ARII, consisting of seven helices (A to G) and a retinal molecule, was determined at 3.2 Å resolution (Fig. 2). Four ARII proteins with eight cholesterol molecules were observed in the asymmetric unit. A structural alignment (Fig. 3) performed by the DALI server revealed that the ARII structure is quite similar to those of other rhodopsins, such as BR, *Natronomonas pharaonis* sensory rhodopsin II (NpSRII), and ASR. The highly conserved regions of helix C and the C-terminal portion of helix F might participate in a common mechanism for ion-pumping and photo-sensing by rhodopsin, because the local flex of helix C at the L-intermediate and the outward movement of helix F at the M2-intermediate have been observed in BR and NpSRII. In helix G, the carbonyl groups of Val208 and Leu209 form hydrogen bonds with the amide NH groups of Leu213 and Asn214, respectively. These interactions create a π-bulge and kink the helix at Lys211, which is bound with the all-*trans* retinal chromophore and forms a Schiff base.

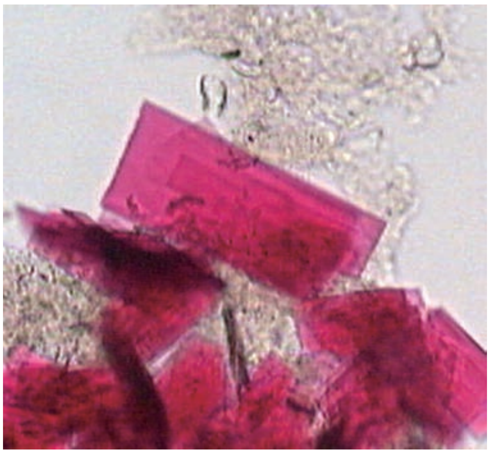

Fig. 1. Crystals of ARII. The reddish-purple plate-like crystals were grown in a monoolein mesophase.

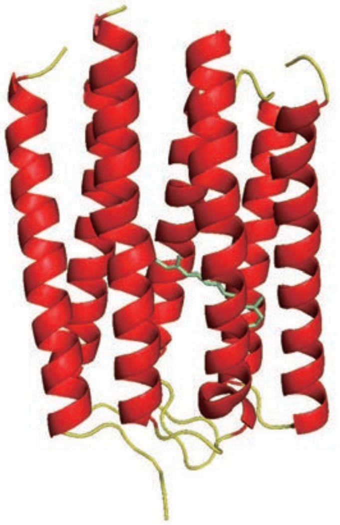

Fig. 2. Crystal structure of ARII. The seven α-helices and the loops in the opsin are colored red and yellow, respectively. The retinal molecule is light green.

At the transition from the L to M state in the BR

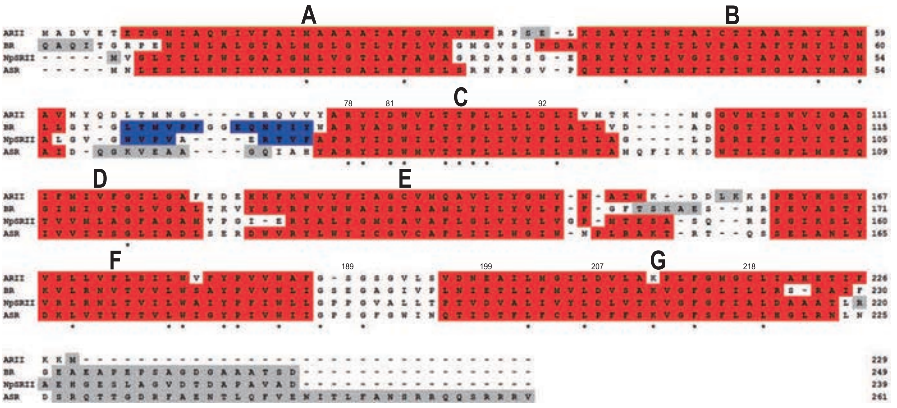

Fig. 3. Structure-based sequence alignment of ARII with BR, NpSRII, and ASR. The α-helices, β-strands, and undetermined regions are shown in red, blue, and gray, respectively. The identical residues in the sequence alignment are marked by asterisks. The residue numbers are provided in the column on the right side of the alignments, and above the ARII residues involved in the proton transfer.

photocycle, a proton is transferred from the protonated Schiff base to the carboxyl oxygen atoms of Asp85. The Schiff base is hydrogen-bonded to a water molecule, which forms a hydrogen-bond network with Asp85, Asp212, Arg82, and two water molecules. A proton is then released to the extracellular space from the proton release group, consisting of Arg82, Glu194, and Glu204. Recently, it was suggested that Glu194 and Glu204 in BR are bonded by a delocalized proton, and a low-barrier hydrogen bond might be advantageous for rapid proton release. In ARII, rapid proton release does not occur at neutral pH. We compared the structure of the proton release pathway in ARII with those in BR and NpSRII. The structure-based alignment diagram (Fig. 3) indicated that Asp85, Asp212, Arg82, Glu194, and Glu204 in BR correspond to Asp81, Asp207, Arg78, Ser189, and Glu199 in ARII, and Asp75, Asp201, Arg72, Pro183, and Asp193 in NpSRII. The superposition of the crystal structure of ARII onto that of BR revealed that the side chains of these residues fit well with those of BR. However, the orientation of the Arg78 side chain is opposite to that of the corresponding Arg82 of BR (Fig. 4), but the same as that of Arg72 of NpSRII, which is capable of proton transfer. In BR, proton release is triggered by the movement of the Arg-82 side chain toward the glutamate pair upon the formation of the M intermediate, causing the p*K*a of the proton releasing residue to dramatically change (9.7 to 5.7). In NpSRII and ARII, this Arg side chain does not move, since its guanidium moiety is oriented toward Asp193$^{\mathrm{NpSRII}}$ or Glu199$^{\mathrm{ARII}}$ at the ground state. The pKa of Asp193 in NpSRII is 6.4 at the ground state, and 4.9 at the M-intermediate, and the rapid proton release occurs at neutral pH, unlike ARII. No electron density was observed between the ε1 oxygen atom of Glu199 and the η1 nitrogen atom of Arg78 at a 3.9 Å distance in the map. Therefore, a water molecule may not exist around Glu199 and Arg78 in ARII. This may disrupt the formation of the low-barrier hydrogen bond at Glu199, resulting in the "late proton release" observed by biochemical analyses, such as proton transfer measurements with the ITO electrode and flash-photolysis. This is the first report on the crystal structure of a eukaryote-derived microbial rhodopsin, synthesized functionally by a cell-free synthetic method.

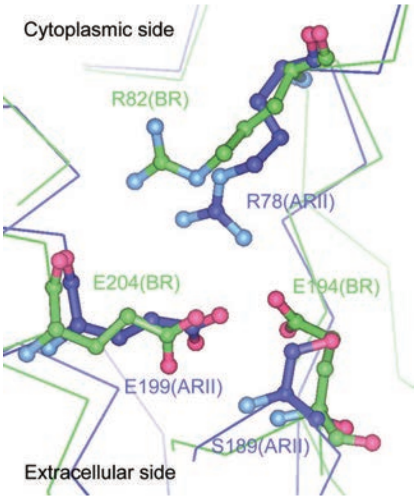

Fig. 4. Amino acid residues involved in the proton transfer. Superimposition of the ARII and BR structures, colored blue and green, respectively.

Takashi Wada[a] and Shigeyuki Yokoyama[a,b,*]

[a] RIKEN Systems and Structural Biology Center (Yokohama)
[b] Lab. of Structural Biology, The University of Tokyo

*E-mail: yokoyama@biochem.s.u-tokyo.ac.jp

References

[1] *T. Wada, K. Shimono, T. Kikukawa, M. Hato, N. Shinya, S.Y. Kim, T. Kimura-Someya, M. Shirouzu, J. Tamogami, S. Miyauchi, K.H. Jung, N. Kamo and S. Yokoyama: J. Mol. Biol.* ***411*** *(2011) 986.*

[2] *K. Shimono, M. Goto, T. Kikukawa, S. Miyauchi, M. Shirouzu, N. Kamo and S. Yokoyama: Protein Sci.* ***18*** *(2009) 2160.*

X-ray structure of functional full-length dynein motor domain

Dyneins are large motor complexes of 1–2 MDa that use ATP as an energy source to move toward the minus ends of microtubules [1,2]. This motor activity is crucial for a variety of cellular processes within eukaryotic cells, including the beating of cilia and flagella, cell division, cell migration, and the intracellular trafficking of various vesicles and organelles along microtubules. Dyneins power a wide range of cellular motility through the coordinated action of a number of subunits of the dynein complex together with various associated cellular components. Among them, the heavy chain (molecular mass ≥500 kDa), belonging to the AAA+ superfamily of mechanochemical enzymes, is solely responsible for dynein's fundamental motor activities, such as ATP-hydrolysis, ATP-sensitive microtubule-binding and microtubule-based motile activities. Truncation studies have shown that the C-terminal 380-kDa portion of the heavy chain alone is sufficient to exert the motor activities, thus defining this portion as the dynein motor domain.

Here, we report an X-ray crystallographic analysis of a functional full-length motor domain of cytoplasmic dynein from *Dictyostelium discoideum* at 4.5 Å resolution, which revealed the detailed architecture of the functional units required for dynein's motor activity [3]. Structural analysis was carried out using beamline **BL44XU**. Our analysis also provides structural insight into how dynein coordinates microtubule-binding and ATPase activities to produce force and movement along microtubules.

On the basis of good-quality maps at 4.5 Å resolution that clearly show α-helices and β-sheets, we assigned the helices to the functional units in the dynein motor domain (Fig. 1). The central AAA+ ring was identified to be composed of six AAA+ modules (AAA1–AAA6) arranged in a ring-shaped structure with pseudo-six-fold symmetry by referring to the structures of typical AAA+ proteins that are usually composed of an N-terminal domain with an α/β Rossmann fold and a C-terminal α-helical domain. In each of the six AAA+ modules, the α domain stretches outward from the α/β domain (Fig. 2). Two prominent coiled coils (CCs) protrude from the AAA+ ring. One is the stalk CC, which includes the small microtubule-binding domain (MTBD) at the tip (Fig. 2, yellow arrowhead). The other is a novel CC that interacts with the side of the stalk CC as if it works as a strut (Fig. 2, orange arrowhead). Therefore, we named it the "strut CC". A series of helices were found above the front face of the AAA+ ring, (Fig. 3, magenta), which we identified as the core of the linker unit, corresponding to the ~550 amino acid residues N-terminal to AAA1. On the back face of the AAA+ ring, two groups of helices were found (Fig. 3, gray), both of which were assigned as the C-terminal non-AAA+ sequence (C-sequence: ~400 residues).

The linker unit, which has been supposed to act as a mechanical lever or winch during dynein's force generation [4], is mainly composed of a series of helices running parallel to the long axis of the unit. This rodlike structure bridges AAA1 and AAA4 by lying over the hole of the AAA+ ring. Notably, the linker is only in contact with AAA1 and AAA4 at the terminal portions, without any significant contacts with the other AAA+ modules. This architecture may allow the linker to swing as a rigid body around the linker-AAA1 junction (Fig. 3, magenta arrowhead) during the ATPase-dependent powerstroke [5].

The stalk and strut CCs are the most striking features of the dynein structure outside the AAA+ ring. One of the two helices of the stalk CC runs to the MTBD directly from one of the helices in the AAA4 α domain, while the other helix of the stalk CC returns from the MTBD to another helix in the same α domain

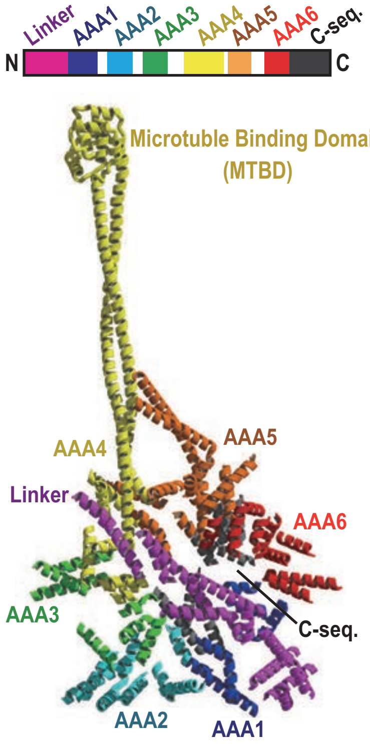

Fig. 1. Structure and sequence diagram of the dynein motor domain, showing the functional units: the linker, the ring containing six AAA+ modules, the C-sequence, and the microtubule-binding domain (MTBD).

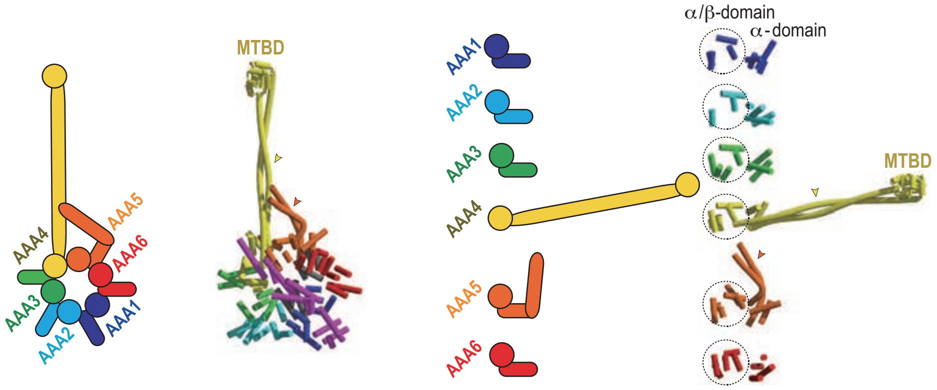

Fig. 2. AAA+ modules of the dynein motor domain. (left) Hexameric organization of the AAA+ modules. (right) Schematic presentation of the α and α/β domains. The yellow and orange arrowheads indicate the stalk and strut coiled coils, respectively.

(Fig. 2). Thus, the stalk CC can be regarded as a huge extension of the two helices in the AAA4 α domain, suggesting its evolutionary origin. Likewise, the strut CC can be described as a long extension of the corresponding helices in the AAA5 α domain (Fig. 2). This second long CC bends sharply at its middle and comes into direct contact with the middle region of the stalk CC, forming a Y-shaped structure together with the stalk CC. Collectively, our structure shows that the stalk unit is not an independent structure located between AAA4 and AAA5 as previously assumed, but is instead a component of a more complex structure composed of the stalk and strut CCs, as extensions of AAA4 and AAA5.

A widely held assumption about the two-way communication is that the structural information would be propagated to the base of the stalk CC through AAA1, 2, 3 and 4 in an ATPase-related manner analogous to other AAA+ proteins, because the first four modules, but not AAA5 or 6, have ATP/ADP-binding or ATP-hydrolyzing activity. However, mutagenesis of the ATP/ADP binding sites in AAA2–4 does not completely block the communication between AAA1 and MTBD, and thus does not support this hypothesis. Instead, we favor the idea that the C-sequence–AAA5–strut CC serves as a two-way communication pathway between the AAA1 ATPase site and the MTBD at the tip of the stalk CC, because of the structural feature that the C-sequence lies on the AAA+ ring, and directly linking the AAA1 and AAA5 modules. This model is also compatible with previous biochemical studies providing evidence that the C-sequence regulates the AAA1 ATPase activity [6].

Even though the resolutions of the crystal structure are not yet high enough to map the motor domains at the atomic level, the α-helical model of the full-length motor domain presented here provides new insights into the mechanism of action of dynein, particularly the long-range two-way communication mechanism between the ATPase site and the MTBD.

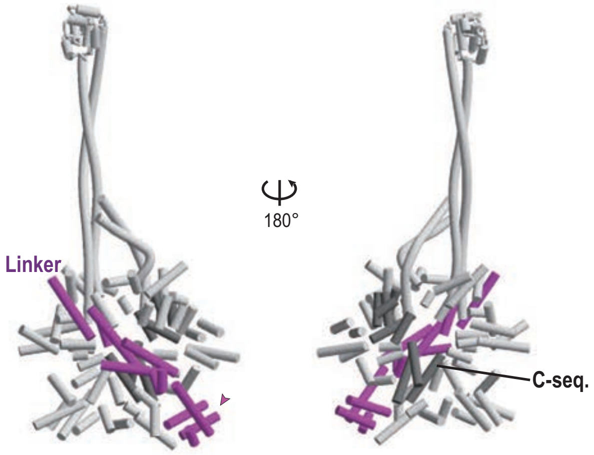

Fig. 3. Front and back views of the cylinder model of the dynein motor domain. The linker and C-sequence units are shown as magenta and gray helices, respectively.

Takahide Kon[a], Kazuo Sutoh[b] and Genji Kurisu[a,*]

[a] Institute for Protein Research, Osaka University
[b] Faculty of Science and Engineering, Waseda University

*E-mail: gkurisu@protein.osaka-u.ac.jp

References

[1] I.R. Gibbons, A.J. Rowe: Science **149** (1965) 424.
[2] B. M. Paschal, R.B. Vallee: Nature **330** (1987) 181.
[3] *T. Kon, K. Sutoh, G. Kurisu: Nature Strut. Mol. Biol. **18** (2011) 638.*
[4] S.A. Burges *et al.*: Nature **421** (2003) 715.
[5] A.J. Roberts *et al.*: Cell **136** (2009) 485.
[6] N. Numata *et al.*: Biochem. Soc. Trans. **36** (2008) 131.

Structure of florigen activation complex

Florigen, a mobile floral induction factor encoded by *FLOWERING LOCUS T (FT)* and its homologs, is thought to form a complex with the bZIP transcription factor FD to activate floral identity genes such as *APETALA1 (AP1)* at the shoot apex. However, many details of the molecular function of florigen remain unclear. Here, we present the 2.4 Å crystal structure of a rice floral induction complex, named the florigen activation complex (FAC), which consists of the rice florigen Hd3a, the FD homolog OsFD1, and a 14-3-3 protein [1]. Unexpectedly, 14-3-3 plays a key role by mediating an indirect interaction between Hd3a and OsFD1.

Florigen is produced in leaves and is transmitted through the phloem to the shoot apex, where it induces flowering. A number of recent reports have provided evidence that *Arabidopsis* FT protein (Hd3a in rice) is a key component of florigen [2]. In the shoot apical meristem, FT activates *AP1* transcription and induces flowering by interacting with the bZIP transcription factor FD, although the details of the interaction between FT and FD have not yet been clarified. In rice, the closest homolog of FD, OsFD1, has been identified on the basis of its function [1] and homology with maize DLF1. The FT-FD interaction is required for flowering, and phosphorylation of residue T282 in the C-terminal region of FD may be critical for this interaction and floral initiation.

We tested for a direct interaction between highly purified Hd3a and OsFD1 using three different methods, glutathione S-transferase (GST) pull-down assay, nuclear magnetic resonance (NMR) and isothermal titration calorimetry (ITC), but none was detected. This result was surprising; by analogy with the FT-FD interaction in *Arabidopsis*, Hd3a was expected to interact with OsFD1. Next, the known interaction between Hd3a and a rice 14-3-3 protein, OsGF14c (hereafter referred to as GF14) [3], was re-examined. A direct interaction was observed by GST pull-down and NMR experiments; NMR also revealed that Hd3a interacted directly with the closely related 14-3-3 protein OsGF14b. In an effort to reconcile these results, the amino acid sequence of the C-terminal region of OsFD1 was investigated, since the corresponding region of FD is important for the FT-FD interaction. One consensus sequence among the bZIP transcription factors that reportedly bind FT and its homologs was found to be R-x-x-(S/T)-A-P-F, which resembles the 14-3-3 protein-binding motif R-S-x-(pS/pT)-x-P. The presence of this sequence in OsFD1 raised the possibility that the interaction between Hd3a and OsFD1 is indirect and is mediated by 14-3-3 proteins. A direct interaction between OsFD1 and GF14 was indeed observed in GST pull-down and yeast two-hybrid assays; moreover, this interaction depended on the phosphorylation of OsFD1 S192 (T282 in FD), which is partially consistent with a previous assertion of the importance of FD T282 phosphorylation for binding to FT. These results indicate that GF14 directly binds both Hd3a and phosphorylated OsFD1, and plays a critical role in the association between the two. This model may extend to the physical relationship between FT and FD in *Arabidopsis*, since FT and 14-3-3 proteins have been reported to interact.

To elucidate the structural basis of the interactions between these three proteins, we determined the crystal structure of an Hd3a-GF14-OsFD1 complex at 2.4 Å resolution (Fig. 1) using diffraction data collected at beamlines **BL41XU** and **BL44XU**. For structure determination, OsGF14c and a peptide comprising the nine C-terminal amino acids of phosphorylated OsFD1 were used; neither OsGF14b nor intact OsFD1 yielded diffraction-quality crystals. The complex is a heterohexamer composed of two molecules each of Hd3a, GF14 and OsFD1. Two Hd3a monomers abut the C-terminal regions of dimeric GF14, about 50 Å apart, resembling two equal weights on a balance, to form a thick and deep W-shaped structure (Fig. 1).

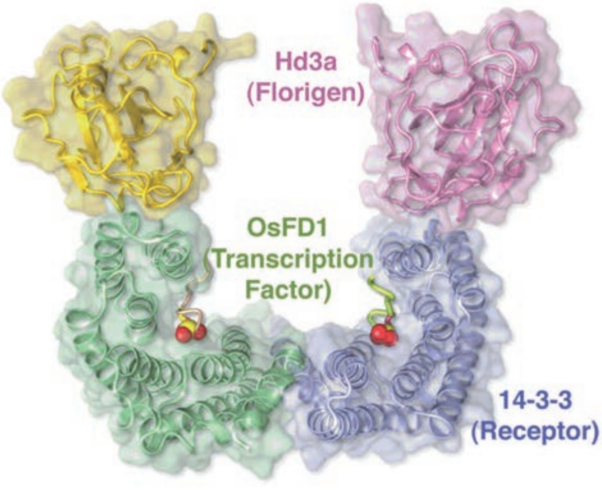

Fig. 1. Structure of the florigen activation complex (FAC). The FAC heterohexameric structure in a ribbon representation, composed of two Hd3a molecules (florigen; gold and magenta), a 14-3-3 dimer (receptor; dark green and blue), and two OsFD1 peptides (transcription factor; khaki and light green). Oxygen atoms in the phosphate groups of phosphoserine 192 of OsFD1 are visible as red spheres.

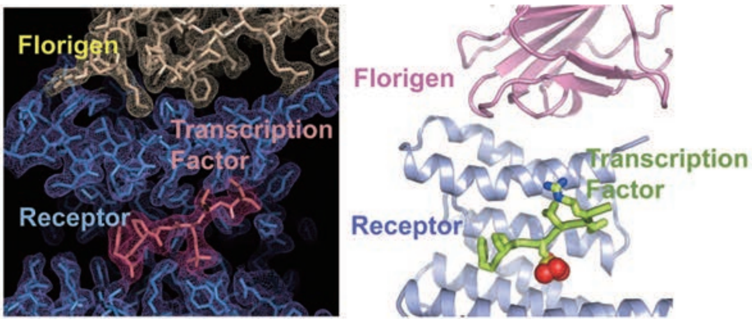

Fig. 2. Expanded view of the FAC structure shown by electron density map (left) and its corresponding ribbon representation (right). The binding sites in the receptor (blue) for florigen (gold and magenta) are more than 20 Å apart from those for the transcription factor (red and green), and no direct contact is observed between florigen and transcription factor.

The two corners at the inner base of the 'W' form positively charged pockets, and the S192-phosphorylated C terminus of OsFD1 binds to these pockets. The binding sites in GF14 for Hd3a are more than 20 Å apart from those for OsFD1 (Figs. 1 and 2), and yeast two-hybrid assays using GF14 mutants confirmed that the two partners are bound independently. Therefore, GF14 forms a stable complex with Hd3a and OsFD1 simultaneously, and mediates indirect binding between Hd3a and OsFD1. We named this complex the florigen activation complex (FAC).

On the basis of biochemical, biophysical and physiological experiments using rice cultured cells and transgenic rice plants, we have shown that the florigen Hd3a forms a complex with 14-3-3 (GF14) and OsFD1, that is required for floral induction [1] (Fig. 3). We also found that 14-3-3 protein functions as a novel mediator of florigen function by bridging Hd3a and OsFD1. The Hd3a-14-3-3 complex may also interact with other bZIP transcription factors containing the R-x-x-(S/T)-A-P-F motif, to which 14-3-3 binds in the FAC. This could provide a mechanistic basis for the proposed participation of florigen in processes other than flowering [4]. In other words, 14-3-3 may not simply be a mediator of flowering but may play an even more central role as an intracellular receptor for florigen.

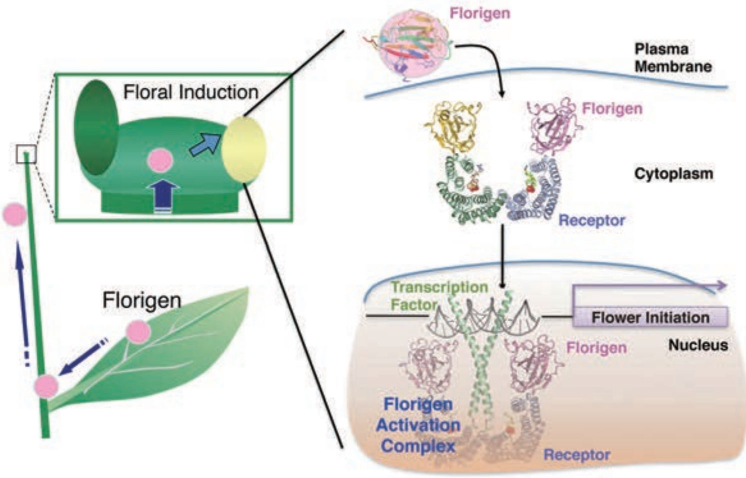

Fig. 3. Model of FAC formation. Florigen (Hd3a) is produced in leaves and is transmitted through the phloem to the shoot apex. Once florigen enters a shoot apical cell, it initially binds to the florigen receptor (14-3-3 proteins) in the cytoplasm. When the florigen–receptor complex enters the nucleus, it forms a complex with the transcription factor (OsFD1), which is retained in the nucleus and activates the flower initiation gene (*OsMADS15*) transcription, leading to floral induction.

Izuru Ohki[a], Ko Shimamoto[b] and Chojiro Kojima[a,c,*]

[a] Lab. of Biophysics, Nara Institute of Science and Technology
[b] Lab. of Plant Molecular Genetics, Nara Institute of Science and Technology
[c] Institute for Protein Research, Osaka University

*E-mail: kojima@protein.osaka-u.ac.jp

References

[1] *K. Taoka, I. Ohki, H. Tsuji, K. Furuita, K. Hayashi, T. Yanase, M. Yamaguchi, C. Nakashima, Y.A. Purwestri, S. Tamaki, Y. Ogaki, C. Shimada, A. Nakagawa, C. Kojima and K. Shimamoto: Nature* ***476*** *(2011) 332.*
[2] S. Tamaki *et al.*: Science **316** (2007) 1033.
[3] Y.A. Purwestri *et al.*: Plant Cell Physiol. **50** (2009) 429.
[4] C. Navarro *et al.*: Nature **478** (2011) 119.

Crystal structure of the human CENP-A nucleosome: Implications for the molecular architecture of centromeric chromatin

The nucleosome is the fundamental repeating unit of chromatin, which compacts genomic DNA as chromosomes for accommodation within the nucleus. In the nucleosome, the core histones form an octamer containing two each of histones H2A, H2B, H3, and H4, and the DNA is wrapped around the histone octamer. Nonallelic histone variants have been identified for histones H2A, H2B, and H3, but not for H4. Nucleosomes containing histone variants are considered to dictate chromatin domains with specific functions. The centromere is one such functional chromatin domain.

Centromeres are unique chromosomal sites where kinetochores, the microtubule attachment sites, are assembled. The proper attachment of microtubules to kinetochores is essential to ensure accurate chromosome segregation during mitosis and meiosis. The centromere is marked by the centromere-specific histone H3 variant, CENP-A. Among the H3 variants, CENP-A is the most distant variant, sharing about 50% amino acid identity with the canonical H3. The centromeric regions of chromosomes are epigenetically inherited through multiple rounds of cell division. To dictate the centromere-specific chromatin domain, CENP-A is thought to constitute a unique chromatin architecture. Several models for the CENP-A nucleosome have been proposed, including the octasome, hemisome, compact octasome, hexasome, and tetrasome models [1].

To obtain structural information about the CENP-A nucleosome, we reconstituted nucleosomes using bacterially expressed human histones H2A, H2B, H4, and CENP-A, by a salt-dialysis method in the presence of DNA [2,3]. For crystallization, a 147 base pair palindromic DNA was used for the CENP-A nucleosome assembly. This 147 base pair DNA was designed from a human α-satellite sequence, and contains binding sites for the centromeric protein, CENP-B, near both DNA ends. The reconstituted CENP-A nucleosome was further purified using a Prepcell apparatus (Bio-Rad), and was crystallized by the hanging drop vapor diffusion method [4]. Crystals of the purified CENP-A nucleosome were obtained after mixing equal volumes of the sample solution and potassium cacodylate buffer (pH 6.5), containing KCl and $MnCl_2$. The CENP-A nucleosome crystals were cryo-protected with polyethylene glycol 400 and trehalose. Diffraction data were collected using the synchrotron radiation source at beamline **BL41XU**. The crystals of the CENP-A nucleosome belonged to the orthorhombic space group $P2_1$, with unit cell constants of a=65.8 Å, b=83.3 Å, c=176.8 Å and β=100.7°. One CENP-A nucleosome is present in the asymmetric unit [4].

The crystal structure of the human nucleosome containing CENP-A was determined at 3.6 Å resolution [4]. In the CENP-A nucleosome structure, two each of histones H2A, H2B, H4, and CENP-A form an octamer, and the DNA is wrapped around it in a left-handed orientation (Fig. 1). This is consistent

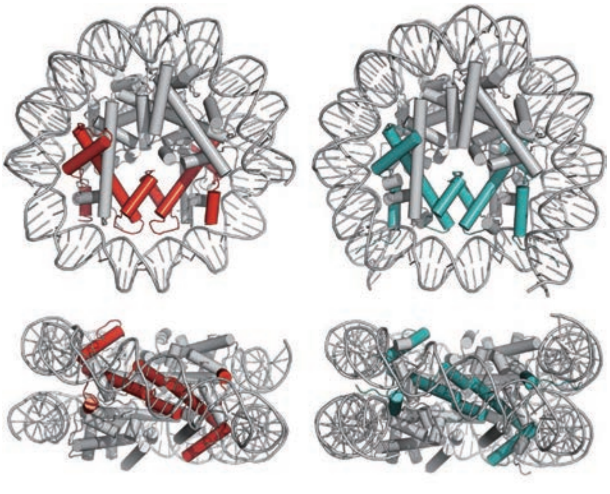

Fig. 1. Crystal structures of the CENP-A and H3 nucleosomes. Two views of the CENP-A nucleosome structure (left) and the H3 nucleosome structure (right) are presented. The two CENP-A molecules and the two H3 molecules are colored red and light blue, respectively.

with the octasome model, in which the histone octamer, containing two each of histones H2A, H2B, H4, and CENP-A, wraps the DNA in a left-handed orientation, as in the canonical H3 nucleosomes. The overall structure of the CENP-A nucleosome is similar to that of the H3 nucleosome (Fig. 1). However, a superposition of the CENP-A and H3.1 structures in the nucleosomes, along with calculations of the root mean square deviation (RMSD) for each residue pair, revealed four CENP-A regions, amino acids 49-51, 79-85, 108-109, and 127-129, that exhibited large deviations (>1Å) from the corresponding regions of H3.1 [5]. The CENP-A 49-51 region does not form a stable α-helix, unlike the corresponding region of the canonical H3 (Fig. 2). The CENP-A 79-85 region is located in the loop 1 (L1) region, which is two amino acid residues longer than the H3 L1 loop. The CENP-A 108-109 and 127-129 regions constitute the direct interaction surface between two CENP-A molecules within the CENP-A nucleosome (Fig. 2). In the nucleosome, these structural differences between CENP-A and H3 may result in the CENP-A-specific function during the centromere-specific chromatin formation.

A striking difference between the CENP-A and H3 nucleosomes is found in the DNA. In the CENP-A nucleosome, the central 121 base pairs of the DNA are tightly wrapped around the histone octamer, but the thirteen base pairs from both ends of the DNA are not visible, and are probably highly flexible (Fig. 3) [4]. This greatly differs from the DNA of the H3 nucleosome, in which 146 base pairs of the DNA are perfectly wrapped around the histone octamer and are visible in the crystal structure (Fig. 3). In general, the DNA wrapped within the nucleosome is inaccessible to DNA-binding proteins. Therefore, the flexible DNA regions at the entrance and the exit of the CENP-A nucleosome may provide binding sites for centromeric DNA binding proteins, such as CENP-B and CENP-C. Further structural studies of the CENP-A nucleosome complexed with those DNA-binding proteins are awaited.

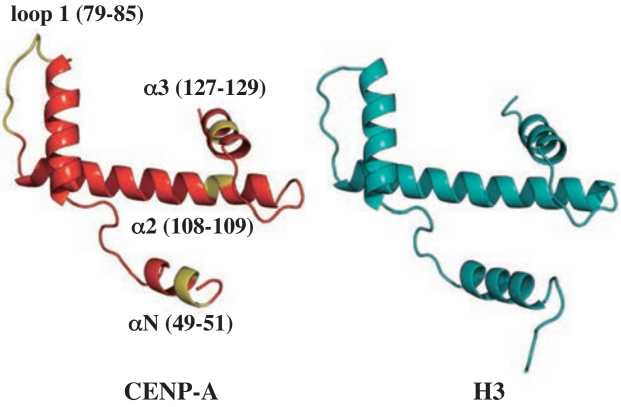

Fig. 2. The CENP-A regions that structurally differ from those of the canonical H3. The CENP-A (left) and H3 (right) structures in the nucleosome are represented. The CENP-A amino acid regions 49-51, 79-85, 108-109, and 127-129 are highlighted in yellow.

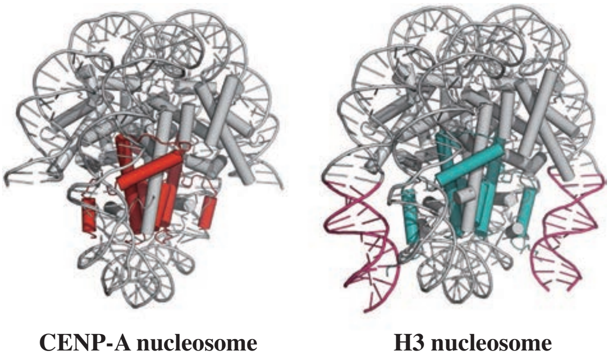

Fig. 3. DNA structures of the CENP-A (left) and H3 (right) nucleosomes. The magenta-colored DNA regions in the H3 nucleosome correspond to the disordered DNA regions in the CENP-A nucleosome.

Hiroaki Tachiwana, Wataru Kagawa
and Hitoshi Kurumizaka*

Laboratory of Structural Biology,
Waseda University

*E-mail: kurumizaka@waseda.jp

References

[1] H. Tachiwana and H. Kurumizaka: Genes Genet. Syst. **86** (2011) 357.
[2] Y. Tanaka *et al.*: Methods **33** (2004) 3.
[3] Y. Tanaka *et al.*: J. Biol. Chem. **280** (2005) 41609.
[4] *H. Tachiwana, W. Kagawa, T. Shiga, A. Osakabe, Y. Miya, K. Saito, Y. Hayashi-Takanaka, T. Oda, M. Sato, S.-Y. Park, H. Kimura and H. Kurumizaka: Nature* ***476*** *(2011) 232.*
[5] H. Tachiwana *et al.*: Nucleus **3** (2012) 6.

Structural basis of type II topoisomerase inhibition by the anticancer drug etoposide

Type II topoisomerases (TOP2s) are ubiquitous enzymes that play essential roles in cellular DNA transactions including replication, transcription, recombination, and chromosome condensation and segregation [1]. These two-fold symmetric enzymes transiently cleave a pair of opposing phosphodiester bonds four base pairs apart, generating a TOP2-DNA cleavage complex. Passage of a second DNA segment through this enzyme-bridged "DNA gate" and its resealing complete the topological change of the DNA.

TOP2's DNA cleavage activity is a double-edged sword; failure to reseal the enzyme-mediated DNA break can lead to cell death. Several potent anticancer drugs, such as etoposide, doxorubicin, and mitoxantrone, exploit this harmful aspect of TOP2 and promote the formation of cytotoxic DNA lesions by increasing the steady-state level of cleavage complexes [2]. Despite the extensive clinical use of these drugs, however, the lack of three-dimensional structures of any drug-stabilized cleavage complexes has left the structural bases of drug actions and resistance largely unresolved. To these ends, we determined the high resolution (2.16 Å) crystal structure of the DNA-binding and cleavage core of the human TOP2β-isoform (residues 445–1201; designated hTOP2β^{core}) (Fig. 1) in complex with DNA and a highly successful anticancer drug etoposide [3]. Structural analysis was carried out using Taiwan beamline **BL12B2**.

This structure reveals the detailed interplays between protein, DNA and drug. The two etoposide molecules bind between the base pairs (+1/+4; –1/+5) immediately flanking the two cleaved scissile phosphates (Fig. 2(a)), thus stabilize the cleavage complex by physically blocking the TOP2-mediated resealing of DNA. Besides the intercalating aglycone core (ring A, B, C and D), the two protruding groups (the glycosidic group and E ring) of etoposide also mediate direct interactions with surrounding amino acid residues, further highlighting the enzyme's central role in stabilizing the bound drug (Fig. 2(b) and 2(c)). Consistent with the observed structure-activity relationships of etoposide, the spatially constrained binding pocket of E ring (Fig. 3(a)) explains why modifications to this part usually compromise drug activity. In contrast, the relatively spacious binding pocket for glycosidic group (Fig. 3(b)) suggests that it is more suitable than E ring for further modifications in developing more effective anticancer drugs. This structure also suggests a molecular basis for a cytosine at the –1 position being strongly favored at etoposide-stabilized DNA cleavage sites (Fig 1(a)). We found that the +5 guanosine base not only stacks nicely with ring A and B of etoposide, it also anchors a major drug-contacting residue R503 by forming a H-bond (Fig. 3(c)). The apparent preference for having a guanosine at position +5 in turn specifies a cytosine at the –1 position. It is known that mutations in TOP2 may confer resistance to TOP2-targeting anticancer drugs and antibiotics. By mapping reported mutation sites onto our structure, we provided the structural basis of drug resistant (Fig. 3(d)).

This structure also offers molecular codes useful for the design of isoform-specific TOP2-targeting agent. This aspect is extremely important because all vertebrates possess two highly similar yet functionally distinct TOP2 isoforms. The α-isoform is particularly important for DNA replication and is usually present at high levels in fast growing cancer cells, whereas the β-isoform is mainly involved in transcription-related processes [4]. Although the inhibition of both TOP2 isoforms contributes to the drug-induced death of cancer cells, targeting of the β-isoform has been implicated in deleterious therapy-related secondary malignancies [5]. Therefore, it is desirable to develop the isoform-specific TOP2-targeting agents. The reported structure further reveals that, while most drug-contacting residues are conserved between isoforms, a key drug-interacting residue Q778 is replaced with methionine (M762) in

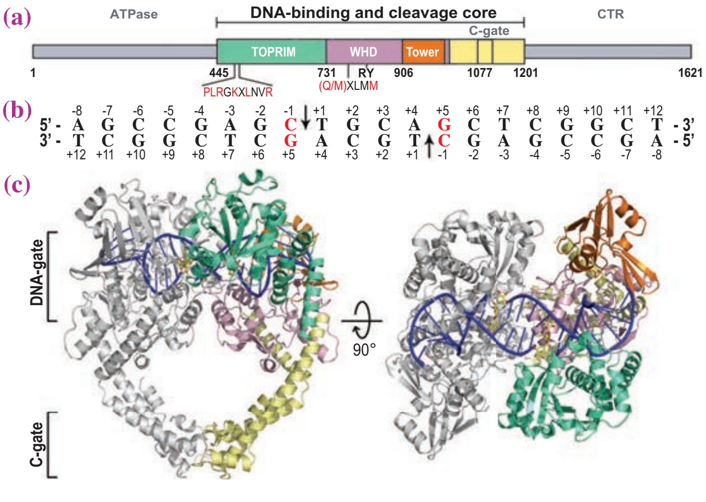

Fig. 1. Structure of the hTOP2β^{core}-DNA cleavage complex stabilized by the anticancer drug etoposide [3]. **(a)** Linear domain organization of hTOP2β. **(b)** The palindromic DNA substrate used for crystallization. The –1/+5 base pairs shown in red highlight the nucleotide preference for this position. **(c)** Orthogonal views of the ternary cleavage complex.

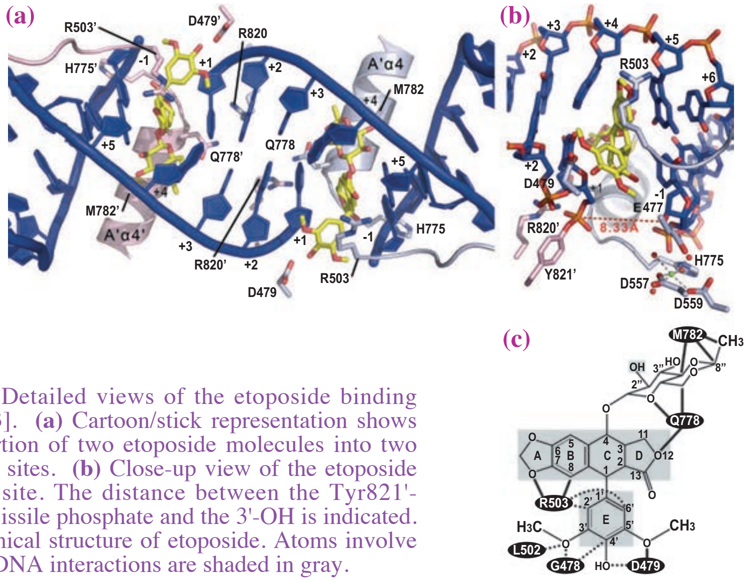

Fig. 2. Detailed views of the etoposide binding site(s) [3]. **(a)** Cartoon/stick representation shows the insertion of two etoposide molecules into two cleavage sites. **(b)** Close-up view of the etoposide binding site. The distance between the Tyr821'-linked scissile phosphate and the 3'-OH is indicated. **(c)** Chemical structure of etoposide. Atoms involve in drug-DNA interactions are shaded in gray.

the α-isoform. Such a change in residue polarity may be exploitable in developing new isoform-specific anticancer drugs with reduced side effects.

In summary, we represented the first observation of a TOP2 ternary cleavage complex stabilized by an anticancer drug. The interplays between protein, DNA and drug reveal structural details of drug-induced stabilization of a cleavage complex, and providing valuable information for developing a better anticancer drug.

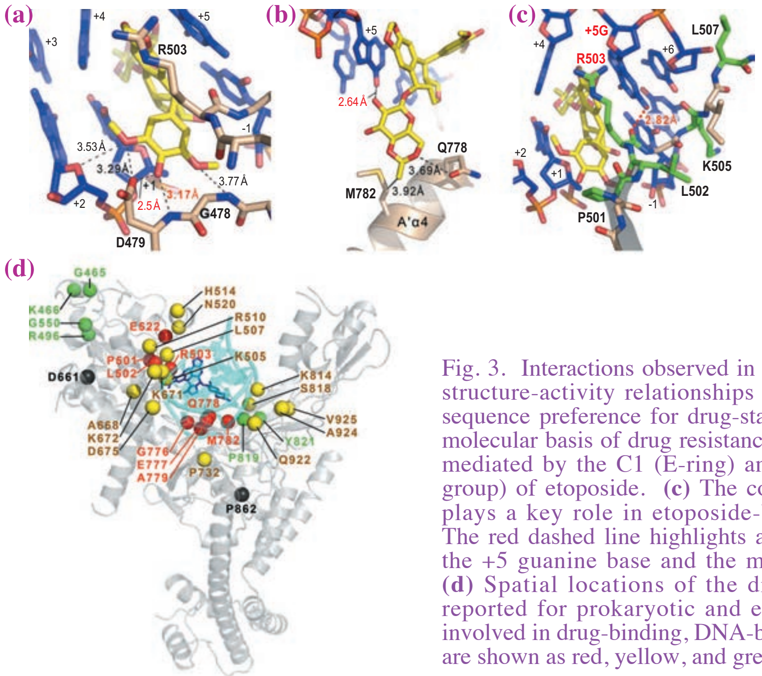

Fig. 3. Interactions observed in etoposide binding site suggest structure-activity relationships of etoposide derivatives, the sequence preference for drug-stabilized cleavage site, and the molecular basis of drug resistance [3]. **(a)** and **(b)** Interactions mediated by the C1 (E-ring) and C4 substituent (glycosidic group) of etoposide. **(c)** The conserved PLRGKXL segment plays a key role in etoposide-binding by harboring R503. The red dashed line highlights a key hydrogen bond between the +5 guanine base and the main chain carbonyl of R503. **(d)** Spatial locations of the drug-resistant mutation sites reported for prokaryotic and eukaryotic TOP2s. Residues involved in drug-binding, DNA-binding, and catalytic functions are shown as red, yellow, and green spheres, respectively.

Chyuan-Chuan Wu[a], Tsai-Kun Li[b] and Nei-Li Chan[a,*]

[a] Institute of Biochemistry and Molecular Biology, National Taiwan University, Taiwan
[b] Department and Graduate Institute of Microbiology, National Taiwan University, Taiwan

*E-mail: nlchan@ntu.edu.tw

References

[1] J.C. Wang.: Cold Speing Harbor, NY, Cold Speing Harbor Laboratory Press, (2009).
[2] J.E. Deweese and N. Osherof: Nucleic Acids Res **37** (2009) 738.
[3] *C.C. Wu, T.K. Li, L. Farh, L.Y. Lin, T.S. Lin, Y.J. Yu, T.J. Yen, C.W. Chiang and N.L. Chan: Science **333** (2011) 459.*
[4] Y. Pommier *et al.*: Chem. Biol. **17** (2010) 421.
[5] M. Azarova *et al.*: Proc. Natl. Acad. Sci. USA **104** (2007) 11014.

LIFE SCIENCE:

"Tsutsuji"- *Azalea*

MEDICAL BIOLOGY

New experimental approaches are always being undertaken at SPring-8. This is particularly the case with medical and biological specimens that require various approaches to elucidate their functions. One good example is reported by Dr. Dilanian in this volume. Membrane proteins play many important roles in cells but they are generally difficult to crystalize for protein crystallography. Even when they form 2D crystals, powder diffraction from them has a large number of overlapping reflections that must be separated for structural analysis. The Australian group from the University of Melbourne and CSIRO proposed a novel technique to separate these reflections. Their method was applied to the best-quality data from bacteriorhodopsin (bR) that was obtained at SPring-8 and the high-resolution structure of the protein was obtained.

Another method of obtaining the protein structure from a 2D crystal is proposed by Dr. Iwamoto of JASRI. It is based on Fourier transform holography that utilizes the coherent X-ray beam from SPring-8. Iwamoto's idea is to make use of a large number of object-reference pairs oriented in the same direction. This dramatically improves the signal-to-noise ratio, and an averaged high-resolution image was successfully obtained. One possible application of this method is to a 2D crystal of membrane protein that is labeled with a marker such as nano-gold.

The intense X-ray beam from SPring-8 has been widely used for imaging experiments. It is well known that X-ray phase-contrast CT has not only higher density resolution than conventional absorption-based CT but also highly quantitative. Hoshino *et al*. applied the technique to an eye lens. Detailed analysis of the density gradient in lens revealed discontinuities that may be related to the formation process of the lens.

High-resolution CT using an X-ray microscope is also an advantage of SPring-8. The work of Professor Matsuo's group in Keio University revealed the internal structure of the semi-spherical protrusion of the malleus (a bone in the middle ear) called the processus brevis from both wild-type mouse and transgenic osteopetrotic mouse that has stone-like bones. Since this structure is only 300 µm in diameter, an effective voxel size of 0.22 µm was necessary. Unlike the wild type, the bone of osteopetrotic mouse lacked blood vessels, suggesting a role of osteoclasts in bone formation.

Dr. Akiyama's group in Nagoya University is working on the circadian clock in a cyanobacterium that is analogous to the circadian clocks of eukaryotes including humans. The clock is realized by the phosphorylation and dephosphorylation of protein KaiC. KaiA stimulates phosphorylation whereas KaiB promotes dephosphorylation, and these proteins are assembled into a complex. Thus, interaction between the proteins in solution can be studied by small-angle X-ray scattering. The results indicated that KaiC ticks through expanding and contracting motions of the part of its structure called the C2 ring. For this measurement, which requires a prolonged experiment, the stability of the X-ray beam from SPring-8 is indispensable.

In all of these studies, X-ray imaging and scattering techniques are used for the same purpose, that is, to resolve the structure of a nonperiodic sample. It is interesting to note that these two techniques are becoming increasingly inseparable, implying a feature of synchrotron radiation science.

Naoto Yagi

A new approach for structure analysis of two-dimensional membrane protein crystals using X-ray powder diffraction data

Integral membrane proteins (IMPs) are involved in such neurological processes as memory and fine motor control. Their dysfunctions are implicated in many diseases including schizophrenia, Alzheimer's and Parkinson's diseases. To date, however, only approximately thirty unique structures of IMPs have been solved to atomic resolution, compared to more than 3000 unique crystal structures for soluble proteins, because of the intrinsic difficulty in extracting these proteins from the membrane and manipulating them to produce three-dimensional crystals for structural analysis [1]. The majority of known IMPs are much more likely to form two-dimensional (2D), rather than three-dimensional (3D) crystals during the crystallization process, which limits the possibility of obtaining their molecular structures using the standard methods of protein crystallography. Powder diffraction methods are, in contrast, not critically sensitive to the quality and dimensions of crystals, and this suggests their use in the structure analysis of 2D crystals. The application of powder diffraction methods for the structure analysis of proteins, however, is still regarded as mostly intractable because of the large number of unresolved (overlapping) reflections.

We have developed a novel approach for the structure analysis of membrane protein crystals using X-ray powder diffraction data [2]. This approach allows severely or completely overlapping reflections to be decomposed using intensity ratios of resolved reflections and a *priori* information, such as unit cell parameters, the crystallographic symmetry group, and the chemical composition of the sample. The approach not only allows the intensity of the individual components of the diffraction pattern to be extracted, but also furnishes initial estimates of the phases for subsequent refinement.

Our method is based on the fact that the electron density distribution of proteins is quite uniform at a low resolution, and scattering from a protein molecule comprised of discrete atoms is almost indistinguishable from that of a homogeneous and continuous envelope. The initial low-resolution shape of the molecule, therefore, can be considered as a solid ellipsoid, Fig. 1. In such a representation, the origin and the orientation of the low-resolution shape of the molecule are characterized by three parameters, R, α , and β. The first two parameters define the origin of the molecule in the asymmetric unit, and the last one defines the orientation of the molecule. For low-resolution structure analysis, therefore, the orientation and origin of the molecule, rather than the actual distribution of electron density inside the molecular envelope, is the dominant factor affecting the amplitude of the structure factor. In this way, different positions and orientations of the molecule give different ratios of intensities for the pair of Bragg reflections. The measured ratios of reflections that can be resolved experimentally, therefore, are used to refine the position, and orientation of low-resolution molecular structures within the unit cell, leading to the resolution of the remaining overlapping reflections. The molecular model is then made progressively more sophisticated as additional diffraction information is included in the analysis.

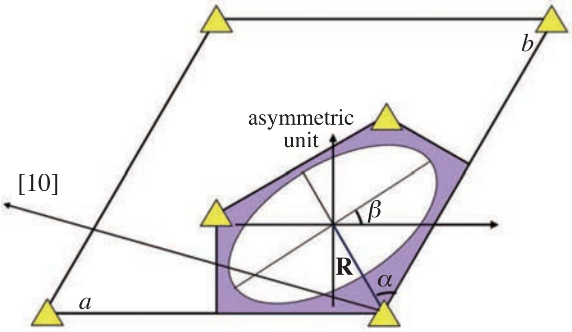

Fig. 1. The model of the molecular envelope located in the asymmetric unit of the $p3$ symmetry unit cell.

The ability of the method to decompose completely overlapping reflections was first tested with the diffraction data simulated using the results presented in [3]. Figure 2 shows the reconstructed and simulated molecular form factor (MFF) of a bacteriorhodopsin molecule (bR). MFF characterizes the scattering from the individual objects (molecular clusters) which make up periodic crystal. One can see that the magnitudes and phases of calculated and simulated MFF are in good agreement.

We then analyzed the powder diffraction pattern obtained from the 2D crystal of purple membrane (PM), the crystalline form of bR [4]. The integrated intensities of diffraction peaks up to a 4 Å resolution were estimated using the Le Bail analysis, shown in Fig. 3(a). The completely overlapping reflections up to 7 Å resolution were decomposed using the method described previously. Structure factors were then

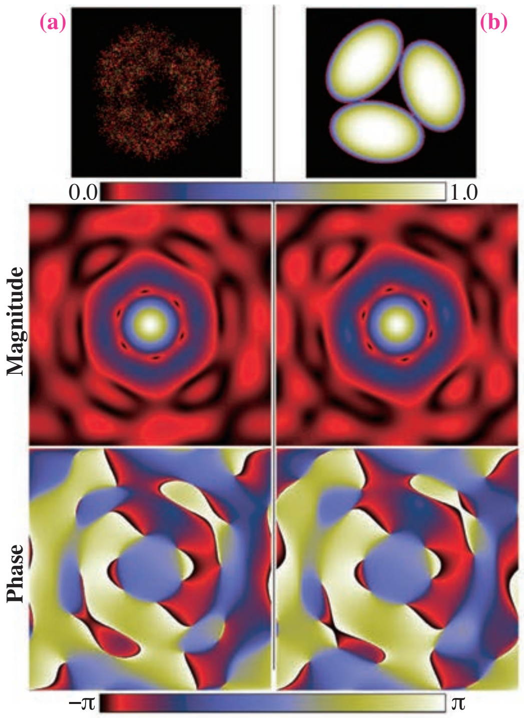

Fig. 2. The normalized molecular form factor of PM **(a)** simulated using discrete representation of the bR molecule, and **(b)** reconstructed using continuous representation of the bR molecule. [2]

analyzed by the maximum entropy method to obtain the 2D electron density map of PM. The resulting low-resolution 2D electron density map of PM is shown in Fig. 3(b). The map clearly indicates the envelope of a bR molecule and the electron density of the transmembrane α-helices. The three helices located in the inner part of the bR molecule have projected density higher than the helices at the outer part of bR.

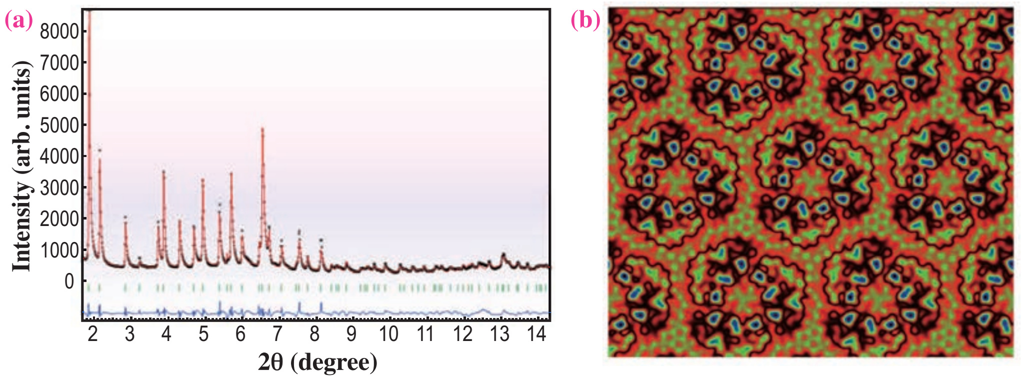

Fig. 3. **(a)** Results of the Le Bail analysis of the powder diffraction pattern obtained from the PM crystals. **(b)** The resulting low-resolution electron density map of bR reconstructed from experimental data. [2]

Ruben A. Dilanian

ARC Centre of Excellence for Coherent X-ray Science,
School of Physics, The University of Melbourne, Australia

E-mail: roubend@unimelb.edu.au

References

[1] M. Baker: Nature Meth. **7** (2010) 429.
[2] *R.A. Dilanian, C. Darmanin, J.N. Varghese, S.W. Wilkins, T. Oka, N. Yagi, H.M. Quiney and K. A. Nugent: Protein Science* ***20*** *(2011) 457.*
[3] H. Luecke *et al.*: J. Mol. Biol. **291** (1999) 899.
[4] T. Oka *et al.*: Synchrotron Rad. **13** (2006) 281.

Hard X-ray Fourier transform holography from an array of oriented referenced objects

The spatial resolution of optical imaging methods depends on the wavelength of the beam used. In the case of light microscopes, a spatial resolution obtained (~100 nm) is comparable to or even better than the wavelength. Magnified images are created by a set of lenses, which in mathematical terms, calculates the reverse Fourier transform of the light scattered from the object (the Fourier transform of the object). With our current technology we can fabricate lenses with precision good enough to reach the theoretical value of spatial resolution.

By using hard X-ray instead of visible light, one should in principle be able to create a microscope with an atomic resolution (~0.1 nm). However, the major difficulty is that we cannot fabricate lenses good enough to ensure atomic resolution. We therefore use computers to calculate the reverse Fourier transforms directly from the patterns of X-ray scattered from the objects. Here we encounter another obstacle, called the "phase problem". As an electromagnetic wave, an X-ray photon has its amplitude and phase, and both are needed to restore the original structure of the object. However, the phase information is lost when the scattering is recorded on a detector.

Then, what we get when we calculate a reverse Fourier transform without phase information? The Fourier transform calculated in this way is called a "Patterson function" (Fig. 1). A Patterson function is the autocorrelation function of the object, i.e., a collection of vectors representing all possible combinations of two points within the object. Although a Patterson function contains information about the structure of the object, it is usually not useful because it is nothing more than a heap of hopelessly overlapping vectors. However, a small trick can dramatically improve the situation. If one places a small dot near the object, and if the distance between the dot and the object is greater than the longest vector within the object, the vectors connecting the dot and the object (called cross-correlation terms) will never overlap with vectors within the object. In this way the structure of the object can be isolated from the rest of the Patterson function. This is a kind of holography, and because the structure is restored through the operation of Fourier transform, this method is called "Fourier transform holography".

The method of Fourier transform holography has been successfully implemented for soft X-ray, with wavelengths of >1 nm. The structures of microfabricated patterns or natural objects such as diatoms have been retrieved. The dots near the objects (reference dots) are also microfabricated, and the spatial resolution is determined by its size (~50 nm) rather than the wavelength.

If the technique of Fourier transform holography is to be extended to the realm of hard X-ray (wavelength ~0.1 nm) and the size of the reference dot is reduced to that of an atom (~0.1 nm), literally an atomic resolution should be obtained. Here we face a third obstacle: If the size of the reference dot is reduced, so is the amplitude of the cross-correlation terms, weakening the signal. To make the matters worse,

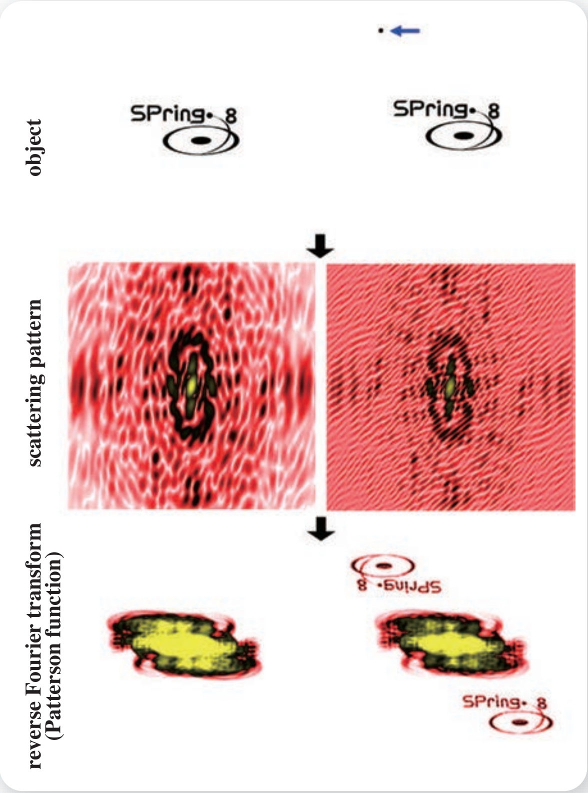

Fig. 1. Principle of Fourier transform holography. Top row, objects; middle row, scattering patterns recorded on the detector (Fourier transform of the objects); bottom row, reverse Fourier transforms of the scattering patterns calculated without phase information (Patterson function). Generally it is difficult to extract useful structural information from the Patterson function (left bottom), but if a reference dot is placed near the object (right top, blue arrow), the structure of the object is directly imaged in the Patterson function as a symmetric pair of cross-correlation terms (right bottom).

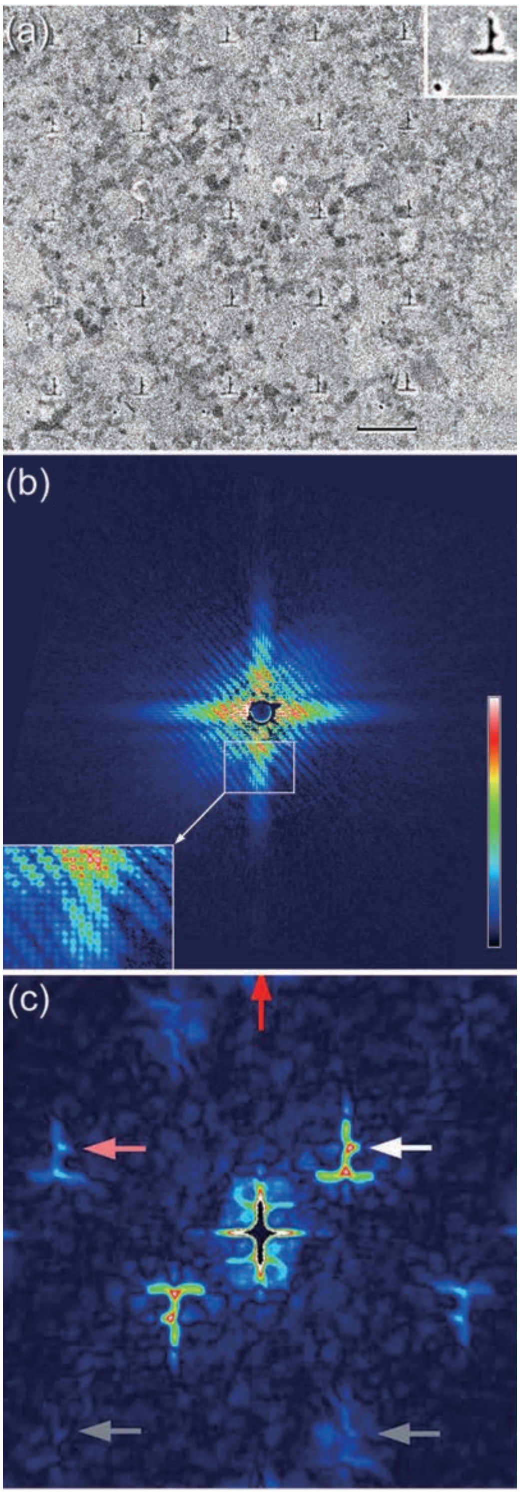

Fig. 2. Fourier transform holography from multiple pairs of reference and object. **(a)** A 5×5 matrix of pairs of reference and object (Chinese character meaning "up"), nanofabricated on gold substrate.
(b) scattering pattern from the test pattern shown in **(a)**, recorded at BL40XU beamline by using hard X-ray (wavelength, 0.15 nm).
(c) Patterson function calculated from the scattering pattern shown in **(b)**. Note that the Chinese characters are clearly retrieved. [1]

hard X-ray interacts with matters much more weakly than soft X-ray, further weakening the signal. As a result of these effects combined, practically no signal will be detected by any of the present-day detectors if, for example, a single atom is used as a reference and a single protein molecule is used as an object.

The paper by Iwamoto and Yagi [1] describes a method to overcome this obstacle. The idea is to prepare a large number of object-reference pairs oriented in the same direction, and illuminate them with hard X-ray simultaneously to obtain stronger signal. To test the feasibility of this method, they nanofabricated a test pattern, in which pairs of a reference dot and a Chinese character are arranged in a 5×5 matrix (Fig. 2(a)). Figure 2(b) shows the scattering pattern from it (hologram). In the scattering pattern, one can observe a series of coarse stripes coming from the interference between the reference dot and the Chinese character. The stripes further consist of fine dots arranged in a square lattice, representing the interference of reference-object pairs within the matrix. Figure 2(c) shows the Patterson function calculated from the scattering pattern (Fig. 2(b)). A pair of symmetrically arranged Chinese characters is clearly reproduced around the center, and weaker characters are also reproduced in the periphery. All experimental data were carried out at beamline **BL40XU**.

This study shows that the technique of Fourier transform holography using multiple oriented pairs of references and objects is as effective as in the single-object case, and can be used as an effective means to increase the signal level. This method will be especially useful for determining the atomic structure of weakly scattering biomolecules or their assemblies, which are not crystallizable but identical particles of which can be prepared in large numbers.

Hiroyuki Iwamoto

SPring-8/JASRI

E-mail: iwamoto@spring8.or.jp

References

[1] *H. Iwamoto and N. Yagi: J. Synchotron Rad.* ***18*** *(2011) 564.*

Discontinuities in the gradient index structure of eye lenses

The eye has a gradient index lens to provide a better optical performance than would be possible with a homogenous index lens. The exact form or shape of this gradient requires further investigation because it is linked closely with the way that the lens grows: by accruing new cell layers over existing tissue, with no concomitant losses. Hence, every lens contains a chronological record of its development and growth and each layer of cells contributes to the shape of the gradient index profile. The index profile may therefore provide some insight into growth phases of the lens. This could eventually lead to a better understanding of the zones of discontinuity, lamellar-like features seen in the living human eye lens that may demarcate phases in lens development [1]. To date there has been no clear explanation of the physical nature of these features nor any confirmation of their purpose. If these 'zones' are signs of protein density changes at certain life stages, they should appear as fluctuations or discontinuities in the refractive index profile. Studies on the refractive index of the lens, thus far, have been unable to detect such fine, localized fluctuations.

Ideally, the refractive index should be measured on whole lenses, in any given plane. Measurements should be made with a level of accuracy that can detect any fluctuations or irregularities in the profile that may be meaningful physiologically. X-ray microtomography allows for quantitative measurement of sample density but does not permit recognition of structures within the eyeball [2]. An X-ray Talbot grating interferometer, that combines phase contrast imaging and microtomography, has been developed by Momose [3,4]. This interferometer makes use of the Moiré fringes generated by two gratings (an absorbance and phase grating). It also has the advantage, over interferometers such as the Bonse-Hart instrument, of being able to tolerate large density differences. This renders the technique applicable to the measurement of density changes within the eyeball. The aim of the study was to investigate whether this instrument could detect subtle changes in the refractive index gradient that could not be found with previously used techniques.

The X-ray grating interferometer, constructed at the bending magnet beamline **BL20B2**, utilizes a monochromatic X-ray beam that is passed through a Si(111) double crystal monochromator (Fig. 1). The X-ray energy was tuned to 15 keV, 25 keV or 35 keV and the photon flux at an energy of 15 keV was 6.5×10^9 (photons/sec/mm^2 @ 15 keV). The instrument has two transmission gratings: a phase (G1) and absorption grating (G2). Grating parameters and materials were varied depending on the size of the lens samples. For large lenses grating G1 was made of tantalum and G2 was made of gold with pattern thicknesses 2.1 μm and 16.6 μm, respectively. The grating pitch of both gratings was 10 μm and the pattern size area was 25 mm (H)×25 mm (V). G2 was inclined by 45° so as to increase the effective X-ray absorption at the grating. For smaller samples, both gratings were made of tantalum and the pattern thicknesses of G1 and G2 were equal to 0.96 μm and 4.75 μm, respectively. The pitch of both gratings was 5 μm and the pattern size area was 5 mm (H)×10 mm (V). The inclination angle of G2 was 60°. An appropriate X-ray imaging detector was selected to acquire an image of the whole eyeball with an adequate field of view.

Phase retrieval was achieved using a fringe-scan method [3,4]. Differential phase shift images were obtained and integrated to provide the phase shift image. Phase shifts are calibrated against solutions of known density and theoretically obtained values are compared to the experimentally derived phase shift values per pixel. The three-dimensional refractive index $\delta(x,y,z)$ is reconstructed from the phase shifts $\Phi(x,y)$ using the following integral:

$$\Phi(x,y) = 2\pi/\lambda \int \delta(x,y,z)\,dz \qquad (1)$$

Lenses from five species: pig (*Sus domestica*), fish (*Carassius auratus auratus*), mouse (*C57BL/6*), frog (*Rana catesbeiana*) and newt (*Cynops pyrrhogaster*) were examined within intact fresh eyeballs. Images of eyeballs from the five species are shown in Fig. 2.

The lens is the prominent structural feature in each image. The image intensity varies across each lens

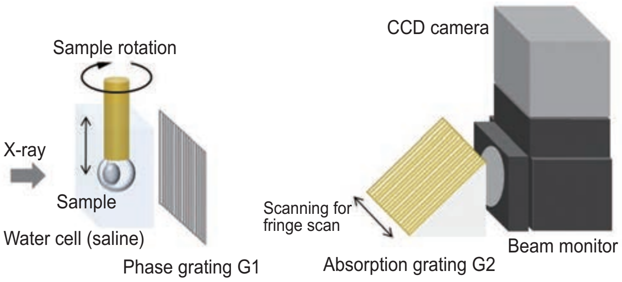

Fig. 1. Diagrammatic representation of the X-ray Talbot interferometer showing the sample cell with sample suspended on a rotatable rod; the phase and absorption gratings (G1 and G2 respectively) and the beam monitor. [2]

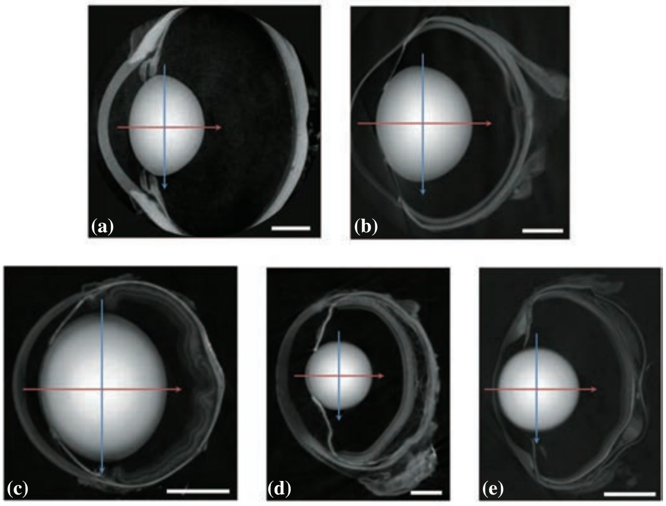

Fig. 2. Images of **(a)** pig; **(b)** frog; **(c)** mouse; **(d)** newt; **(e)** fish eyes in the sagittal plane. The position of the equatorial plane is marked with the blue arrow and the optic axis, along which the sagittal refractive index profiles were measured, is marked with a red arrow. The scale bars in the right hand lower corner are equal to **(a)** 4 mm (pig); **(b)** 2 mm (frog); **(c)** 1 mm (mouse); **(d)** 0.5 mm (newt); **(e)** 1 mm (fish) [2].

and it is possible to discern regions of different density. Refractive index variations were measured in the equatorial and sagittal planes: images for the equatorial plane are shown in Fig. 3. Whilst the profile shapes can be approximated to second order polynomials, there are 'discontinuities' in some of the functions where the curves deviate from second order polynomial fits. These kinks, seen in the peripheral sections of the profiles, are most prominent in the newt (Fig. 3(d)) and fish lenses (Fig. 3(e)) and least obvious in the frog lens (Fig. 3(b)).

The deviations from a smooth gradient may suggest some changes in the growth mode of the lens, in its rate or in the complement of proteins laid down in the cells in the region of these irregularities. It is still not clear what these features may manifest physiologically, but they may be the first optical evidence of the zones of discontinuity [1]. Thus far these have only been observed in human lenses in the living eye. These zones of discontinuity do not affect refraction nor impair vision. They may, however, be indicative of important stages in the growth and development of the lens [4] and require further investigation. As each lens contains a chronological record of its growth, these processes can be studied in single lenses.

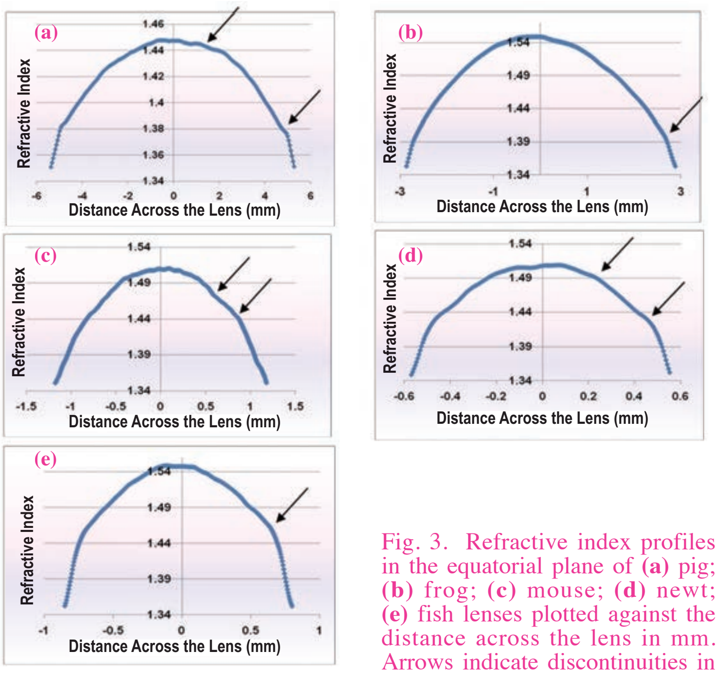

Fig. 3. Refractive index profiles in the equatorial plane of **(a)** pig; **(b)** frog; **(c)** mouse; **(d)** newt; **(e)** fish lenses plotted against the distance across the lens in mm. Arrows indicate discontinuities in the gradient index profiles. [2]

Masato Hoshino[a], Naoto Yagi[a]
and Barbara Pierscionek[b,*]

[a] SPring8/JASRI
[b] School of Biomedical Sciences,
University of Ulster, UK

*E-mail: b.pierscionek@btinternet.com

References

[1] J.F. Koretz *et al.*: Vision Research **34** (1994) 2955.
[2] *M. Hoshino, K. Uesugi, N. Yagi, S. Mohri, J. Regini and B. Pierscionek: PLoS ONE* ***6*** *(2011) e25140.*
[3] A. Momose: Jpn. J. Appl. Phys. **44** (2005) 6355.
[4] A. Momose *et al.*: Jpn. J. Appl. Phys. **42** (2003) L866.

Phase-contrast X-ray imaging of auditory ossicles in osteopetrotic mice

The three smallest bones of the middle ear, the malleus (hammer), incus (anvil) and stapes (stirrup), may be highly suitable for high-resolution structural analysis using synchrotron radiation. Figure 1 shows conventional microCT images of the auditory ossicles of an adult mouse. The malleus (green) attaches to the tympanic membrane (ear drum) (blue) and transmits sound through the incus (yellow) and stapes (red) to the cochlea in the inner ear (not shown). Using phase contrast X-ray microscopy, Kanzaki *et al.* revealed the internal structure of the semi-spherical protrusion of the malleus called the processus brevis (short process, mb in Fig. 1) for both wild-type and osteopetrotic (*stone-like bones*) mice [1] (Fig. 2). Osteopetrotic mice lack bone resorbing cells called osteoclasts. Osteopetrotic mice lack osteoclasts due to disruption of the gene encoding the transcription factor c-Fos, which is essential for osteoclast formation [2,3].

Most mammalian bones including long bones, vertebrae and auditory ossicles are formed through a process called endochondral (*inside* the *cartilage*) ossification. During development, chondrocytes form cartilage “models” of future bones. Chondrocytes within cartilage terminally differentiate into hypertrophic chondrocytes, which are often paired. Hypertrophic chondrocytes produce the vascular endothelial growth factor (VEGF) to stimulate angiogenesis (new blood vessel formation). In response to the VEGF, endothelial cells begin to invade cartilage to form capillary walls. Concomitantly, both osteoclasts, which resorb cartilage/bone, and osteoblasts, which produce bone matrix, enter into cartilage and replace it with bone, which contains proteins such as collagen fibers and crystals of a calcium phosphate mineral called hydroxyapatite. One question in the field has been whether and how endochondral ossification occurs in the absence of osteoclasts.

More than other bones, the malleal processus brevis of the mouse may be highly advantageous for high resolution analysis of endochondral ossification. It is small in size, which is a prerequisite for high resolution imaging, which requires a narrow field of view. The “diameter” of the processus brevis is approximately 300 μm, which is small enough to fit without processing into the field of view of the X-ray microscope used for analysis. It is also round, unlike femurs, tibias and other long bones in which chondrocytes proliferate and differentiate in columnar organization. By contrast, the malleal processus brevis forms a semi-spherical protrusion that does not grow lengthwise. Thus, its analysis could provide insight into endochondral ossification that is not limited to the growth plate. Finally, auditory ossicles are not buried in soft-tissue or muscle but are sustained largely in the air, making them easy to isolate. In particular, the malleus is easily identifiable at the inner surface of the tympanic membrane.

To visualize auditory ossicles, a synchrotron X-ray phase contrast microscope was constructed with an X-ray Fresnel zone plate (ATN/FZP-S86/416; NTT-AT, Tokyo) and gratings using 9.0 keV

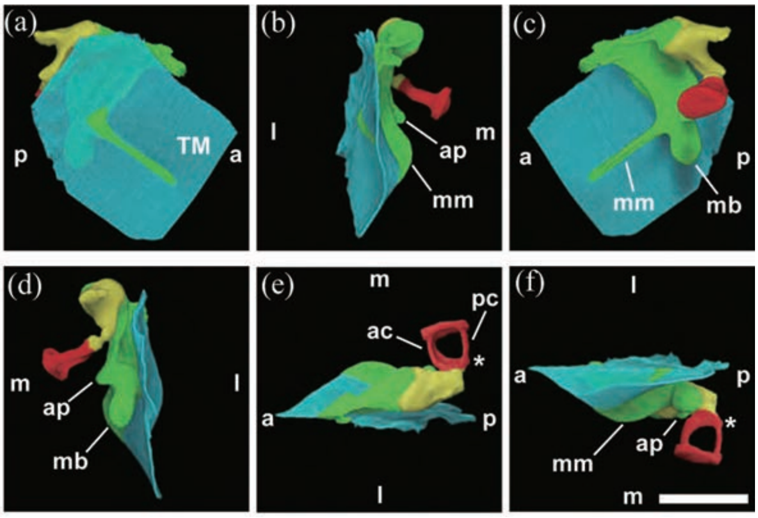

Fig. 1. MicroCT images of right auditory ossicles of an adult mouse. **(a)** lateral [l], **(b)** anterior [a], **(c)** medial [m], **(d)** posterior [p], **(e)** top, and **(f)** bottom views. TM, tympanic membrane; ap, anterior process; mb, malleal processus brevis; mm, malleal manubrium; ac, anterior crus; pc, posterior crus; *, a tubercle for stapedius muscle insertion. Scale bar = 1 mm. [1]

monochromatic X-rays at beamline **BL20XU** [4]. The resulting optical magnification was 20.2. In addition to phase contrast imaging on-focus, we also performed "defocus" imaging in the absence of gratings to enhance edges of osteocyte lacunae and chondrocytes by shifting samples 4 mm downstream from the on-focus position. Reconstructed tomographic images had an effective voxel size of 0.22 μm and the field of view was approximately 300 μm in diameter.

Kanzaki *et al*. compared the processus brevis structure in wild-type and c-Fos null osteopetrotic mice [1]. In adult wild-type mice, the malleal processus brevis contained osteocyte lacunae [1] (Fig. 2(a)) and blood vessels, indicating that endochondral ossification was complete. Curiously, in c-Fos null osteopetrotic mice the malleal processes brevis was filled with chondrocytes and lacked blood vessel invasion (Fig. 2(b)). Persistent chondrocytes and a lack of blood vessels have also been seen in other mouse models of osteopetrosis, which lack RANKL or TRAF6 [1]. Therefore, without osteoclasts, endochondral ossification is impaired and blood vessel invasion is blocked. Why blood vessels fail to invade the malleal processus brevis in the absence of osteoclasts is currently unclear. One possibility is that osteoclasts precede and lead blood vessel invasion. Alternatively, osteoclasts might stimulate hypertrophic chondrocytes to secrete VEGF, which induces angiogenesis. It is worth noting that, at the metaphyseal side of growth plates of long bones in osteopetrotic mice, numerous blood vessels invade cartilage presumably by secreting metalloproteinases such as metalloproteinase-9. Further three-dimensional and biochemical analyses will be necessary to analyze roles of osteoclasts in endochondral ossification.

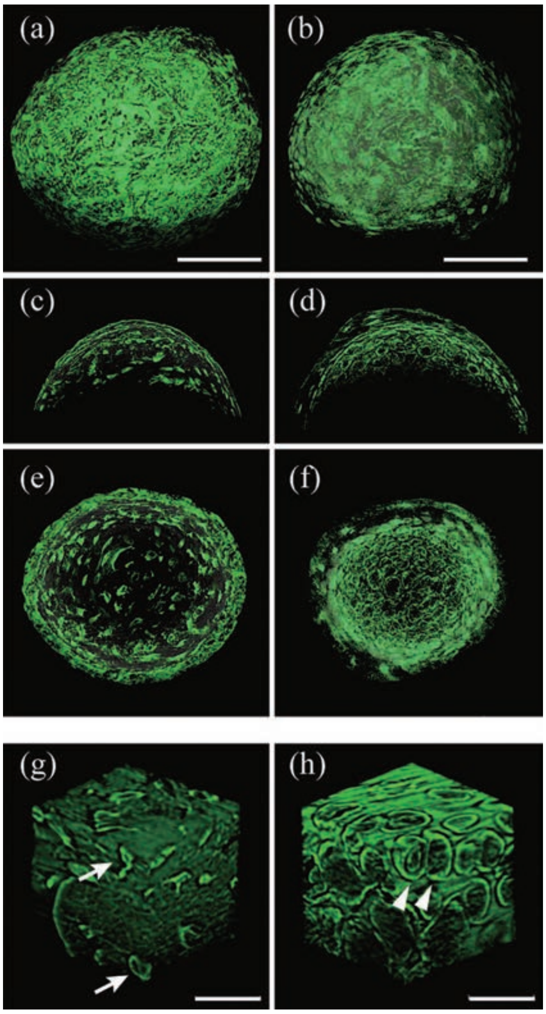

Fig. 2. Synchrotron tomographic microscopic images of the malleal processus brevis with defocus phase contrast. **(a, b)** 3D images of the processus brevis. **(c, d)** vertical sections. **(e, f)** horizontal sections. Scale bar = 100 μm. **(g, h)** Internal 30-μm cubes generated *in silico*. Scale bar = 20 μm. **(a, c, e, g)** wild-type adult mice. **(b, d, f, h)** adult osteopetrotic mice lacking c-Fos. Arrows indicate osteocyte lacunae in the bone matrix, while arrowheads indicate paired chondrocytes. Voxel size was 0.22 μm. [1]

Kanzaki *et al*. also found that mice made osteopetrotic either by c-Fos or RANKL knockout, exhibit impaired hearing based on the auditory brainstem response, which revealed that a higher threshold (louder sound) was required to generate brain-waves at the brain stem level [1]. Persistent chondrocytes seen in osteopetrosis may contribute to inefficient sound conductance. Surprisingly, Kanzaki *et al*. found that the size of auditory ossicles was larger and the middle ear cavity containing the ossicles was smaller than that of wild-type mice, causing direct contact between malleus and the middle ear cavity wall and apparently decreasing ossicle vibration. Therefore, osteoclasts are required for both endochondral ossification inside cartilage/bone and sculpting of the outer surface of bones.

Koichi Matsuo[a,*], Nobuhito Nango[b] and Atsushi Momose[c]

[a] School of Medicine, Keio University
[b] Ratoc System Engineering Co., Ltd.
[c] School of Frontier Sciences, The University of Tokyo

*E-mail: matsuo@z7.keio.jp

References

[1] *S. Kanzaki, Y. Takada, S. Niida, Y. Takeda, N. Udagawa, K. Ogawa, N. Nango, A. Momose and K. Matsuo: Am. J. Pathol.* ***178*** *(2011) 1270.*
[2] Z.Q. Wang *et al*.: Nature **360** (1992) 741.
[3] K. Matsuo *et al*.: Nat. Gent. **24** (2000) 184.
[4] Y. Takeda *et al*.: Appl. Phys. Exp. **1** (2008) 117002.

Visualization of circadian ticking of cyanobacterial clock protein KaiC in real time

Circadian clocks are endogenous timing systems for various organisms to adapt to dairy alterations in external environments. The cyanobacterium *Synechococcus elongatus* PCC7942 is one of the simplest organisms known to possess a circadian oscillator consisting of the three clock proteins KaiA, KaiB, and KaiC [1]. KaiC is rhythmically phosphorylated and then dephosphorylated *in vivo* without a transcriptional-translational negative feedback mechanism, which has been proposed to underlie eukaryotic circadian clocks. In addition, Nakajima *et al.* have shown that the phosphorylation cycle of KaiC is reconstituted simply by co-incubating the three Kai proteins in the presence of ATP [2]. KaiC possesses autokinase/autophosphatase activities. KaiA stimulates the auto-phosphorylation of KaiC, whereas KaiB promotes the auto-dephosphorylation of KaiC by attenuating the effect of KaiA. During the KaiC phosphorylation cycle, the three Kai proteins are assembled into hetero-multimeric complexes and then disassembled in a rhythmic manner [3]. The frequency of the phosphorylation cycle of KaiC is closely correlated with the rate of ATP hydrolysis exhibited by KaiC only [4]. The ATPase activity of KaiC, which is extremely low and is kept constant in a range of physiological temperatures, plays a central role in generating the temperature-compensated circadian period of the Kai oscillator.

KaiC is a dumbbell-shaped molecule composed of tandemly duplicated N-terminal (C1) and C-terminal (C2) domains. Six protomers are assembled into a hexamer to attain a double-doughnut shape. A KaiC mutant having only a C1 domain forms a C1 ring and exhibits approximately 70% of the ATPase activity of full-length KaiC. KaiC has two phosphorylation sites, i.e., Ser431 and Thr432, in the C2 domain, and both residues are phosphorylated and then dephosphorylated in a programmed sequence during the phosphorylation cycle as follows: KaiC$^{S/pT}$ →KaiC$^{pS/pT}$ →KaiC$^{pS/T}$ →KaiC$^{S/T}$ (where 'S' represents Ser431, 'pS' represents phosphorylated Ser431, 'T' represents Thr432, and 'pT' represents phosphorylated Thr432). The phospho-mimicking mutant of KaiC$^{S/T}$ exhibits a higher ATPase activity than the phospho-mimicking mutant of KaiC$^{pS/pT}$, indicating a functional coupling between ATPase and the phosphorylation state through the KaiC hexamer. Hence, the determination of the structural change of KaiC interlocked with ATPase and the phosphorylation state is of great importance.

Taking advantage of the fact that the ATPase activity is closely coupled with the phosphorylation state, we investigated the structure of KaiC in solution along the reaction sequence of the phosphorylation cycle. Auto-dephosphorylation reaction was induced by a temperature jump from 'on ice' to 30°C, and the structural transition was monitored using time-resolved small-angle X-ray scattering (SAXS) at beamline **BL45XU** [5]. Concomitantly with the shift in the phosphorylation state, we observed a gradual increase in the apparent radius of gyration (R_g) estimated from the measured SAXS curves. As a result of the detailed Guinier analysis, a substantial increase in R_g by 5% was observed in the KaiC$^{pS/pT}$ →KaiC$^{pS/T}$ transition. The 5% increase in R_g indicates the occurrence of a

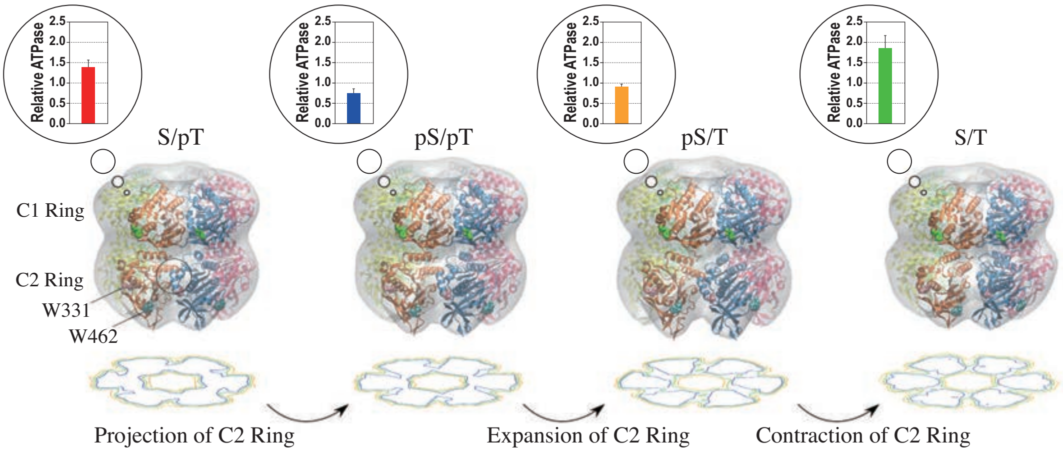

Fig. 1. Expansion and contraction motions of C2 ring of KaiC interlocked with ATPase activity. The protomer-protomer arrangement of the known X-ray structure of KaiC was refined against the SAXS data under the assumption of P6 symmetry. The ATPase activity of each phosphorylation state is plotted relative to that of KaiC-WT at 30°C.

large conformational change in the KaiC hexamer.

The structural transition of the KaiC hexamer was further monitored by time-resolved fluorescence spectroscopy. KaiC intrinsically has three tryptophan (Trp) residues, which are useful for monitoring local structural changes. One Trp residue is located in the C1 ring, whereas the other two are located in the C2 ring. We observed a gradual change in the fluorescence intensity during auto-dephosphorylation, and then identified that the observed change was mainly attributed to the change in the local environments around the two Trp residues in the C2 ring.

To visualize the structural change, we built low-resolution SAXS models of the KaiC hexamer by the rigid-body refinement of a known X-ray crystal structure (Fig. 1). The global shape remains almost unchanged in the transition from KaiC$^{S/pT}$ to KaiC$^{pS/pT}$, whereas the radius of the C2 ring is dramatically enlarged in the subsequent transition from KaiC$^{pS/pT}$ to KaiC$^{pS/T}$. The expanded C2 ring is partly contracted in the transition from KaiC$^{pS/T}$ to KaiC$^{S/T}$, and further contracted in the subsequent transition from KaiC$^{S/T}$ to KaiC$^{S/pT}$. Our model implies that KaiC ticks through expanding and contracting motions of the C2 ring.

The Trp fluorescence coming from KaiC displays a circadian oscillation in the presence of both KaiA and KaiB (Fig. 2(a)), providing direct evidence of the dynamic structural ticking of KaiC in solution. The observed oscillation in the fluorescence intensity can be well explained by a combination of the fluorescence intensity of the each phosphorylation state and its abundance, supporting the expanding and contracting motions of the C2 ring during circadian oscillation.

The dynamic structural change of the KaiC hexamer revealed in this study provides notable insights into the cyanobacterial circadian clock. The ATPase activity of KaiC is less sensitive to the C2 ring expansion in the transition from KaiC$^{pS/pT}$ to KaiC$^{pS/T}$, and the partial contraction of the C2 ring in the transition from KaiC$^{pS/T}$ to KaiC$^{S/T}$ results in a significant activation of ATPase (Fig. 1). These observations suggest that ATPase activity is not as simple as an on/off (contraction/expansion) switching process. Our results may reflect the auto-inhibitory mechanism proposed in a previous study [4]. Additionally, the timing of the accumulation of KaiC$^{pS/T}$ with the expanded C2 ring is coincident with that of the accumulation of the ternary complex with KaiA and KaiB [3]. Considering that KaiA and KaiB bind to the C2 ring of KaiC, the conformational ticking of KaiC serves as a timing cue for assembly/disassembly with KaiA and KaiB (Fig. 2(b)).

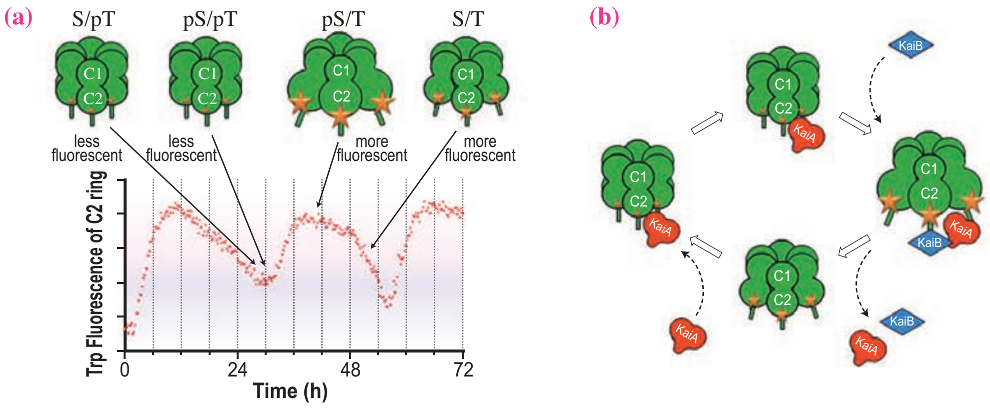

Fig. 2. Circadian ticking of KaiC. **(a)** Trp fluorescence intensity in the presence of KaiA, KaiB, and KaiC. **(b)** Schematic presentation of Kai protein oscillator. The dynamic structural change of the C2 ring of KaiC serves as a timing cue for recruiting KaiA and KaiB.

Atsushi Mukaiyama[a,b], Takao Kondo[a,b] and
Shuji Akiyama[a,b,c,d,e,*]

[a] Division of Biological Science, Nagoya University
[b] CREST, Japan Science and Technology Agency
[c] SPring-8/RIKEN
[d] PRESTO, Japan Science and Technology Agency
[e] Institute for Molecular Science

*E-mail: akiyamas@ims.ac.jp

References

[1] M. Ishiura *et al*.: Science **281**(1998) 1519.
[2] M. Nakajima *et al*.: Science **308** (2005) 414.
[3] S. Akiyama *et al*.: Mol. Cell **29** (2008) 703.
[4] K. Terauchi *et al*.: PNAS **104** (2007) 16377.
[5] *Y. Murayama, A. Mukaiyama, K. Imai, Y. Onoue, A. Tsunoda, A. Nohara, T. Ishida, Y. Maéda, K. Terauchi, T. Kondo and S. Akiyama: EMBO J.* ***30*** *(2011) 68.*

MATERIALS SCIENCE:

The argument that the nature of matter originates from the type and arrangement of atoms is widely accepted. Conventional structural analysis, however, has done little to connect structural information directly with macroscopic properties of materials. High brilliance, low emittance and highly polarized synchrotron radiation (SR) provided by SPring-8 is now being applied to elucidate the direct relationship between them. Successful applications in this year are widely distributed among research fields on superconducting, structural, hydrogen-storage, strongly correlated, glass, and soft materials.

In the superconducting materials with the layered structure, it had been considered that the substitution of the primary element with other ones is baneful to superconductivity. Nohara *et al*. overturned this common sense: they discovered a high-T_c iron-based superconductor by substituting Pt for a large portion of the primary element of Fe. They also observed two types of superconducting phase due to the bistable valence states of As ions, As^{3-} and $[As_2]^{4-}$, in the newly discovered $Ca_{10}(Pt_nAs_8)(Fe_{2-x}Pt_xAs_2)_5$ ($n = 3,4$) system.

The difference in valence is directly related to the ionic size. Azuma *et al*. exploited this feature of the macroscopic structural property. They found colossal negative thermal expansion (CNTE) in the perovskite $BiNiO_3$ compound at high pressure and/or high temperature, which originates from the valence change from Ni^{2+} to Ni^{3+} owing to charge transfer between Bi and Ni ions. By tuning the transition temperature and pressure through the substitution of Bi with La, they succeeded in realizing CNTE under ambient conditions.

STRUCTURE

The increase in the ionic size can also be used as evidence of hydrogen absorption. Matsuoka *et al*. have clarified that EuH_x, which was considered to be different from other rare-earth metals RH_x, is no longer an irregular member of the rare-earth metal hydrides. They conducted high-pressure diffraction and Mössbauer experiments in the EuH_x system, and found that the phase-transition sequence in EuH_x is similar to those of other RH_x systems. In systematic analyses, a small but non-negligible increase in the lattice constant, indicating a valence change in Eu through hydrogen absorption, was one of the key pieces of evidence supporting their conclusion.

Not only the number of electrons (valence) but also the orbital degree of freedom can now be examined by a sophisticated SR measurement technique. Ishii *et al*. developed polarization-analyzed resonant inelastic X-ray scattering (RIXS) for the first time, and succeeded in observing selectively the excitation between the e_g orbitals, corresponding to the orbital degree of freedom, from two types of excitations in a typical orbital order material, $KCuF_3$. The nature of orbital ordering will be unveiled by this new approach.

Reverse Monte Carlo analysis combined with density functional theory has become one of the most powerful tools for discussing the unique local and intermediate-range structures that govern the physical properties of non-periodic systems. Kohara *et al*. interpreted the glass forming ability from the viewpoint of cavity and ring distribution in glasses. Furthermore, they found that the local environment around the atoms in $MgO\text{-}SiO_2$ glass shows wide variation, depending on both the coordination number and bond strength, which is the origin of the discrepancy between the interpretations based on X-ray diffraction and NMR.

The small-angle X-ray scattering (SAXS) measurements shed light on the development of functional polymers and soft materials on the basis of their chemical properties and hierarchical structures. Takahara *et al*. found that electrostatic interaction of one of polyelectrolytes, so-called PMTAC, strongly depends on the concentration of hydrated ions without significant change in the conformation, as revealed by SAXS analysis, and succeeded in fabricating a reversible and solvent-free adhesion system using its novel characteristics.

Structural analysis is a basic method for the characterization of materials, and is still being developed by cutting-edge SR technologies and many analytical approaches in order to gain deeper insight into materials science.

Akihiko Fujiwara

Discovery of iron-based superconductor with platinum arsenide layers

We often compare the crystal structures of copper oxide superconductors and iron-based superconductors to a sandwich. The copper oxide (CuO_2) layers of copper oxide superconductors and the iron arsenide (FeAs) layers of iron-based superconductors comprise the bread portion of the sandwich. Since we have only two types of bread at the moment, we have to be creative with the ingredients (interlayer substances) to be placed between the slices of bread to make a delicious sandwich (to raise the transition temperature of the superconductor). Three types of ingredients have been discovered for iron-based superconductors thus far. The first consists of substances made of alkaline metals and alkaline earth metals, such as lithium in LiFeAs and barium in $BaFe_2As_2$. In this group, $(Ba_{0.6}K_{0.4})Fe_2As_2$ has the highest transition temperature of 38 K. The second type consists of substances made of fluorite-type structures, such as lanthanum oxide (LaO) in LaFeAsO and calcium fluoride (CaF) in CaFeAsF. The maximum superconducting transition temperature for this group is 56 K. The third type consists of metal oxide substances; superconductivity is observed at 47 K when calcium magnesium titanium oxide $Ca_4(Mg,Ti)_3O_8$ are used. The superconductor we discovered this time —$Ca_{10}(Pt_4As_8)(Fe_{2-x}Pt_xAs_2)_5$— contains a fourth type of interlayer substance, $Ca_{10}(Pt_4As_8)$, which does not belong to any of the above three groups [1,2]. This ingredient shows great potential and diversity of iron-based materials, since interlayer substances with strong covalency, such as platinum arsenides, have not been available for copper oxides.

The crystal structure of α-$Ca_{10}(Pt_4As_8)(Fe_{2-x}Pt_xAs_2)_5$ is shown in Fig. 1(a). This is a triclinic crystal (space group P-1) with 21 atoms in the unit cell. The interlayer substance with one less platinum, β-$Ca_{10}(Pt_3As_8)(Fe_{2-x}Pt_xAs_2)_5$, is a triclinic crystal (space group P-1) with 42 atoms in the unit cell. Synchrotron radiation X-ray diffraction experiments at beamlines **BL02B1** and **BL02B2** were essential for analyzing such complex crystal structures with low symmetry. Both α-$Ca_{10}(Pt_4As_8)(Fe_{2-x}Pt_xAs_2)_5$ and β-$Ca_{10}(Pt_3As_8)(Fe_{2-x}Pt_xAs_2)_5$ have iron arsenide (FeAs) layers, with some iron (Fe) replaced by platinum (Pt). The FeAs layer, which induces superconductivity, laminates in alternating Pt_4As_8 layers in the α-phase, and Pt_3As_8 layers in the β-phase. The Ca^{2+} ions act as a glue to attach the FeAs layers and the Pt_4As_8 (Pt_3As_8) layers to each other. α-$Ca_{10}(Pt_4As_8)(Fe_{2-x}Pt_xAs_2)_5$, shown in Fig. 1(a), consists of planar quadrangles of $PtAs_4$ that are connected at a shared apex. Dimer-like As-As bonds (As_2 molecules) are formed in-plane as the $PtAs_4$ planar quadrangles rotate alternately. This kind of As_2 molecule often appears in pyrite-type structure such as $PtAs_2$. When the interlayer substance Pt is periodically absent, β-$Ca_{10}(Pt_3As_8)(Fe_{2-x}Pt_xAs_2)_5$ is obtained, as shown in Fig. 2(b).

Arsenic ion favors an electron count of As^{3-} in solid to fill up 4*p* atomic orbital. Arsenic molecule prefers to

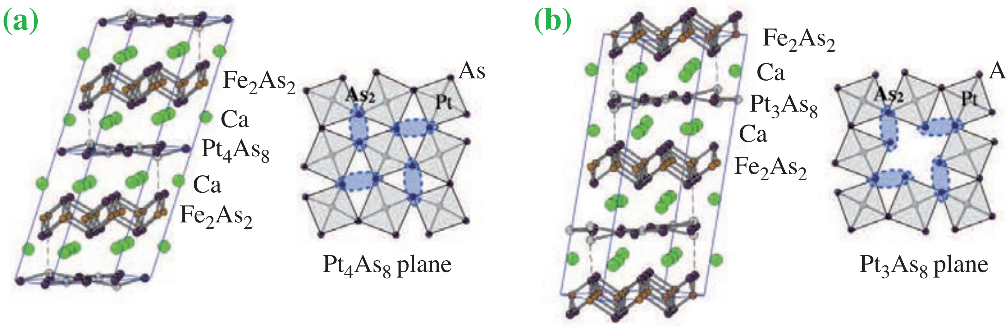

α-$Ca_{10}(Pt_4As_8)(Fe_{2-x}Pt_xAs_2)_5$ **β-$Ca_{10}(Pt_3As_8)(Fe_{2-x}Pt_xAs_2)_5$**

Fig. 1. Crystal structures of **(a)** α-$Ca_{10}(Pt_4As_8)(Fe_{2-x}Pt_xAs_2)_5$ and **(b)** β-$Ca_{10}(Pt_3As_8)(Fe_{2-x}Pt_xAs_2)_5$. Thin solid lines represent unit cells. Two unit cells are shown for α-$Ca_{10}(Pt_4As_8)(Fe_{2-x}Pt_xAs_2)_5$ along the *c* axis, while one is shown for β-$Ca_{10}(Pt_3As_8)(Fe_{2-x}Pt_xAs_2)_5$. Details of Pt_4As_8 and Pt_3As_8 layers are also shown. The dashed ellipsoids represent As_2 dimers. [2]

be $[As_2]^{4-}$ in solid to fill up π^* molecular orbital. In the present compound, there exist arsenic in the form of As^{3-} in the FeAs layers and in the form of $[As_2]^{4-}$ in the Pt_4As_8 (Pt_3As_8) layers. Thus, according to the charge balance, we estimate a formal electron count of iron and platinum to be Fe^{2+} and Pt^{2+} for β-$Ca_{10}(Pt_3As_8)(Fe_{2-x}Pt_xAs_2)_5$ when $x = 0.0$. Thus β-$Ca_{10}(Pt_3As_8)(Fe_2As_2)_5$ can be regarded as a parent compound of the present material. Superconductivity emerges when platinum is partially substituted for iron in the FeAs layers to induce additional electrons in FeAs layers. Rietveld analysis from the X-ray data gives an estimate of platinum content of $x = 0.16$ for β-$Ca_{10}(Pt_3As_8)(Fe_{2-x}Pt_xAs_2)_5$. Further electron doping can be realized for α-$Ca_{10}(Pt_4As_8)(Fe_{2-x}Pt_xAs_2)_5$, owing to one more Pt in the Pt_4As_8 layers together with an increased Pt content in the FeAs layers ($x = 0.36$) as determined by Rietveld analysis. In the latter compound, the highest superconducting transition temperature was observed.

Data on electrical resistivity and magnetization are shown in Fig. 2(a) and 2(b), respectively. Superconductivity with a transition temperature of 38 K, which was signaled by zero resistivity and shielding effects (negative magnetization), was observed in α-$Ca_{10}(Pt_4As_8)(Fe_{2-x}Pt_xAs_2)_5$ for $x = 0.36$. Superconductivity with a transition temperature of 13 K was seen for β-$Ca_{10}(Pt_3As_8)(Fe_{2-x}Pt_xAs_2)_5$ for $x = 0.16$. This demonstrates the surprising discovery that despite substituting Pt for a large portion of the primary element Fe of iron-based superconductor, superconductivity occurs at a high temperature of 38 K. In contrast, when Cu, the principal element for high-temperature superconductivity in copper oxides, is partially replaced, superconductivity does not occur owing to strong pair-breaking effects. Our findings will provide clues to the occurrence mechanisms of iron-based superconductors [3].

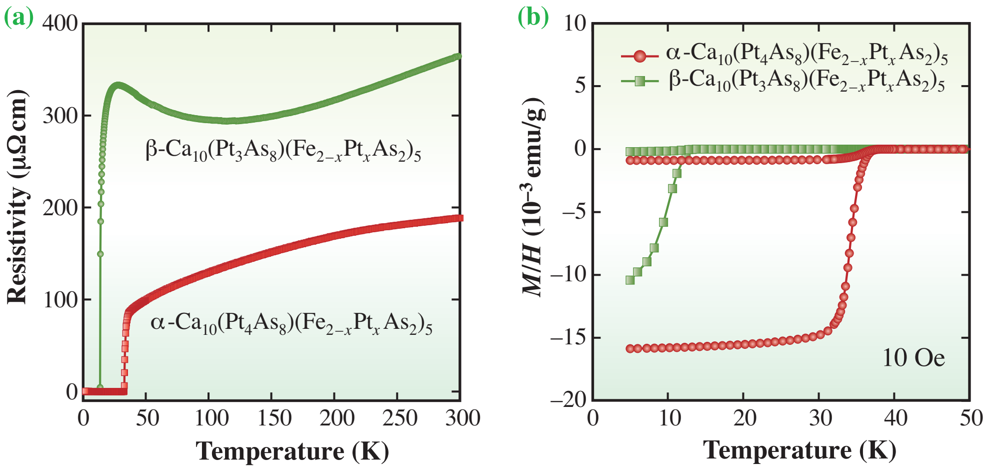

Fig. 2. Temperature dependence of **(a)** electrical resistivity and **(b)** magnetization for α-$Ca_{10}(Pt_4As_8)(Fe_{2-x}Pt_xAs_2)_5$ with $x = 0.36$ and β-$Ca_{10}(Pt_3As_8)(Fe_{2-x}Pt_xAs_2)_5$ with $x = 0.16$. The former shows superconducting transition at 38 K, while the latter shows at 13 K.

Minoru Nohara[a,b,*] and Hiroshi Sawa[c]

[a] Department of Physics, Okayama University
[b] JST, TRIP
[c] Department of Applied Physics, Nagoya University

*E-mail: nohara@science.okayama-u.ac.jp

References

[1] *S. Kakiya, K. Kudo, Y. Nishikubo, K. Oku, E. Nishibori, H. Sawa, T. Yamamoto, T. Nozaka and M. Nohara: J. Phys. Soc. Jpn.* ***80*** *(2011) 093704.*
[2] *M. Nohara, S. Kakiya, K. Kudo, Y. Oshiro, S. Araki, T.C. Kobayashi, K. Oku, E. Nishibori and H. Sawa: Solid State Commun.* ***152*** *(2012) 635.*
[3] K. Ishida *et al.*: J. Phys. Soc. Jpn. **78** (2009) 062001.

Colossal negative thermal expansion in $BiNiO_3$ induced by intermetallic charge transfer

Useful negative thermal expansion (NTE) materials for zero or controlled expansion composites should show a smooth contraction while heating through a wide temperature range. Volume shrinkages in framework type materials can extend over very wide ranges, for example, ZrW_2O_8 shows a near-continuous volume decrease of $\Delta V/V = -2.0\%$ over 0.3–1050 K, equivalent to an average linear expansion of $\alpha_L = (1/L)(\Delta L/\Delta T) = -7\times10^{-6}\ K^{-1}$ where the linear dimension L is the cubic unit cell parameter. NTE can also result from transitions between different electronic or magnetic states strongly coupled to the lattice, giving large negative expansions down to a previous record dilatometric value of $-25\times10^{-6}\ K^{-1}$ for $(Mn_{0.96}Fe_{0.04})_3(Zn_{0.5}Ge_{0.5})N$ at 316-386 K.

Perovskite $BiNiO_3$ has a triclinically distorted crystal structure with the unusual valence distribution $Bi^{3+}_{0.5}Bi^{5+}_{0.5}Ni^{2+}O_3$ and shows the charge ordering of the Bi valences, as illustrated in the inset of Fig. 1(a) [1]. Powder neutron diffraction and X-ray absorption spectroscopy (XAS) studies revealed the pressure-induced melting of the Bi-charge disproportionation at 3–4 GPa and a simultaneous Ni to Bi charge transfer accompanied by a structural change to the orthorhombic $GdFeO_3$ type perovskite superstructure with valence distribution $Bi^{3+}Ni^{3+}O_3$ [2]. Figure 1(a) shows the pressure dependence of the unit cell volume derived by fitting the neutron diffraction data [3]. It shows that the unit cell volume decreases by 2.5% across the transition. This large change results from the dominant contraction of the Ni-O perovskite framework as Ni^{2+} is oxidized to the smaller Ni^{3+} at the transition, which outweighs the lattice expanding effects of reducing Bi^{5+} to Bi^{3+} and increases in the Ni-O-Ni angles.

The charge transfer transition in $BiNiO_3$ has a negative dT/dp slope, which enables the same structural change accompanying the volume reduction to be observed by heating at a moderate pressure. Figure 1(b) shows the temperature dependence of the lattice parameters and unit cell volume of $BiNiO_3$ on heating at a pressure of 1.8 GPa, with the transition occurring at around 500 K. Structure refinements from neutron data and XAS and resistivity measurements confirm that the high pressure and temperature state is the same orthorhombic, metallic $Bi^{3+}Ni^{3+}O_3$ phase generated by pressurization at ambient temperature. Figure 1(c) shows the Ni-*K* edge XAS spectra for $BiNiO_3$ measured at beamline **BL39XU** at various temperatures and 2.3 GPa. The edge energy E_0^K shifts to a higher value between 414 and 463 K indicating the Ni^{2+} to Ni^{3+} valence state change. The volume drop of 3.4% observed by heating in Fig. 1(b) has a similar value to the pressure-induced change in Fig. 1(a).

Our neutron diffraction and XAS results have been used to construct the P-T phase diagram for $BiNiO_3$ shown in Fig. 2. $BiNiO_3$ decomposes above 500 K at ambient pressure, but is stabilized up to at least 565 K at 1.8 GPa (and to ~1300 K at 6 GPa under synthesis conditions). The boundary between the low pressure and temperature (LPT) and high pressure and temperature (HPT) phases has the slope $dT_{CT}/dp = -140\ KGPa^{-1}$. The 2.5–3.4% volume contraction occurs on both pressurization and heating.

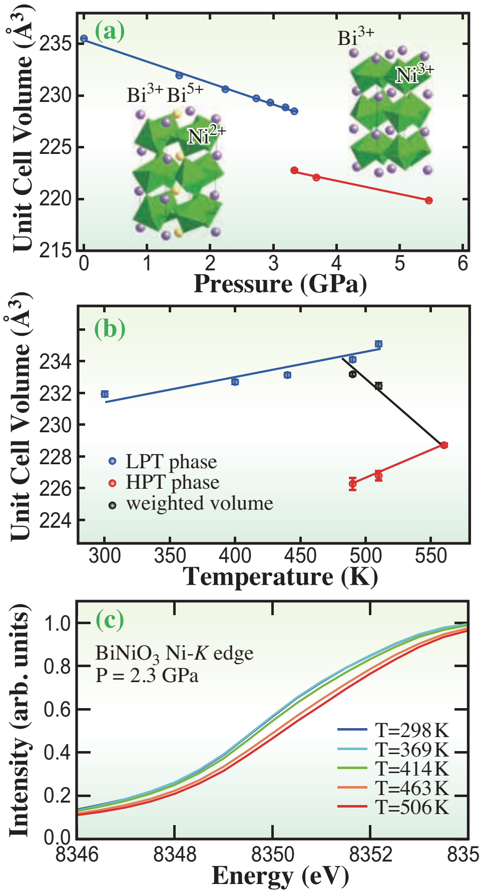

Fig. 1. Structural and spectroscopic data indicating the intermetallic charge transfer and the volume shrinkage. **(a)** Pressure dependence of the unit cell volume of $BiNiO_3$. **(b)** Temperature dependence of the unit cell volume at 1.8 GPa. Both show the $Bi^{3+}_{0.5}Bi^{5+}_{0.5}Ni^{2+}O_3$ to $Bi^{3+}Ni^{3+}O_3$ phase transition accompanied by volume shrinkage at around 3.5 GPa and 500 K. **(c)** Ni-*K* edge XAS spectra for $BiNiO_3$ at various temperatures and 2.3 GPa indicating the Ni^{2+} to Ni^{3+} valence state change between 414 and 463 K.

The large ΔT_{CT} of $BiNiO_3$ shows that colossal NTE is feasible but the transition is only observed above the pressure of 1.5 GPa in pure $BiNiO_3$. However, chemical substitutions for Bi may be used to suppress the charge disproportionation in the $Bi^{3+}{}_{0.5}Bi^{5+}{}_{0.5}Ni^{2+}O_3$ phase and thereby shift the charge transfer transition to near ambient conditions. This is conveniently achieved by a partial substitution of La for Bi, which suppresses the characteristic insulator to metal transition accompanying charge transfer to around 350 K at ambient pressure in $Bi_{0.95}La_{0.05}NiO_3$.

X-ray diffraction measurements at beamline **BL02B2** on $Bi_{0.95}La_{0.05}NiO_3$ in Fig. 3(a) show the 2.9% volume shrinkage, which has a similar magnitude to that observed in undoped $BiNiO_3$ under a pressure of 1.8 GPa. Coexistence of the low and high temperature phases is observed at three points in the transition region and a linear fit to the weighted average volumes is used to obtain the transition width of ΔT_{CT} = 70 K. The crystallographic volume thermal expansion coefficient between 300 and 370 K is $\alpha_V = -413\times10^{-6}$ K^{-1} and the linear coefficient is $\alpha_L = -137\times10^{-6}$ K^{-1}, showing that CNTE magnitudes are also observable in $Bi_{1-x}La_xNiO_3$. Crystallography predicts the upper limit of the magnitude of thermal expansion as the formation of pores and other microstructural defects can lessen the effect in bulk ceramics. Dilatometric measurements on a polycrystalline ceramic of $Bi_{0.95}La_{0.05}NiO_3$ prepared at high pressures were performed during heating and cooling cycles, as shown in Fig. 3(b). The strain $\Delta L/L$ (400 K) increases with increasing temperature up to 270 K, indicating a normal positive thermal expansion, but decreases above 270 K. The average observed α_L between 270 and 400 K is -49×10^{-6} K^{-1} and the maximum negative slope between 320 and 380 K corresponds to a linear thermal expansion coefficient of -82×10^{-6} K^{-1} [3]. This is more than three times larger than the previous maximum NTE value of -25×10^{-6} K^{-1} by dilatometry, reported for the linear expansion of an anti-perovskite manganese nitride $(Mn_{0.96}Fe_{0.04})_3(Zn_{0.5}Ge_{0.5})N$ ceramic over a similar temperature range.

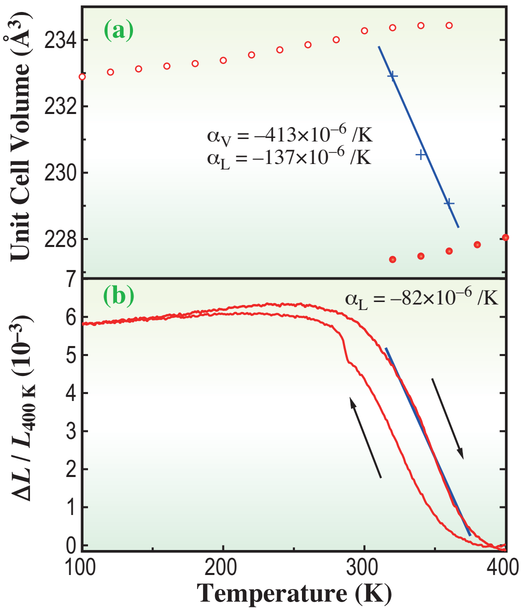

Fig. 3. Thermal measurements for $Bi_{0.95}La_{0.05}NiO_3$ at ambient pressure showing thermal expansion coefficient values over the linear regions indicated. **(a)** Temperature dependence of the unit cell volume on heating with LPT and HPT data denoted by open and closed circles, and crosses showing the weighted average volume in the transition region. **(b)** Dilatometric linear thermal expansion of $Bi_{0.95}La_{0.05}NiO_3$ on heating and cooling showing a 20 K hysteresis [3].

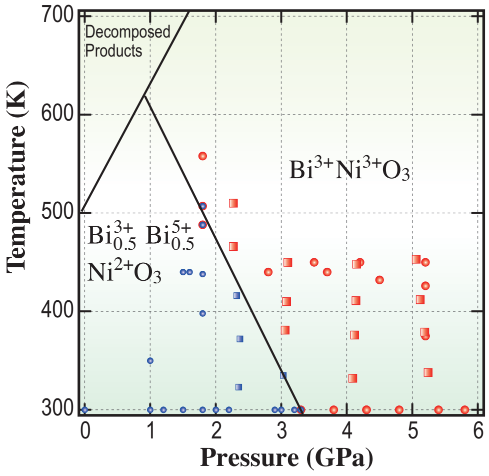

Fig. 2. Pressure-temperature phase diagram of $BiNiO_3$ determined by powder neutron diffraction (PND) and XAS studies. Circles and squares show PND and XAS data, and blue and red symbols correspond to the LPT and HPT phases, respectively [3].

Masaki Azuma[a,*], Masaichiro Mizumaki[b]
and Tetsu Watanuki[c]

[a]Materials and Structures Laboratory,
Tokyo Institute of Technology
[b]SPring-8/JASRI
[c]SPring-8/JAEA

*E-mail: mazuma@msl.titech.ac.jp

References

[1] S. Ishiwata *et al.*: J. Mater. Chem. **12** (2002) 3733.
[2] M. Mizumaki *et al.*: *Phys. Rev. B* **80** (2009) 233104.
[3] *M. Azuma, W. Chen, H. Seki, M. Czapski, S. Olga, K. Oka, M. Mizumaki, T. Watanuki, N. Ishimatsu, N. Kawamura, S. Ishiwata, M.G. Tucker, Y. Shimakawa and J.P. Attfield: Nat. Commun.* **2** *(2011) 347.*

Structural and valence transitions of EuH_x exposed to high pressure H_2 conditions

Rare-earth metals R, including yttrium (Y) and scandium (Sc), can absorb large amounts of hydrogen (e.g., 300 mol% in YH_3, at ambient pressure). This has led to extensive studies of their physical and chemical properties for industrial applications and academic interest.

This study [1] is conducted to establish a clear connection between the structural phases of EuH_x and the other RH_x, and to contribute to a full understanding of the interaction between hydrogen and rare-earth metals. In particular, we are interested in phase transformations and valence states of EuH_x under H_2 pressures that exceed 1 GPa to identify the known phases of other "regular" RH_x.

Systematic studies of RH_x have revealed common features in the crystal structure. RH_x crystallizes into essentially three structural phases, α, β and γ phases, depending on the hydrogen composition of x = H/R. The α phase is a solid solution where H atoms are distributed statistically at the tetrahedral (T) interstitial sites of the metal lattice as impurities. The β phase has an fcc structure. The β phase has been observed for dihydrides and several trihydrides RH_3 (for R = La, Ce, or Pr) [2]. In dihydrides, H atoms occupy T sites, forming an fcc fluorite structure. The γ phase possesses an hcp structure with the ideal composition RH_3 (R = Y, Nd, Sm, Gd, Tb, Dy, Ho, Er, or Lu) [2]. It is known to transform to an fcc structure at high pressures [3].

Europium hydride EuH_x has been an irregular member among the RH_x family because of its unique structural properties. Reflecting its divalent ground state $4f^{n+1}(5d6s)^2$, the dihydride EuH_2 crystallizes into the orthorhombic *Pnma* ($PbCl_2$-type, Z(Eu) = 2) structure. EuH_x is the only rare-earth metal hydride for which other structural phases have not been clearly observed. When EuH_2 is exposed to high-pressure H_2, one can expect an increase in hydrogen composition and valence changes that lead to structural phase transitions. The chemical potential of hydrogen on hydrogen solubility is significantly enhanced by high pressures exceeding 1 GPa [4]. The valence state of Eu can be changed between $4f^{n+1}(5d6s)^2$ and $4f^{n}(5d6s)^3$ by high pressure or by chemical manipulation. Thus, at a sufficiently high pressure, the β or γ phase may result from additional hydrogen uptake and a valence transition.

We have studied the crystal structures of europium hydride compressed in H_2 and He environments by X-ray diffraction (XRD) in **BL10XU** and DFT calculation. These systems are denoted as EuH_x/H_2 and EuH_2/He, respectively. To investigate the valence state of EuH_x, synchrotron Mössbauer spectroscopy measurements of EuH_x/H_2 were carried out in **BL09XU**.

Figure 1 shows the typical integrated X-ray diffraction diagram of EuH_x/H_2 with the crystal structures of the three new phases denoted as EuH_x-II, III and IV. At 7.2 GPa, EuH_x-I, which has *Pnma* structure, transformed to the EuH_x-II, which crystalizes in $P6_3/mmc$ (Ni_2In-type) structure. The EuH_x-II transforms to EuH_x-III with a tetragonal *I*4/*m* structure at 8.7 GPa and subsequently to EuH_x-IV

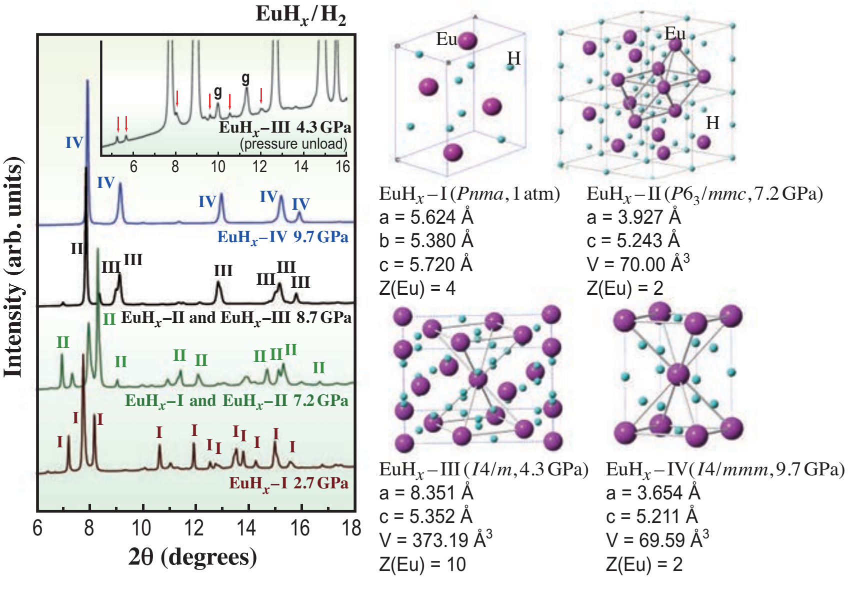

Fig. 1. Integrated XRD profiles of the EuH_x/H_2 system with crystal structures of EuH_x-I, II, III, and IV phases. The inset graph indicates the XRD profile of EuH_x-III at 4.3 GPa when pressure is unloaded. The downward arrows in the inset graph show the satellite peaks of the EuH_x-III phase. The "g" labels show the diffraction peaks of the Re-metal gasket.

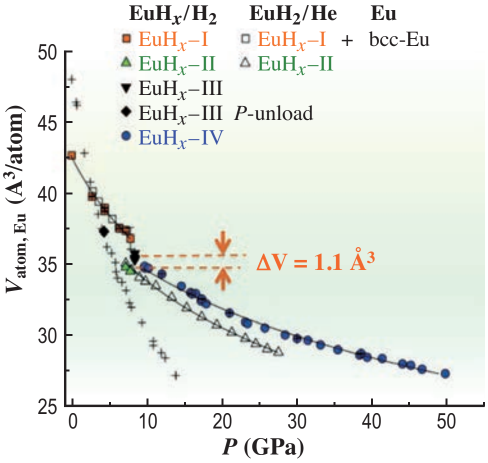

Fig. 2. Pressure dependence of $V_{atom,Eu}$. Solid lines are guides for eyes. The volume data of pure bcc-Eu were taken from Ref. 5.

with the *I*4/*mmm* structure. In the EuH_2/He system, the EuH_x-I to EuH_x-II transition was observed at 7.2 GPa where the same transition was observed in the EuH/H_2 system. However, the EuH_x-II phase was found to be stable up to 28 GPa. Here, it is clear that the transition I→II is a thermodynamic effect by external pressure and that II→III→ IV transformations are induced by the reaction between the sample and surrounding high-pressure H_2.

To investigate the hydrogen composition x in EuH_x-III and EuH_x-IV, we compared the atomic volume per Eu, i.e., $V_{atom,Eu}$, values at the transition pressures. $V_{atom,Eu}$ is calculated from the refined unit cell parameters and plotted as a function of pressure in Fig. 2. We observed a volume expansion of 1.1 Å^3 in EuH_x/H_2 at 8.7 GPa, where EuH_x-II and EuH_x-III coexist. We make a rough estimate for it on the basis of the empirical observation that the absorption of a H atom into a rare-earth metal lattice induces 4±0.5 Å^3 atomic volume expansion ΔV in the host metal lattice at ambient pressure. At high pressures, the anticipated volume expansion should be less than that at ambient pressure. Assuming that the volume expansion results only from the absorption of hydrogen atoms, the increase Δx in hydrogen composition in the II→III transition can be estimated to be at least 0.2.

We investigated the valence states of EuH_x/H_2 by synchrotron Mössbauer spectroscopy measurements. Figure 3 shows the typical Mössbauer spectra of EuH_x at 2.7 and 14.3 GPa. The velocity scale was calibrated relative to the single line of EuF_3 at ambient pressure. The isomer shift at 2.7 GPa, where the sample is in the EuH_x-I phase, was –10.50 mm/s relative to Eu^{3+}:EuF_3, indicating the divalent state. At 14.3 GPa, the isomer shift changed to 0.71 mm/s, showing that EuH_x-IV was in the trivalent state. This is clear evidence for the hydrogen-induced valence transition of EuH_x.

We compare the EuH_x-IV phase with other rare-earth metal hydrides. The fcc structure is a bct structure whose c/a ratio is $\sqrt{2}$. EuH_x-IV with c/a = 1.425 is a slight (0.8%) distortion of fcc. Because of its trivalent character and the small distortion from the fcc structure, EuH_x-IV corresponds to the β phase observed commonly for other RH_x. This is the first observation of the β phase and the trivalent state for EuH_x. Henceforth, EuH_x is no longer an irregular member of the rare-earth metal hydride family.

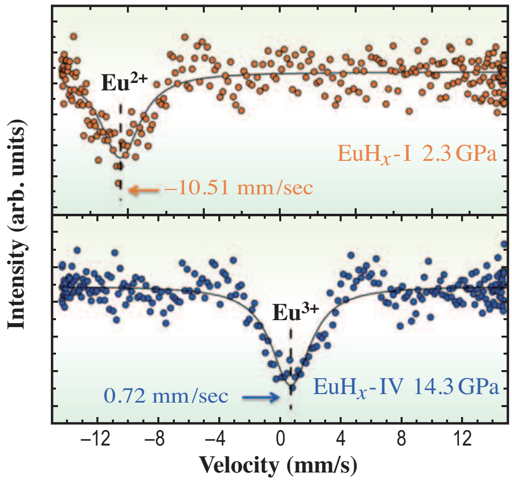

Fig. 3. High-pressure Eu-Mössbauer spectra of EuH_x-I at 2.3 GPa and EuH_x-IV at 14.3 GPa. Solid lines show the fit of the experimental data. The velocity scale was calibrated relative to the center of a single line of EuF_3 under ambient conditions. [1]

Takahiro Matsuoka* and Katsuya Shimizu

KYOKUGEN, Center for Quantum Science and Technology, Osaka University

*E-mail: matsuoka@cqst.osaka-u.ac.jp

References

[1] *T. Matsuoka, H. Fujihisa, N. Hirao, Y. Ohishi, T. Mitsui, R. Masuda, M. Seto, Y. Yoda, K. Shimizu, A. Machida and K. Aoki: Phys. Rev. Lett.* ***107*** *(2011) 025501.*
[2] P. Vajda, in Handbook on the Physics and Chemistry of Rare Earths, ed. by K.A. Gschneidner and L. Eyring (Elsevier Science B.V, Amsterdam **20** (1995) 207.
[3] M. Tkacz and T. Palasyuk: J. Alloys Compd. **446-447** (2007) 593.
[4] H. Sugimoto and Y. Fukai: Acta Metall. **40** (1992) 2327.
[5] K. Takemura and K. Syassen: J. Phys. F Met. Phys. **15** (1985) 543.

Orbital state of excited electron identified by polarization-analyzed resonant inelastic X-ray scattering

Strongly correlated transition metal compounds attract great interest because they exhibit a variety of interesting phenomena, such as high-temperature superconductivity in cuprates and colossal magnetoresistance in manganites [1]. It is widely recognized that the orbital degree of freedom of the *d* electrons often plays a crucial role in the occurrence of these phenomena. For example, it controls the anisotropy of electron mobility and the propagation of interactions. Orbital excitations, where the orbital state changes by gaining energy, at zero momentum transfer can be observed by Raman scattering, but an experimental technique with momentum resolution is crucial to the complete understanding of the elementary orbital excitation, the so-called orbiton. Recently, resonant inelastic X-ray scattering (RIXS) using brilliant synchrotron radiation X-rays has been developed as a new spectroscopic technique to measure excitations of correlated electrons [2], and it is a potent method to observe momentum-resolved orbital excitations. However, various excitations are often entangled in the spectrum of RIXS, and it has been difficult to distinguish between them experimentally.

To identify the orbital excitations, we utilize polarization, which is an inherent and important characteristic of the photon [3]. So far, most RIXS studies have focused on energy and momentum dependences and the polarization has been overlooked. Although the role of the incident photon polarization was investigated in relation with the resonant conditions in a few experimental and theoretical studies, the scattered photon polarization has not been identified at all. Similarly to conventional Raman spectroscopy, polarization in RIXS must be connected to the symmetry of the excitations. Because the symmetry argument is rigorous and independent of the parameters in theoretical models, the polarization can be very useful for the assignment of the excitations in RIXS.

The experiments were carried out at **BL11XU** beamline. We measured the orbital excitations of single-crystalline $KCuF_3$, which is an archetypal material with orbital order, at the Cu *K*-edge. Linearly polarized incident X-rays were monochromatized by a double crystal Si(111) monochromator and a secondary Si(400) channel-cut monochromator, and irradiated on the sample. The energy of scattered X-rays was analyzed using spherically bent Ge(800) crystals. The total energy resolution was about 600 meV. To resolve the polarization of the scattered X-rays, we developed a polarization analyzer system which is schematically shown in Fig. 1 and installed in the spectrometer. A pyrolytic graphite (PG) crystal was placed in front of the detector and the (006) reflection of PG was measured. The polarization extinction ratio of the reflection ($\sin^2 2\theta_P$, where θ_P is the Bragg angle) is 0.94. The experimental reflectivity of the (006) reflection was about 0.02. By rotating the PG crystal and the detector about the axis of the beam, one can select the polarization of the scattered photon.

Polarization-analyzed RIXS spectra are shown in Figs. 2(a) and 2(b); these spectra were measured under the two polarization conditions of $\pi \rightarrow \pi'$ and $\pi \rightarrow \sigma'$, where π is the incident photon polarization parallel to the scattering plane, and π' and σ' denote the scattered photon polarizations parallel and perpendicular to the scattering plane, respectively. The incident photon energy is fixed at 8994 eV, near the peak of the X-ray absorption spectrum. The incident photon polarization (ε_i) lies in the scattering plane and the scattering angle (2θ) is chosen to be close to 90° in order to reduce the elastic scattering. The incident and scattered polarizations are therefore orthogonal to each other, which is the so-called depolarized configuration.

Orbital excitations are observed at 1.0–1.5 eV. There are two types of orbital excitations in $KCuF_3$: One excitation is a transition of an electron from the t_{2g} orbital to the e_g orbital (t_{2g} excitation) and the other one is a transition of an electron between the e_g orbitals (e_g excitation). The latter corresponds to the orbital degree of freedom in $KCuF_3$. In Fig. 2(a), the 1.4 eV peak in the red spectrum of the $\pi \rightarrow \sigma'$ condition corresponds to an orbital excitation. From a phenomenological consideration of the symmetry of the RIXS process, we can assign the excitation as the t_{2g} excitation. On the other hand, in addition to the peak at 1.4 eV, a spectral weight exists at around 1.0 eV for the blue spectrum of the $\pi \rightarrow \pi'$ condition, and it comes from the e_g excitation. This implies that the two

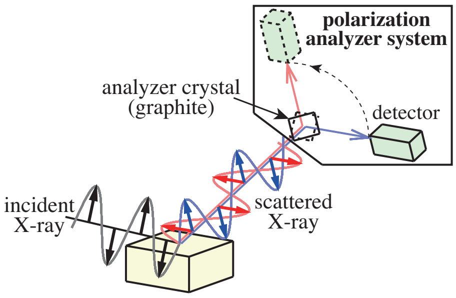

Fig. 1. Schematic view of polarization analyzer system installed at BL11XU.

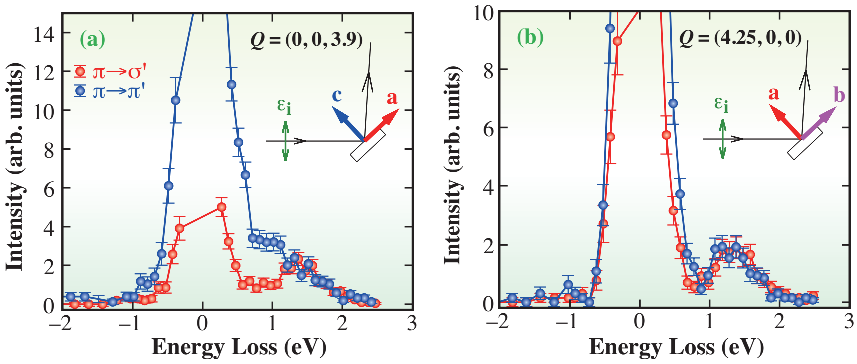

Fig. 2. Polarization-analyzed RIXS spectra. Spectra with red and blue circles are measured under the π→σ' and π→π' and conditions, respectively. The momentum transfer ($\boldsymbol{Q}$) is represented by the Miller indices in the tetragonal unit cell of the primitive perovskite structure ($a = 4.1410$ Å and $c = 3.9237$ Å) and corresponding experimental geometries are shown in insets.

orbital excitations show clear dependence on the scattered photon polarization. Our assignments based on the results of polarization analysis are consistent with a recent optical absorption study, where different orbital excitations were identified and their respective energies were estimated. When we change the polarization relative to the crystal orientation, both π→π' and π→σ' spectra become identical, as shown in Fig. 2(b), namely, the e_g excitation disappears under this polarization condition.

Now that we are able to distinguish the e_g excitation from the t_{2g} excitation, it becomes possible to investigate the momentum dependence of each orbital excitation separately. Figures 3(a) and 3(b) show the polarization-analyzed RIXS spectra obtained near the high-symmetry points of the Brillouin zone. The excitation energy of the orbital excitations is analyzed by fitting the spectra and the excitations are found to be dispersionless within our experimental resolution. Since the improvement in energy resolution is still in progress, the dispersion relation of orbital excitations should become observable by *K*-edge RIXS in the future.

In summary, we have performed a polarization-analyzed RIXS study of the orbital excitations in $KCuF_3$ at the Cu *K*-edge. The polarization of the scattered photons in RIXS was identified for the first time. Our result demonstrates that the polarization analysis is quite useful for the identification of the excitations.

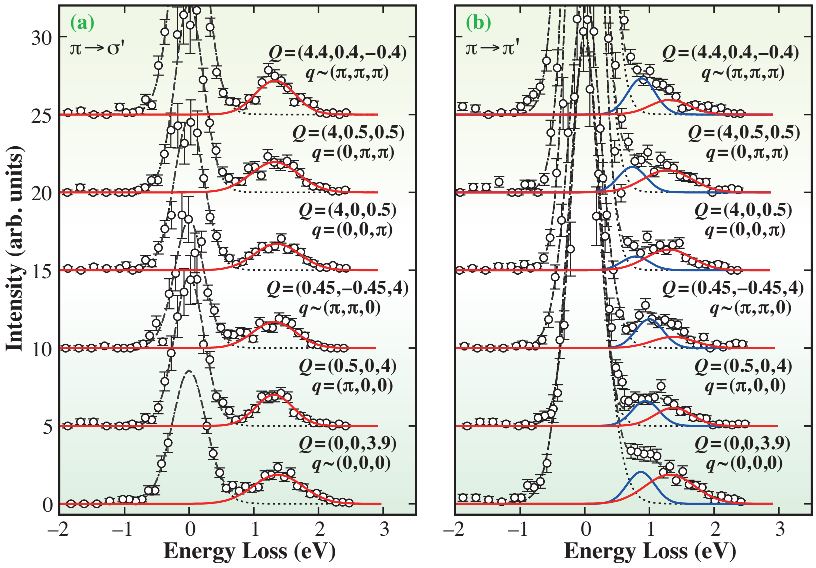

Fig. 3. Momentum dependence of polarization-analyzed RIXS spectra. $\boldsymbol{Q}$ and $\boldsymbol{q}$ are the absolute and reduced momentum transfer, respectively. Open circles correspond to the experimental data. Red and blue solid-line spectra are the fitted t_{2g} and e_g excitations, respectively. Dashed-line spectra represent the sum of the fitted elastic line (dotted line) with the fitted orbital excitations (solid line). [3]

Kenji Ishii[a,*], Sumio Ishihara[b] and Yoichi Murakami[c]

[a]SPring-8/JAEA
[b]Department of Physics, Tohoku University
[c]High Energy Accelerator Research Organization (KEK)

*E-mail: kenji@spring8.or.jp

References

[1] Y. Tokura and N. Nagaosa: Science **288** (2000) 462.
[2] L.J.P. Ament *et al.*: Rev. Mod. Phys. **83** (2011) 705.
[3] *K. Ishii, S. Ishihara, Y. Murakami, K. Ikeuchi, K. Kuzushita, T. Inami, K. Ohwada, M. Yoshida, I. Jarrige, N. Tatami, S. Niioka, D. Bizen, Y. Ando, J. Mizuki, S. Maekawa and Y. Endoh: Phys. Rev. B* ***83*** *(2011) 241101.*

Atomic and electronic structures of binary silicate glasses

Glass is abundant in nature and has been made by man for over 3000 years. Glass has evolved from a basic structural material to an enabling material for advanced electronic, biological and photonic products as well as high-volume window and fiber glass devices. Despite its rich history, many aspects of glass remain mysterious: The theory of glass transition is one of the most challenging problems in physics and chemistry in the 21st century.

The $PbO-SiO_2$ system is interesting even though lead compounds are unfavorable materials nowadays. It is well known that PbO acts both as a glass former and a glass modifier and hence the $PbO-SiO_2$ system shows a wide glass formation composition range. Therefore, it is interesting to know the underlying reason through the atomic structure of glass. Atomic structures of magnesium silicate melts are the key to understanding the processes related to the evolution of the Earth's mantle and represent precursors of the formation of most igneous rocks. Magnesium silicate compositions also represent a major component of many glass ceramics, and, depending on their composition, can span the entire fragility range of glass formation. It is worth mentioning that glass of Mg_2SiO_4 composition shows an extremely low glass forming ability (GFA), while $MgSiO_3$ composition shows a higher GFA. Therefore, we have tried to understand the relationship between glass structure and GFA at atomic and electronic levels by a combination of high-energy X-ray diffraction (**BL04B2**) and neutron diffraction measurements, reverse Monte Carlo (RMC) simulations, and density functional theory (DFT) calculations [1,2].

Figure 1 shows the cavity distribution in SiO_2 and $PbO-SiO_2$ glasses obtained by RMC simulation. It is well known that SiO_2 glass shows a large fraction of cavities (~30%), but we can see a significant amount of cavities in $PbO-SiO_2$. This is very unusual, since cavity sites are usually occupied by cations in typical binary silicate glasses (e.g., Na_2O-SiO_2 and $CaO-SiO_2$ glasses). Lead is known to act as a network former and a network modifier in binary oxide glasses. Thus, we have succeeded in visualizing the role of lead in $PbO-SiO_2$ glass, suggesting that the large fraction of cavities is the reason for the high GFA in a wide composition range.

On the other hand, both $MgSiO_3$ and Mg_2SiO_4 glasses do not have any cavities, because magnesium occupies cavity sites in binary silicate glasses. To understand the relationship between GFA and atomic structure, we compared the distribution of "-Si(Mg)-O-Si(Mg)-O-Si(Mg)-" rings in $MgSiO_3$ and Mg_2SiO_4 glasses with the distribution of "-Si-O-Si-O-Si-" rings in SiO_2 glass in Fig. 2. The ring distribution of SiO_2 glass shows the maximum fraction of 6-fold rings (comprising 6 SiO_4 tetrahedra) and is broad up to

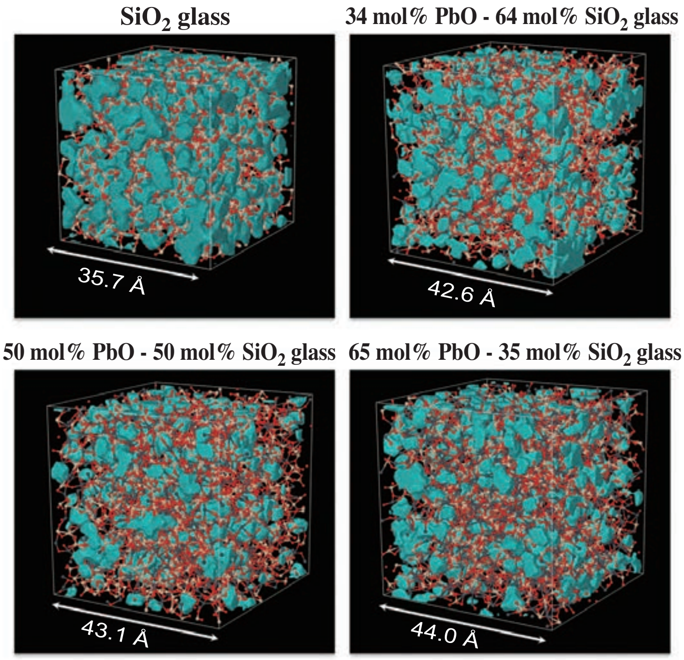

Fig. 1. Atomic configurations and voids of SiO_2 and $PbO-SiO_2$ glasses. Color key: light gray, silicon; red, oxygen; gray, lead; and cyan; voids [1].

10-fold rings. According to Gupta and Cooper, this distribution is the signature of "topological disorder", since the crystalline SiO_2 (cristobalite) has only 6-fold rings [3]. On the other hand, Mg_2SiO_4 glass shows the narrowest ring distribution, suggesting that it is "topologically ordered", which is related to the low GFA of the glass.

The coordination numbers of oxygen around magnesium derived from the RMC model are 4 and 5 for $MgSiO_3$ and Mg_2SiO_4, respectively, which do not support the formation of MgO_6 octahedra confirmed by recent NMR measurements for both glasses [4,5]. To obtain insight regarding this inconsistency, we optimized the RMC structures by DFT calculations. Furthermore, we calculated chemical strength (bond orders) for Mg-O bonds in both $MgSiO_3$ and Mg_2SiO_4 crystals and glasses. The Mg-O bond orders of glasses shown in Fig. 3 are larger than those of the corresponding crystalline phases owing to the fact that the Mg-O coordination is smaller in the glassy phase, where the cations compensate the smaller number of oxygen contacts by increasing the ionic bond strength correspondingly. The DFT calculations explain the discrepancy between the NMR and diffraction results, because NMR probes chemical shifts that are very sensitive to the electronic environment of the nuclei, while diffraction is a direct probe of the average coordination number through known neutron scattering lengths or the number of electrons surrounding an atom (provided that the partial functions are known). Previous studies [4,5] indicated that for the $MgSiO_3$ and Mg_2SiO_4 glasses, the NMR shifts are in line with the octahedral crystalline environment, although in this study we find that the Mg-O coordination is actually smaller in the glasses.

The structure of disordered materials is very ambiguous owing to the lack of long-range periodicity manifested by a broad diffraction pattern. However, a combination of synchrotron X-ray diffraction measurements and theoretical simulations is a powerful technique for studying the relationship between atomic/electronic structure and physico-chemical properties, which is crucial for revealing and understanding the origin of unique functional properties in disordered materials.

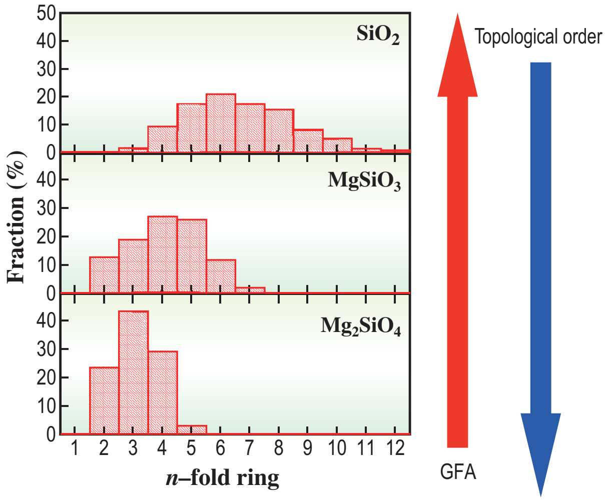

Fig. 2 The distribution of "-Si(Mg)-O-Si(Mg)-O-Si(Mg)-" rings in $MgSiO_3$ and Mg_2SiO_4 glasses and the distribution of "-Si-O-Si-O-Si-" rings in SiO_2 glass.

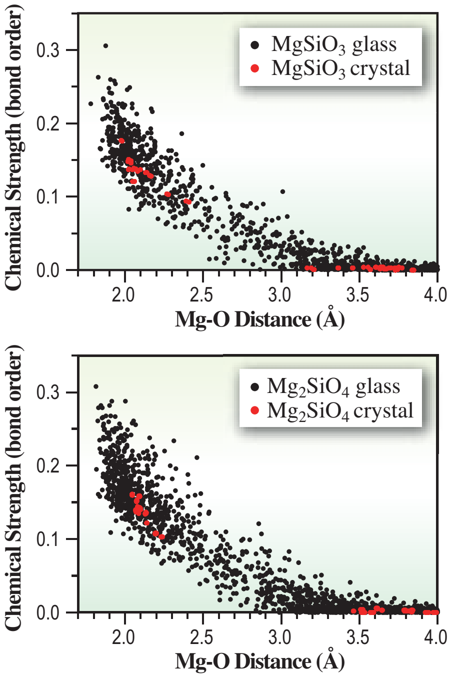

Fig. 3. Scatter plot of the chemical bond order as a function of distance for Mg-O pairs in MgO-SiO_2 glass. The crystalline reference values are included in red. [2]

Shinji Kohara[a,*] and Jaakko Akola[b]

[a] SPring-8/JASRI
[b] Dept. of Physics, Tampere University of Technology, Finland

*E-mail: kohara@spring8.or.jp

References

[1] *S. Kohara, H. Ohno, M. Takata, T. Usuki, H. Morita, K. Suzuya, J. Akola and L. Pusztai: Phys. Rev. B* ***82*** *(2010) 134209.*
[2] *S. Kohara, J. Akola, H. Morita, K. Suzuya, J.K.R. Weber, M.C. Wilding and C.J. Benmore: Proc. Nat. Acad. Sci. USA* ***108*** *(2011) 14780.*
[3] P.K. Gupta and A.R. Cooper: J. Non-Cryst. Solids **123** (1990) 14.
[4] K. Shimoda *et al.*: Am. Mineral. **92** (2007) 695.
[5] S. Sen *et al.*: J. Phys. Chem. B **113** (2009) 15243.

Application of polyelectrolytes to novel adhesion system

Adhesion utilizing the ionic interaction between oppositely charged polyelectrolytes is a simple adhesion system as an organic solvent-free adhesion system. To realize this adhesion system, it is necessary to understand the solution characteristics of polyelectrolytes because the chain dimension is an important parameter for adhesion and debonding. However, little is known on the chain dimension of a polyelectrolyte in aqueous media, which is used for adhesion and debonding solvents. In the present research, the chain dimension of the polyelectrolyte was characterized by small angle X-ray scattering (SAXS). The adhesion, debonding and reversible adhesion between the ionic polymer brush substrates were demonstrated using a deionized water as an adhesion solvent and an aqueous salt solution as a debonding solvent [1].

To characterize the effect of ionic strength on chain dimension, the authors prepared poly(2-(methacryloyloxy)ethyltrimethylammonium chloride) (PMTAC) and studied their chain dimension by synchrotron radiation SAXS at **BL03XU** beamline using an incident X-ray wavelength λ of 0.10 nm with a sample-to-detector distance of 2180 mm. The weight-average molecular weight of PMTAC was 73000. Figure 1(a) shows SAXS profiles of PMTAC of various concentrations (C_p, g·cm^{-3}) dissolved in an aqueous NaCl solution (1.0 mol·L^{-1}). The experimental excess scattering intensity $\Delta I(q)$ *versus* scattering vector q (nm^{-1}) was well simulated by Debye function fitting, which gave the radius of gyration $\langle S^2\rangle_z^{1/2}$ (nm) of PMTAC of 4.3 nm. The radius of gyration is the average distance from the center of the gravity to the chain segment, which tells us the dimension of PMTAC in the solution. The $\langle S^2\rangle_z^{1/2}$ of PMTAC in 3.0 mol·L^{-1} NaCl solution was also determined to be 4.2 nm using a similar protocol. In addition, SAXS curves showed similar slopes around the $q = 10^0$ nm^{-1} region, indicating that PMTAC maintained similar random coil conformations at various C_p when the salt concentrations were 1.0 and 3.0 mol·L^{-1}.

On the other hand, the second virial coefficient A_2 of PMTAC in the aqueous NaCl solution was obtained using the proportional relationship between the inverse of $\Delta I(0)$ and the polymer concentration C_p, as shown in Fig. 1(b). $\Delta I(0)$ was obtained using the intercept of $\Delta I(q)/C_p$ in Fig. 1(a). The A_2 values of PMTAC in the aqueous NaCl solution with 1.0 and 3.0 mol·L^{-1} were 2.0×10^{-4} and 6.3×10^{-5} g^{-1}·cm^3·mol, respectively. In this case, the decrease in A_2 with increasing NaCl concentration indicates the reduction in electrostatic repulsive interaction among the ammonium cations of PMTAC. In general, the electrostatic interactions among the ionic functional groups are screened by hydrated ions in the aqueous salt solution. The dependence of electrostatic interaction of ion-containing polymers on the ionic strength in the solution can be utilized for the reversible adhesion system.

The authors prepared 100-nm-thick polyelectrolyte brushes by the surface-initiated atom transfer radical polymerization of MTAC [2], 3-sulfopropyl methacrylate potassium salt (SPMK), and 3-(*N*-2-methacryloyloxyethyl-*N*,*N*-dimethyl) ammonatopropanesulfonate) (MAPS) [3] on the silicon wafers. As shown in Fig. 2, 2 μL of deionized water was placed on a brush-immobilized silicon substrate and then another substrate was pressed onto it under a constant load of 4.9 N at 298 K. The contact area

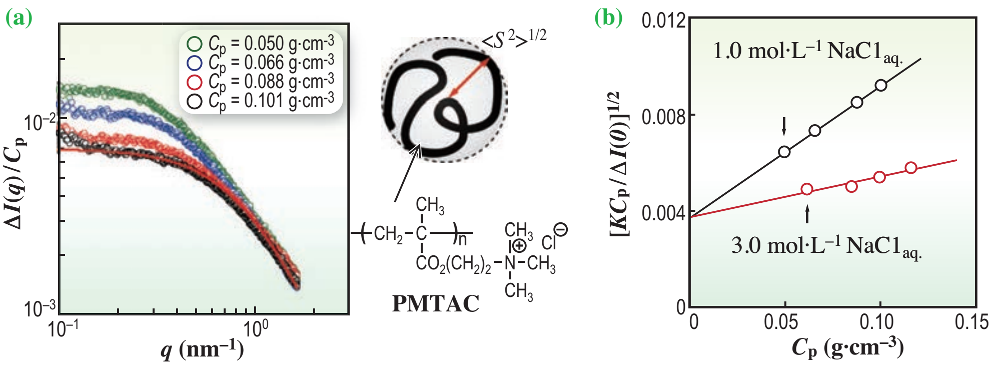

Fig. 1. **(a)** SAXS profiles of PMTAC with various polymer concentrations (C_p, g·cm^{-3}) in aqueous NaCl solution at 1.0 mol·L^{-1} (open circles) and the corresponding fit based on Debye function (red solid line), and **(b)** dependence of $[KC_p/\Delta I(0)]^{1/2}$ on C_p for PMTAC in aqueous NaCl solutions at 1.0 and 3.0 mol·L^{-1}. $\Delta I(q)$ is the experimental excess scattering intensity at q. Scattering vector $q = 4\pi\, sin\theta/\lambda$.

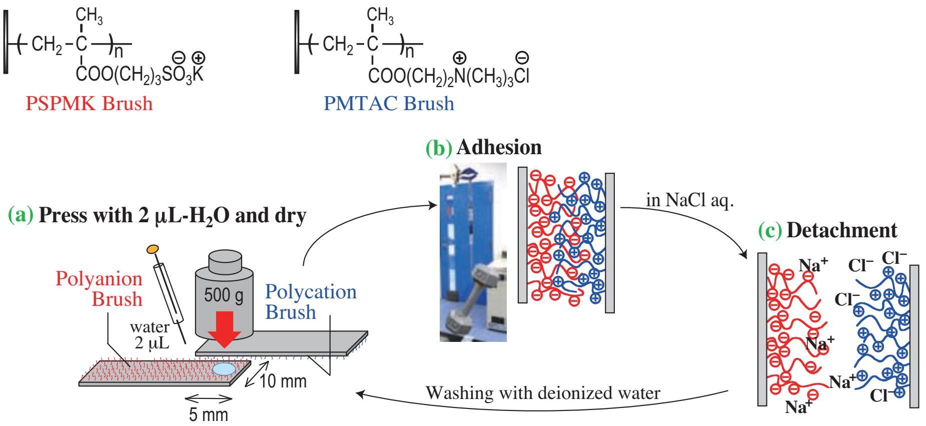

Fig. 2. Schematic view of **(a)** adhesion process of cationic PMTAC and anionic PSPMK brushes, **(b)** the bonded substrate hanging a 5 kg dumbbell, and **(c)** detachment of oppositely charged polyelectrolyte brushes in 0.5 mol·L^{-1} NaCl aqueous solution.

of the substrates was maintained at 5×10 mm^2. After 2 h of drying, the adhesion strength was measured using the lap shear adhesion force in an ambient atmosphere.

In the case of the PMTAC and poly(SPMK) (PSPMK) brush pair, the average adhesion strength reached about 1.52 MPa, as shown in Fig. 3. This strength was lower than the typical adhesion strength of commercially available adhesives (10–30 MPa); however, it would be a sufficiently useful adhesion strength for many applications because the adhered brush substrates with 1 cm^2 adhesion area could lift up a weight of *ca*. 15 kg. The lap shear adhesion strength between the poly(sodium methacrylate) (PMANa) brush and PMTAC brush substrates was 1.08 MPa. The sulfonate anion group of PSPMK interacted strongly with the ammonium cation group in PMTAC compared with carboxylic acid of PMANa. This result indicates that the electrostatic interaction contributed to the adhesion of anionic/cationic polymer brushes.

Since the polymer brushes remained on the substrate even after the lap shear test, a specimen combined with PMTAC and PSPMK brushes was rebonded several times by repeating the swelling with water and debonding in air, although the adhesive strength decreased in a stepwise fashion from 1.52 to 0.85 MPa.

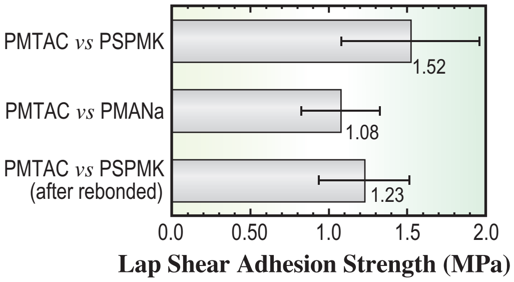

Fig. 3. Lap shear adhesion strengths of pairs of polyelectrolyte brushes at 298 K in an ambient atmosphere and 55% relative humidity.

To measure the debonding time, a specimen prepared by the adhesion of oppositely charged polymer brushes was attached to a hanging weight of 100 g and slowly immersed in deionized water at 298 K. The debonding did not occur in deionized water for over 24 h because of the formation of a polyion complex between brushes. On the other hand, the specimen was separated within 10–60 min in the aqueous NaCl solution with 0.5–5.0 mol·L^{-1}, because the hydrated salt ions permeated the adhesion interface to reduce the electrostatic interaction between brushes. After the debonded substrates were washed with deionized water to remove the salt, they readily adhered to each other again. The lap shear adhesion strength of the re-adhered substrates was 1.23 MPa, which was close to the initial adhesion strength. In this case, adhesion and debonding can be repeated without damages to the brushes by using deionized water as an adhesion solvent and salt aqueous solution as a debonding solvent.

Motoyasu Kobayashi[a], Moriya Kikuchi[a]
and Atsushi Takahara[a,b,*]

[a]JST-ERATO Takahara Soft Interfaces Project
[b]Institute for Materials Chemistry and Engineering,
Kyushu University

*E-mail: takahara@cstf.kyushu-u.ac.jp

References

[1] M. Kobayashi *et al*.: Soft Matter **7** (2011) 5717.
[2] M. Kobayashi *et al*.: Macromolecules **43** (2010) 8409.
[3] *Y. Terayama, M. Kikuchi, M. Kobayashi, A. Takahara: Macromolecules* ***44*** *(2011) 104.*

MATERIALS SCIENCE:

A variety of spectroscopic and light scattering studies are performed at SPring-8, covering a wide photon energy range from the infrared to hard-X-ray region with high energy and high momentum resolutions. Such studies provide important information on the electronic and magnetic properties of functional materials.

The performance of hard-X-ray scattering methods such as inelastic and Compton scattering at SPring-8 is very high and these methods are now applied to the investigation of many kinds of materials. H. Sakai and co-workers successfully synthesized a high-quality single crystal of perovskite $Sr_{1-x}Ba_xMnO_3$. They obtained high-resolution phonon-dispersion data by inelastic X-ray scattering at BL35XU. The ferroelectric transition related to a soft phonon was clearly observed.

High-resolution Compton profiles taken at BL08W show drastic changes in the electronic structures of materials associated with phase transitions. Y. Sakurai and K. Yamada clearly showed the difference between the electronic structures of a cuprate superconductor in the underdoped and overdoped regions. A change in electronic structures from the itinerant to the localized states in heavy-fermion Ce compounds was observed by A. Koizumi. The images of electron occupation number density are rich in information concerning the properties of such materials.

ELECTRONIC & MAGNETIC PROPERTIES

Investigations of magnetic materials are also very active at SPring-8. Recently, activities combined with microscopic techniques habe become important. In addition, studies under extreme conditions are required. An unexpected magnetic nature in high-pressure phase β(fcc)-Co was found by the hard-X-ray magnetic circular dichroism (MCD) technique at BL39XU. N. Ishimatsu successfully observed the X-ray absorption spectra and dichroism signals under high-pressure conditions up to 150 GPa. T. Nakamura and Y. Narumi succeeded in developing a high-magnetic field (~30 T) MCD at the soft-X-ray beamline BL25SU. Because MCD in the soft-X-ray region has the advantage of direct probing of the 3*d* bands of transition metals and the 4*f* bands of the rare earths, the development is very important for further studies for a variety of magnetic materials.

Hard-X-ray photoemission spectroscopy (at BL15XU, BL29XU, BL46XU and BL47XU), HAXPES, provides accurate bulk and interface information of materials. Recently, excitation by polarized-X-ray is widely utilized. G. Fecher demonstrated the linear and circular dichroism effects in angle-resolved HAXPES of Heusler compounds at BL47XU. The methods will be widely applied for the investigation of the properties of magnetic multilayers and especially of their buried interface.

Y. Takeda studied the bonding nature of aluminum hydride, which is known as a hydrogen storage material, using soft-X-ray absorption and emission spectroscopy at BL27SU. He showed the covalent nature of Al-H bonding. The applicability of the absorption and emission spectroscopy for such insulating materials with large band gaps is essential.

Other new developments and activities in the field of spectroscopy are in progress at SPring-8. These frontiers are expected to be introduced in the near future.

Toyohiko Kinoshita

Ferroelectric transition and soft-phonon dynamics associated with off-center displacement of magnetic ions in perovskite $Sr_{1-x}Ba_xMnO_3$

Since ferroelectricity was discovered in perovskite $BaTiO_3$ in 1940s, a variety of ferroelectric oxides have been extensively studied in terms of electronic device engineering as well as academic interest. Most of the perovskite ferroelectrics ABO_3 so far identified, however, consist of non-magnetic B (transition metal) site with no d-orbital electrons (Fig. 1(a)). Typical examples include $Pb(Zr,Ti)O_3$ and $KNbO_3$. The requirement of the d^0 electronic configuration in the off-center transition metal ions can be interpreted in terms of the covalent bonding [1]. Since electrons can virtually hop from the filled $2p$ orbital in oxygen to the empty d shells in the transition metal ions, the d^0 states are energetically stabilized by forming a covalent bond (Fig. 1(b)). This empirical rule for the ferroelectric perovskites, however, has been a severe restriction in designing new multiferroic materials where magnetism and ferroelectricity coexist. Since magnetic ordering in contrast requires the partial occupation of the d shell of the transition metal ions, mutually exclusive conditions are necessary for the emergence of both ferroelectricity and magnetism [2].

Against this empirical rule, a few multiferroic perovskites have been investigated, as exemplified by $TbMnO_3$ with the spiral magnetic order [3] and $BiFeO_3$ with an off-center Bi (A site) ion [4]. However, they show only small polarization or otherwise weak magnetoelectric coupling. Recently, several first-principles calculations have pointed out the possible ferroelectric ground state with large polarization (tens of $\mu C/cm^2$) for $AMnO_3$ (A=Ca, Sr, and Ba), accompanied by the Mn^{4+} ion displacement due to strong Mn-O bond covalency [5]. In reality, cubic $SrMnO_3$ is a typical Mott insulator with G-type (staggered in all three directions) antiferromagnetism and to be paraelectric down to the lowest temperature. Although the ferroelectric instability was predicted to be promoted with increasing the ionic radius of the A site ions, no ferroelectric transition was experimentally observed up to 20% Ba substitution for Sr. For a larger radius of the A site ion, the hexagonal polymorph becomes so stable that the cubic perovskite structure cannot be synthesized by the conventional solid-state reaction.

To overcome this problem, we have developed a two-step crystal growth technique, consisting of a floating-zone method and high-pressure oxygen annealing (~6 GPa) [6]. This enabled the synthesis of single crystals with the perovskite structure up to 50% Ba substitution.

Figure 2(a) shows the dependence of lattice constant a on Ba concentration (x) for $Sr_{1-x}Ba_xMnO_3$ ($0 \leq x \leq 0.5$). As x increases from 0 to 0.4, the lattice constant at 300 K monotonically increases from 3.807 to 3.856 Å with keeping the cubic symmetry. Around x=0.45, the crystal structure changes from cubic to tetragonal, indicating ferroelectric distortion with an elongation of the c-axis. Figure 2(b) shows a magnetoelectric phase diagram for $Sr_{1-x}Ba_xMnO_3$ as a function of x. The ferroelectric transition temperatures T_C were determined as the temperatures where the tetragonal distortion vanishes (Fig. 2(d)). The G-type antiferromagnetic phase is stable for the entire doping range ($0 \leq x \leq 0.5$), although the transition temperature T_N gradually decreases from 230 K (x=0) to 185 K (x=0.5). For $x \geq 0.45$, a novel multiferroic phase thus appears below $T_N(<T_C)$, associated with the antiferromagnetic ordering of off-center Mn^{4+} ions.

Spontaneous electric polarization, P_S, along the c-axis was clearly observed in the P-E hysteresis curve, as shown in Fig. 2(c). The measured P_S value at 2 K is ~4.5 $\mu C/cm^2$ in a specimen with heavily-twinned tetragonal domains, suggesting the intrinsic P_S value of 13.5 $\mu C/cm^2$ for a single domain. The values of P_S and T_C for x=0.5 are almost comparable with those for $BaTiO_3$ (P_S=26 $\mu C/cm^2$ and T_C=406 K). Since there are no lone pairs in Sr^{2+}/Ba^{2+} ions, the observed ferroelectricity is attributed to the displacement of the magnetic Mn^{4+} ion with d^3 configuration.

The long-range ordering of Mn^{4+} spins has strikingly large effects on the spontaneous polarization and lattice distortion, as shown in Fig. 2(d). The c/a value, which reaches 1.012 around room temperature, begins to decrease with decreasing temperature around 225 K ($>T_N$) probably due to the antiferromagnetic fluctuation, and then steeply drops at T_N. Below 150 K, the c/a value is almost constant (~1.0035),

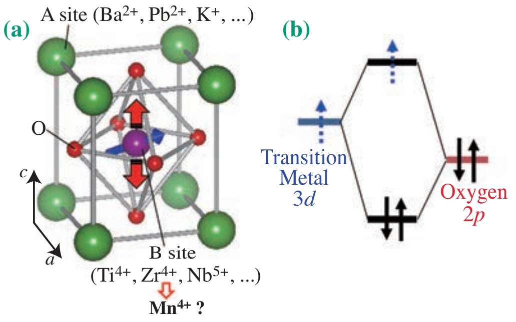

Fig. 1. **(a)** Crystal structure of perovskite oxides. For most proper ferroelectrics, the transition metal ions in the B sites are nonmagnetic. **(b)** Energy diagram of covalent bonding between transition metal $3d$ and oxygen $2p$ orbitals. Partially occupied $3d$ states in transition metal ions are energetically unfavorable in forming a covalent bond. (d^0-ness rule)

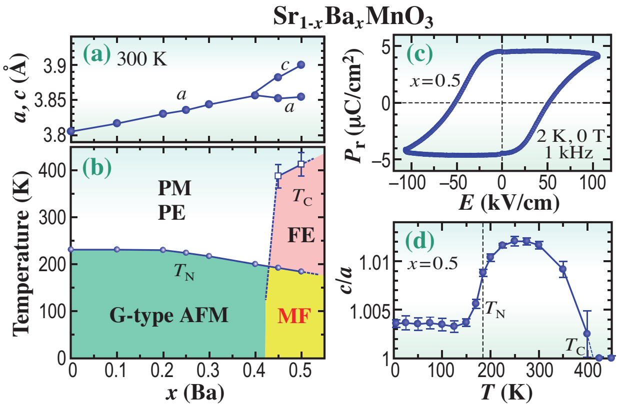

Fig. 2. **(a)** Lattice constant and **(b)** phase diagram for $Sr_{1-x}Ba_xMnO_3$ as a function of Ba concentration (x). PM, AFM, PE, FE, and MF denote paramagnetic, antiferromagnetic, paraelectric, ferroelectric and multiferroic phases, respectively. **(c)** Remnant P-E hysteresis curve for $x = 0.5$ along [001] and **(d)** temperature profile of ferroelectric distortion (c/a) for $x = 0.5$ measured by powder X-ray diffraction.

at approximately 30% of the maximum deviation from the cubic value (c/a=1). Based on a simple relation $(c/a-1)\propto P_S^2$, the P_S value above T_N is estimated to be about 1.9 times as large as that below T_N: ~25 μC/cm^2. The antiferromagnetic ordering thus can produce huge variation in P_S of the order of μC/cm^2.

The ferroelectric transition in $Sr_{1-x}Ba_xMnO_3$ is governed by a soft phonon, reflecting the displacement-type ferroelectricity. Figure 3 shows the phonon dispersion along the [110] direction for x=0–0.4, revealed by the inelastic X-ray scattering experiments at **BL35XU**. The measurements were performed on single crystals with a typical dimension of ~1×1×1 mm^3. The dispersion of the transverse optical (TO1) mode markedly varies with x, whereas those of the acoustic mode (TA) and TO2 do not change notably. In particular, the energy of TO1 mode around the zone center decreases toward zero as the doping level approaches the ferroelectric phase, showing typical soft-mode behavior. More interestingly, strong coupling between soft phonon mode and magnetism was observed. Detailed temperature dependence of inelastic X-ray scattering for x=0.3 has revealed that the soft-mode energy hardens by as much as ~50% upon the magnetic order. From Lyddane-Sachs-Teller relation, this corresponds to 60% drop in dielectric constant at T_N, suggesting significant magnetodielectric effects in paraelectric systems as well [6].

Our results confirm the violation of the empirical "d^0-ness" rule for ferroelectric perovskites and open up a promising class of new multiferroic materials with large electric polarization and huge magnetoelectric coupling. Future studies may seek a ferromagnetic ground state in further Ba-substituted compounds, which may realize switching of magnetization (polarization) with electric (magnetic) fields feasible for novel spintronics devices.

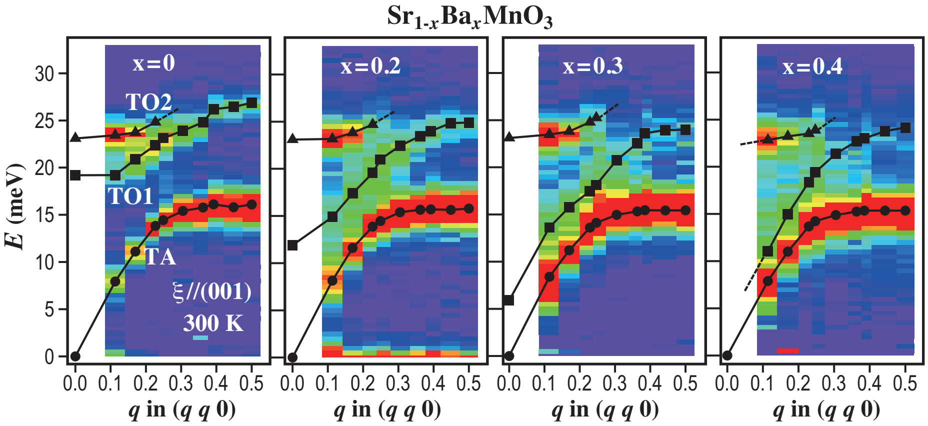

Fig. 3. Plots of the inelastic-X-ray-scattering intensity at 300 K in the energy-wave-vector (ω-q) plane in the [110] (Γ-M) direction for x = 0–0.4. The measurements were performed around the 005 Bragg reflection to detect the phonons with polarization vector ξ parallel to [001]. The closed symbols denote the phonon frequency ω_q, obtained by the fitting based on the damped harmonic oscillators. The points at q=0 were determined from the optical spectra. [6]

Hideaki Sakai[a,†,*], Yasujiro Taguchi[a] and Yoshinori Tokura[a,b,c]

[a] RIKEN Advanced Science Institute (Wako)
[b] Dept. of Applied Physics, The University of Tokyo
[c] ERATO Multiferroics Project, JST

*E-mail: hs36@st-andrews.ac.uk

[†] Present address: School of Physics and Astronomy, University of St. Andrews, UK

References

[1] R.E. Cohen: Nature **358** (1992) 136.
[2] N.A. Hill: J. Phys. Chem. B **104** (2000) 6694.
[3] T. Kimura *et al.*: Nature **426** (2003) 55.
[4] For a review, G. Catalan and J.F. Scott: Adv. Mat. **21** (2009) 2463.
[5] S. Bhattacharjee *et al.*: Phys. Rev. Lett. **102** (2009) 117602; J.M. Rondinelli *et al.*: Phys. Rev. B **79** (2009) 205119; J.H. Lee *et al.*: Phys. Rev. Lett. **104** (2010) 207204.
[6] *H. Sakai, J. Fujioka, T. Fukuda, D. Okuyama, D. Hashizume, F. Kagawa, H. Nakao, Y. Murakami, T. Arima, A.Q.R. Baron, Y. Taguchi and Y. Tokura: Phys. Rev. Lett.* ***107*** *(2011) 137601.*

Imaging doped holes in a cuprate superconductor

Superconductivity is induced by carrier doping in layered cuprates. The superconducting transition temperature T_c commonly shows a dome-shaped doping dependence and reaches the maximum at the optimal carrier doping x_{op} (see Fig. 1); below x_{op} (underdoped region) and beyond x_{op} (overdoped region) the physical properties are quite different. Despite comprehensive studies on the doping dependence of magnetism as well as lattice dynamics, the microscopic explanation for such contrasting behavior is still an unresolved issue related to the mechanism of high-temperature superconductivity. Information on the orbital character of doped carriers and its doping evolution is indispensable for solving this problem.

In hole-doped cuprates, it is established that holes predominantly enter the oxygen 2*p* orbitals in the underdoped (UD) region, but the robustness of such orbital characters in the overdoped (OD) region has not been fully understood. Distinct doping dependences of neutron scattering [1,2], and X-ray and optical spectroscopies [3,4] suggest a change in the oxygen 2*p* orbital character in the OD region. In order to detect a change in the orbital character, we must consider the spectral differences between different doping levels; this requires high-quality data for extracting weak wave function effects. Moreover, it is essential to measure a physical quantity that is connected to wave functions, such as the electron momentum density (EMD). Compton scattering is one of the most promising techniques for investigating the doped holes because it allows direct access to the EMD.

The advantages of Compton scattering over other spectroscopies are that we do not need a nearly defect-free single crystal or clean surface or ultrahigh vacuum or low temperature. Since the matrix element involved in the scattering process is much simpler, the conversion from Compton X-ray line shapes to EMDs is straightforward. For example, using Compton scattering, we can measure the EMD of a disordered compound at any temperature, even under an electric or magnetic field. Synchrotron-based X-ray Compton scattering has established itself as a viable technique for investigating orbital characters and Fermi surfaces of bulk systems in wide classes of materials.

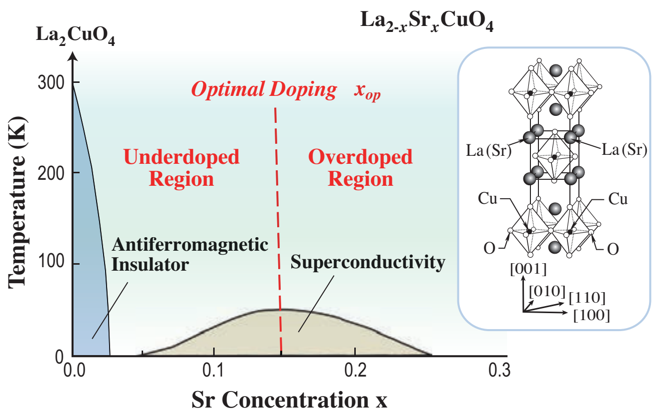

Fig. 1. Phase diagram and crystal structure of $La_{2-x}Sr_xCuO_4$. [5]

In this study [5], we obtained two-dimensional electron momentum densities (2D-EMDs), which represent one-dimensional integrals along the [001] direction of three-dimensional EMDs, for single crystalline samples of $La_{2-x}Sr_xCuO_4$ (LSCO) with four different hole concentrations, x=0.0, 0.08, 0.15, and 0.30 at room temperature. The experiment was carried out at beamline **BL08W**, using 115 keV X-rays. The 2D-EMDs were reconstructed by the direct Fourier method from each set of ten Compton profiles measured equally spaced between the [100] and [110] directions. Because of the strong two-dimensionality of LSCO, the directional character of the electronic ground state is preserved in the 2D-EMDs. To clarify the evolving nature of doped holes, we examined the differences in 2D-EMD between two samples with different doping levels. This subtraction provides information on changes in orbital occupation numbers associated with doped holes.

Our experimental data clearly show the difference between the UD and OD regions. This is demonstrated in Fig. 2, where the difference 2D-EMD between the x_{op} (x=0.15) and heavily OD (x=0.30) samples displays a markedly different feature from that in the UD region between the nondoped (x=0.0) and x_{op} (x=0.15) samples. Although some parts are still puzzling and subject to future research, we observed two distinct images with different symmetry properties: one (A-type) shows the peaks along the [100] axes and the other (B-type) has peaks along the diagonal directions (see Fig. 3). The evolution of these features with hole doping is evidence that a change or crossover behavior in the doped-hole character take place near the optimal doping x_{op}.

In layered cuprates, the angular dependence of wave functions is primarily set by the *d* orbitals of Cu, which hybridize with properly symmetrized combinations of *p* orbitals on nearest-neighbor oxygen atoms (see Fig. 4). The EMD, which is the squared modulus of the momentum-space wave function, of its orbital electron has the same directional symmetry as the corresponding charge density since the momentum-space wave function is connected to

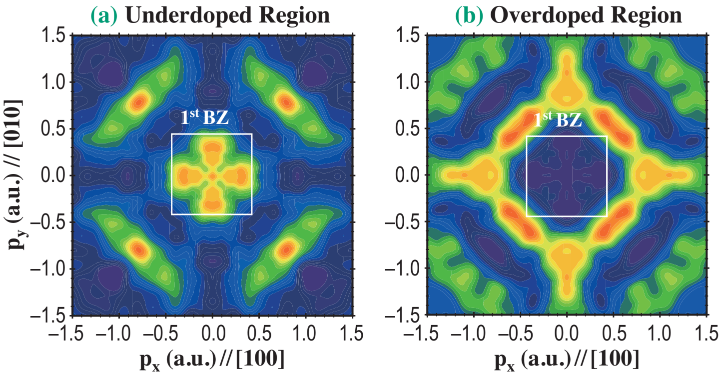

Fig. 2. Experimental difference 2D-EMDs in $La_{2-x}Sr_xCuO_4$ between two hole doping concentrations. **(a)** Underdoped: nondoped (x=0.0) minus optimal doped (x=0.15), **(b)** Overdoped: optical doped (x=0.15) minus heavily overdoped (x=0.30). The white square represents the first Brillouin zone. a.u.: atomic units.

the real-space wave function through the Fourier transformation. Our experimental data, which reveal two directionally different images, suggest a two-orbital model that incorporates both the e_g states, namely, the $x^2 - y^2$ and z^2 hybridized states. The A-type feature is associated with predominantly Cu $3d_{x^2-y^2}$ states, coupled with the molecular orbital state $P_{ZR} = P_{1x}\text{-}P_{2y}\text{-}P_{3x}\text{+}P_{4y}$ to form the so-called Zhang-Rice singlet, where numbers 1 to 4 label the four O atoms and subscripts x and y denote the direction of the O 2p orbital in the plaquette of four O atoms surrounding a Cu atom in the CuO_2 plane. The B-type feature is assigned to the Cu $3d_{z^2}$ state hybridized with the molecular orbital $P_0 = P_{1x}\text{-}P_{2y}\text{-}P_{3x}\text{+}P_{4y}$. By varying the relative Cu character of the molecular states, the model properly describes the experimental data, i.e., the weight shift from low momenta (within 1st BZ) to high momenta (in higher BZs) as it moves from UD to OD. This indicates that, although holes in the UD region primarily populate the O $2p_{x/y}$ orbitals, the character of doped holes in the OD region is very different in that these holes mostly enter Cu e_g orbitals.

The present result demonstrates that holes in the Cu e_g orbital are newly induced in the OD region. The coexistence of two types of holes either in the O $2p_{x/y}$ or Cu e_g orbital may cause electronic phase separation, as the Cu-holes locally destroy the superconductivity and degrade the incommensurate antiferromagnetic correlation in the OD region [2]. Therefore, it is important to increase the robustness of O $2p_{x/y}$ holes to achieve higher T_c.

Finally, we show the use of Compton scattering for direct, bulk-sensitive imaging of the orbital character of dopants in the ground state of complex materials. This information is inaccessible by other highly resolved spectroscopies.

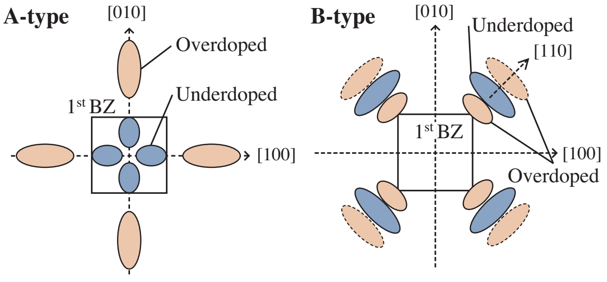

Fig. 3. Two features with different symmetry properties observed in Fig. 2.

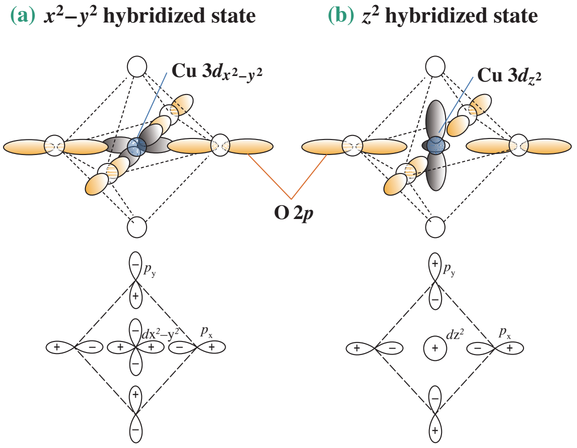

Fig. 4. Two hybridized states: **(a)** $x^2–y^2$ state and **(b)** z^2 state. (Top) Orbital configurations in CuO_6 octahedron. (Bottom) Wave function phase relationship on CuO_2 plane.

Yoshiharu Sakurai[a,*] and Kazuyoshi Yamada[b,†]

[a] SPring-8/JASRI
[b] Institute for Materials Research, Tohoku University

*E-mail: sakurai@spring8.or.jp

† Present address: Institute of Materials Structure Science, KEK

References

[1] K. Yamada *et al*.: Phys. Rev. B **57** (1998) 6165.
[2] S. Wakimoto *et al*.: Phys. Rev. Lett. **92** (2004) 217004.
[3] D.C. Peets *et al*.: Phys. Rev. Lett. **103** (2009) 087402.
[4] S. Uchida *et al*.: Phys. Rev. B **43** (1991) 7942.
[5] *Y. Sakurai, M. Itou, B. Barbiellini, P.E. Mijnarends, R.S. Markiewicz, S. Kaprzyk, J.-M. Gillet, S. Wakimoto, M. Fujita, S. Basak, Y.- J. Wang, W. Al-Sawai, H. Lin, A. Bansil and K. Yamada: Science* ***332*** *(2011) 698.*

Change of electronic structure from itinerant to localized state in heavy-fermion Ce compound: A Compton scattering study

The heavy fermion system shows a variety of interesting properties since a strongly correlated *f* electron changes its aspects depending on conditions such as temperature, magnetic field, pressure, and chemical substitution. Studies of the *f* electronic state have so far ranged over many heavy fermion materials. In particular, $CeRu_2Si_2$ is still an intriguing substance as a typical heavy fermion compound. The Ce-4*f* electron is considered to hybridize with a conduction electron below the Kondo temperature, T_K, with the result that it acquires the itinerant character as a heavy quasiparticle. In the meantime, above T_K, the Ce-4*f* electron is thought to localize in the paramagnetic phase. So far, the electronic structure of $CeRu_2Si_2$ has been frequently investigated by several experimental techniques. For instance, the de Haas–van Alphen effect measurement has been used to observe the Fermi surface (FS) topology of the itinerant state [1]; however, since this method requires a very low temperature, it is difficult to apply this method to the localized state at high temperature. The angle-resolved photoelectron spectroscopy (ARPES) experiment is also an effective technique for investigating the electronic structure. Recent ARPES experiments revealed the detailed band structure and FS of $CeRu_2Si_2$. In those studies, however, measurements were performed in the vicinity of T_K and the temperature dependence was not measured, hence the electronic structure of $CeRu_2Si_2$ was discussed in comparison with that of related compounds such as $LaRu_2Si_2$ and $CeRu_2(Si_{1-x}Ge_x)_2$ [2-4]. In this study, we employed high resolution Compton profile (HRCP) measurement as another approach for investigating the change in the Ce-4*f* electronic state in $CeRu_2Si_2$ [5].

The sample measured was a single crystal of $CeRu_2Si_2$ grown by the Czokralski pulling method in a triarc furnace. The T_K of the sample was evaluated to be 20 K from the result of magnetic susceptibility measurement. The HRCP measurements were made at beamline **BL08W**. The energy of incident X-ray was 115 keV, and the scattered X-ray was energy resolved with a Ge(620) analyzer crystal and detected by a position sensitive detector. The momentum resolution was 0.11 atomic units (a.u.). For the purpose of reconstructing a momentum density (MD), five directional HRCPs were measured at even intervals between the [100] and [110] crystal axes at 5 K and room temperature (RT). The two-dimensional MD projected onto the (001) plane in momentum space was reconstructed from the HRCPs by the direct Fourier transform method. Then the LCW analysis, which folds the MD back into the projected first Brillouin zone (BZ), was applied to the 2D MD to obtain the 2D electron occupation number density (EOND), where the EOND is the number density of electrons (holes) at each wave number, *k*, in the BZ. The EOND thus obtained has the following advantage in investigating the change in the *f*-electronic state in this system. The MDs of core electrons and fully occupied bands, in principle, make no contribution to the structure of the EOND. Therefore, the structure found in the EOND reflects the electronic state of the itinerant electron, that is, we have a chance of detecting the variation of *f* electron from the itinerant to the localized states.

Figures 1(a) and 1(b), respectively, show 2D EONDs of itinerant electrons at 5 K and RT. In this

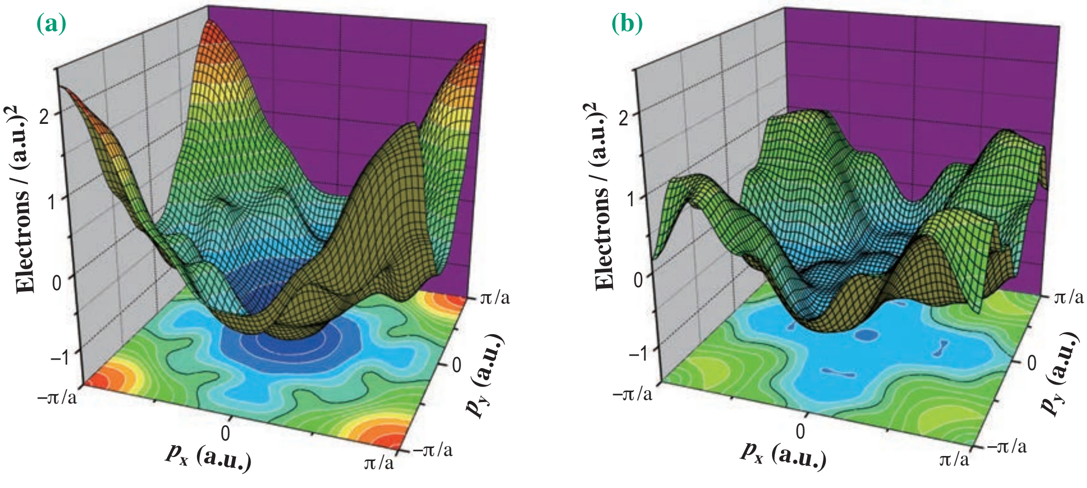

Fig. 1. Experimental 2D EONDs obtained at (a) 5K and (b) RT. [5]

regard, however, in order to emphasize the structure arising from itinerant electrons, the mean 2D EOND, which was derived from the average of the directional profiles, was subtracted from the original 2D EOND. Here, note that in the case of the 3D EOND, the boundaries between occupied and unoccupied areas correspond to the FS. In the 2D case, the densities perpendicular to a view plane are projected onto the view plane. Even so, the change in the electronic state involved with f electrons can be detected in the 2D EOND. In fact, the most striking change is observed around the corner of the projected BZ; that is, a columnar structure observed at 5 K is reduced in size at RT. To identify the cause of the change, we have also carried out a band calculation on this system by the local-density approximation based on the full-potential linearized augmented plane wave method, where the Ce-4*f* electron is treated as an itinerant one. Figure 2 shows 2D EONDs of (a) the 14th, (b) the 15th, and (c) the sum total of relevant bands derived from the calculation result. These bands across the Fermi energy level and hence are involved in the formation of the FS including f electron contribution. The depressed area in Fig. 2(a) reflects the contribution of holes in the 14th band to the FS, and the pillar section at the corner in Fig. 2(b) is the contribution of electrons in the 15th band. The theoretical 2D EOND in Fig. 2(c) well reproduces the general appearance of the experimental one in Fig. 1(a), and the pillar section in Fig. 2(b) well describes the difference in density between Figs. 1(a) and 1(b). In the present case, the densities at the X, W, and P symmetric points in the BZ are projected on the corner of the 2D EOND. The band calculation reveals that these symmetric points are highly occupied by the Ce-*f* (ℓ=3) component in the 15th band. Therefore, the columnar structure in Fig. 1(a) is attributed to the Ce-4*f* electron in the 15th band, and the shrinkage of the columnar structure in Fig. 1(b) clearly specifies the localization of the Ce-4*f* electron.

As described above, in the present study, the Ce-4*f* electron, which changes its nature from the itinerant to the localized states, was well detected in CeRu$_2$Si$_2$. The Compton experiment is feasible without constraint on the experimental conditions such as temperature, magnetic field, pressure, and chemical substitution. Therefore, this technique will also be effective in systematically investigating the change in the electronic structure along with the metamagnetic transition in CeRu$_2$Si$_2$, the hidden order in URu$_2$Si$_2$, and other interesting phenomena of the heavy fermion system.

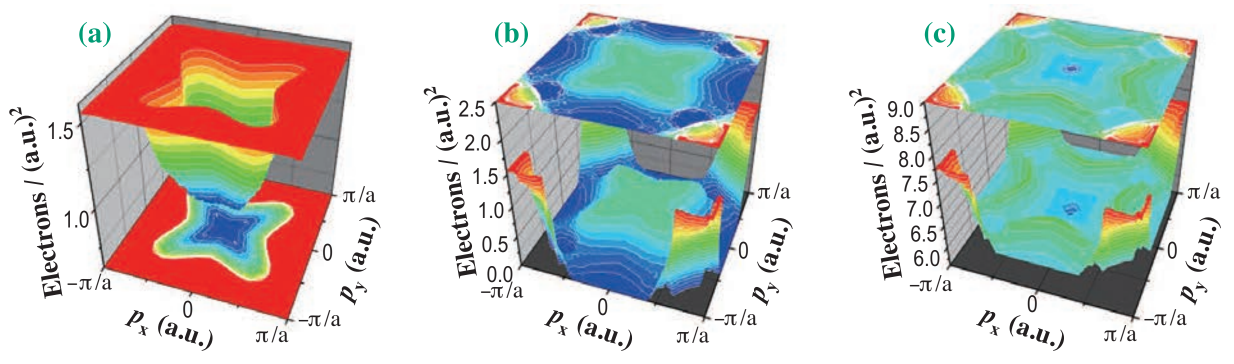

Fig. 2. Theoretical 2D EONDs of **(a)** the 14th, **(b)** the 15th, and **(c)** the sum total of relevant bands. [5]

Akihisa Koizumi

Graduate School of Material Science,
University of Hyogo

E-mail: akihisa@sci.u-hyogo.ac.jp

References

[1] M. Sugi *et al.*: Phys. Rev. Lett. **101** (2008) 056401.
[2] J.D. Denlinger *et al.*: J. Electron Spectrosc. Relat. Phenom. **117-118** (2001) 347.
[3] M. Yano *et al.*: Phys. Rev. B **77** (2008) 035118.
[4] T. Okane *et al.*: Phys. Rev. Lett. **102** (2009) 216401.
[5] *A. Koizumi, G. Motoyama, Y. Kubo, T. Tanaka, M. Itou and Y. Sakurai: Phys. Rev. Lett.* ***106*** *(2011) 136401.*

Discovery of paramagnetism with anomalously large magnetic susceptibility in high-pressure phase β(fcc)-cobalt

Pressure-induced magnetic transitions have received much attention because a new phase at high pressure gives considerable insight into the correlation between the crystal structure and ferromagnetism. In 2000, Yoo *et al*. discovered the ε→β (hcp→fcc) martensitic structural transition of Co at ~100 GPa by means of X-ray powder diffraction [1]. Because this transition is regarded to be analogous to the pressure-induced martensitic transition of Fe (ferromagnetic bcc→nonmagnetic hcp at ~14 GPa), they proposed that β-Co is nonmagnetic. Theoretical calculations have also predicted that β-Co is nonmagnetic [2]. However, the transition pressure is so high that the direct observation of the magnetic states has so far not been achieved.

X-ray magnetic circular dichroism (XMCD) is a spectroscopic technique that enables us to probe magnetically polarized electronic states even under high pressure. To investigate the magnetic state of β-Co, XMCD measurement at the Co *K*-edge was carried out at beamline **BL39XU** using a diamond anvil cell. XMCD spectra were measured by the helicity-modulation method. A magnetic field H of 0.6 T was applied parallel to the incident X-ray beam and in the direction of surface normal of the sample. In this study, we succeeded in the direct observation of the magnetic state up to 170 GPa [3]. The measurement was done at room temperature. The incident X-ray beam was focused using Kirkpatrick and Baez (K-B) mirrors; a circularly polarized beam with a size of 7 (v) × 6 (h) μm^2 was realized at the sample position, which is a suitable condition for a very small sample in the diamond anvil cell at $P > 100$ GPa.

Figure 1 shows the pressure dependence of XANES spectra. The marked changes in the XANES profile can be recognized in the absorption maximum referred to as **b** (**b**') and **c** (**c**'), which is caused by the ε-β structural transition. The pressure variation in the XANES can be divided into three regions, I, II, and III. The ε-Co single phase is stable in region I, the ε- and β-Co phases coexist in region II, and the β single phase is formed in region III. The boundary pressures were determined to be P_t = 81(8) GPa and P_t' = 134(6) GPa. P_t represents the onset of the structural transition. In region III ($P > P_t'$), the residual ε phase disappears, and Co completely transforms to the β-phase.

The magnetic states in ε- and β-Co are investigated by the pressure variation in the XMCD spectrum shown in Fig. 2. As the pressure increases, the *K*-edge XMCD amplitude shows a gradual reduction. Figure 2 demonstrates that the small amplitude is maintained up to 170 GPa without changes in the spectral shape. The integrated intensity of XMCD, I_{XMCD}, plotted in the inset of Fig. 2, shows that a sharp drop of I_{XMCD} occurs at the onset of the ε-β transition (P_t). As the pressure increases, I_{XMCD} gradually decreases again at region II, and it reaches a constant value at region III above P_t'. The nonzero I_{XMCD} in region III suggests that β-Co possesses finite magnetization due to the magnetic polarization of 3*d* electrons. Hence, β-Co is not nonmagnetic, in contrast to the theoretical predictions.

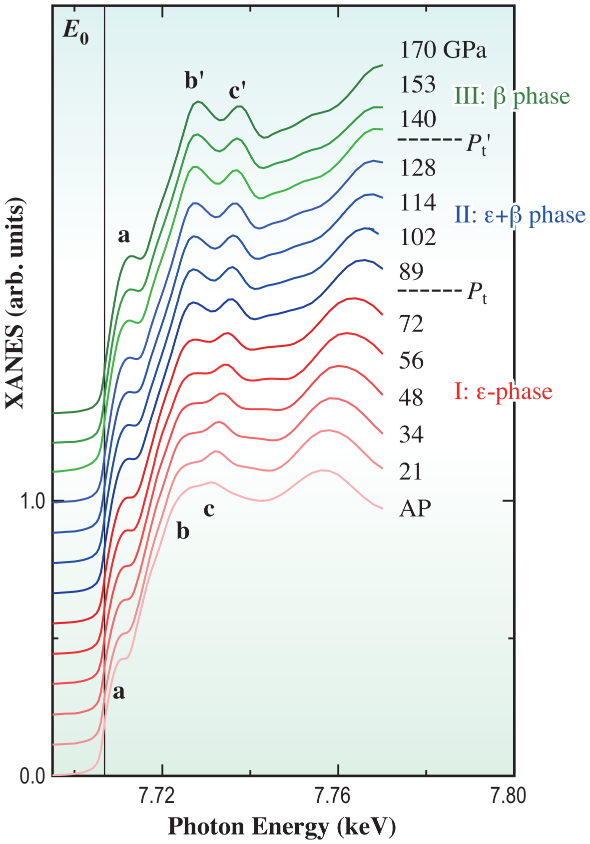

Fig. 1. XANES profiles at the *K*-edge of Co up to 170 GPa. For clarity, each profile is shifted upward. The pressure dependence is divided into three regions, I, II, and III.

In region III, the XMCD amplitude is nearly proportional to the magnetic field (H) and approaches zero at H = 0 T without hysteresis, suggesting that β-Co is paramagnetic. The marked H dependence indicates that measurable magnetization is easily induced by an external magnetic field in the paramagnetic β-Co. Under the assumption that I_{XMCD} is proportional to the magnetization, the mass susceptibility of β-Co is estimated to be $\chi = 1.5(4)\times10^{-3}$ cm^3/g. The evaluated χ is three orders of magnitude larger than the typical value for nonmagnetic 4d and 5d transition metals and is nearly the same as the reported value of γ(fcc)-Co above T_{C} at ambient pressure (AP). The anomalously large susceptibility indicates that the total energies of the states with and without a finite magnetic moment are comparable. Our result also reveals that the magnetic states of the high-pressure phases in Co and Fe are clearly different. In the case of ε(hcp)-Fe, the zero intensity of XMCD demonstrates the nonmagnetic state of ε(hcp)-Fe [4]. Because this experiment was carried out at room temperature, the magnetic ground state of β-Co is still an open question. There are two possible magnetic states of β-Co: (i) a ferromagnetic ground state with the Curie temperature T_{C} located below room temperature or (ii) a paramagnetic ground state accompanied with large magnetic susceptibility. The present results encourage theoretical researchers to reexamine the magnetic states of β-Co. XMCD measurements at low temperature should be carried out to investigate the magnetic ground state.

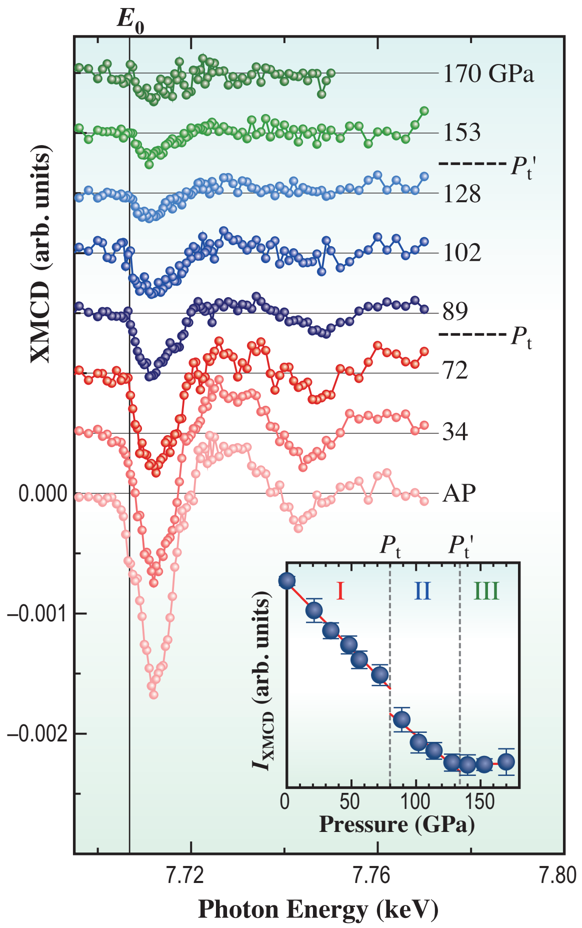

Fig. 2. XMCD spectra at the K-edge of Co at selected pressures. The inset shows integrated intensity of XMCD, I_{XMCD}, as a function of pressure (filled circles).

Naoki Ishimatsu

Graduate School of Science,
Hiroshima University

E-mail: naoki@sci.hiroshima-u.ac.jp

References

[1] C.S. Yoo *et al*.: Phys. Rev. Lett. **84** (2000) 4132.
[2] J.E. Saal *et al*.: J. Phys.: Condens. Matter **22** (2010) 096006.
[3] *N. Ishimatsu, N. Kawamura, H. Maruyama, M. Mizumaki, T. Matsuoka, H. Yumoto, H. Ohashi and M. Suzuki: Phys. Rev. B* ***83*** *(2011) 180409(R).*
[4] N. Ishimatsu *et al*.: J. Phys. Soc. Jpn. **76** (2007) 064703.

High-magnetic-field soft X-ray spectroscopy using a 30 T pulse magnet

Magnetic materials are generally synthesized and used as alloys and compounds. They are also stacked as a multilayer film for spintronics device such as a reading-head sensor of a hard disk drive. The evaluation of magnetization is the most fundamental characterization in studies of magnetic materials. Magnetic field and temperature dependence of the magnetization gives rich information on magnetic properties including magnetic order and anisotropy. In alloys and compounds involving more than two elements, the partial magnetization originating from individual elements, which is called the element-specific magnetization, promises to provide a deeper understanding of their magnetic property.

X-ray magnetic circular dichroism (XMCD) in absorption spectroscopy is one of the magneto-optical effects and provides the element-specific magnetization, where element selectivity follows the selection rule of core-electron excitation. In particular, XMCD in the soft X-ray region have the inherent advantage of probing the 3*d* bands of transition metals and the 4*f* band of the lanthanoids. With the increasing popularity of XMCD, high magnetic fields have become more important for the study of magnetic materials by means of XMCD, in order to investigate paramagnetic, antiferromagnetic, and metamagnetic materials. The available magnetic field used for soft XMCD, however, has remained at 10 T for the last decade. In order to far exceed 10 T, the possibility of using a pulse magnet that provides a field over 20 T was considered. Although the total electron yield (TEY) method is the most used and the most convenient detection method for soft X-ray absorption measurements, it is anticipated that TEY detection might be strongly affected by large amounts of noise due to an eddy current. Nevertheless, the TEY method is crucial for the practical application of high-magnetic-field XMCD to not only transmittable thin films but also bulk and powder samples. By considering of the use of high-magnetic-field XMCD as a universal method in the future, we have decided to use the TEY method in high-magnetic-field XMCD experiments. In the present article, we introduce our attempts to measuring soft XMCD under pulsed high magnetic fields.

A new apparatus for high-magnetic-field XMCD measurements was installed at the soft X-ray beamline **BL25SU**, at which the helicity switching technique was developed using twin helical undulators. An ultra-high vacuum (UHV) chamber of the XMCD apparatus is shown in the schematic drawing in Fig. 1. A nondestructive pulse magnet capable of generating 30 T is mounted outside of the vacuum chamber and is directly cooled by liquid nitrogen. The duration of the pulse is about 50 ms. The TEY signal and the induction voltage from the magnetic field are simultaneously recorded with a frequency of 1 MHz. XMCD (μ_m (H)) is given by the difference in the magnetic field dependence of the absorption profiles for the plus (h_+) and minus (h_-) helicities, represented by $\mu_+(H)$ and $\mu_-(H)$, respectively. A multilayer film, Ta(1)/Ru(1)/Co$_{70}$Fe$_{30}$(4)/Mn$_{75}$Ir$_{25}$(10)/Ru(30)/Ta(10)/SiO$_2$/Si(substrate), was used as the sample in the present study. The numbers in parentheses represent the thickness of each layer in nanometers.

Figure 2(a) shows the absorption and XMCD spectra for the Co $L_{2,3}$-edges. The spectra were recorded under a static magnetic field of 1.9 T by the conventional helicity switching technique in 1 Hz. The photon energy of 780 eV, at which the XMCD effect reaches a maximum, was chosen for the element-specific magnetization measurements using the pulse magnet. Figure 2(b) shows the results of high-magnetic-field XMCD measurement. The time dependence of the variations in absorption for h_+ and h_- have opposite signs, and successfully yields the XMCD profile. The magnetic field dependence of the XMCD intensity, $\mu_m(H)$, is shown in the inset of Fig. 2(b) and gives an identical magnetization curve to that measured with a SQUID magnetometer (not shown). The inset of Fig. 2(b) also confirms that the accuracy improves by using the appropriate statistical processing, which takes the average XMCD intensity for every 0.25 T of magnetic field and gives a reliability of about ±1% with respect to the saturated XMCD value. In order to confirm the fact that photon energy

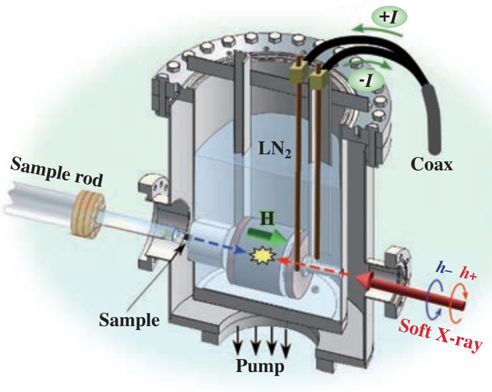

Fig. 1. Schematic drawing of the ultra-high vacuum (UHV) chamber equipped with a nondestructive pulse magnet. The magnet is directly cooled by liquid nitrogen.

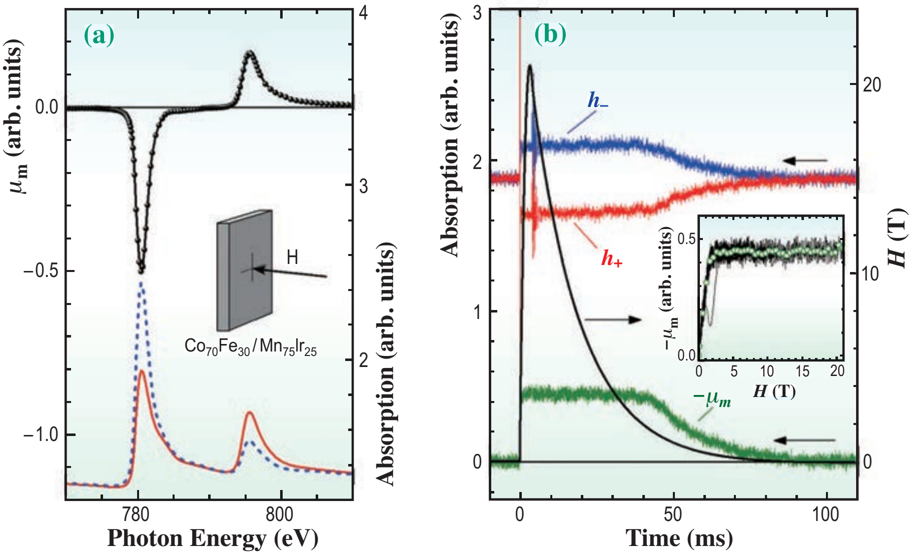

Fig. 2. **(a)** Absorption and XMCD spectra at Co $L_{2,3}$-edges of Ta/Ru/$Co_{70}Fe_{30}$/$Mn_{75}Ir_{25}$/Ru/Ta/SiO_2/Si(substrate) film. **(b)** Main window: time dependence of magnetic field, absorptions for plus (h_+) and minus (h_-) helicities at 780 eV, and XMCD (μ_m) given as the difference between the two absorption profiles. [1]

dependence of $\mu_m(H)$ profiles gives magnetic field dependence of XMCD spectra, the $\mu_m(H)$ profiles were measured at 41 photon energy points. Figure 3 shows the result of the measurement with a magnetic field of up to 6 T and confirms that the XMCD spectrum can be obtained by projecting $\mu_m(H)$ profiles onto the photon energy axis.

In the present study, we successfully developed the high-magnetic-field XMCD technique using the pulse magnet, which greatly exceeded the previous maximum field of 10 T. The maximum magnetic field of 30 T has already been used for soft XMCD studies, and a project for generating a field of 40 T is going to be operational by summer 2012.

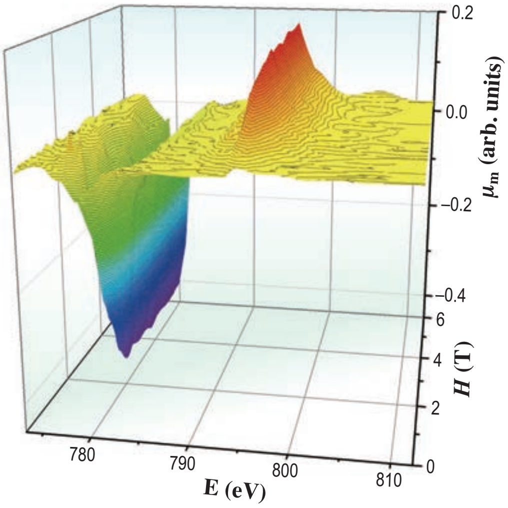

Fig. 3. Three-dimensional display of the energy dependence of high-magnetic-field XMCD profiles up to 6 T. [1]

Tetsuya Nakamura[a,*] and Yasuo Narumi[b]

[a] SPring-8/JASRI
[b] IMR, Tohoku University

*E-mail: naka@spring8.or.jp

Reference

[1] *T. Nakamura, Y. Narumi, T. Hirono, M. Hayashi, K. Kodama, M. Tsunoda, S. Isogami, H. Takahashi, T. Kinoshita, K. Kind and H. Nojiri: Appl. Phys. Express.* ***4*** *(2011) 066602.*

Linear and circular magnetic dichroism in angle-resolved hard X-ray photoemission from Heusler compounds

Heusler compounds have attracted scientific and technological interest and are now widely used as materials for magneto-electronic devices [1]. One major technology where Heusler compounds are used is on tunneling magneto resistive (TMR) junctions. To develop high performance spintronic devices, it is essential to clarify the electronic structures of these films and compare them to bulk materials. Hard X-ray photoelectron spectroscopy (HAXPES) is a powerful method to probe both chemical states and electronic structure of bulk materials and buried layers in a non-destructive way [2]. The combination of HAXPES with polarized radiation for excitation significantly extends its applicability. The use of linearly *s* and *p* polarized light in HAXPES enables the analysis of the symmetry of bulk electronic states [3]. In the present study the valence band electronic structure of NiMnSb bulk material was investigated by means of HAXPES and linear dichroism. The 2*p* core level of a thin exchange biased thin film of Co_2FeAl as used in TMR devices was studied by means of HAXPES combined with circular magnetic dichroism.

The polarized HAXPES experiments were performed at **BL47XU** using 7.94 keV linearly and circularly polarized photons for excitation. Horizontal (*p*) polarization was obtained directly from the undulator without any additional polarization optics. An in-vacuum phase retarder based on a 300-μm-thick diamond crystal was used to produce vertical, linearly s-polarized light or circularly σ+ or σ− polarized light, all with a degree of polarization above 90%. Gracing incidence ($\alpha = 88°$) – normal emission ($\theta = 2°$) geometry was used that ensures that the polarization vector was nearly parallel (*p*) or perpendicular (*s*) to the surface normal or that the polarization vector σ coincides with the magnetization. The energy resolution was set to 150 meV and was verified by spectra of the Au valence band at the Fermi energy. For further details of the experiment see [3,4].

Figure 1 compares the valence band spectra and calculated electronic structure of NiMnSb. The density of states exhibits a typical 4-peak structure in the energy range of the *d* states as well as the split-off *s*-band with a_1 symmetry. These structures are clearly resolved in the spectra. The sum of the polarization-resolved spectra corresponds to a spectrum with unpolarized photons. The width of the *d*-part of the density of states (0…5 eV) corresponds to the width of the measured spectra. The spectrum exhibits a rather high intensity in the a_1-part below –7 eV that is caused by the higher cross section for *s*-states compared to *d*-states at high excitation energy. The intensity of the *d*-states states is governed by the states localized at the Ni atoms. It is evident that striking differences appear in the spectra if the polarization is changed from *p* to *s*. The spectra indicate that the a_1 states have a higher intensity for *p* polarization and the *s* polarization result in a higher intensity in the energy range of the *d*-states. In particular, the intensity of the Ni 3*d* states at –2 eV is enhanced and the structure of the density of states becomes better resolved under illumination with *s* polarized photons. These observations show that the symmetry of the states can be explored using linearly polarized photons [3].

Figure 2 shows the Fe 2*p* and the "*shallow*" core level of a deeply buried Co_2FeAl film underneath

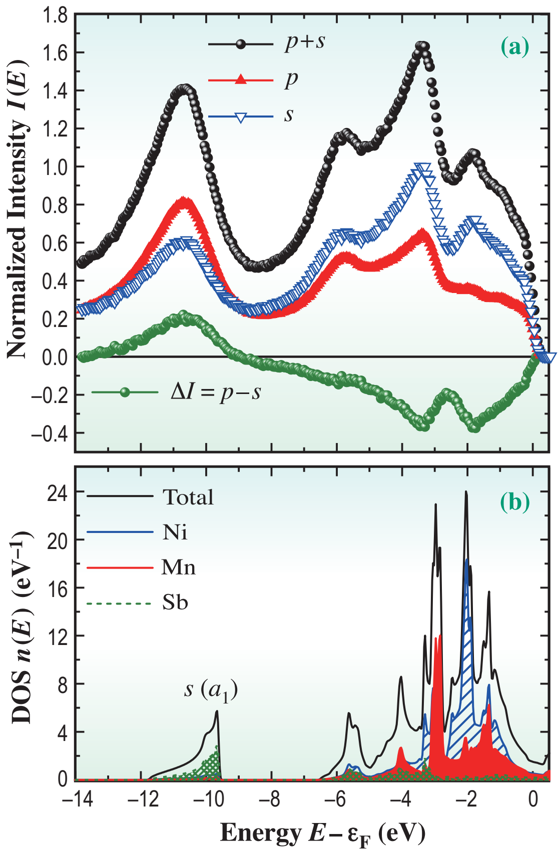

Fig. 1. Electronic structure and polarization-dependent photoelectron spectra of NiMnSb. **(a)** Spectra obtained with *s* and *p* polarized light together with the sum and difference and **(b)** total and partial density of states (DOS).

10 nm of MnIr. The differences in the spectra taken with opposite helicity of the photons at a fixed direction of magnetization are very pronounced. The spin-orbit splitting of the Fe 2*p* states is clearly resolved, as expected. If going from $2p_{3/2}$ to $2p_{1/2}$, the dichroism changes its sign across the 2*p* spectra in the series −++− what is typical for a Zeemann-type m_j sub-level ordering. Details of the MCDAD reveal, however, that the situation is more complicated. For such complex multilayer structures the situation becomes complicated in the way that the signals from all the elements contained in the system are detected. One still notices strong signals from the buried elements even though the ferromagnetic Co_2FeAl layer lies underneath the antiferromagnetic IrMn layer. As expected no MCDAD is observed for the Ir and Mn states. A non-vanishing asymmetry is clearly observed only for Co and Fe signals that are just the ones being responsible for the ferromagnetic properties of the system. The asymmetry of 50% in the Fe 3*p* signal is huge. At the Co 3*p* it is well detected even though the direct spectra overlap with Ir states.

Overall, the high bulk sensitivity of HAXPES combined with linearly and circularly polarized photons will have a major impact on the study of the magnetic phenomena of magnetic materials. It will allow an element-specific study of the magnetism of buried layers and make feasible the investigation of the properties of magnetic layers not only at the surface but also at buried interfaces. The results obtained with circularly polarized photons confirm the possibility to distinguish between localized or itinerant character of the magnetic moments in complex compounds. The symmetry of valence states can be determined when using linearly polarized photons.

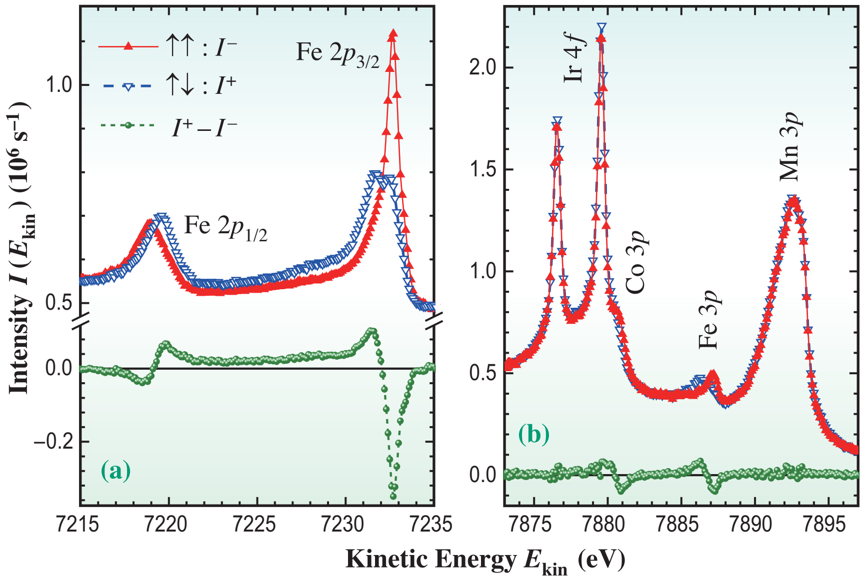

Fig. 2. High kinetic energy core level spectra and MCDAD from Co_2FeAl underneath a 10 nm thick IrMn film. **(a)** Fe 2*p* core level; **(b)** shallow core levels. [4]

Gerhard H. Fecher

Max Planck Institute for Chemical Physics of Solids,
Germany

E-mail: fecher@cpfs.mpg.de

References

[1] C. Felser *et al*.: Angew. Chem. Int. Ed. **46** (2007) 668.
[2] G.H. Fecher *et al*.: Appl. Phys. Lett. **92** (2008) 193513.
[3] *S. Ouardi, G.H. Fecher, X. Kozina, G. Stryganyuk, B. Balke, C. Felser, E. Ikenaga, T. Sugiyama, N. Kawamura, M. Suzuki, K. Kobayashi: Phys. Rev. Lett.* ***107*** *(2011) 036402.*
[4] *X. Kozina, G.H. Fecher, G. Stryganyuk, S. Ouardi, B. Balke, C. Felser, G. Schönhense, E. Ikenaga, T. Sugiyama, N. Kawamura, M. Suzuki,T. Taira, T. Uemura, M. Yamamoto, H.Sukegawa, W. Wang, K. Inomata, K. Kobayashi: Phys. Rev. B* ***84*** *(2011) 054449.*

Clarifying bonding nature in aluminum hydride using soft X-ray synchrotron radiation

Hydrogen is an ultimate source of clean energy. The key to utilizing hydrogen as an energy source is to develop materials in which a large amount of hydrogen can be stored and for which the hydrogen storage and release processes can be regulated under pressures and temperatures close to those of atmospheric conditions. Aluminum hydride (α-AlH_3) is a candidate for a hydrogen storage material owing to its large gravimetric and volumetric hydrogen content (10.1 wt% and 149 kgm^{-3}, respectively) [1]. Although α-AlH_3 is lightweight and can store a large amount of hydrogen, high temperature and pressure are required to enable hydrogen storage. To solve this problem, it is essential to understand the bonding nature of aluminum and hydrogen atoms.

Many theoretical studies of the electronic structure of α-AlH_3 have been reported so far. On the other hand, there have been very few experimental studies. Whether the nature of bonding between aluminum and hydrogen atoms is ionic or covalent has not yet been settled in the theoretical research. Therefore experimental studies of the electronic structure are urgently required.

Soft X-ray emission spectroscopy (SXES) and soft X-ray absorption spectroscopy (SXAS) with a total fluorescence yield (TFY) method are feasible techniques for investigating experimentally bulk electronic structures. These techniques are applicable to the investigation of insulating α-AlH_3. A successful example of their application to an amide hydride, which is a large gap insulator, has been reported recently [2]. Photon-in-photon-out spectroscopy is insensitive to surface conditions and hence has advantages over surface-sensitive spectroscopies, such as photoemission spectroscopy, in measuring bulk electronic structures. SXES and SXAS experiments enable us to measure the occupied and the unoccupied electronic states, respectively, and to obtain the whole feature of the electronic states by combination of their spectra. In addition, one can extract a partial density of states (PDOS) for a specific element by the tuning photon energy to the excitation energy of the target element in the SXES and SXAS experiments.

A polycrystalline sample of α-AlH_3 was synthesized by the hydrogenation of Al metal with hydrogen fluid at 600°C and 8.9 GPa [3]. In order to investigate the change in the electronic structures upon hydrogenation, an Al metal sample with a purity of 6N (Nilaco Corporation, Japan) was also prepared as a reference material. In the present measurements, we focused our interest on the Al 3*p* electronic states

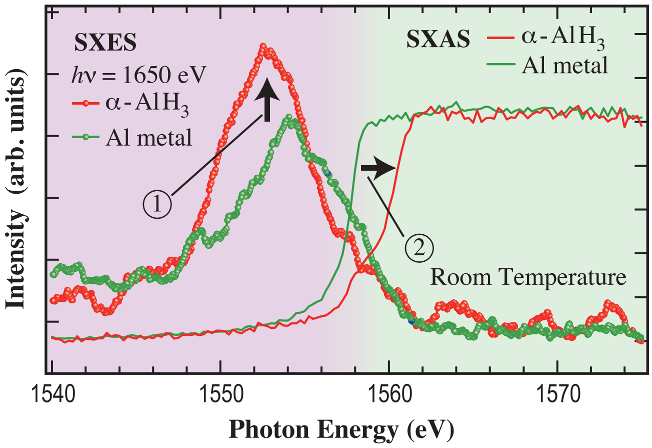

Fig. 1. Electronic states of Al metal (green) and aluminum hydride α-AlH_3 (red) obtained by soft X-ray emission spectroscopy (SXES: closed circles) and soft X-ray absorption spectroscopy (SXAS: solid lines). SXES and SXAS can reveal the occupied and unoccupied electronic states, respectively. The integrated value of the spectral intensity can be considered to be the number of electrons. [6]

of the two samples. The Al 3*p* PDOS in the occupied and unoccupied states were observed by SXES at the Al K_β emission (3*p* → 1*s*) and by SXAS at the Al *K* (1*s* → 3*p*) absorption edge, respectively. SXES and SXAS measurements were performed at the experimental station of the soft X-ray beamline **BL27SU** [4]. SXAS spectra were measured by the TFY method. Both the experiments were performed on the same sample at room temperature. Neither cleaning nor treatment of the sample surface was carried out in the vacuum chamber. The energy resolution (ΔE) of the incident photon was set to $E/\Delta E = 3000$. The total ΔE in the SXES experiment was 4 eV from the peak width of the elastic scattering of the incident excitation X-rays.

Figure 1 shows the whole Al 3*p* electronic structures of α-AlH_3 and Al metal obtained by combining the SXES and SXAS spectra. The SXES spectrum of α-AlH_3 is normalized so as to have the same integrated intensity as the SXES spectrum of Al metal at the characteristic $K\alpha$ emission at $h\nu$ = 1486.6 eV, because one can assume that the $K\alpha$ emission has the intensity independent of materials. The SXAS spectrum of α-AlH_3 is normalized so as to be the same spectral height of the SXAS spectrum of Al metal at $h\nu$ = 1600 eV. The electronic states of the Al 3*p* PDOS obviously show two significant differences between α-AlH_3 and Al metal. After hydrogenation, the SXES spectral intensity is increased and an energy gap is formed as shown by arrows 1 and 2, respectively. The enhancement of the SXES spectral intensity means that the number of Al 3*p* electrons in the occupied states increases by the hydrogenation. If the Al-H bond is completely ionic, it is expected that the Al 3*p* electrons transfer to the H atom according to the electronegativity [5], namely $AlH_3 \rightarrow Al^{3-} + 3H^+$. However, this assumption is opposite to the observed result that the distribution of the Al 3*p* electrons increases. It is also found that the band-structure calculation (not shown here) qualitatively reproduces the energy gap and the increase of Al 3*p* electrons upon hydrogenation. The present findings from the experimental and theoretical investigations, namely, that the energy-gap formation and the increase of the Al 3*p* electrons occur simultaneously, suggest that the covalent nature should be significant in the Al-H bond [6]. This clarification will not only contribute to understanding the hydrogen-storage and -release processes of aluminum hydrides but also provide directions for the design of new hydrogen-storage materials based on lightweight and inexpensive aluminum.

Yukiharu Takeda

SPring-8/JAEA

E-mail: ytakeda@spring8.or.jp

References

[1] J. Graetz and J.J. Reilly: J. Alloys Compd. **424** (2006) 262.
[2] N. Kamakura *et al.*: Phys. Rev. B **83** (2011) 033103.
[3] H. Saitoh *et al.*: Appl. Phys. Lett. **93** (2008) 151918.
[4] T. Tokushima *et al.*: Rev. Sci. Instrum. **77** (2006) 063107.
[5] L. Pauling: J. Am. Chem. Soc. **54** (1932) 3570.
[6] *Y. Takeda, Y. Saitoh, H. Saitoh, A. Machida, K. Aoki, H. Yamagami, T. Muro, Y. Kato, and T. Kinoshita: Phys. Rev. B* ***84*** *(2011) 153102.*

CHEMICAL SCIENCE

Many excellent articles have been published this year by SPring-8 users in this Chemical Science category, covering research areas including FEL applications, atomic and molecular spectroscopy, porous coordination networks, metal-organic complexes, liquid structures, and catalysts. Some representative topics are selected as follows.

In the field of atomic and molecular spectroscopy, the first topic highlighted here is the first observation of free-electron-laser-induced collective spontaneous emission (superfluorescence). The process was observed in He gas using the extreme ultraviolet FEL pulses of the RIKEN SCSS. In the second topic, interatomic electronic decay processes in rare gas dimers NeAr and Ar_2 have been investigated using electron-ion-ion coincidence momentum-imaging techniques at BL27SU by Prof. Ueda *et al*. (Tohoku Univ.). Three-electron interatomic Coulombic decay (ICD) and electron-transfer mediated decay (ETMD) phenomena were observed for the first time.

In the field of large scale molecular networks, Prof. S. Kitagawa *et al*. (Kyoto Univ.) used a four-circle diffractometer at BL13XU to demonstrate a crystal extractor based on porous coordination polymers with core-shell heterostructures. In this system the storage container is the core crystal, and the size separation filter is the shell crystal. In addition, it was demonstrated at BL02B2 and BL19B2 that "instant synthesis" can form kinetic microcrystalline porous coordination networks suitable for *ab initio* XRPD structure determination, and also how new porous structures could be obtained by the annealing of kinetic products. Synthetic methods for multi component metal-organic complexes (molecular spheres) using self-assembly of transition metal ions and bidentate ligands were developed, and synchrotron X-ray diffraction studies were applied to determine their single crystal structures at BL38B1.

SCIENCE

Interesting new information on liquid structures has been obtained at BL04B2 and BL08W. A better understanding of the origin and the extension of nanoheterogeneities in ionic liquids is a crucial step towards a better comprehension of their unusual properties. Studies combining high-energy synchrotron X-ray diffraction (BL04B2) with atomistic molecular dynamics simulations were carried out to explore the atomic structure of imidazolium-based ionic liquids with three different alkyl chain lengths. The possibility of designing a liquid adapted to a particular application by combining appropriate cations and anions was revealed. In related work, in order to characterize hydrogen bond and solvation structures in ethanol-water mixtures at various alcohol concentrations, X-ray Compton scattering experiments were carried out at BL08W, and inhomogeneities in alcohol-water systems were found. This study demonstrated the power of X-ray Compton scattering for studying the detailed geometrical properties of liquids.

In the catalysis field, a joint group from Kyushu University and Hokkaido University used CuPd bimetallic alloy nanoparticles to perform reduction of NO_3^- into NH_3 with photocatalytically-generated hydrogen, an environmentally-benign process that could produce NH_3 without releasing CO_2 and consuming excess energy. In this study, it was found that photocatalytically-generated hydrogen exhibits high selectivity for conversion of NO_3^- to NH_3. The CuPd alloy structure was analyzed using XRD techniques at BL44B2. A research team from the Institute for Molecular Science has succeeded in scanning μ-XRF and μ-XAFS measurements of a single catalyst particle of $NiO_x/Ce_2Zr_2O_y$ ($0 \leq x \leq 1$, $7 \leq y \leq 8$), which is known to exhibit high oxygen storage/release properties and is thus expected to become a highly important automobile exhaust catalyst. The experiments used an X-ray μ-beam (1000 nm (h) × 800 nm (v)) at BL37XU. Use of the μ-XAFS technique will provide structural information of each catalyst particles with different catalytic behaviors, and contribute to the development of more precise catalyst design for chemical reactors.

Yuden Teraoka

Observation of free-electron-laser-induced collective spontaneous emission (superfluorescence)

Superfluorescence is a phenomenon in which N atoms in excited states (N is a number greater than one) decay collectively and simultaneously to produce a burst of highly-directional radiation with a peak intensity many times higher ($\propto N^2$) and duration many times shorter ($\propto 1/N$) than would be observed if the atoms were to decay individually. First described by Dicke in 1954 [1], the effect shows similarities with laser emission (high directionality and high coherence) but is fundamentally different since the decay is **collective**, and can only occur if 1) the spacing between the atoms is less than λ, the wavelength of the emitted radiation, and 2) the population inversion is created near-instantaneously (see below).

Since the first description of the phenomenon, superfluorescence has been observed for both very large ($N>10^{12}$) and very small ($N=2$) collections of atoms, for emitted wavelengths ranging from a few hundred to a few thousand nanometers, and on timescales ranging from picoseconds to microseconds. The physics behind the phenomenon is of direct relevance to many effects in quantum optics [2]. To observe the phenomenon a population inversion must be created in an ensemble of atoms on a timescale shorter than the superfluorescence decay, and in this work we have used pulses of 100 fs duration from the RIKEN SCSS free-electron laser (FEL) facility located at SPring-8. The FEL radiation was focussed to a spot of diameter ~10 μm at the center of a 44 mm sided cubic gas cell (see Fig. 1), into which helium gas was introduced via a pulsed nozzle synchronized to the 30 Hz FEL pulses. This setup allowed us to maximize the number density of ground state atoms present at the time of each FEL pulse, and also control the density of these atoms by varying the gas pressure behind the nozzle. Each FEL pulse then created up to 10^8 helium atoms in $1s3p$ excited states (see Fig. 2) within a volume of less than 1 mm^3.

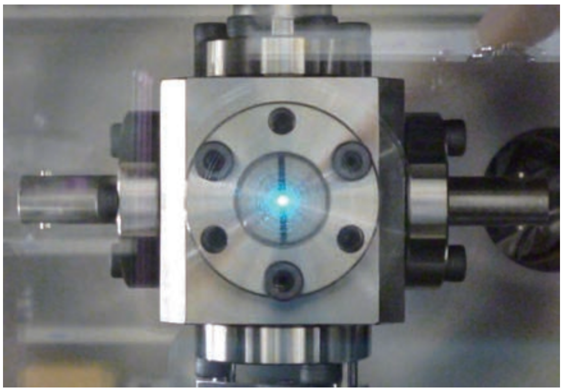

Fig. 1. Photograph of a single flash of 501.6 nm superfluorescence from helium at the centre of a gas cell, as viewed through a glass window at the end of the SCSS beamline.

Intense bursts of superfluorescence were observed as the atoms simultaneously decayed to the $1s2s$ state emitting 501.6 nm radiation. Using a calibrated photodiode we determined that up to around 2.5×10^{11} photons were produced in each superfluorescence pulse – a photon number conversion efficiency of around 10%. The emitted radiation was found to be highly directional, with an angular divergence only slightly larger than that of the FEL radiation itself.

Figure 2 shows a simplified level scheme of the neutral helium atom. Helium has two electrons, and in the ground state both electrons are in $1s$ states. The wavelength of the FEL radiation was set to 53.7 nm, which corresponds to the $1s1s$ to $1s3p$ transition. Due to the 'spiky' nature of the SASE pulses the overlap with the transition varied shot-by-shot. The radiative lifetime of the $1s3p$ state is about 1.7 ns, which means that if an excited population (N) of atoms in the $1s3p$ state were to decay **independently**, a histogram of decay times with respect to excitation would show an exponential decay, with the upper state population dropping from N to N/e after 1.7 ns. In the independent decay regime, an excited helium atom in the $1s3p$ state decays with 97% probability back to the $1s1s$ ground-state, with only around 3% of the decays populating the metastable $1s2s$ state and leading to fluorescence at 501.6 nm. When the inter-atomic spacing is less than 501.6 nm, however, as was the case in our experiments where the number density of neutral atoms in the gas cell was up to around 10^{17} cm^{-3} (a gas pressure of 3000 Pa), **collective** superfluorescence decay can occur on this transition. In this process the entire population of interacting atoms is transferred from the $1s3p$ state to the $1s2s$ state. The superfluorescence pulse width is given by $\tau = 8\pi/(3\lambda^2\,\Gamma\rho L)$, where $\lambda=501.6$ nm, Γ is the natural decay rate (1.3×10^7 s^{-1}), ρ is the number density of excited atoms ($\lessapprox 10^{17}$ cm^{-3}), and L the length of the extent of the inversion (< 44 mm). As well as a temporal width much shorter than that for independent decay, superfluorescence is characterized by a delay between excitation and emission of the pulse. This is given by $\tau\times(\ln(2\pi N)^{1/2})/4$, where τ is the pulse width defined above. This delay can be understood as the time required for N oscillating dipoles to become in-phase due to the coupling through the electromagnetic field, and has a statistical variation shot-by-shot. It can be seen from the two equations that both the width and the delay scale as 1/N. Since the width of the pulse scales as 1/N it is clear that the peak intensity must scale as N^2, in order to conserve photon number.

To characterize the observed superfluorescence we used a streak camera to record the time profile of the pulses shot-by-shot. An overview of the results is given in Fig. 3. Each trace is the average of several streak camera traces recorded at several different gas pressures P, ranging from 0.5 atm to 9 atm. These gas pressures correspond to pressures in the gas cell of around 300 Pa to around 3000 Pa, and a proportional variation of N, the number of excited atoms. The general trend is that higher pressures (larger N) lead to narrower pulses with shorter delays. The inset to the figure shows that whereas the total intensity scales as P^1 (and thus N^1), the peak intensity scales as P^2 (N^2), consistent with superfluorescence. A more detailed analysis reveals that the width and delay both scale as 1/N [3].

This work represents the first observation of superfluorescence following excitation in the extreme ultraviolet wavelength region, and also the first observation using FEL pulses as the excitation source. Extension by suitable choice of system suggests a way of generating tailor-made pulses in the EUV and even X-ray wavelength regions which are 'cleaner' than the initial SASE-derived pump pulses, and complements more traditional atomic laser techniques [4]. A further tantalizing prospect is that of superfluorescence occurring in large molecular systems, where for example a large number of C atoms are separated by less than the C 2*p*→1*s* transition wavelength of 4 nm.

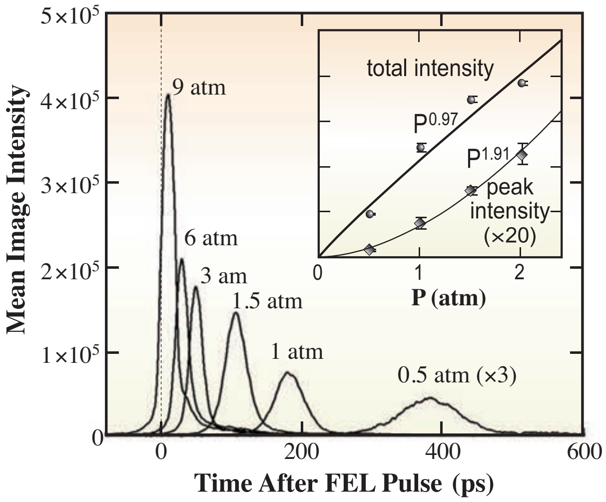

Fig. 3. Representative streak camera traces. Each trace is the average of several traces recorded at each gas pressure (proportional to the number of excited atoms N). The inset shows the pressure dependence of peak and total intensity [3].

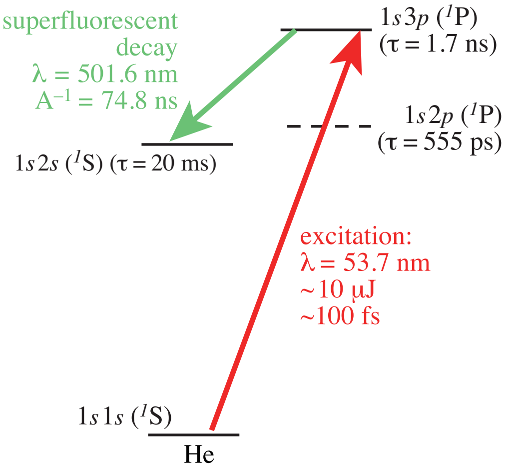

Fig. 2. Simplified level scheme of neutral helium. FEL pulses with a centre wavelength of 53.7 nm (23.1 eV) can excite atoms to the 1*s*3*p* state. Superfluorescence is observed at 501.6 nm on the 1*s*3*p* → 1*s*2*s* transition [3].

M. Nagasono[a,*], J. R. Harries[a,b], H. Iwayama[a,c]
and E. Shigemasa[a,c]

[a] SPring-8/RIKEN
[b] SPring-8/JAEA
[c] UVSOR/IMS and SOKENDAI

*E-mail: nagasono@spring8.or.jp

References

[1] R.H. Dicke: Phys. Rev. **93** (1954) 99.
[2] see for example M.O. Scully and A.A. Svidzinsky: Science **325** (2009) 1510.
[3] *M. Nagasono, J.R Harries, H. Iwayama, T. Togashi, K. Tono, M. Yabashi, Y. Senba, H. Ohashi, T. Ishikawa, E. Shigemasa: Phys. Rev. Lett.* ***107*** *(2011) 193603.*
[4] N. Röhringer *et al.*: Nature **481** (2012) 488.

Interatomic electronic decay following multiple ionization of rare gas dimers

Inner-valence vacancy states in molecules are usually not subject to autoionization and thus relax via fluorescence decay and/or dissociation. In 1997, Cederbaum *et al*. noted that such inner-valence vacancy states may be subject to autoionization if they are in close proximity to other molecules. They called this new type of autoionization intermolecular or interatomic Coulombic decay (ICD) [1]. In ICD, two electrons are involved: one electron fills the vacancy and another electron is emitted as an ICD electron. If the electron that fills the vacancy originally belongs to the species with the vacancy and the electron that is emitted originally belongs to the other neighboring species, the process is called direct ICD (Fig. 1(a)). If the emitted electron originally belongs to the species with the vacancy and the electron that fills the vacancy originally belongs to the other neighboring species, the process is called exchange ICD (Fig. 1(b)). Exchange ICD is usually much weaker than direct ICD but becomes experimentally visible if direct ICD is energetically closed. If both electrons that participate in the decay originally belong to the neighboring species that does not have the vacancy, the process is called electron-transfer mediated decay (ETMD) (Fig. 1(c)). ETMD is usually much weaker than ICD but may become visible if ICD is energetically closed. If an inner-valence double-vacancy state is created, another class of ICD may occur, i.e., three-electron ICD, in which two outer-valence electrons fill two inner-valence vacancies and another electron is emitted from outer-valence orbitals. Three-electron ICD is usually much weaker than two-electron ICD but may become visible if two-electron ICD is energetically closed.

We have investigated the above-described different interatomic electronic decay processes in the rare gas dimers NeAr and Ar_2, as typical prototype examples, by electron-ion-ion coincidence momentum-imaging at beamline **BL27SU**. The coincidence momentum-imaging is based on recording the electron and ion times-of-flight (TOFs) with position- and time-sensitive multihit-capable detectors. Knowledge of position and arrival time on the particle detectors, (*x,y,t*), allows us to extract information about the 3D momentum of each particle. The electron and ion TOF spectrometers were placed face to face. The TOF spectrometer axis was horizontal and perpendicular to both the horizontal photon beam and the vertical cluster beam. The argon dimers (Ar_2) were produced by the expansion of argon gas at 300 K, while the heterodimers (NeAr) were produced by expanding a mixture of neon and argon gases at 103 K. Signals from Ar_2 and NeAr were extracted by momentum conservation for ion pair formation.

For NeAr, when we tuned the photon energy above the Ne 1s ionization threshold, we found a significant amount of Ne^{2+}-Ar^{+} ion-pair formation. Figure 2(a) depicts kinetic energy release (KER), i.e., the sum of the kinetic energies for the two dissociating ions Ne^{2+} and Ar^{+} recorded in coincidence. Assuming the Coulomb repulsion between Ne^{2+} and Ar^{+}, we found that the measured KER peak of ~8 eV corresponds to an internuclear distance of 3.5 Å, in good agreement with the equilibrium distance of the neutral ground state of NeAr. Figure 2(b) depicts the energy distribution of electrons recorded in coincidence with

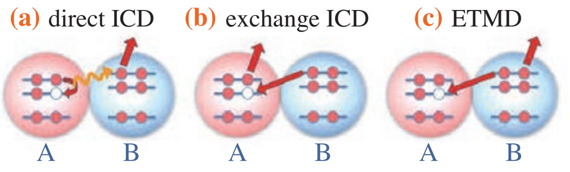
(a) direct ICD (b) exchange ICD (c) ETMD

Fig. 1. Schematic diagrams of **(a)** direct ICD, **(b)** exchange ICD, and **(c)** ETMD. [4]

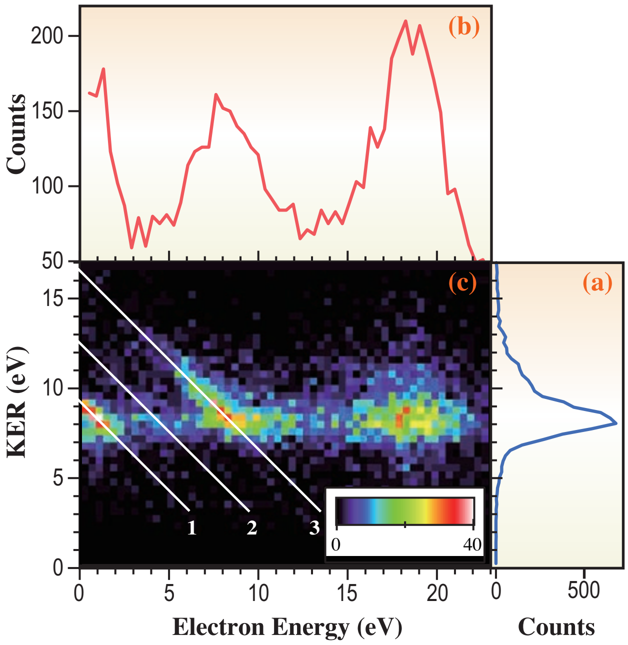

Fig. 2. **(a)** KER for Ne^{2+}-Ar^{+} fragmentation channel. **(b)** Kinetic energy distribution of electrons detected in coincidence with Ne^{2+}-Ar^{+} pairs. **(c)** Correlation map between electron emission and KER. The three straight lines of slope –1 correspond to the energies of the ICD transitions. [2]

Ne^{2+}-Ar^{+} ion pairs. The peak that appears at ~19 eV corresponds to the Ne 1*s* photoelectron peak, while other peaks at low energies correspond to the ICD electron emission. Figure 2(c) shows a correlation between the electron emission and the KER recorded in coincidence. In this correlation diagram, the island of the ICD transition appears as the line of slope –1, because the sum of ICD electron kinetic energy and KER is constant in the ICD transition. The three lines with slope –1 correspond to the sum energies of the expected direct ICD transitions: (1) $Ne^{2+}(2s^{-1}2p^{-1}\ ^3P)Ar$ to $Ne^{2+}(2p^{-2}\ ^3P)$-$Ar^{+}(3p^{-1}\ ^2P)$, (2) $Ne^{2+}(2s^{-1}2p^{-1}\ ^1P)Ar$ to $Ne^{2+}(2p^{-2}\ ^1S)$-$Ar^{+}(3p^{-1}\ ^2P)$, and (3) $Ne^{2+}(2s^{-1}2p^{-1}\ ^1P)Ar$ to $Ne^{2+}(2p^{-2}\ ^1D)$-$Ar^{+}(3p^{-1}\ ^2P)$. In the figure, we can identify all three ICD transitions [2]. We cannot identify any exchange ICD or ETMD here.

When we tuned the photon energy above the Ar 2*p* ionization threshold, we found a significant amount of Ne^{+}-Ar^{2+} ion-pair formation. Detecting two electrons with the Ne^{+}-Ar^{2+} ion pair in coincidence (i.e., four-fold coincidence), we confirmed that the low-energy electrons below 2 eV are emitted following Ar 2*p* Auger decay after 2*p* photoionization, resulting in the ionization of the neighboring Ne atom. Thus, this low energy electron emission may be assigned as ICD. Figure 3(b) depicts the distribution of KER for Ne^{+} and Ar^{2+}, whereas Fig. 3(c) shows a schematic energy diagram for the initial and final states of ICD. Assignments of these initial and final states are given in the figure caption. The *x*-axis is given by the inverse of the internuclear distance (1/R decreases to the right); thus, we can directly correlate the value of 1/R to KER in Fig. 3(b). From this energy scheme, we expect four transitions to contribute to the KER spectrum: from A to 1, from B to 1, from C to 1, and from D to 1. The transition from B to 1 peaking at 9.4 eV is three-electron exchange ICD. The reasonable agreement of simulated KER spectra given in Fig. 3(a) to the experimental one in Fig. 3(b) supports this assignment. This is the first observation of three-electron ICD [3]. Although three-electron ICD relies on higher-order correlations, it became visible because lower-order ICD is energetically closed for the state B.

For Ar_2, we focus on triple ionization that forms Ar^{3+}-Ar as initial states of ICD and ETMD. The Ar^{3+}-Ar^{+} ion pair is expected to be produced by ICD, and Ar^{2+}-Ar^{2+} ion pair formation implies that ETMD occurs. By detecting low-energy electrons in coincidence with Ar^{3+}-Ar^{+} and Ar^{2+}-Ar^{2+} (i.e., three-fold coincidence) we could identify the ICD and ETMD processes, respectively. This is the first observation of ETMD [4]. ETMD became visible because, for low-lying Ar^{3+}-Ar inner-valence-hole states, ICD is energetically closed, while ETMD is open.

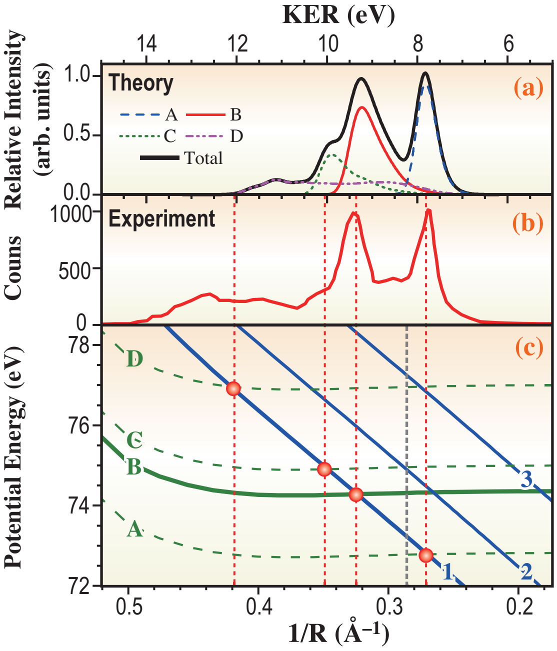

Fig. 3. **(a)** Simulated partial and total KER distributions for the transitions from the initial states A–D. **(b)** Experimental total KER distribution. **(c)** Schematic energy diagram for the initial (labeled A-D) and final (labeled 1-3) states of the ICDs. A, Ne-$Ar^{2+}(3p^{-3}(^2P)3d\ ^1P)$; B, Ne-$Ar^{2+}(3s^{-2}\ ^1S)$; C, Ne-$Ar^{2+}(3p^{-3}(^2P)4p\ ^1S)$; D, Ne-$Ar^{2+}(3p^{-3}(^2P)4d\ ^1P,^3D,^3P)$. 1, $Ne^{+}(2p^{-1}\ ^2P)$-$Ar^{2+}(3p^{-2}\ ^3P)$; 2, $Ne^{+}(2p^{-1}\ ^2P)$-$Ar^{2+}(3p^{-2}\ ^1D)$; 3, $Ne^{+}(2p^{-1}\ ^2P)$-$Ar^{2+}(3p^{-2}\ ^1S)$. [3]

Kiyoshi Ueda*, Kentaro Sakai and Hironobu Fukuzawa

Institute of Multidisciplinary Research
for Advanced Materials, Tohoku University

*E-mail: ueda@tagen.tohoku.ac.jp

References

[1] L.S. Cederbaum *et al.*: Phys. Rev. Lett. **79** (1997) 4778.
[2] *T. Ouchi, K. Sakai, H. Fukuzawa, I. Higuchi, Ph.V. Demekhin, Y.-C. Chiang, S.D. Stoychev, A.I. Kuleff, T. Mazza, M. Schöffler, K. Nagaya, M. Yao, Y. Tamenori, N. Saito and K. Ueda: Phys. Rev. A* ***83*** *(2011) 053415.*
[3] *T. Ouchi, K. Sakai, H. Fukuzawa, X.-J. Liu, I. Higuchi, Y. Tamenori, K. Nagaya, H. Iwayama, M. Yao, D. Zhang, D. Ding, A.I. Kuleff, S.D. Stoychev, Ph.V. Demekhin, N. Saito and K. Ueda: Phys. Rev. Lett.* ***107*** *(2011) 053401.*
[4] *K. Sakai, S. Stoychev, T. Ouchi, I. Higuchi, M. Schöffler, T. Mazza, H. Fukuzawa, K. Nagaya, M. Yao, Y. Tamenori, A.I. Kuleff, N. Saito and K. Ueda: Phys. Rev. Lett.* ***106*** *(2011) 033401.*

Multifunctional porous crystals by hybridizing coordination polymers

Porous coordination polymers (PCPs) or metal-organic frameworks (MOFs) are an intriguing class of porous crystalline materials in which the properties can be modulated by chemical functionalities on organic ligands. The wide variety of organic ligands allows PCPs to exhibit versatile porous properties, such as gas storage, separation and catalysis. A key to accessing advanced PCPs suitable for more specialized and sophisticated applications is to integrate several functionalities into a single crystal. However, an extra chemical modification on organic ligands in PCPs sacrifices the porosities or spoils the original porous properties. One way to overcome this issue is to hybridize different types of PCP crystals, thus creating a core-shell-type PCP crystal [1]. Core-shell PCPs are able to implement multifunctionality even when two contradictory properties are combined; for instance, small and large pore sizes simultaneously provide size selectivity and high storage capacity. Such materials can be designed by attributing the small aperture to the core crystal and large cavity to shell the crystal. Here, we demonstrate a crystal extractor based on PCPs with the core-shell heterostructures, in which the storage container is the core crystal and the size separation filter is the shell crystal (Fig. 1) [2].

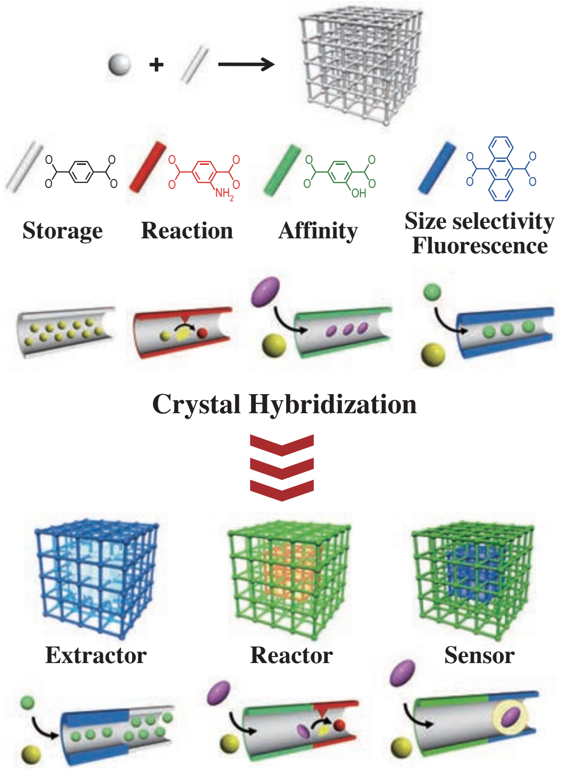

Fig. 1. Schematic illustrations of PCP crystal hybridization for sequential functionalization system.

A series of three-dimensional PCPs, $[Zn_2(dicarboxylate)_2(diamine)]_n$, gives a single micrometer-scale crystal with a well-defined cuboid morphology. The key synthetic protocol is the epitaxial growth of the second crystal that surrounds the core crystal because a lattice match results in pore connections at the interface between two crystals. To achieve the significant differences in pore sizes between the core and shell crystals, we selected $[Zn_2(bdc)_2(dabco)]_n$ (**1**) as the core crystal (bdc = 1,4-benzene dicarboxylate; dabco = 1,4-diazabicyclo[2.2.2]octane; pore sizes: 7.5 × 7.5 Å^2 along the *c*-axis and 5.3 × 3.2 Å^2 along the *a*- and *b*-axes, and micropore volume: 0.75 cm^3/g) and $[Zn_2(adc)_2(dabco)]_n$ (**2**) as the shell framework (adc = 9,10-anthracene dicarboxylate, pore sizes: 1.7 × 1.7 Å^2 along the *c*-axis and 4.5 × 2.7 Å^2 along the *a*- and *b*-axes, and micropore volume: 0.31 cm^3/g). Two crystals were successfully hybridized by solvothermal synthesis, in which pieces of single crystals of (**1**) were heated in a solution of $Zn(NO_3)_2 \cdot 6H_2O$, H_2adc and dabco in *N,N*-dimethylformamide (DMF) for several days. The core/shell crystals (**1/2**) were harvested after cooling to room temperature. The confocal laser scanning microscopy and microscopic Raman spectroscopy indicated the formation of the core/shell crystals (**1/2**).

To elucidate the structural relationship between the core framework and the shell framework, we performed synchrotron X-ray diffraction measurements for film structural analysis using a four-circle diffractometer at beamline **BL13XU** for surface and interfacial structures. Both the core (**1**) and the shell crystals (**2**) had the same tetragonal frameworks and similar unit cell parameters (a = 10.9288(15) Å and c = 9.6084(12) Å for **1**, and a = 10.8444(10) Å and c = 9.541(9) Å for **2**). As we observed the sharp and single diffraction peaks at the 110 and 1$\bar{1}$0 Bragg positions with 180° periodicity and at the 101, 011, $\bar{1}$01, and 0$\bar{1}$1 Bragg positions with 90° periodicity, we found that the shell crystal grew epitaxially on both the {100} and {001} surfaces (Fig. 2). These results suggest the hybridization of two frameworks into one crystal with pore connections at the crystal interfaces.

The preference for adsorbing cetane over isocetane was demonstrated by immersing single crystals of (**1**) and (**2**) and the core/shell crystal of

(**1/2**) into a mixture of cetane/isocetane (1:1). After filtration and drying, these crystals were decomposed by hydrochloric acid and the adsorption ratio was determined by gas chromatography-mass spectrometry (GC-MS). Although the large pores of (**1**) barely discriminated between these isomers, the small pores of (**2**) accumulated only the linear cetane molecules. The core/shell crystal also selectively adsorbed cetane owing to the small aperture of the shell crystal. When the cetane/isocetane ratio was decreased to 1:10 and 1:100, the adsorption of isocetane in (**1**) increased. By contrast, the crystal of (**2**) and the core/shell crystal maintained their perfect selectivity for cetane.

The storage capacity of cetane in the core/shell crystal of (**1/2**) was elucidated by thermogravimetric (TG) analysis. For the (1:100) mixture of cetane/isocetane, the amount of cetane adsorbed in the core/shell crystal was estimated as 26.9 wt%, which was twice that in the shell crystal of (**2**) (10.0 wt%). This significant improvement in the cetane storage capacity arose from the large pore volume of the core framework of (**1**). By contrast, the single crystal of (**1**) alone showed no selective adsorption, and both cetane (6.9 wt%) and isocetane (24.5 wt%) accumulated in its pores. Thus, covering the core crystal with the thin shell crystal is the key to the combination of selectivity and high storage capacity for cetane (Fig. 3).

This successful integration of two contradictory functions into one crystal was achieved by the heterogeneous arrangement of chemical functionalities on one basic framework skeleton. This methodology to create a multifunctional PCP crystal will enable further integration of other porous properties.

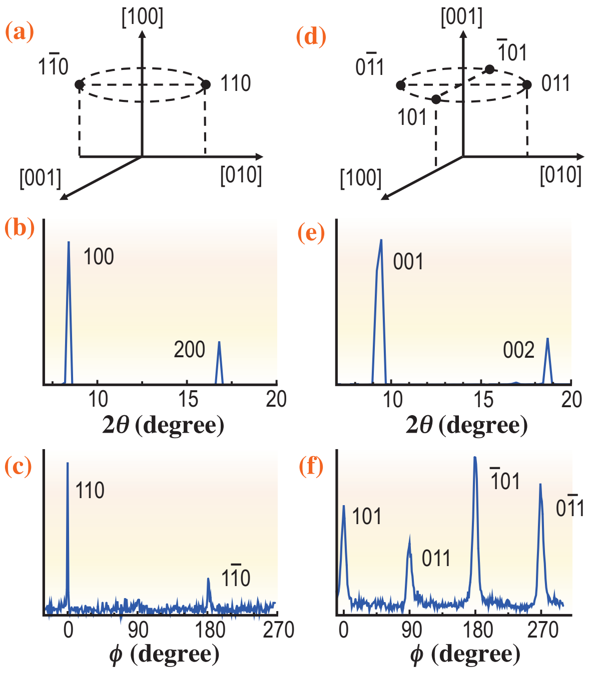

Fig. 2. Reciprocal lattice spaces corresponding to the rotational scan results obtained around the **(a)** [100] and **(b)** [001] directions. θ–2θ scan results of the core/shell crystals (**1/2**) on the glass substrates at the initial position (χ = 90°) with the **(c)** *a*-axis and **(d)** *c*-axis orientations. Scan results of the rotation angles around the **(e)** [100] direction (ϕ scan) and **(f)** [001] direction.

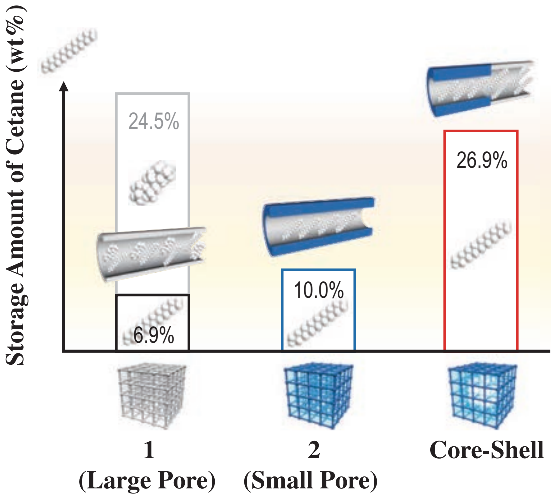

Fig. 3. Amount of cetane stored in (**1**), (**2**), and (**1/2**) when using a (1:100) mixture of cetane/isocetane.

K. Hirai[a], O. Sakata[b], S. Kitagawa[a,c,d] and S. Furukawa[c,d,*]

[a] Graduate School of Engineering, Kyoto University
[b] Synchrotron X-ray Station at SPring-8,
National Institute for Materials Science
[c] ERATO Kitagawa Integrated Pores Project, JST
[d] Institute for Integrated Cell-Material Sciences,
Kyoto University

*E-mail: shuhei.furukawa@icems.kyoto-u.ac.jp

References

[1] S. Furukawa *et al*.: Angew. Chem. Int. Ed. **48** (2009) 1766.
[2] *K. Hirai, S. Furukawa, M. Kondo, H. Uehara, O. Sakata and S. Kitagawa: Angew. Chem. Int. Ed.* ***50*** *(2011) 8057.*

Structural memory effect in solid-state transformation of kinetic coordination networks

The chemistry of porous coordination networks has shown a rapid advance in the last 15 years owing to the hybrid nature of their building blocks (i.e., metal ions and organic ligands) [1]. The selective synthesis of kinetic over thermodynamic products is an important aspect in porous coordination networks. In general, kinetic or thermodynamic structures can be prepared by fast or slow crystallization methods, respectively. However, synthetic routes enabling such selectivity as homogeneous products are not trivial. Fast precipitation can generate metastable products but as microcrystals that are not suitable for single-crystal X-ray analysis. We have recently demonstrated that "instant synthesis" can form kinetic microcrystalline porous coordination networks suitable for *ab initio* XRPD structure determination [2] and how new porous structures could be obtained by the annealing of kinetic products [3].

Herein, we studied a kinetically controlled family of isostructural porous coordination networks $[(ZnX_2)_3(TPT)_2]_n$•5.5(solvent) (where X = I, Br, and Cl), where TPT is tris(4-pyridyl)triazine (**1-3**) (Fig. 1) obtained by "instant synthesis" and studied its solid-state reactivity at high temperatures (above 573 K). Insights on the solid-state reactions were obtained using state-of-the-art methods for *ab initio* XRPD structure determination by synchrotron X-ray diffraction at **BL19B2** and **BL02B2** beamlines [4].

Upon heating from 300 to 673 K, network **1** undergoes a crystalline-to-amorphous-to-crystalline (CAC) phase transition. *In situ* XRPD shows that **1** changes to an amorphous phase at 473 K, and upon further heating, a new crystalline porous phase (**1a**) appears uniformly at 573 K and is stable up to 673 K (Fig. 1). We demonstrated the guest inclusion ability of **1a** by immersing it in nitrobenzene and exposing **1a** to I_2 vapor. *Ab initio* XRPD structure determination (BL19B2 beamline) indicated that **1a** can reversibly encapsulate nitrobenzene [3] and I_2 [4].

The CAC reaction in **1** involves the guest removal and concurrent shrinking of the networks, followed by the unlocking of interpenetrated networks (cleavage of coordination bonds), and crystallization by bond formation to yield **1a** (Fig. 2).

To test if the molecular prearrangement in **1** is necessary for the formation of **1a**, we performed control experiments by mixing, grinding, and heating using the same stoichiometric amounts of starting materials of **1** as in instant synthesis. X-ray analysis proved that **1a** was not formed (Fig. 2).

Intrigued by the results, we investigated the isostructural networks **2** and **3**. Microcrystalline **2** was heated to 573 K and monitored by *in situ* XRPD analysis. The diffraction data shows also two phase transitions through a CAC process. Elemental analysis results suggest the formation of the compound $[(ZnBr_2)_3(TPT)_2]_n$•(H_2O) (**2a**). The high quality synchrotron XRPD data of **2a** was recorded at BL19B2 and structure determination was carried out by *ab initio* XRPD followed by Rietveld refinement (Fig. 3) [4]. Compound **2a** is an interpenetrated network obtained after guest removal and molecular

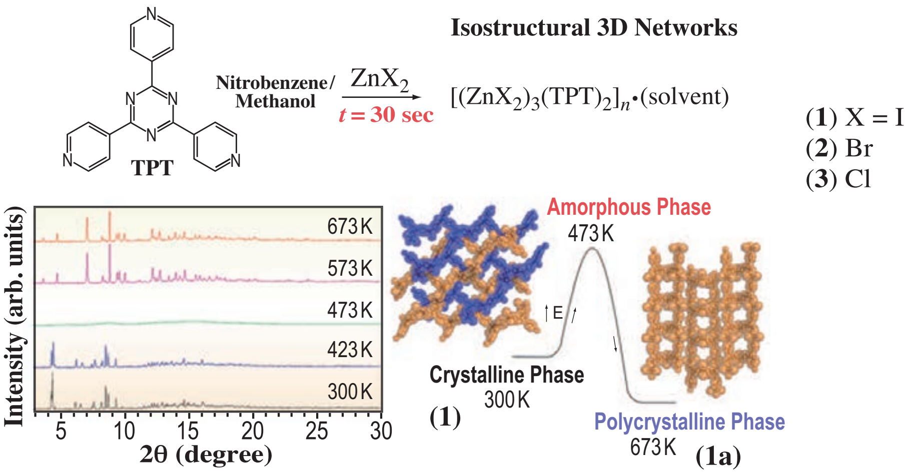

Fig. 1. Top: Fast crystallization of **1-3** by the "instant synthesis" method. Bottom: XRPD of **1** measured at different temperatures (left). Crystal structures of **1** and **1a** and energy plot depicting the transformation from kinetic to thermodynamic products upon heating via an amorphous phase. Interpenetrating networks are shown in blue and orange (right).

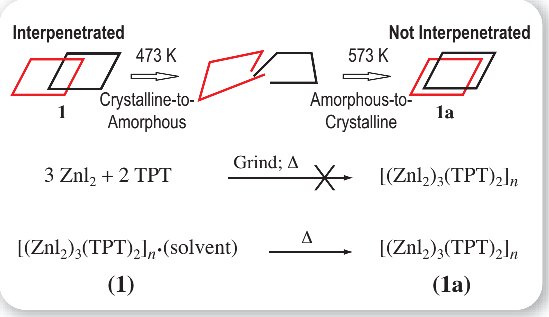

Fig. 2. Top: Cartoon showing the structural transformation from **1** to **1a**. Middle: control experiments showed that it is not possible to obtain the porous network **1a** if the building blocks (ZnI_2 and TPT) are mixed, grinded, and heated. Bottom: the molecular prearrangement in **1** is necessary to form **1a**, which is only formed upon heating.

rearrangement (Fig. 3). To determine whether the unlocking of networks occurs, we investigated a non-interpenetrated (**2b**) network (not shown here, see Ref. [4]) with the same chemical composition of **2**. Heating **2b** to 553 K yields the same XRPD pattern and therefore the crystal structure of **2a** [4]. Clearly, the cleavage and formation of coordination bonds occur during the CAC transformation from non-interpenetrated (**2b**) to interpenetrated (**2a**).

Control experiments performed by mixing the starting materials using the same stoichiometry and grinding followed by annealing did not form **2a**, indicating that the atomic-level preorganization in the starting solids is crucial for the formation of the structures obtained after annealing. To our understanding, in the amorphous phase, structural information is retained and is passed via a type of memory effect from metastable (**2**) to a more stable (**2a**) (Fig. 3, bottom).

Further heating to 723 K and slow cooling of **2** produced single crystals with a new bromide-bridged network. In this case, the high temperature induced a certain level of calcination and, most likely, partial melt of **2** allowed crystallization upon slow cooling. A similar behavior was observed for the chloride version **3** (see Ref. [4]), which also through a CAC process formed a new phase (nonporous desolvated structure) that was unstable; thus, it transformed to a new chloride-bridged network at 723 K. The different solid-state reactivity can be attributed to the different halides in **1-3**.

In summary, we demonstrated that the frequently observed limitation in the single-crystal X-ray analysis of crystalline solids with good crystallinity and size has been tackled using a state-of-the-art *ab initio* synchrotron XRPD structure solution. In a type of memory effect, the amorphous phase in the CAC process is an intermediate state retaining structural information from the kinetic structure that is passed to a more stable structure upon heating. Clearly, such a detailed structural analysis of organic-inorganic materials is trivial in single-crystal X-ray analysis but not in *ab initio* XRPD analysis.

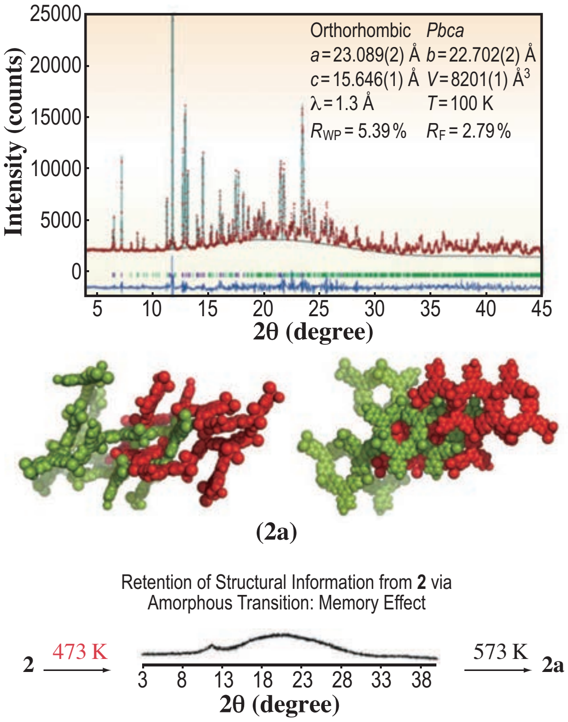

Fig. 3. Top: Experimental (red), calculated (pale-blue), and difference (dark-blue) XRPD profiles from the final Rietveld refinement of **2a**. Middle: crystal structure of **2a** with the two interpenetrated circuits in green and red (side view) and viewed along the *c*-axis (right). Bottom: XRPD showing the amorphous phase upon heating **2** and formation of **2a**. The very broad "peaks" indicate that the long-range order allows the passing of structural information from **2** to **2a**.

Javier Martí-Rujas[a] and Masaki Kawano[b,*]

[a] Italian Institute of Technology, Centre for Nano Science and Technology, Italy
[b] The Division of Advanced Materials Science, Pohang University of Science and Technology, Korea

*E-mail: mkawano@postech.ac.kr

References

[1] S. Kitagawa *et al.*: Angew. Chem. Int. Ed. **43** (2004) 2334.
[2] M. Kawano *et al.*: Angew. Chem. Int. Ed. **47** (2008) 1269.
[3] K. Ohara *et al.*: J. Am. Chem. Soc. **131** (2009) 3860.
[4] *J. Martí-Rujas, N. Islam, D. Hashizume, F. Izumi, M. Fujita and M. Kawano: J. Am. Chem. Soc.* **133** *(2011) 5853.*

Single crystal structure determination using synchrotron X-ray of molecular spheres synthesized by temporary labilization of the metal-ligand association

We have developed synthetic methods for multicomponent metal-organic complexes using the self-assembly of transition metal ions (M) and bidentate ligands (L). Typically, square planar coordinative Pd (II) ions and bidentate, organic ligands bearing two pyridyl groups as coordination sites are mixed in an organic solvent, and all the coordination bonds are formed between the Pd (II) ions and pyridyl groups to form hollow, spherical complexes with well-defined numbers of components M and L in quantitative yield. We have found that the bend coordination angles between two pyridyl groups control the product compositions, such as M_6L_4, $M_{12}L_{24}$, $M_{18}L_{24}$, $M_{24}L_{24}$, and $M_{24}L_{48}$. One of the most important key points in these successful syntheses is the appropriate strength of coordination bonds between M and L that realizes reversible bond formation and cleavage where the destruction of unstable, intermediary structures proceeds and self-assembly affords the most thermodynamically stable final product. When we attempted to replace Pd (II) ions with the same square planar coordinative Pt (II) ions in the self-assembly reaction, we only obtained a complex mixture of oligomers owing to the stronger coordination bonds between Pt (II) ions and pyridyl groups. Here, we report a novel, practical method to accelerate the self-assembly of well-defined $Pt_{12}L_{24}$ spheres by the addition of 2,2,2-trifluoroethanol (TFE) to weaken the Pt(II)-L interaction and to obtain a thermodynamically controlled, desired product (Fig. 1) [1]. In this method, the kinetically inert M-L interaction is switched to a labile one by external stimuli (TFE as an additive), which is termed “temporary labilization.” Once the $Pt_{12}L_{24}$ complex was formed, volatile TFE (bp 78°C) was easily removed in vacuo to switch the bond again into an inert one and to afford an acid-durable complex.

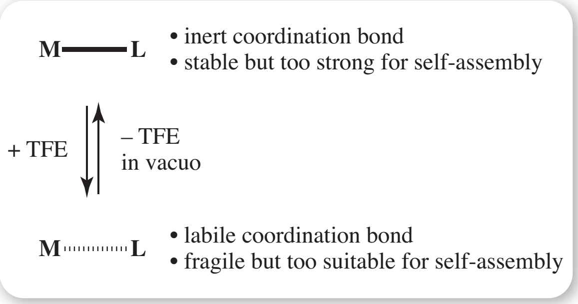

Fig. 1. Illustration of temporary labilization of coordination for self-assembly and stabilization of the product structure.

TFE is known to be a weak acid and to donate a hydrogen bond, comparable to that of phenol, and a 1:1 complex of TFE and pyridine as an acid-base pair is reported. Therefore, we expected that the dissociated pyridyl moiety from the metal ion center would be stabilized by the strong hydrogen bond of a TFE to achieve the self-asembly of the desired product. We focused on ligand 1 shown in Fig. 2 as a simple bidentate ligand, which forms a $Pd_{12}L_{24}$ complex by the self-assembly with Pd(II) ions. Ligand 1 (7.0 μmol) and $Pt(NO_3)_2$ (5.6 μmol) were dissolved in TFE/dimethyl sulfoxide (DMSO) (60/40 v/v%) mixed solvent (700 μL) and heated at 100°C (Fig. 2). The time-dependent NMR monitoring of the reaction solution revealed that the self-assembly completed after 24 h. The formation of a giant product was first indicated by the broadness of the ^{1}H NMR signals due to the slow tumbling motion of the product in a solution. The diffusion coefficient *D* is the swimming speed of a molecule in a solution, which is useful for evaluating the size of the product: a large molecule shows a small *D*. DOSY NMR measurement is simple and reliable way to determine *D* for NMR signals. All the ^{1}H signals of the product showed the same *D* value of 6.31×10^{-11} (m^2/s), which indicated a single product formation of $Pt_{12}L_{24}$ sphere **2** shown in Fig. 2 and was comparable to that of the $Pd_{12}L_{24}$ counterpart. The control experiment for the reaction without TFE, i.e., in DMSO only, showed no convergence to a single product: the unassignable mixture of unstable intermediates, which are kinetic products, remained unchanged in 24 h, because the strong Pt-pyridyl group bonds were not effectively cleaved under the reaction conditions. Another additive-like protic solvents, such as EtOH and acetic acid, were effective for the self-assembly.

The composition of the product was clearly determined to be $Pt_{12}L_{24}$ by high-resolution cold-spray ionization time-of-flight mass spectrometry (CSI TOF MS) from a series of $[M - (\text{counter anion})_n]^{n+}$ peaks (n = 10-15), each of which is further resolved into an isotopic distribution pattern consistent with the theoretical simulation result. The MS studies revealed the solution-state structure of the product to be $Pd_{12}L_{24}$, and a consistent solid-state structure was determined by X-ray single-crystal diffraction studies. Single crystals suitable for crystallographic study were obtained by the slow diffusion of isopropyl acetate

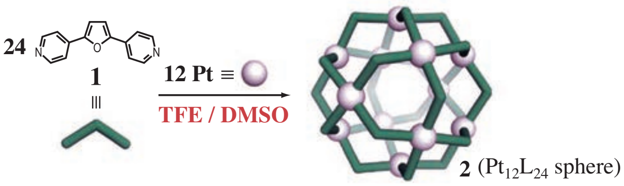

Fig. 2. Self-assembly of Pt(II)$_{12}$L$_{24}$ complex 2 in DMSO with a weakly acidic, H-bond-donating TFE solvent.

vapor into a DMSO solution of the product **2**. Owing to a severe disorder of solvents and counter ions in the large void of the crystals, the diffraction intensities obtained on an in-house X-ray diffractometer were very low and limited at a too low resolution to solve the molecular structure. We improved the method of treating the fragile crystals containing a volatile solvent and the method of mounting the crystal on the diffractometer. Finally, a high-flux and low-divergence synchrotron X-ray beam with an efficient and high-resolution CCD detector afforded high-quality data from which the $Pt_{12}L_{24}$ spherical shell **2** was confirmed (Fig. 3). Mapping the 24 ligands to edges and 12 metal ions to vertices, the framework $Pt_{12}L_{24}$ **2** forms a cuboctahedron. Reasonable bond lengths and angles, especially, the almost perfect square planar orientation of the four pyridyl groups around Pt(II) centers, were confirmed. Importantly, these structural features of the product were essentially the same as those of previously reported $Pd_{12}L_{24}$ spheres with the same shell frameworks.

The preliminary synchrotron X-ray diffraction studies were carried out at NE3A beamline in the PF-AR using a diffractometer equipped with an ADSC Quantum 270 CCD detector. The final synchrotron X-ray diffraction studies were carried out at **BL38B1** beamline in SPring-8 using a diffractometer equipped with an ADSC Quantum 315 CCD detector (λ = 0.75000 Å, 293 K).

The stronger Pt-L bond length should result in a more stable property of the product complex; accordingly, we determined the durability of complexes for nitric acid. When even a large excess amount of nitric acid (480 eq.) was added to the DMSO solution of $Pt_{12}L_{24}$ complex **2**, the NMR spectrum hardly changed, confirming the rigid complex structure. In contrast, the counterpart $Pd_{12}L_{24}$ complex was not tolerant to the same acidic conditions and immediately decomplexed into an unassignable mixture of oligomers owing to the labile nature of the Pd(II)-pyridine scoordination. The high stability of the Pt complex is suitable for applications in a wide variety of media firmly retaining the well-defined three-dimensional spherical structures.

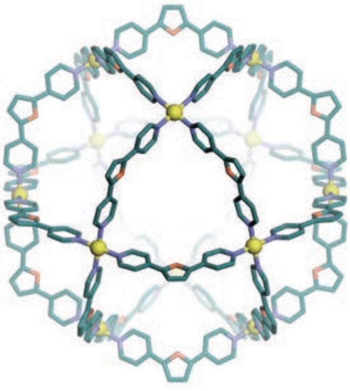

Fig. 3. Crystal structure of $Pt_{12}L_{24}$ sphere 2. Hydrogen atoms and the two counter ions at the apical positions of each Pt^{2+} are omitted for clarity.

Sota Sato[a,b] and Makoto Fujita[a,b,*]

[a] Department of Applied Chemistry,
The University of Tokyo
[b] JST-CREST

*E-mail: mfujita@appchem.t.u-tokyo.ac.jp

References

[1] *D. Fujita, A. Takahashi, S. Sato and M. Fujita: J. Am. Chem. Soc.* ***133*** *(2011) 13317.*

Heterogeneous nanoscale structure in alkyl-methylimidazolium bromide ionic liquids: a step towards greener solvents?

Ionic liquids, organic salts with low melting points (<100°C), are receiving increasing attention in the chemical industry due to their interesting properties. In particular they are considered as promising environmental-friendly replacements for conventional organic solvents [1]. A remarkable feature of ionic liquids is their large tunability, since they can be obtained by the combination of a large number of possible cations based on several main groups with many different anions ranging from simple halides to complex organic groups. As a result it is theoretically possible to design a liquid adapted to a particular application by combining the appropriate cation and anion. Unfortunately, the basic understanding needed to achieve such a goal is still lacking, due to the high complexity of the molecular interactions leading to the macroscopic properties of the resulting liquid. As a step in this direction, we have combined the high-energy synchrotron X-ray diffraction (XRD) technique with atomistic Molecular Dynamics (AMD) simulations to explore the atomic structure of imidazolium-based ionic liquids with three different alkyl chain lengths, 1-alkyl-3-methyl-imidazolium bromide ($C_{n=2,4,6}$mimBr, Fig. 1).

High-energy XRD experiments were carried out at the high-energy X-ray diffraction beamline **BL04B2** with a photon energy of 61.5 keV in symmetric transmission geometry over the scattering vector Q ($=4\pi\sin\theta/\lambda$, 2θ: scattering angle, λ: wavelength of photons) range of 0.15–22 Å^{-1}. Classical AMD simulations were carried out with the DL_POLY 2.18 code employing the same conditions that proved to reproduce well both the structure and dynamics of C_2mimBr [2,3].

Figure 2 shows the $S(Q)$s for the three liquids measured at temperatures close to that of the simulations, 360 K. Five major features can be identified, indicated by the labels I–V. Only Peak I, at Q = 0.44 and 0.33 Å^{-1} for C_4mimBr and C_6mimBr, respectively, corresponding to correlation lengths D = 14 and 19 Å, shows a strong dependence on alkyl chain length; this feature appears to resemble the first sharp diffraction peak (FSDP) seen in molecular and network liquids and glasses, but its amplitude decreases with temperature unlike the increase generally observed with FSDPs. The AMD simulations reproduce well the total static structure factor of the three systems [4], including the low-Q peak that proved problematic in previous work in the literature. Therefore we have employed them to characterize in real space the structural heterogeneity implied by this feature, by defining a density heterogeneity order parameter (DHOP):

$$H_i\,(R) = \exp\left(\frac{\delta_i(R)}{d_i} - 1\right)$$

where δ_i(R) is the density of atoms of type i lying within a sphere of radius R about a reference atom of type i, making allowance for the periodic boundary conditions, d_i is the density of those atoms averaged over the entire system, and the angular brackets represent an average over all saved configurations.

The DHOPs for four types of atoms in C_6mimBr are shown in Fig. 3. An atom type dispersed homogeneously would be characterized by a DHOP gradually rising to one as R increases, while one dispersed heterogeneously would rise rapidly to a value higher than one and then decrease. Figure 3 shows that the distribution of the methylene groups next to the ring is rather homogeneous, while those of the ring centers and anions are slightly heterogeneous, with the DHOP reaching a maximum around 9 Å, a value close to D/2. In contrast, the tail distribution is extremely heterogeneous, with the DHOP reaching a maximum value of 1.2 at 6 Å.

Our results are consistent with the concept of a nanoscale heterogeneity with small, crystal-like moieties similar to that elaborated by Annapureddy *et al.* [5]. As the authors point out, there is no justification in either the experimental or simulation literature for more complex structural motifs such as micelles or strands. The similarity between the liquids and corresponding crystals on the nanoscale is supported by our detailed XRD and AMD comparison

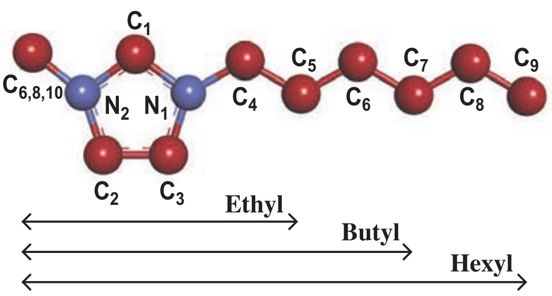

Fig. 1. 1-alkyl-3-methylimidazolium [$C_n$mim] cation. The carbon of the methyl group is named as C_6 for the ethyl- (n = 2), C8 for the butyl- (n = 4), and C10 for the hexyl- (n = 6) methylimidazolium cation.

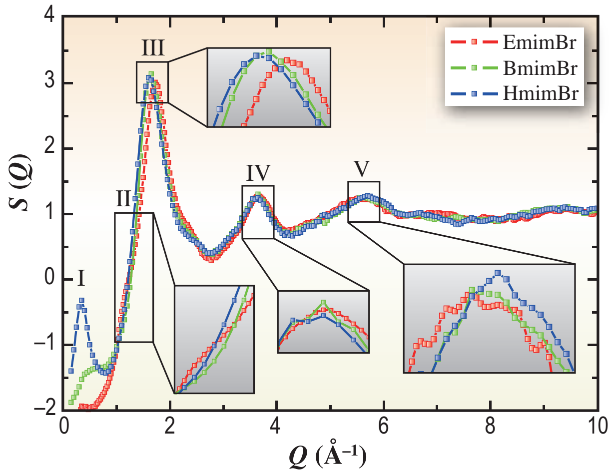

Fig. 2. X-ray structure factors for the three liquids, C_2mimBr (EmimBr), C_4mimBr (BmimBr), and C_6mimBr (HmimBr), at 360 ± 2 K. The lines joining the points are a guide to the eye.

of the structure [2] and dynamics [3] of liquid and crystalline C_2mimBr. A better understanding of the origin and the extension of nanoheterogeneities in ionic liquids is a crucial step towards a better comprehension of their unusual properties and will hopefully lead to the design of new ionic liquids having the required properties to replace standard solvents by more ecologically friendly substitutes.

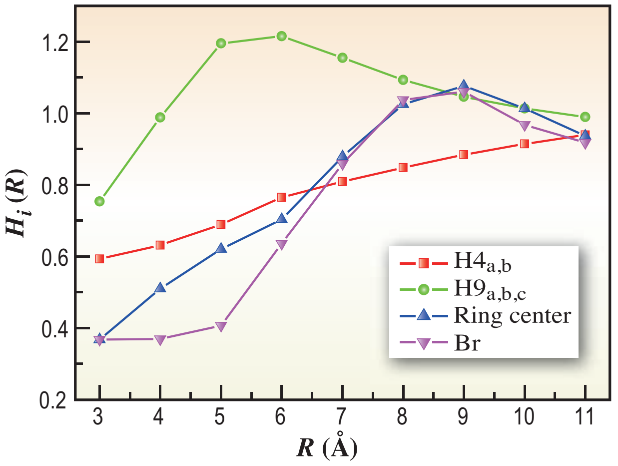

Fig. 3. Density heterogeneity order parameters [Eq. (1)] in C_6mimBr as a function of sphere radius for methylene group hydrogen atoms next to the ring, tail group hydrogen atoms, ring centers and anions. The labels $H4_{a,b}$ and $H9_{a,b,c}$ refer to hydrogen atoms on the C4 and C9 carbons, respectively (Fig. 1).

Bachir Aoun[a,b], Miguel A. González[a] and
Marie-Louise Saboungi[b,*]

[a] Institut Laue Langevin, France
[b] Centre de Recherche sur la Matière Divisée,
CNRS-University d'Orléans, France

*E-mail: saboungi@cnrs-orleans.fr

References

[1] R.D. Rogers and K.R. Seddon: Science **302** (2003) 792.
[2] *B. Aoun, A. Goldbach, S. Kohara, J.-F. Wax, M. A. González and M.-L. Saboungi: J. Phys. Chem. B* ***114*** *(2010)12623.*
[3] B. Aoun *et al.*: J. Phys. Chem. Lett. **1** (2010) 2503.
[4] *B. Aoun, A. Goldbach, M.A. González, S. Kohara, D.L. Price and M.-L. Saboungi: J. Chem. Phys.* ***134*** *(2011) 104509.*
[5] H.V.R. Annapureddy *et al.*: J. Phys. Chem. B **114** (2010) 16838.

Ethanol-water structures at the microscopic level studied by X-ray Compton scattering: extreme sensitivity to geometries

Water-ethanol mixtures are industrially important substances, but surprisingly little is known about them at the detailed microscopic level. In general, characterization and understanding of liquid mixtures at the molecular level is needed in order to explain and design their macroscopic properties. Liquid mixtures are ubiquitous in our environment, ranging from household chemicals to seawater. Industry handles and manufactures a wide variety of liquid mixtures, which could be in many cases better tailored if one had the precise knowledge of the microscopic structure and behavior. From a purely scientific perspective, the most interesting questions are related to structural inhomogeneities and hydration structures, and how for example the water molecules behave in complicated structures, when they are not any more in their bulk environment.

Accurate computer simulations on the structure of complicated liquids are still at their infancy. In principle, quantum mechanical molecular dynamics (MD) simulations should reveal all the aspects of the liquid, but in practice such calculations cannot be yet performed even at supercomputers. The difficulty stems first of all from the heavy computational demand regarding the time-scale of the simulation runs. Secondly, the complexity of the physical interaction model for the electrons is such that only very small systems can be studied highly accurately. These challenges require new experimental approaches.

In a joint experimental and theoretical study [1], an X-ray Compton scattering experiment on ethanol-water mixtures was carried out at beamline **BL08W**. The purpose of the experiment was to characterize the hydrogen bond and solvation structures in the mixtures at various alcohol concentrations. X-ray Compton scattering experiments suit to this project since the measured data is extremely sensitive to subtle changes in the molecular level geometries [2]. The experiments are demanding, since very large statistics are needed to observe the sub-Ångström scale effects. The samples were prepared by researchers from Suntory, Japan. The molar concentration of ethanol in the samples was chosen to be 5.5-73.1%, which corresponds to the volume percentages 20-90%.

In the experiment an interesting behavior was found, which suggests that there is a structural change in the water-ethanol mixture between the concentrations 5.5% and 15.7% (see Fig 1). The data is shown as difference profiles, for which the Compton profiles of pure liquids are subtracted from the Compton profile of the mixture according to the molar percentages. The experimental data was analyzed by scientists at the University of Helsinki using model calculations based on modified structures obtained from classical molecular dynamics simulations. In the models, systematic changes were made in the internal covalent bonds and in the intermolecular distances between the molecules. An example of the results of these changes is shown in Fig. 2. A noteworthy point is that changes in the covalent bond lengths produce qualitatively different effects compared to changes in the intermolecular distances.

The comparison of the model calculations to the experimental data led to the characterization and interpretation of the structure. In the low-concentration sample (5.5 mol-%), there is a lengthening of the O-H covalent bonds by approx. 0.003 Å. Based on other studies in the literature, this lengthening can be interpreted as a stronger hydrogen-bond network of water in the mixture as compared to the pure liquids. In the higher-concentrations samples (15.7-73.1 mol-%), it was found that the intermolecular distances between the molecules became shorter. Macroscopically, this means a denser system compared to the pure liquids, which is a well-known

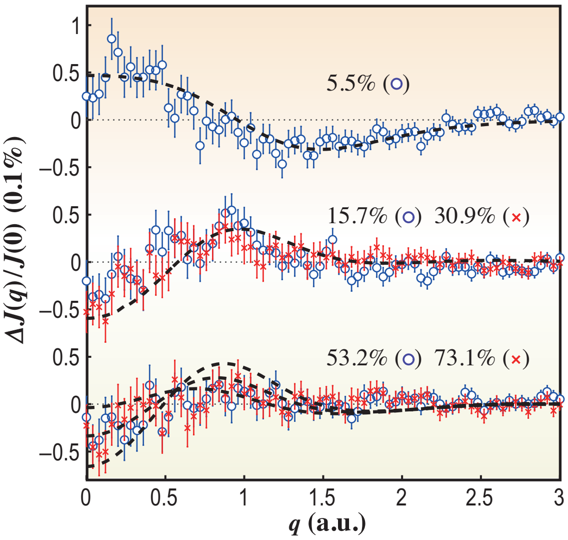

Fig. 1. Experimental Compton profile differences. The experimental data are given by red crosses (×) and blue circles (○). The molar percentages of ethanol have been indicated, and the data have been shifted for clarity. The black dashed curves are model calculations from modified MD clusters. Uppermost curve: O-H bonds elongated by 0.003 Å in the 5% mixtures; middle curve: O...O distances decreased by 1% in the 15% mixtures; lowermost three curves: O...O distances decreased by 1%, 2%, and 3% in the 95% mixtures.

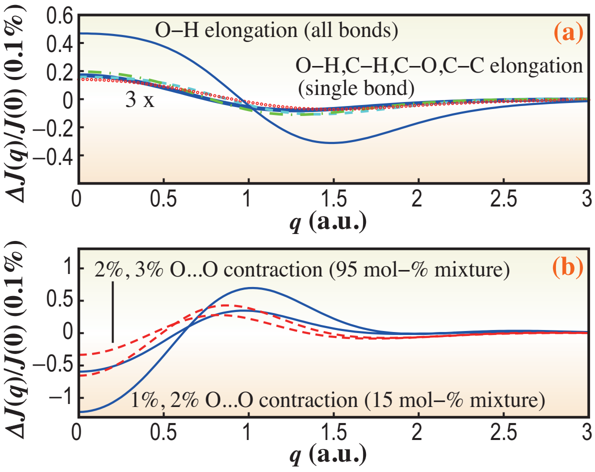

Fig. 2. **(a)** Changes in the Compton profile when all the intramolecular O-H bond lengths are increased by 0.003 Å (blue solid line) and one bond [O-H of water or ethanol (red), C-O (cyan), C-C (green), or C-H (blue)] in a cluster increased by 0.01 Å (latter multiplied by 3 for better clarity). **(b)** Changes in the Compton profile when the density increases: intermolecular O…O distances decreased by 1% and 2% (for 15% mixture) and 2% and 3% (for 95% mixture). For both concentrations, larger features arise for larger contractions.

property of ethanol-water mixtures. The two regimes are represented schematically in Fig. 3.

The present findings are a new way to characterize inhomogeneities in alcohol-water systems. For the first time, the quantitative changes related to the intra- and intermolecular structures were determined. The study demonstrates the power of X-ray Compton scattering to study detailed geometrical properties. It complements a previous demonstration of the observation of configurational energetics of materials [3]. In the future, advanced materials could be characterized in a new and unique way using these methods.

Low concentration: longer O-H distances

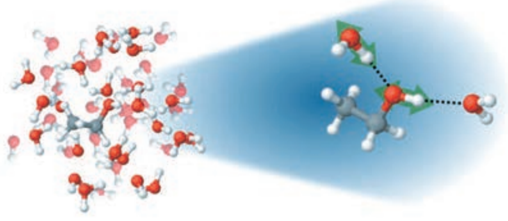

High concentration: shorter distances between molecules

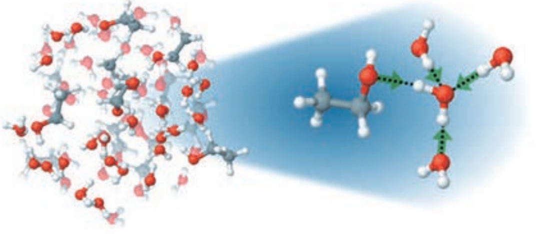

Fig. 3. Schematic representation of the structural changes in the two solvation regimes in water-ethanol mixtures compared to pure liquids.

Mikko Hakala[a,*], Iina Juurinen[a] and Koichi Nakahara[b]

[a] Dept. of Physics, University of Helsinki, Finland
[b] Frontier Center for Value Creation,
Suntory Business Expert Limited

*E-mail: mikko.o.hakala@helsinki.fi

References

[1] *I. Juurinen, K. Nakahara, N. Ando, T. Nishiumi, H. Seta, N. Yoshida, T. Morinaga, M. Itou, T. Ninomiya, Y. Sakurai, E. Salonen, K. Nordlund, K. Hämäläinen and M. Hakala: Phys. Rev. Lett.* ***107*** *(2011) 197401.*
[2] M. Hakala *et al.*: Phys. Rev. B **73** (2006) 035432.
[3] K. Nygård *et al.*: Phys. Rev. Lett. **99** (2007) 197401.

Green ammonia synthesis from nitrate with photocatalytically generated hydrogen on CuPd nanoalloys supported by TiO_2

Ammonia (NH_3) is not only the main component in chemical fertilizers but also has been noted as an energy carrier for alkaline fuel cells [1]. Presently, we are confronted with both food and energy crises, so a greater demand for NH_3 is therefore forecasted. NH_3, containing no carbon, seems to be far away from contributing to the release of carbon dioxide (CO_2). Since the hydrogen gas produced by fuel reforming is generally utilized for the hydrogenation of inert nitrogen (N_2), industrial NH_3 production is actually accompanied by both a great deal of energy consumption and CO_2 release. The fossil fuel-free H_2 gas produced using renewable energy sources, such as photocatalytically generated H_2 from water utilizing solar light, has therefore received much attention as a clean energy carrier [2], as well as a raw material for various chemical production processes, including that for NH_3. At the same time, over-manuring with synthetic fertilizers increases in the concentrations of the nitrate ion (NO_3^-) and its derivatives in ground water. Here, we performed the reduction of NO_3^- into NH_3 with photocatalytically generated hydrogen as an environmentally benign process that could produce NH_3 without releasing CO_2 and consuming excess energy [3].

Copper-palladium (CuPd) bimetallic alloy nanoparticles loaded on a support are known to be active for NO_3^- reduction into N_2 in the presence of hydrogen dissolved in a solution. It has been proposed that the NO_3^- ions are firstly reduced to nitrite ions (NO_2^-) on the bimetallic CuPd surface. Then, NO_2^- is reduced to N_2 or NH_3. Previous reports suggested that the distribution of Pd and Cu in the bimetallic particles determines the selectivity in the latter step [4]. On the particulate alloys where Pd atoms form relatively large domains, NO_2^- is preferentially reduced into N_2. On the other hand, NH_3 generation appears to preferentially occur on the well-mixed alloy surfaces.

To prepare homogeneously mixed nanoalloys, we synthesized CuPd alloy nanoparticles first. We then deposited them on a TiO_2 support. CuPd nanoalloys were produced by a chemical reduction method using poly[n-vinyl-2-pyrrolidone] (PVP) as a protective reagent to control the alloy size [5].

To investigate the alloy structure in detail, an X-ray diffraction pattern with a high signal to noise ratio was obtained at beamline **BL44B2** and is displayed in Fig. 1(a). Although both metals have an fcc structure in the bulk state, the XRD pattern of the nanoalloy was reproduced by assuming a bcc-type structure. This implies that the nanoalloy is constructed from a homogeneous mixture of Cu and Pd atoms, and not from a mixture of Cu and Pd clusters. Photocatalysts were prepared by the simple mixing of TiO_2 powder (P25) and an aqueous solution of the CuPd nanoalloy. As a reference sample, we also prepared a catalyst with PVP-coated Pd nanoparticles (Pd/TiO_2). The commonly used CuPd bimetallic catalyst (*n*-CuPd/TiO_2) was prepared using the impregnation method. Photocatalytic hydrogen generation and NO_3^- reduction under UV irradiation ($\lambda > 300$ nm) were carried out in the presence of methanol as a sacrificial electron donor after the substitution of argon for air in the reaction system. As separate control reactions, we examined NO_3^- reduction without UV irradiation, i.e, in the dark, but with *ca.* 350 Torr of added H_2(g), which corresponds to twice the amount of hydrogen generated under UV irradiation for 3 h.

Time courses of hydrogen evolution over CuPd/TiO_2, Pd/TiO_2, and TiO_2 are shown in Fig. 1(b). CuPd/TiO_2 including Cu, on the basis of the amount of a half atomic percentage of the nanoalloy, showed an excellent activity, much higher than that of Pd/TiO_2 [4].

Percentages of residual NO_3^-, generated NO_2^-, and NH_3 relative to the initial concentration of NO_3^- in the reaction solutions are shown in Fig. 2 [4]. During the reaction over Pd/TiO_2 in the dark, almost none of the products are generated (a). Under UV irradiation, a small amount of NO_3^- ions was converted,

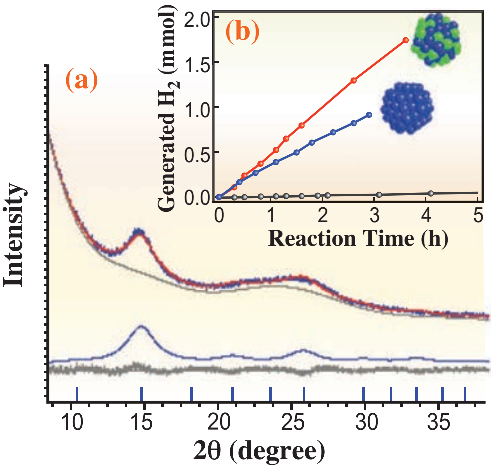

Fig. 1. **(a)** Powder XRD pattern and Rietveld profile of the CuPd nanoalloy. The observed pattern (blue) was reproduced by the curve calculated assuming a B2-type structure (lattice const. = 3.096(10) Å, diameter = 2.0(6) nm, R_w = 1.57 %, and GOF = 1.56) (red). **(b)** Time courses of hydrogen evolution over CuPd/TiO_2 (●), Pd/TiO_2 (●), and TiO_2 (●).

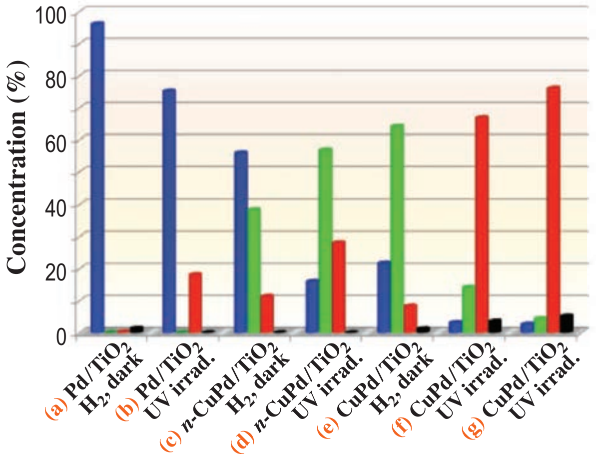

Fig. 2. Concentrations of NO_3^- (blue), NO_2^- (green), NH_3 (red) and N_2 (black) relative to the initial NO_3^- concentration after reaction in a 470 μM NO_3^- aqueous solution including 10 vol% methanol. The catalytic reactions were conducted with the following: **(a)** Pd/TiO_2 (0.46 wt%) with H_2 in the dark and **(b)** under UV irradiation, **(c)** *n*-$CuPd/TiO_2$ (0.37 wt%) with H_2 in the dark and **(d)** under UV irradiation, and **(e)** $CuPd/TiO_2$ (0.37 wt%) with H_2 in the dark and **(f)** and **(g)** under UV irradiation. The reaction time for **(a)**–**(f)** was 3 h and that for **(g)** is 5 h.

15% of them to NH_3 (b). Compared with the results for Pd/TiO_2, a large amount of NO_3^- was converted to NO_2^- and NH_3 over *n*-Cu-Pd/TiO_2 in the dark (c). In the reaction over $CuPd/TiO_2$ in the dark, NO_2^- ions were found to be the main product with a concentration of 64% and a small amount of NH_3 was detected (e). On the other hand, a large amount of NH_3 was produced under UV irradiation (f). After 5 h of irradiation, all NO_3^- ions were converted and NH_3 was identified as a product with a concentration of 76% (g), which corresponds to 78% of selectivity. This concentration is higher than 28% in the photocatalytic NO_3^- reduction over *n*-Cu-Pd/TiO_2 (d).

To rationalize the high selectivity to NH_3 observed in the reaction over $CuPd/TiO_2$ under UV irradiation, we propose two explanations. First is the homogeneous mixing of Cu and Pd on the surface of the alloy. NO_2^- hydrogenation is considered to be a critical step controlling selectivity towards N_2 and NH_3. As discussed above, we found that Cu and Pd atoms are homogeneously distributed in the CuPd nanoalloy. The percentage of single Pd sites where a Pd atom is directly surrounded by copper atoms is possibly large, resulting in highly selective NH_3 production. Second is the high hydrogenation ability of photocatalytically generated hydrogen. The selectivity of NO_2^- hydrogenation over CuPd nanoalloys can be connected to the ratio of the surface coverage of reductant species that of N species (H:N). Given that the amount of hydrogen evolved on $CuPd/TiO_2$ is larger than that on Pd/TiO_2, it is likely that hydrogen atoms are generated not only in the proximity of Pd sites but also around Cu sites. It is, hence, supposed that nitrogen oxides absorbed on the surface are continuously surrounded by nascent hydrogen atoms unremittingly. In such a case, a high H:N ratio is attained, resulting in a high selectivity to NH_3. The schematic image is described in Fig. 3.

In the present study, it was found that photocatalytically generated hydrogen exhibits a high selectivity for the conversion of NO_3^- to NH_3. Highly selective NH_3 production via NO_3^- reduction using hydrogen from solar energy represents a promising approach for fossil-free NH_3 production from waste treatment.

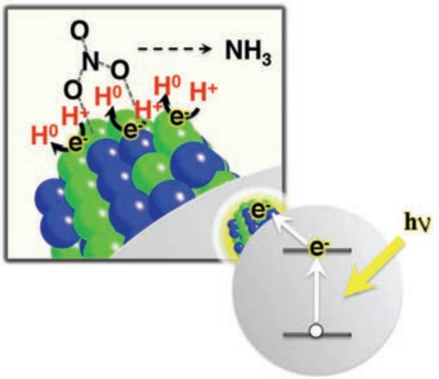

Fig. 3. Schematic image for selective nitrate hydrogenation to ammonia. Absorbed substrates are surrounded by a large number of nascent hydrogen atoms generated from water.

Miho Yamauchi[a,b,d,*], Ryu Abe[b,d] and Kenichi Kato[c,d]

[a] International Institute for Carbon-Neutral Energy Research, Kyushu University
[b] Catalysis Research Center, Hokkaido University
[c] SPring-8/RIKEN
[d] JST-CREST

*E-mail: yamauchi@i2cner.kyushu-u.ac.jp

References

[1] J.W. Erisman *et al.*: Nat. Geosci. **1** (2008) 636.
[2] R. Abe *et al.*: J. Am. Chem. Soc. **132** (2010) 11828.
[3] *M. Yamauchi, R. Abe, T. Tsukuda, K. Kato, M. Takata: J. Am. Chem. Soc.* ***133*** *(2011) 1150.*
[4] Y. Yoshinaga *et al.*: J. Catal. **207** (2001) 37.
[5] M. Yamauchi and T. Tsukuda: Dalton Trans. **40** (2011) 4842.

μ-XAFS analysis of a single catalyst particle of $NiO_x/Ce_2Zr_2O_y$ on a SiO_2 membrane using X-ray μ-beam

Various heterogeneous catalysts have been used in chemical industry processes, such as oil and natural gas conversions, energy conversions, and the synthesis of fundamental chemical compounds. Solid catalysts are usually inhomogeneous powder assemblies of heterogeneous solid particles with nm–μm size, and each powder particle has different shape and structure. Therefore, the structures of solid catalysts are often complex and difficult to characterize by a simple method.

Synchrotron XAFS is one of the most powerful methods for characterizing oxidation states and local coordination structures of heterogeneous solid catalysts, such as supported metal catalysts. However, conventional XAFS measurements are performed using X-ray beams with mm size and they provide macroscopically averaged structural information on a large number of heterogeneous catalyst particles with different sizes, compositions, and local coordination structures in beam-spot size.

We have succeeded in performing the scanning μ-XRF and μ-XAFS analyses of a single catalyst particle of $NiO_x/Ce_2Zr_2O_y$ ($0 \le x \le 1$, $7 \le y \le 8$) using an X-ray μ-beam (1000 nm (h) × 800 nm (v)) at beamline **BL37XU**. $Ce_2Zr_2O_y$ solid solution is known to exhibit a high oxygen storage/release property, which is highly important for automobile exhausting catalysts [1]. Its oxygen composition can be controlled between $Ce_2Zr_2O_7$ and $Ce_2Zr_2O_8$, and the Ni species supported on $Ce_2Zr_2O_7$ is active for CH_4 steam reforming reaction ($CH_4 + H_2O \rightarrow 3H_2 + CO$) to produce hydrogen [2]. Its activity highly depends on the oxidation state and local coordination structure of the Ni species supported on $Ce_2Zr_2O_y$. The average particle size of the $NiO_x/Ce_2Zr_2O_y$ catalyst was 750±370 nm, which is similar to the size of the X-ray μ-beam. The scanning μ-XRF and μ-XAFS analyses of a single catalyst particle of $NiO_x/Ce_2Zr_2O_y$ revealed the microscopic structural information (oxidation state and local coordination structure) of catalytically active and inactive phases of a single particle of the supported Ni catalyst for CH_4 steam reforming reaction for the first time [3].

Figure 1(a) shows the experimental setup used for the μ-XRF and fluorescent μ-XAFS analyses at BL37XU. The X-ray beam was focused by Kirkpatrick-Baez (KB) mirrors and the size of the obtained X-ray μ-beam was 1000 nm (h) × 800 nm (v) at the Ni *K*-edge (8.332 keV) (Fig. 1(b)). The $NiO_x/Ce_2Zr_2O_y$ catalyst particles were dispersed on a thin SiO_2 membrane (30 μm), and the membrane in a XAFS cell was mounted on a piezoelectric translation stage at the focusing point of the X-ray μ-beam. The fractions of aggregated particles on the membranes were estimated to be less than 1.9% by the analysis of SEM images. We prepared $Ni/Ce_2Zr_2O_7$ and $NiO/Ce_2Zr_2O_8$ dispersed on the SiO_2 membranes and recorded the results of the μ-XRF and fluorescent μ-XANES and μ-EXAFS analyses.

Two-dimensional (2D) scanning for μ-XRF mapping was performed using the X-ray μ-beam at 8.248 keV, and Ni Kα (7.478 keV) and Ce Lα (4.840 keV) + $L\beta_1$ (5.262 keV) fluorescent X-rays were measured. The piezoelectronic stage was shifted every 200 nm and 2D μ-XRF images of the fluorescent X-ray intensity were obtained. In the case of a conventional XAFS measurement using an mm-sized X-ray beam, the observed XAFS data involves contribution from all catalyst particles in the beam spot, but the μ-XAFS data provides the structural information of a single catalyst particle in the μ-beam spot, as illustrated in Fig. 2(a). Similar contrast images were observed for Ni Kα and Ce Lα + $L\beta_1$ fluorescent X-rays, indicating the

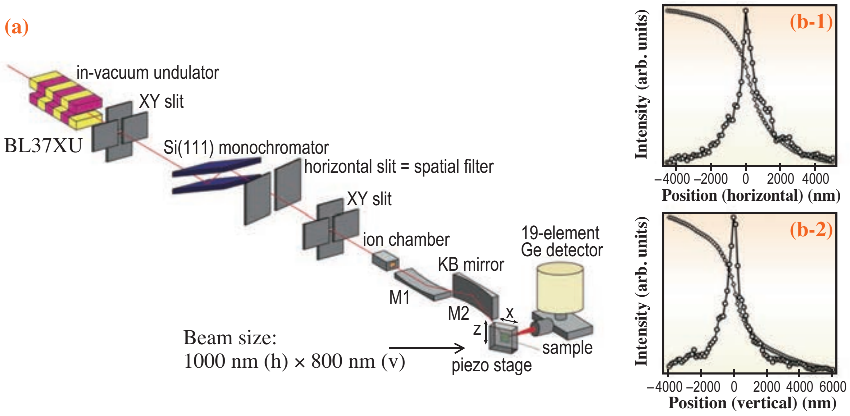

Fig. 1. **(a)** Experimental setup of μ-XAFS. **(b)** Measured knife-edge profiles of focused X-ray μ-beam at 8 keV. (b-1) Horizontal direction and (b-2) vertical direction.

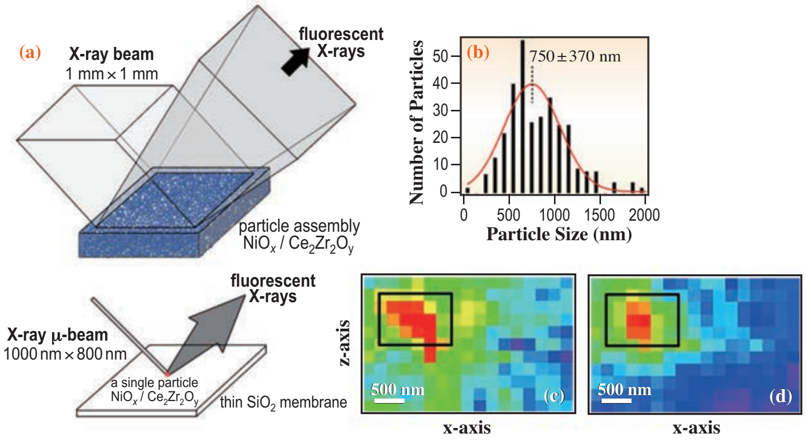

Fig. 2. **(a)** Schematic of conventional XAFS and μ-XAFS measurements. **(b)** Particle size distribution of the $NiO_x/Ce_2Zr_2O_y$ catalyst. **(c)** and **(d)** 2D μ-XRF mappings of a $NiO/Ce_2Zr_2O_8$ particle on a SiO_2 membrane ((**c**): Ni Kα and (**d**): Ce Lα+Lβ_1).

position of the catalyst particle on the SiO_2 membrane (Figs. 2(b) and 2(c)).

Significant differences in Ni *K*-edge XANES were observed for $Ni/Ce_2Zr_2O_7$, which is active for CH_4 steam reforming reaction and $NiO/Ce_2Zr_2O_8$, which is inactive for the reaction, as shown in Fig. 3(a). The μ-XANES spectra of $Ni/Ce_2Zr_2O_7$ (i) and $NiO/Ce_2Zr_2O_8$ (iii) were similar to the XANES spectra of the $Ni/Ce_2Zr_2O_7$ particle assembly (ii) and $NiO/Ce_2Zr_2O_8$ particle assembly (iv), respectively. The Ni *K*-edge energies of μ-XANES were 8.338 and 8.341 keV for $Ni/Ce_2Zr_2O_7$ (i) and $NiO/Ce_2Zr_2O_8$ (iii), respectively, reflecting the oxidation state of the supported Ni species on $Ce_2Zr_2O_y$. Although the white line intensity of μ-XANES of the active $Ni/Ce_2Zr_2O_7$ catalyst (i) was slightly higher than that of conventional XANES (ii) owing to the probable oxidation with impurity oxygen under the measurement conditions, these results show that the oxidation state of the single catalyst particle can be discriminated by μ-XANES analysis. Intermediate oxidation states between $Ni/Ce_2Zr_2O_7$ and $NiO/Ce_2Zr_2O_8$ were also observed with $NiO_x/Ce_2Zr_2O_y$ samples ($7 < y < 8$).

We have succeeded in analyzing a Ni *K*-edge μ-EXAFS spectrum of a single catalyst particle of the inactive $NiO/Ce_2Zr_2O_8$ (Figs. 3(b)–3(d)). The EXAFS spectrum was measured for 3 h and its k^3-weighted EXAFS oscillations and Fourier transforms were successfully fitted. The obtained structural parameters of the local coordination of Ni species on the $NiO/Ce_2Zr_2O_8$ catalyst particle showed that the Ni species was NiO(II) (CN of Ni-O (at 0.208±0.003 nm) = 5.4±1.2; CN of Ni-Ni (at 0.292±.001 nm) = 11.7±0.9). To our knowledge, this was the first example of the μ-EXAFS curve-fitting analysis of a single catalyst particle of a practical catalyst. μ-XAFS will provide structural information regarding the catalyst particles with different catalytic behaviors excluding noise information from the heterogeneous property of catalyst particle assembly and contribute to the development of a more precise catalyst design in chemical reactors.

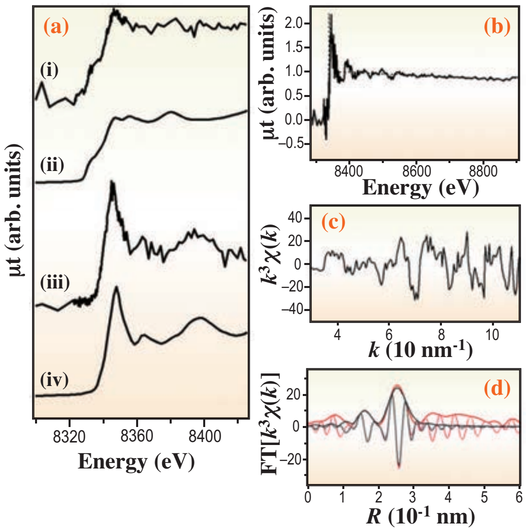

Fig. 3. **(a)** Ni *K*-edge XANES spectra of $Ni/Ce_2Zr_2O_7$ (i: μ-XANES of a single particle on a SiO_2 membrane and ii: conventional XANES of particle assembly) and $NiO/Ce_2Zr_2O_8$ (iii: μ-XANES of a single particle on a SiO_2 membrane and iv: conventional XANES of particle assembly). **(b)** μ-EXAFS data of $NiO/Ce_2Zr_2O_8$, **(c)** its k^3-weighted EXAFS oscillation, and **(d)** its Fourier transforms.

Mizuki Tada[a,*], Nozomu Ishiguro[a] and Tomoya Uruga[b]

[a] Institute for Molecular Science
[b] SPring-8/JASRI

*E-mail: mtada@ims.ac.jp

References

[1] A. Suda *et al.*: J. Ceram. Soc. Jpn. **110** (2002) 126.
[2] M. Tada *et al.*: in preparation.
[3] *M. Tada, N. Ishiguro, T. Uruga, H. Tanida, Y. Terada, S. Nagamatsu, Y. Iwasawa and S. Ohkoshi: Phys. Chem. Chem. Phys.* ***13*** *(2011) 14910 (Front cover of Issue 33).*

EARTH & PLANETARY

"Tsubaki"- *Camellia*

SCIENCE

The success of the asteroid sample-return mission of JAXA, HAYABUSA mission, was one of the hottest scientific topics in 2011 and had a huge impact on the broad area of research. Japanese researchers have first analyzed samples from the asteroid Itokawa using a nondestructive analytic method based on synchrotron radiation at SPring-8. Tsuchiyama reported X-ray absorption imaging tomography results for samples of the S-type asteroid Itokawa, revealing that most of Itokawa rock samples were similar to the most common type of meteorite on Earth, the ordinary chondrites, in terms of mineral assemblage, abundances and texture. The researchers also discussed the regolith formation and evolution of Itokawa, on the basis of three-dimensional shape features of the particles.

Recent advances in synchrotron radiation instruments and techniques make it possible to understand the physical and chemical properties of deep Earth materials as well as extraterrestrial matter. Here, we introduce four topics as a result of important research on the high-pressure and high-temperature behavior of iron alloys and iron-bearing compounds. Yoshino performed an electrical conductivity measurement of ferropericlase (Mg,Fe)O with a low iron content, which would form the top of the lower mantle, using a large-volume press and accurately determined the generated pressures using the equation of state of gold, in order to investigate the electronic high-spin-to-low-spin transition pressure of iron in ferropericlase. As a result, he revealed that the low iron content in (Mg,Fe)O results in a marked decrease in spin transition pressure. Hirose's group has studied iron spin crossover in silicate glass by X-ray emission spectroscopy and reported that the change in the degree of Fe-Mg partitioning between solid silicate and melt at high pressures was caused by the spin transition. The density calculation of silicate melt indicates that silicate melt is present at the base of the mantle, producing a possibly ultralow-velocity zone above the core-mantle boundary.

The next two reports present the latest results regarding the core materials of Earth and a Jupiter satellite. Ozawa and coworkers have investigated the phase relation of FeO, a candidate of Earth's core materials, under the whole Earth's outer core conditions by *in situ* X-ray diffraction using a laser-heated diamond anvil cell. They discovered a B1-B2 structural phase transition at 230 GPa and 3850 K, and found the volume change relevant to the transition. The present experiments and numerical simulations suggest the presence of two-layered convection in the outer core, having a significant effect on the Earth's magnetic field. For modeling the internal structure of Ganymede, a Jupiter satellite, Shibazaki *et al*. determined the melting temperature at high pressures in the Fe–S–H system. The reaction of the FeS alloy with hydrogen was observed, and hydrogenation was found to cause the depression of the melting temperature of the FeS alloy. On the basis of the experimental results on the Fe–S–H system, they discussed Ganymede's core.

Yasuo Ohishi

Three-dimensional structures of Hayabusa samples using X-ray microtomography

Asteroids are small objects that have not grown into planets and that contain information on the formation of the solar system. Particles of Asteroid Itokawa were successfully recovered by the Hayabusa mission of JAXA (Japan Aerospace Exploration Agency). They are the first samples recovered from an asteroid, and the second extraterrestrial regolith (sandy particles) to have been sampled, the first being the Moon, which was sampled by the Apollo and Luna missions.

It is accepted that most meteorites originate from asteroids, as demonstrated by orbital determination from observed meteorite falls. The materials on asteroids have been estimated by comparing reflectance spectra between asteroids and meteorites. Itokawa has an S-type spectrum, which is one of the major types and similar to those of ordinary chondrites, particularly LL5 or LL6 chondrites. However, there is a spectrum discrepancy between the asteroid and meteorites, which is considered to result from space weathering. Itokawa samples allow a direct validation of the relation between asteroids and meteorites. In addition, the properties of Itokawa particles allow studies of regolith formation and evolution.

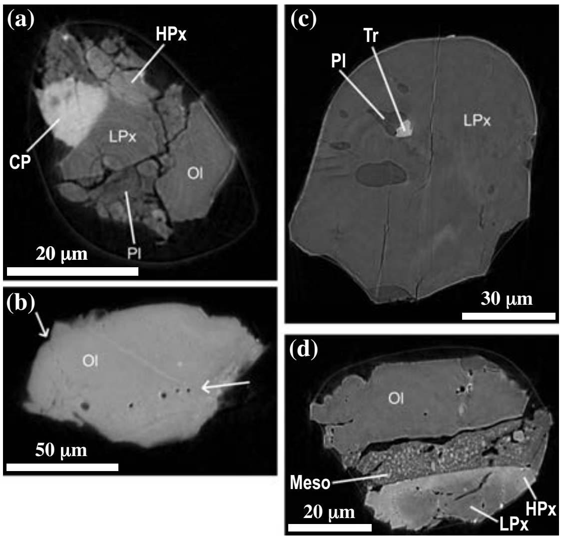

Fig. 2. Representative CT images of Itokawa particle [2]: samples **(a)** RA-QD02-0063, **(b)** RA-QD02-0014, **(c)** RA-QD02-0042, and **(d)** RA-QD02-0048. Concentric structure is a ring artifact. Bright edges of particles and voids are artifacts resulting from refraction contrast. CP indicates Ca phosphate; Tr, troilite; and Meso, mesostasis. The other abbreviations are the same as those in Fig. 1.

About 2000 recovered particles (< ~300 μm and most of them are <~10 μm) have been identified as having an Itokawa origin by curation at JAXA. About fifty particles were allocated for preliminary examination (PE) [1]. Our team examined three-dimensional (3D) structures by non-destructive X-ray microtomography as the first analysis in a sequential PE analytical flow [2]. The purposes are to understand their materials in comparison with meteorites and the 3D shape features in connection with regolith formation and evolution, and to provide information for the design of later destructive analyses. The latter is one of the key features of the Hayabusa PE strategy.

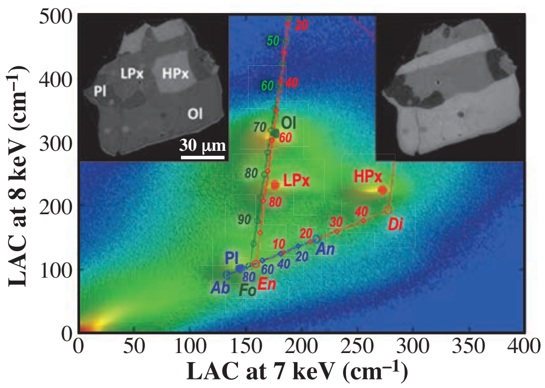

Fig. 1. A two-dimensional histogram of linear attenuation coefficient (LAC) values at 7 and 8 keV for an Itokawa particle (RA-QD02-0024) (original figure in [3] was changed). Solid symbols correspond to the mean chemical compositions of the minerals in Hayabusa samples [1]. Ol: olivine, *Fo*: forsterite, LPx: low-Ca pyroxene, *En*: enstatite, HPx: high-Ca pyroxene, Pl: plagioclase, *Ab*: albite, *An*: anorthite. Numbers along olivine, pyroxene, and plagioclase solid solutions are the forsterite, enstatite, wollastonite, and albite contents (in mol.%). Inserted images are CT images at 7 keV (left) and 8 keV (right).

Forty particles (~30 to 180 μm) were imaged at beamline **BL47XU** with an effective spatial resolution of ~200 or ~500 nm by absorption imaging tomography [2]. Imaging at two X-ray energies of 7 and 8 keV made the identification of minerals in CT images possible (analytical dual-energy microtomography [3]) since the *K*-absorption edge of Fe (7.11 keV) is present between the two energies (Fig. 1). Chemical compositions of olivine $[(Mg,Fe)_2SiO_4]$, low-Ca pyroxene $[(Mg,Fe)SiO_3]$, high-Ca pyroxene $[(Ca,Mg,Fe)SiO_3]$, and plagioclase $[(Na,Ca)(Al,Si)AlSi_2O_8]$ can be obtained by this method. A successive set of 3D CT images, which shows quantitative 3D mineral distribution, was obtained for each particle.

Tomography gave the total volume of 4.2×10^6 μm^3, which corresponds to a sphere of ~200 μm in diameter (total mass of ~15 μg). The mineral assemblage and their abundances in whole samples (64% olivine, 19% low-Ca pyroxene, 3% high-Ca pyroxene, 11% plagioclase, 2% troilite (FeS), and minor amounts (<0.2%) of kamacite [α-(Fe,Ni)], taenite [γ-(Fe,Ni)], chromite $[(Mg,Fe)(Cr,Al,Fe)_2O_4]$, and Ca-phosphates) are similar to those of LL chondrites. A slightly larger amount of olivine and smaller amounts of high-Ca pyroxene, troilite, and (Fe,Ni) in the Itokawa particles can be regarded as statistical errors due to picking up the small sample amount [4]. Other PE data, such as the chemical compositions of minerals [1], also indicate LL chondrites.

The 3D structures of most particles have highly equilibrated textures owing to thermal metamorphism (Figs. 2(a-c)), which correspond to the petrologic type of 5 and/or 6 in ordinary chondrites (LL5 and/or LL6), whereas some of them (~10%) have less-equilibrated textures (LL4) (Fig. 2(d)). SEM observation and the homogeneity of minerals show the same results [1]. Fe-rich nanoparticles observed in thin surface layers (<60 nm) of Itokawa particles show evidence of space weathering [5]. These results showed that the Itokawa surface material is consistent with LL chondrites suffering space weathering, as expected, and brought an end to the mystery of the origin of meteorites.

Sphere-equivalent diameter and three-axial lengths of each particle were obtained from the 3D CT images [2]. The cumulative size distribution of the particles has the log-slope of ~ –2, which indicates a dominance of ~cm size regoliths in the Itokawa smooth terrain by considering the size distribution of boulders (0.1–5 m) with the log-slope of ~ –3. The 3D shape (three axial length ratios) distribution cannot be distinguished from that of fragments produced in impact experiments (Fig. 3(a)), showing that the Itokawa particles are consistent with impact fragments. No particles showing melting were observed, indicating relatively low impact velocities similar to typical relative impact velocities among asteroids (~5 km/s). Most of the particles have sharp edges (Fig. 4(a)), whereas others (~25%) have rounded edges (Fig. 4(b)) and they were probably formed by abrasion from particles that were originally more angular as grains migrated during impact (Fig. 4(c)). The spherical shapes of lunar regolith particles (Fig. 3(b)) may be due to their longer residence time in the regolith. Systematic studies on regolith shapes together with micro-structures of particle surfaces, space weathering, and solar wind noble gas analysis will lead to a comprehensive understanding of processes on celestial bodies without atmosphere, such as small steroids and the Moon.

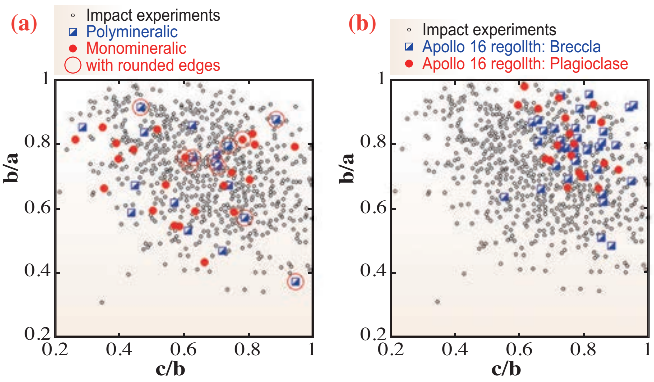

Fig. 3. 3D shape distributions of **(a)** Itokawa particles and **(b)** lunar regolith [2]. Fragments of impact experiments are also shown. Large circles in **(a)** show particles with rounded edges.

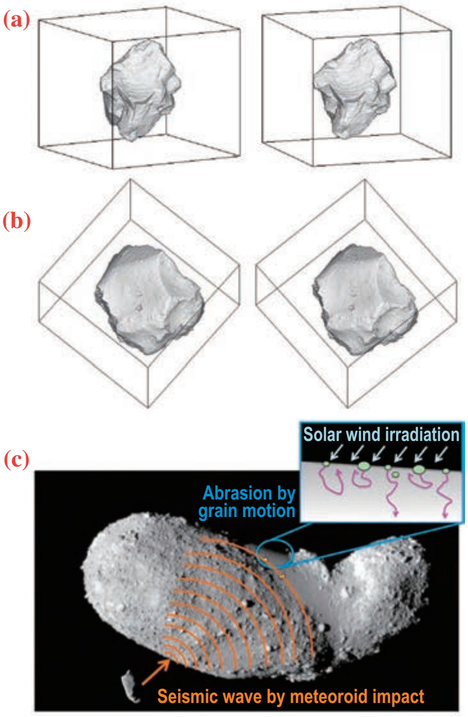

Fig. 4. Stereograms showing the 3D external shapes of Itokawa particles of **(a)** RA-QD02-0023 (232×232×203 μm^3) and **(b)** RA-QD02-0042 (112×112×93 μm^3) [2], and **(c)** an schematic illustration of possible abrasion process of regolith particles on Itokawa by granular processes induced by seismic vibration due to impact of a meteoroid.

Akira Tsuchiyama[†]

Dept. of Earth and Space Science, Osaka University

E-mail: atsuchi@kueps.kyoto-u.ac.jp

[†] Present address: Dept. of Earth and Planetary Science,
Kyoto University

References

[1] T. Nakamura *et al.*: Science **333** (2011) 1113.
[2] *A. Tsuchiyama, M. Uesugi, T. Matsushima, T. Michikami, T. Kadono, T. Nakamura, K. Uesugi, T. Nakano, S.A. Sandford, R. Noguchi, T. Matsumoto, J. Matsuno, T. Nagano, Y. Imai, A. Takeuchi, Y. Suzuki, T. Ogami, J. Katagiri, M. Ebihara, T.R. Ireland, F. Kitajima, K. Nagao, H. Naraoka, T. Noguchi, R. Okazaki, H. Yurimoto, M.E. Zolensky, T. Mukai, M. Abe, T. Yada, A. Fujimura, M. Yoshikawa, J. Kawaguchi: Science* ***333*** *(2011) 1125.*
[3] A. Tsuchiyama: submitted to Geochim. Cosmochim. Acta.
[4] T. Nagano: Abstract in Lunar and Planetary Science Conference, IVIII (2012).
[5] T. Noguchi *et al.*: Science **333** (2011) 1121.

Melting relation of FeS-H system under high pressure: Implications for the core of Ganymede

Ganymede is one of the Galilean satellites of Jupiter, and is the largest moon in our solar system. The observation data of the Galilean mission suggest that Ganymede has an intrinsic magnetic field and the interior is strongly differentiated into an outermost H_2O layer, a silicate rock mantle, and an iron-rich core [1]. The core is considered to consist of iron (Fe) and light elements. Sulfur (S) is one of the plausible light elements in the core because iron sulfide is found in many meteorites. Hydrogen (H) is also most probably present in the core. This is because, before the differentiation occurred in an early period, the silicate rock and the iron alloy mixed with and then may have reacted with H_2O in the interior of Ganymede. As a result, it may well be that the silicate rock layer contains a significant amount of water, and the iron alloy may contain hydrogen. It is known that hydrogen significantly lowers the melting temperature of metals. However, it has not been reported whether hydrogen affects the melting temperature of Fe–S alloy. If hydrogen lowers the melting temperature of Fe–S alloy, the previous models of Ganymede's core (e.g. [2]) may need to be revised. Therefore, in order to constrain the state and degree of melting of Ganymede's core, we first determined the melting temperatures of the FeS–H system ($FeSH_x$) at pressures up to 16.5 GPa [3].

Energy-dispersive X-ray diffraction experiments were carried out at high temperature and high pressure using a Kawai-type multianvil apparatus at **BL04B1**. The diffraction patterns were collected for a period of 120 or 300 s at each 50–100 K temperature step and at high pressure. In this study, melting of the sample was determined on the basis of observations of the disappearance of the diffraction peaks from the sample and the appearance of a broad halo peak. The FeS sample powder was packed into a NaCl container along with $LiAlH_4$, because NaCl is reported to effectively seal hydrogen at high pressures and temperatures. Hydrogen was supplied to the sample from the thermal decomposition of $LiAlH_4$.

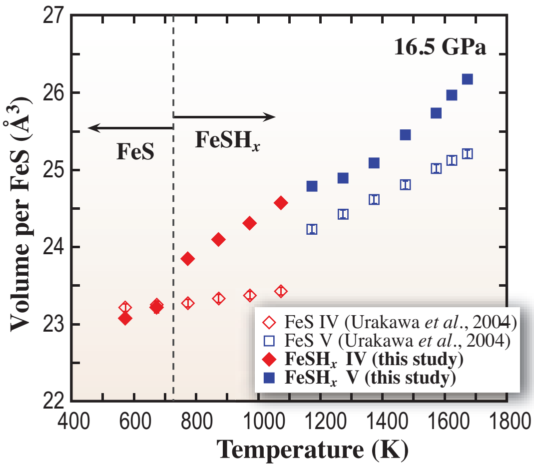

Fig. 1. Thermal expansion of FeS and $FeSH_x$ at 16.5 GPa. The volume per FeS is defined as V (unit cell volume) divided by Z (where Z = 8 for phase IV, and Z = 2 for phase V). The solid diamonds and squares correspond to $FeSH_x$ IV and $FeSH_x$ V, respectively. The open diamonds and squares correspond to FeS IV and FeS V, respectively, from Ref. [4].

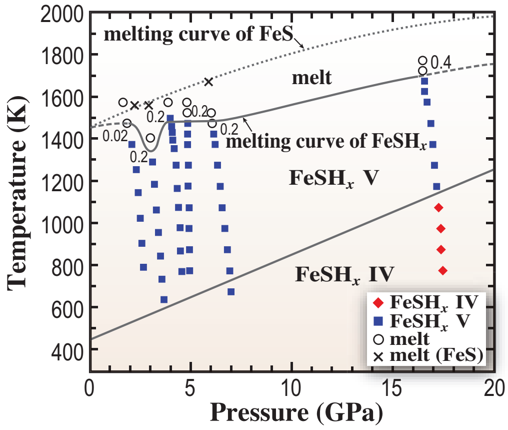

Fig. 2. Pressure-temperature phase diagram of $FeSH_x$, together with Boehler's melting curve of FeS [5]. The solid diamonds and squares correspond to $FeSH_x$ IV and $FeSH_x$ V, respectively, as determined in this study. The open circles correspond to the $FeSH_x$–melt. The crosses denote the observed melting temperatures of FeS. The numbers on the melting curve show the hydrogen concentration (x) just before the melting of $FeSH_x$, where x is defined as the number of hydrogen atoms per FeS in a unit cell.

The observed unit cell volumes of FeS and $FeSH_x$ with increasing temperature at 16.5 GPa are shown in Fig. 1. On the basis of the present X-ray diffraction measurements, the low-temperature phases of FeS and $FeSH_x$ have a hexagonal NiAs-type superstructure (Phase IV) and the high-temperature phase has a simple NiAs-type structure (Phase V). This is consistent with the previously reported phase relations of pure FeS [4]. However, above 800 K, the observed volume was clearly larger than that of pure FeS up to the melting point as shown in Fig. 1. This expansion in volume can be explained by hydrogenation, i.e., synthesis of $FeSH_x$. The drastic volume increase at high temperature was observed throughout the pressure range studied, except at 1.9 GPa. We considered that the structure of $FeSH_x$ is the same as that of FeS whereas the volume of $FeSH_x$ is larger than that of FeS owing to the dissolution of hydrogen in the interstitial sites of FeS.

The observed phase relationships of $FeSH_x$ are plotted on the pressure-temperature diagram shown in Fig. 2, together with the melting temperature of pure FeS [5]. The melting temperature of $FeSH_x$ was clearly decreased by 150–250 K compared with that of FeS between 3.0 and 16.5 GPa owing to hydrogenation. The melting temperature of $FeSH_x$ exhibited a minimum and the concentration of hydrogen increased at about 3 GPa ($x \approx 0.2$ at 3.0 GPa, whereas $x \approx 0.02$ at 1.9 GPa). This indicates that hydrogen starts to dissolve into the interstitial sites of FeS between 1.9 and 3.0 GPa. As a result, the depression of the melting temperature at about 3.0 GPa occurred.

Figure 3 shows the predicted phase diagram of the FeH_x–$FeSH_x$ system at 5 GPa with model temperatures equivalent to those of Ganymede's core. We assume that the FeH_x–$FeSH_x$ system has the same eutectic relation as the Fe–FeS system. Since the melting temperatures of Fe and FeS are depressed due to hydrogenation, the liquidus of the FeH_x–$FeSH_x$ binary system is lower than the core temperatures over a wide range of sulfur content in the core (Region I in Fig. 3). Then, Ganymede's core could be completely molten in Region I. If the core contains much sulfur (Region II in Fig. 3), it could be partially molten (solid $FeSH_x$ coexisting with liquid Fe–S–H) because the liquidus is higher than the core temperatures. Hauck *et al.* [2] showed that a completely molten core cannot sustain the Ganymede dynamo up to the present day by thermal convection. Thus, the partially molten core (Region II in Fig. 3) is more reasonable for sustaining the dynamo, suggesting that the core contains more than about 33 wt.% S.

The present study suggests that Ganymede's core could have a solid $FeSH_x$ inner core and liquid Fe–S–H outer core if the core consists of the Fe–S–H system (Fig. 4). The results of this study strongly indicate that hydrogen is certainly important for understanding the internal structures of planets and satellites outside the snow line, although additional experiments for the FeH_x–$FeSH_x$ system are needed in order to discuss the core in more detail.

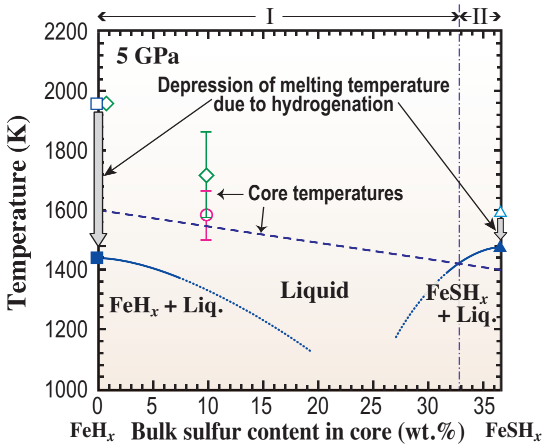

Fig. 3. Predicted phase diagram of the FeH_x–$FeSH_x$ system at 5 GPa, assuming it has the same eutectic relation as the Fe–FeS system. The open and solid squares denote the melting temperatures of Fe (Shen *et al.*, 1998) and FeH_x (Fukai *et al.*, 2003), respectively. The open and solid triangles denote those of FeS (Boehler, 1992) and $FeSH_x$ (this study) [3], respectively. The solid and dotted lines denote the predicted liquidus. The broken line denotes Ganymede's core temperatures with various bulk sulfur contents in the core, taken from Kimura *et al.* (2009) (1030 km H_2O layer). The open circle and diamonds denote the core temperatures reported by Hauck *et al.* (2006) (S = 10 wt.%) and Bland *et al.* (2008) (S = 1 and 10 wt.%), respectively.

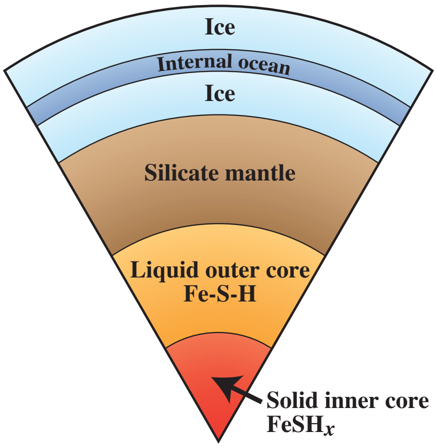

Fig. 4. Schematic figure of the internal structure of Ganymede with Fe–S–H core.

Yuki Shibazaki[a,†,*], Eiji Ohtani[a] and Hidenori Terasaki[b]

[a] Department of Earth and Planetary Material Sciences,
Tohoku University
[b] Department of Earth and Space Science,
Osaka University

*E-mail: yshibazaki@ciw.edu

† Present Address: Geophysical Laboratory,
Carnegie Institution of Washington, USA

References

[1] J.D. Anderson *et al.*: Nature **384** (1996) 541.
[2] S.A. Hauck *et al.*: J. Geophys. Res. 111(2006) doi:10.1029/2005JE002557.
[3] *Y. Shibazaki, E. Ohtani, H. Terasaki, R. Tateyama, T. Sakamaki, T. Tsuchiya, K. Funakoshi: Earth Planet. Sci. Lett.* ***301*** *(2011) 153.*
[4] S. Urakawa *et al.*: Phys. Earth Planet. Inter. **143-144** (2004) 469.
[5] R. Boehler: Earth Planet. Sci. Lett. **111** (1992) 217.

Effect of iron content on electrical conductivity of ferropericlase with implications for the spin transition pressure

The lower mantle constitutes more than 50% of the Earth's volume and plays an important role in the evolution and dynamics of the Earth's interior. The lower mantle is believed to be composed of two main minerals: $MgSiO_3$-rich perovskite (Mg-Pv) and ferropericlase (FP). Since Badro *et al.* [1] experimentally observed the pressure-induced electronic high spin (HS) to low spin (LS) transition of iron in FP under lower mantle conditions, recent experimental and theoretical studies have demonstrated that an electronic HS to LS transition of Fe^{2+} occurs in iron-rich FP at high pressures exceeding 50 GPa. The electronic spin-pairing transition of iron affects many physicochemical properties such as volume, density, incompressibility, optical absorption spectra, sound velocity, electrical conductivity, and Fe-Mg partitioning.

The pressure at which the HS-LS transition occurs would depend on the iron content in FP. Fei *et al.* [2] suggested that the spin transition pressure largely decreases with decreasing iron content in FP, on the basis of the compression curve at room temperature. At the top of the lower mantle, the iron content in FP coexisting with Al-bearing Mg-Pv would be considerably low. Therefore, the accurate determination of the spin transition pressure for iron-poor FP is fundamental in understanding the current mantle structure and mineralogy. However, the low iron content in FP makes it difficult to detect the spin transition because of the weak signal from the electronic state of iron. Electrical conductivity measurement would be a powerful tool for detecting the spin transition pressure of FP as a function of iron content, because electrical conduction in FP occurs through electron hole hopping between ferrous and ferric iron sites. Although high-pressure studies exceeding 30 GPa have been performed using the diamond anvil cell (DAC), the very small sample volume precludes the electrical conductivity measurement of high-resistance materials. In this study [3], the electrical conductivity of FP, $(Mg_{1-x},Fe_x)O$, was measured using the Kawai-type multianvil apparatus (large volume). The recent technical development of high-pressure generation using sintered diamond anvils [4] can allow the accurate electrical conductivity measurement of FP with a lower iron content, because of the use of larger volume samples than in the DAC.

The starting materials were sintered aggregates of FP with various amounts of iron content (x = 0.07, 0.10, 0.13, 0.17, 0.24). The high pressures and high temperatures were generated using a Kawai-type multianvil apparatus with a DIA-type guide block system, SPEED mkII, installed at beamline **BL04B1**. We used sintered diamond cubes with an edge length of 14 mm as a second stage anvil. The anvil truncation was 1.5 mm. The generated pressures were calibrated by *in situ* X-ray diffraction with the Au pressure scale. The cell assembly for the electrical conductivity measurement and X-ray radiography are shown in Fig. 1. One side of the rectangular-shaped sample with a thickness of 0.5 mm was connected to the $W_{97}Re_3$–$W_{75}Re_{25}$ thermocouple and the other side was in contact with a Au electrode electrically connected to the heater through the sintered diamond anvil and guide block. The sample was heated using a pair of TiB_2 sheet heaters. The sample temperature was measured using a thermocouple. Electrical conductivity was measured by a 2-wire method with an alternating current signal with an amplitude of 1 V and a frequency range of 0.1–1 Hz. The samples were once heated to 500 or 600 K and then cooled to room temperature while measuring the conductivity.

All samples examined in this study behaved as a semiconductor. Figure 2 shows the electrical conductivity of FP with various iron contents at 300 K as a function of pressure. At lower pressures, the electrical conductivity of all FP samples increases with increasing pressure. For the FP with higher iron

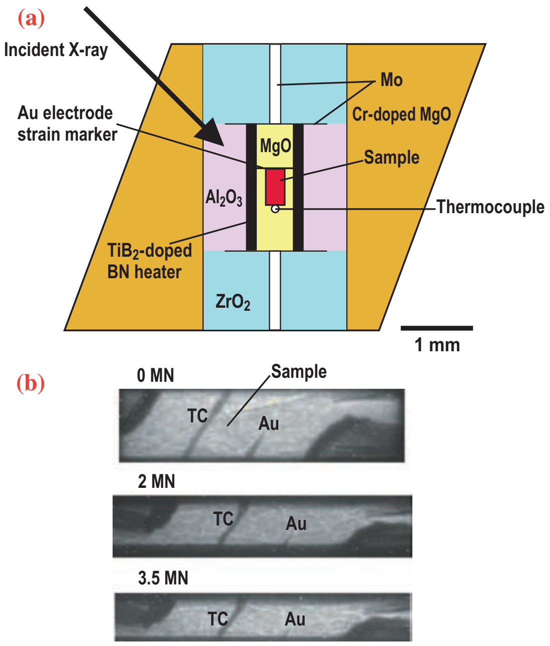

Fig. 1. **(a)** Schematic cross section of the cell assembly used in our experimental runs. **(b)** X-ray radiography images of the sample and the thermocouple through the TiB_2 heater at various press loads (in MN).

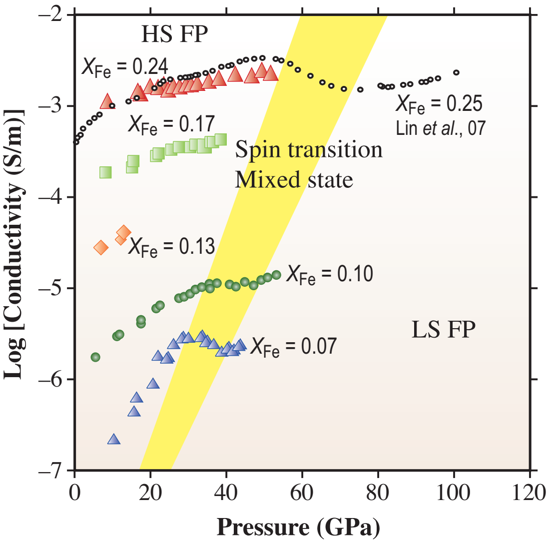

Fig. 2. Electrical conductivities of $(Mg_{1-x},Fe_x)O$ as a function of pressure at a constant temperature of 300 K. At low pressures, the conductivity constantly increases but the conductivity of FP with relatively lower X_{Fe} drops or becomes constant from 30 to 45 GPa. Large symbols denote the data obtained in this study. Small open symbols denote the electrical conductivity of $(Mg_{0.75},Fe_{0.25})O$ obtained from the DAC study.

content (x = 0.17 and 0.24), the electrical conductivity monotonically increases with pressure up to 38 and 53 GPa, respectively. For the FP with lower iron content (x = 0.07 and 0.10), the electrical conductivity slightly decreases or becomes constant with increasing pressure. Further increase in pressure leads to an increase in electrical conductivity. This trend is consistent with that of the electrical conductivity of FP through the HS-LS transition measured at room temperature in the DAC. This conductivity change suggests that the spin transition pressure would decrease with decreasing iron content in FP. FP with lower iron content prefers a smaller ionic radius in the Mg site compared with high-Fe FP. The ionic radius of Fe^{2+} in the HS state is much larger than that of Mg^{2+}, whereas the ionic radius of Fe^{2+} in the LS state is smaller than that of the Mg ion. Therefore, the spin transition of low-Fe FP is likely to occur at lower pressures.

In the present study, we demonstrated that low iron content in FP yields significantly lower spin transition pressure, as shown in Fig. 3. The spin transition of FP affects the nature of Fe-Mg partitioning between Mg-Pv and FP [$K_D = (Fe/Mg)_{Mg\text{-}Pv}/(Fe/Mg)_{FP}$]. Recent laser-heating DAC studies demonstrated a decrease in K_D in San Carlos olivine with a composition of $(Mg_{0.9}Fe_{0.1})_2SiO_4$ from 50 to 100 GPa. For the Al-free system, the iron content (X_{Fe}) in FP coexisting with Mg-Pv is around 0.2. The HS-LS transition in FP should start above 50 GPa. Pyrolite, which is a hypothetical rock composition of the mantle, contains a considerable amount of Al. The effect of alumina on K_D decreases X_{Fe} in FP in association with the incorporation of Fe^{3+} to Pv. On the basis of the present results, the spin transition pressure is expected to be around 35–40 GPa, which is consistent with that at which the K_D determined from rocks with pyrolite composition considerably decreases [5]. Our experimental results suggested that the spin transition in FP occurs at pressures lower than the 50 GPa predicted from FP with high iron content (x > 0.17).

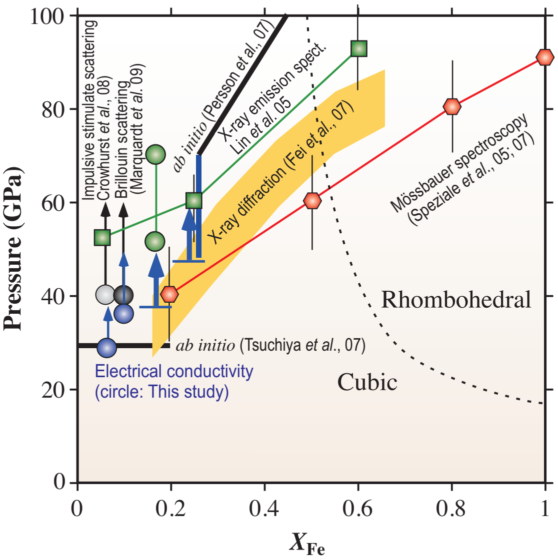

Fig. 3. Spin transition pressures as a function of X_{Fe} in the $(Mg_{1-x},Fe_x)O$ solid solution at 300 K. Blue solid circles indicate the spin transition pressure determined in this study and the arrow represents the mixed spin state. Blue horizontal bars indicate the minimum transition pressure. The other symbols represent the spin transition pressure or crossover predicted by different experimental techniques (modified after [2]).

Takashi Yoshino

Institute for Study of the Earth's Interior,
Okayama University

E-mail: tyoshino@misasa.okayama-u.ac.jp

References

[1] J. Badro *et al*.: Science **300** (2003) 789.
[2] Y. Fei *et al*.: Geophys. Res .Lett. **34** (2007) L17307.
[3] *T. Yoshino, E. Ito, T. Katsura, D. Yamazaki, S. Shan, X. Guo, M. Nishi, Y. Higo, K. Funakoshi: J. Geophys. Res. **116** (2011) B04202.*
[4] E. Ito *et al*.: Earth Planet. Sci. Lett. **293** (2010) 84.
[5] T. Irifune *et al*.: Science **327** (2010) 193.

Phase transition in FeO and its implications for two-layered convection in Earth's outer core

Earth's core resides in the center of our planet and constitutes one-sixth of the planet's volume and one-third of its mass. At a depth of 5150 km, the core is divided into two parts, a solid inner core and a molten outer core (Fig. 1). The Earth's liquid outer core includes substantial amounts of light elements in addition to iron and nickel. As the Earth cools, the solid core grows by crystallizing from the liquid core. The latent heat of fusion and chemical buoyancy arising from the exclusion of light elements from the inner core, which are released at the inner-core boundary, drive the outer core convection responsible for dynamo action and thus the Earth's magnetic field. The existence of oxygen as a light element in the core has been put forward to account for the observed seismic-wave velocities and the density jump at the inner core boundary. The structures of light element-bearing phases in the outer core conditions not only impart density variation, but may also influence the geodynamic processes that are controlled by core convection. Iron monoxide (FeO), the major oxygen-bearing phase, adopts the sodium chloride-type (B1) structure under ambient conditions and the nickel arsenide-type (B8) structure under high pressure [1,2] (Fig. 2); however, phase relations under high-pressure and -temperature (*P*-*T*) conditions of the outer core are unknown.

All the high *P*-*T* experiments were conducted at beamline **BL10XU**. The high *P*-*T* conditions were generated in a laser-heated diamond-anvil cell using double-beveled anvils with a 40 μm culet. We prepared the starting material by mixing the powders of $Fe_{0.96}O$ and metallic iron. The sample mixture was loaded into a hole in a pre-indented rhenium gasket, together with thermal insulation layers of SiO_2 glass. The samples were heated by a couple of 100 W single-mode Yb fiber lasers by the double-side heating technique. The laser-heated spot was ~15 μm in diameter. Temperature was measured by the spectroradiometric method. Angle-dispersive X-ray diffraction (XRD) spectra were collected on a charge coupled device or an imaging plate detector with typical exposure times of 10 s and 3 min, respectively. A monochromatic incident X-ray beam with a wavelength of 0.41388–0.42387 Å was collimated to about a 6-μm area (full-width of half maximum) on the sample.

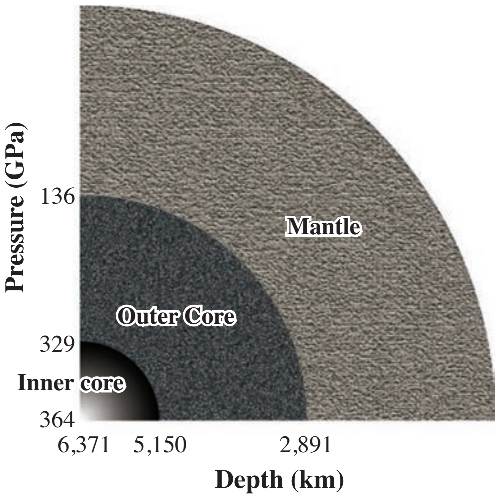

Fig. 1. Cross section of the Earth.

Two separate sets of experiments were conducted at pressures between 227 and 324 GPa and temperatures up to 4880 K [3] (Fig. 2). In the first run, the sample was initially compressed to 266 GPa and subsequently heated. We observed the diffraction peaks only from hexagonal-close-packed (hcp) iron and rhenium before heating and then those from B8 FeO during heating to 2430 K. After a pressure increment at room temperature (Fig. 3(a)) and reheating to 3170 K at 305 GPa, new peaks, which are assigned to 100 and 110 lines of the cesium chloride-type (B2) structure, appeared in the diffraction patterns. During additional heating at 2990 to 4180 K, these B2 peaks became more intense (Fig. 3(b)), indicating the stability of B2 FeO under these *P*-*T* conditions. Similarly, in the second set of experiments, B8 FeO was first synthesized at 287 GPa and 2400 K. The B2 phase appeared with increasing temperature to 4100 K at 311 GPa, whereas the diffraction from the B8 phase became weaker. Additional heating cycles were then performed with decreasing/increasing pressure. Whereas only the broad diffraction peaks from B2 FeO and rhenium (gasket) were found after decompression to ~210 GPa at 300 K, we observed the B8 phase upon heating to 3400 K and subsequently the B1 phase above 3690 K at 230 GPa.

These results indicate that the B2 phase of FeO is stable above 230 GPa along the melting curve (Fig. 2). B1 FeO transforms directly to B2 above 3850 K. The volume change across the B1-B2 transition is 1.9%, on the basis of the volumes of B1, B2, and B8 phases (11.901, 11.679, and 11.815 $Å^3$ per formula unit, respectively) coexisting in the XRD pattern collected at 230 GPa and 3690 K near the triple point. While the B1/B2 phase transition boundary is not tightly constrained in the present experiments, its Clapeyron slope is calculated to be −6.2 MPa/K from those of B1/B8 and B2/B8 boundaries (–50 MPa/K) and the volume differences between these three phases described above. The negative slope of the B1/B2 boundary is consistent with the fact that the nearest Fe–O bond becomes longer and weaker across the transition owing to an increase in the coordination number from six to eight. Since the volume change is relatively small, this results in smaller vibrational frequencies overall and thus higher entropy for the high-pressure B2 phase.

As in crystalline FeO, the structure of liquid FeO would change from a B1- to B2-like arrangement in a comparable or slightly lower pressure range as suggested by previous studies on liquid alkali halides. The oxygen-bearing core liquid would thus change its Fe–O local structure with an increase in the mean coordination number from six to eight at around 240 GPa in the middle of the outer core (Fig. 2). The resulting density increase may be as much as 0.6%, considering the maximum abundance of oxygen in the outer core (~20 atm%). According to the numerical simulations, such a density increase and negative Clapeyron slope of the structural boundary suppress the convection, resulting in two-layered convection in the Earth's outer core [3]. The two-layered structure of core convection offers an alternative explanation for the flux patches that characterize Earth's magnetic field. If flows in the upper and lower layers generate magnetic fields with opposite polarities in isolation, reversed patches may be a manifestation of a two-layer dynamo. Such a situation is possible only if the upper and lower dynamos behave independently as a result of strong stratification. Sudden mixing of the upper and lower regions, induced by magnetic and/or kinematic instabilities, may act as a trigger of geomagnetic polarity reversal, because dipole field collapse and subsequent polarity reversal are probably consequences of vigorous convective mixing of the core fluid.

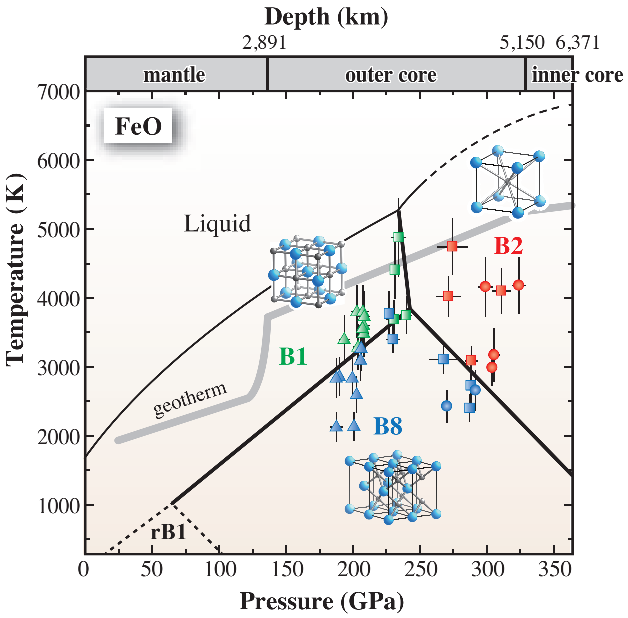

Fig. 2. Phase diagram of FeO. Green, red, and blue symbols represent the stabilities of B1, B2, and B8 structures, respectively. Circles, run 1; squares, run 2; triangles, Ozawa *et al.* [2]. Stability of rhombohedrally distorted B1 (rB1) phase is from Fei and Mao [1]. Melting curve of B1 FeO is from previous experimental work [4]. Crystal structures are also shown: oxygen atoms are represented by blue spheres and iron atoms by gray spheres. The inferred temperature profile inside Earth is shown by gray line.

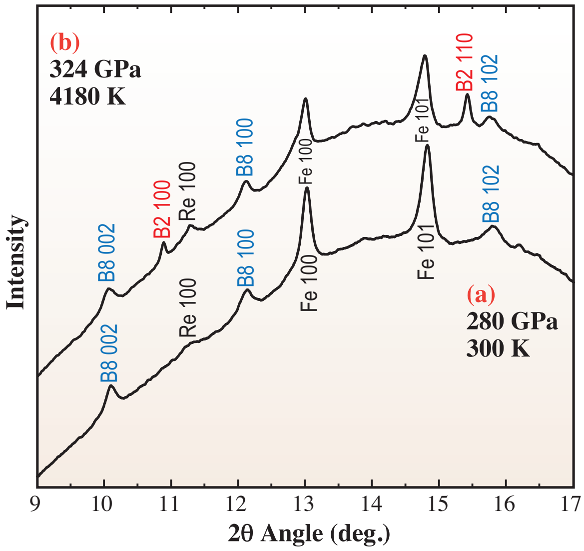

Fig. 3. XRD patterns obtained at **(a)** 280 GPa and 300 K and **(b)** 324 GPa and 4180 K in run 1. Fe, hcp-iron; Re, rhenium (gasket).

Haruka Ozawa[a,b]

[a] Institute for Research on Earth Evolution, Japan Agency for Marine-Earth Science and Technology
[b] Department of Earth and Planetary Sciences, Tokyo Institute of Technology

E-mail: h-ozawa@jamstec.go.jp

References

[1] Y. Fei *et al*.: Science **266** (1994) 1678.
[2] H. Ozawa *et al*.: Phys. Earth Planet. Inter. **179** (2010) 157.
[3] *H. Ozawa, F. Takahashi, K. Hirose, Y. Ohishi, N. Hirao: Science* ***334*** *(2011) 792.*
[4] R.A. Fischer *et al*.: Am. Mineral. **95** (2010) 1473.

Spin crossover and iron-rich silicate melt in the Earth's deep mantle

It is known that iron included in (Mg,Fe)O ferropericlase changes its spin state from low-spin to high-spin at high pressure corresponding to the Earth's lower mantle. Such iron spin crossover has been reported to occur in (Mg,Fe)SiO_3 perovskite as well at a similar pressure range. The change in the spin state of iron strongly affects the partitioning of iron between the coexisting phases.

We have performed X-ray emission spectroscopy measurements on $(Mg_{0.95}Fe_{0.05})SiO_3$ glass at beamline **BL12XU** [1]. The spectra were collected at 300 K in a diamond-anvil cell (DAC) with increasing pressure from 8 to 85 GPa (Fig. 1). At low pressures, the Fe $K\beta$' satellite peak was clearly observed at 7,045 eV, showing high-spin Fe^{2+} in the glass sample. The satellite peak diminished weakly at 59 GPa and vanished at 77 GPa. This indicates a high-spin to low-spin crossover of ferrous iron included in the glass.

In order to evaluate the effect of such iron spin crossover on the partitioning of iron, additional experiments have been performed at beamline **BL10XU** [1]. By using the laser-heated DAC techniques, we melted the $(Mg_{0.89}Fe_{0.11})_2SiO_4$ sample, in which (Mg,Fe)SiO_3 perovskite or post-perovskite coexisted with partial melt. The samples were then recovered from the DAC and examined with a high-resolution field-emission-type electron probe micro-analyzer (FE-EPMA) (Fig. 2). Quenched melt was found at the center of the sample, where the temperature was highest and surrounded by perovskite above 36 GPa, a primary mineral in the Earth's lower mantle. On the basis of the chemical analyses of coexisting quenched melt and perovskite, we have determined the Fe-Mg distribution coefficient $K_D = ([Fe^{Pv}]/[Mg^{Pv}]) / ([Fe^{melt}]/[Mg^{melt}])$ between the two. The results obtained in a pressure range from 36 to 159 GPa are demonstrated in Fig. 3. The K_D values were approximately constant at 0.22-0.29 below 73 GPa. On the other hand, melt composition suddenly became Fe-rich and the K_D dropped to 0.07±0.02 at 76 GPa. It was again almost constant at 0.06-0.08 to 159 GPa.

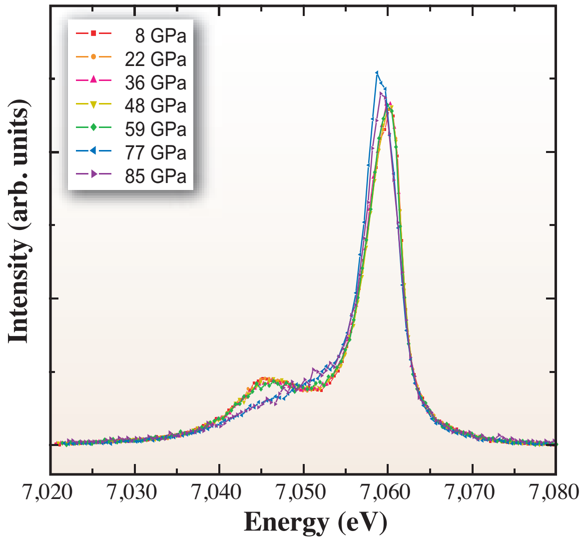

Fig. 1. Evolution of X-ray emission spectra of $(Mg_{0.95}Fe_{0.05})SiO_3$ glass with increasing pressure.

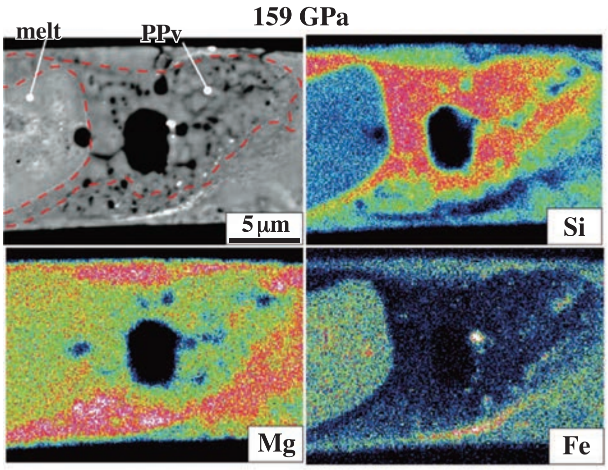

Fig. 2. Backscattered electron images and the X-ray maps for Si, Mg, and Fe for samples recovered from high-pressure melting experiments at 159 GPa. Partial melt is surrounded by post-perovskite (PPv).

The pressure range of the spin crossover observed in our glass matches the pressure where K_D changed dramatically (Fig. 1). Insofar as the glass is a good analogue for the liquid state, a high-spin to low-spin crossover of iron observed in the glass may also occur in melt at a similar pressure range, thus providing an explanation for the measured jump in Fe-enrichment in partial melt (Fig. 3).

A strong change in iron partitioning suggests that partial melt becomes more dense above 76 GPa, corresponding to 1,800-km depth in the Earth's deep mantle. We calculated the density of (Mg,Fe)SiO_3 liquid in equilibrium with $(Mg_{0.92}Fe_{0.08})SiO_3$ perovskite, a typical composition for the Earth's lower mantle, at 4,000 K as a function of pressure (Fig. 4). For simplicity, we used K_D = 0.25 below 75 GPa and K_D = 0.07 at higher pressures. While (Mg,Fe)SiO_3 melt is buoyant compared to any of the typical lower mantle minerals below 75 GPa, it suddenly becomes more dense at higher pressures (at depths greater than 1,800 km). The density difference between the solid mantle and partial melt reaches 8% at the base of the mantle.

Seismological studies show the presence of ultra-low velocity zone at the base of the mantle, suggesting the presence of melt at ~2,900 km depth. The present results indicate that such melt is gravitationally stable. Moreover, in Earth's early history when the mantle was much hotter, a stable melt layer below the solid mantle could be as thick as around 1,000 km [2]. The bottom ~1,000 km layer comprises about 25% of the mantle's mass. Upon cooling, fractional crystallization and sequestering of incompatible heat producing elements (e.g., U, Th) in the melt layer would therefore account for the mass of "missing" chondritic complement of these species expected to be sequestered in a reservoir inside the mantle [3]. The residual liquid now possibly observed as ultra-low velocity zone above the core-mantle boundary may be enriched in such heat producing elements.

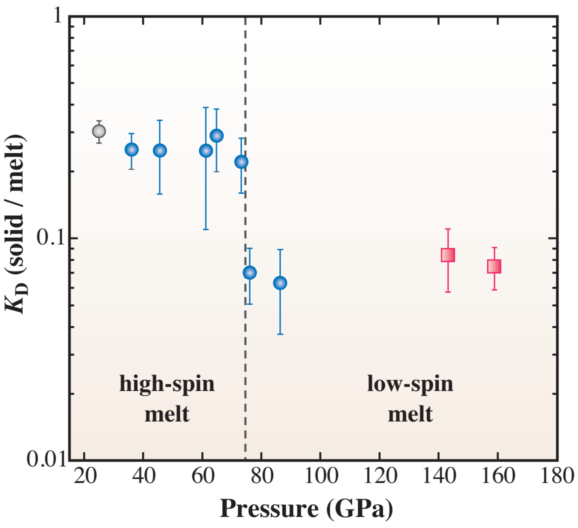

Fig. 3. Change in Fe-Mg distribution coefficient between perovskite and melt.

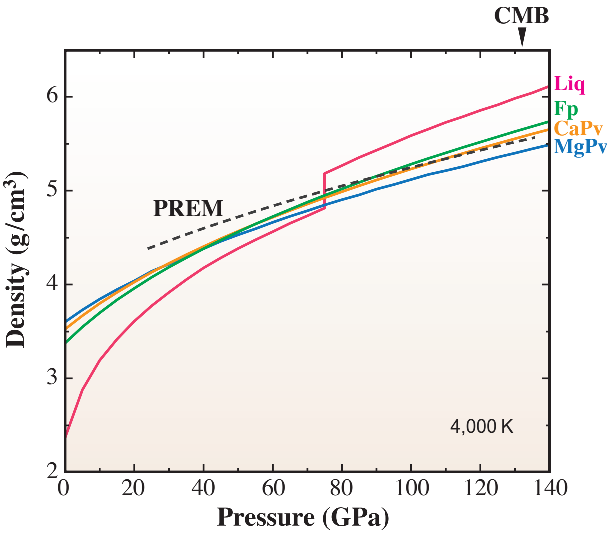

Fig. 4. Density of (Mg,Fe)SiO_3 liquid coexisting with ($Mg_{0.92}Fe_{0.08}$)SiO_3 perovskite is calculated at 4,000 K using newly obtained Fe-Mg partitioning data. Those of ($Mg_{0.86}Fe_{0.14}$) O ferropericlase, Ca-perovskite, and PREM (seismic observation) are also shown for comparison.

Kei Hirose

Department of Earth and Planetary Sciences,
Tokyo Institute of Technology

E-mail: kei@geo.titech.ac.jp

References

[1] *R. Nomura, H. Ozawa, S. Tateno, K. Hirose, J. Hernlund, S. Muto, H. Ishii and N. Hiraoka: Nature* ***473*** *(2011) 199.*
[2] S. Labrosse *et al.*: Nature **450** (2007) 866.
[3] A. Hofmann: Nature **385** (1997) 219.

ENVIRONMENTAL

"Tsuyukusa" - *Asiatic dayflower*

SCIENCE

This section covers various research fields relating to "environment", such as environmental problems and technology, geochemistry, and the analysis of archaeological heritages exposed to the environment for a long time. In many cases, the environmental samples are microscale complex systems, and contain traces of various elements to be investigated. Also, these samples require nondestructive investigation for various reasons, such as they are living specimens or precious samples or there is a risk of chemical change. Thus, analytical techniques using SR X-rays, such as XAFS, XRF, XRD and micro-imaging, are very powerful and useful in environmental research fields.

The first three topics are research on environment problems. The first topic is about the cooling effect on the Earth of anthropogenic aerosols in atmosphere. Takahashi revealed, by XAFS combined with ICP-AES, that almost all oxalate species in aerosols are in the non-hygroscopic form because of the formation of insoluble metal complexes, which inhibit the effect of the aerosol particles as cloud condensation nuclei. Takahashi concludes that reevaluation of the contribution of the aerosols on the Earth's climate is necessary.

The second topic concerns the distribution and behavior of iodine including radioactive iodine, which strongly affects human health, in the environment. Togo *et al*. determined the species of iodine in the soil-water system nondestructively by XAFS and HPLC-ICP-MS for the first time, which provided information that enables the estimation of iodine mobility in the environment.

The third topic is the formation mechanism of toxic chlorinated aromatic compounds (aromatic-Cls) in fly ash. Takaoka *et al*. investigated the role of metal elements during the formation of aromatic-Cls. In this study, they studied the thermochemical behavior of zinc and chloride by investigating the chemical state of zinc chloride at the temperature of aromatic-Cl formation for model and real fly ash samples, by the *in situ* XAFS method.

The fourth topic is the detoxification process of Hg in tissues of striped dolphin. Although Hg might be detoxified by forming HgSe in tissues other than the liver, there has been no solid evidence of the presence of HgSe in these tissues. Nakai *et al*. nondestructively clarified the structure and chemical species of trace Hg in these tissues by combining μ-XRF-XRD and XAFS.

The last topic is an analytical study of archaeological heritages. The identification of wood from archaeological heritages at the genus level provides useful information and new perspectives on the origin of the heritages. Nondestructive microscopy techniques are suited to the investigation of archaeological wood samples, since these samples are often precious, small, and brittle owing to biological attack or degradation over a long time. Sugiyama *et al*. applied X-ray micro-CT imaging to old wood masks made in the 16th century, and showed this technique to be a powerful tool for the identification of archaeological wood.

Tomoya Uruga

Metal complexation inhibits the effect of oxalic acid in aerosols as cloud condensation nuclei (CCN)

Some anthropogenic aerosols, such as organic and sulfate aerosols, have a direct cooling effect by scattering solar radiation and an indirect cooling effect (cloud albedo effect) by acting as cloud condensation nuclei (CCN) because of their hygroscopic properties [1] (Fig. 1). In the report of the Intergovernmental Panel on Climate Change (IPCC) [2], the sum of the direct and indirect cooling effects of aerosols is almost equivalent to the warming effect of carbon dioxide (Fig. 1). However, a large uncertainty exists because of the indirect effect discussed in the IPCC report [2], which must be evaluated more precisely for a better understanding of the Earth's climate. Thus, many studies have been performed on sulfate and organic aerosols because of their complex nature in terms of composition and chemical transformation in the atmosphere, and also because of their importance in the global CCN budget. Among the various organic aerosols studied, water-soluble dicarboxylic acids (DCAs) contribute to the CCN activity, considering that DCAs, which are major constituents of organic aerosols, are hygroscopic [2,3]. Oxalic acid is a major component of DCA and also an important component of identified secondary organic aerosols [3]. In this study, we focused on oxalic acid as a representative component of low-molecular-weight DCAs in the atmosphere. It is possible that oxalic acid can form metal oxalate complexes in aerosols, since polyvalent metal ions can form stable complexes with oxalate ions. However, if the metal oxalate complexes are insoluble, it is possible that the role of oxalic acid as the CCN with the cooling effect can be discounted. Nevertheless, there have been few studies identifying the oxalic acid species, whether noncomplexed oxalic acid or metal oxalate complex, in the atmosphere. Thus, we applied X-ray absorption fine structure (XAFS) spectroscopy, a powerful tool for the speciation of various elements in aerosols [4], to show the presence of metal oxalate complexes in aerosols. In this study, XAFS was employed for calcium (Ca) and zinc (Zn) to demonstrate the presence of their oxalate complexes [5]. Coupled with ion chromatography (IC) and inductively coupled plasma atomic emission spectrometry (ICP-AES) analyses, it was possible to determine the ratio of metal oxalate to noncomplexed oxalate species. The ratio determined can contribute to the precise evaluation of the effects of oxalic acid and other DCAs on the hygroscopicity and CCN activity of aerosol particles.

We measured the Ca and Zn *K*-edge XAFS spectra to characterize Ca and Zn species in aerosols collected at Tsukuba. For Ca, X-ray absorption near-edge structure (XANES) spectra were mainly used for the speciation of Ca in aerosols [4]. For Zn, both XANES and extended X-ray absorption fine structure (EXAFS) spectra were measured at **BL01B1** beamline in SPring-8. Size-fractionated aerosol samples were collected in summer (July-Aug. 2002) and winter (Jan.-Feb. 2003) for this purpose using an impactor aerosol sampler. For example, Zn *K*-edge EXAFS spectra in *k*-space for Zn in aerosols at various particle sizes in summer and winter are shown in Fig. 2. The spectra

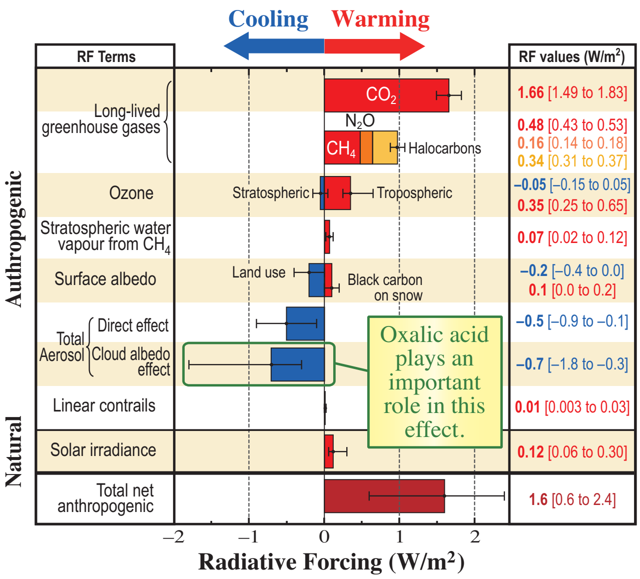

Fig. 1. Radiative forcing (RF) showing the degree of each factor that causes global warming/cooling after 1750 estimated by IPCC (2007).

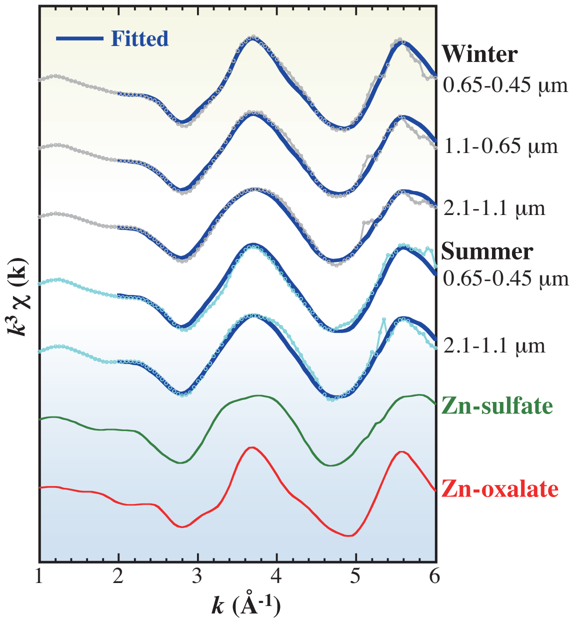

Fig. 2. *K*-edge EXAFS spectra of Zn in aerosols at various particle sizes in summer (July-Aug. 2002) and winter (Jan.-Feb. 2003), Zn sulfate, and Zn oxalate.

can be well fitted by those of Zn sulfate and Zn oxalate, which are possible species for these particle sizes, considering the relatively large amounts of total Zn, sulfate, and oxalate species compared with those in larger particle size fractions. The successful fitting provides us the ratio of metal oxalate to noncomplexed oxalate species. Based on the calculation considering the total amounts of oxalate, Ca, and Zn determined by IC and ICP-AES coupled with the Ca- and Zn-oxalate fractions determined by XAFS, it was found that 10–60% and 20–100% of the total Ca and Zn in the finer particles (<2.1 μm) were present as Ca- and Zn-oxalate complexes, respectively (Fig. 3). Considering other metal ions abundant in aerosols that can form stable oxalate complexes such as Cu^{2+} and Pb^{2+}, it is likely that almost all oxalate species are in the form of insoluble metal complexes.

Oxalic acid is hygroscopic and can thus increase the CCN activity of aerosol particles, while complexes with various polyvalent metal ions such as Ca and Zn are not hygroscopic; thus, they cannot contribute to the increase in the CCN activity of aerosols (Fig. 3). Therefore, the contribution of oxalic acid to the hygroscopicity of aerosol particles must have been overestimated. Thus, the present study suggests the reevaluation of the contribution of oxalic acid to the CCN activity of aerosols. Similar to oxalic acid, other dicarboxylic acids in the atmosphere, such as malonic and succinic acids, can also transform to metal complexes in aerosols. Therefore, in discussing the hygroscopicity and related effects of organic aerosols, it is necessary to evaluate the contribution of the complexation of dicarboxylic acids with metal ions.

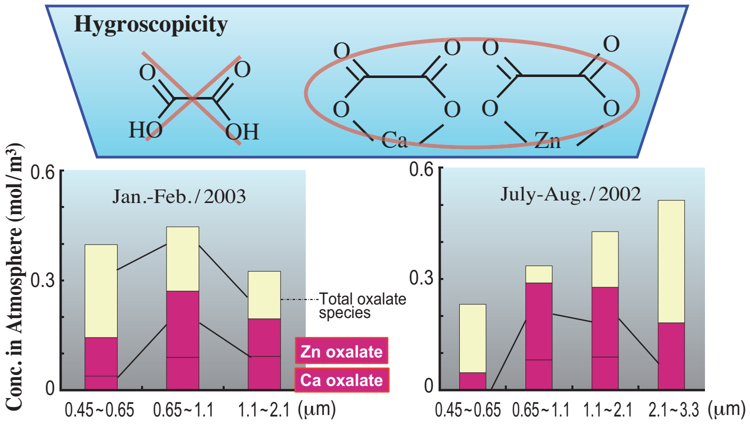

Fig. 3. Ca- and Zn-oxalate fractions relative to total oxalate species in aerosols with schematics of hygroscopicities of various oxalate species.

Yoshio Takahashi

Department of Earth and Planetary Systems Science,
Hiroshima University

E-mail: ytakaha@hiroshima-u.ac.jp

References

[1] M. Kanakidou *et al*.: Atmos. Chem. Phys. **5** (2005) 1053.
[2] IPCC Climate Change 2007: Synthesis Report, the Intergovernmental Panel on Climate Change, Cambridge University Press, UK, 2007.
[3] K. Kawamura and K. Ikushima: Environ. Sci. Technol. **27** (1993) 2227.
[4] Y. Takahashi *et al*.: Environ. Sci. Technol. **43** (2009) 6535.
[5] *T. Furukawa and Y. Takahashi: Atmos. Chem. Phys.* ***11*** *(2011) 4289.*

Speciation of iodine in soil-water system based on XANES and HPLC-ICP-MS

In 2011, the Fukushima Daiichi Nuclear Power Plant released radioactive iodine to wide areas in Japan (^{131}I and ^{129}I, half-lives = 8 days and 1.57×10^7 years, respectively). Since radioactive iodine can strongly affect human health, an urgent investigation of the distribution and behavior of radioactive iodine is required. However, the estimation of iodine behavior is difficult because of its different mobility among their possible species in the environment [1]. In soil-water systems, possible iodine species are iodide (I^-), iodate (IO_3^-), molecular iodine (I_2), and organic iodine species [1,2]. Iodine speciation in soils is occasionally investigated by sequential extraction. This method is practically an effective speciation method for a sample with low iodine concentration. However, the sequential extraction approach is associated with some uncertainties caused by readsorption in the remaining solid during the experimental procedure, cross-contamination, incomplete digestion and release of organic iodine, and transformation of chemical forms during the sequential extraction, especially in a strong acid/base solution [1]. In this study, we investigated iodine speciation in a natural soil-water system by nondestructive analysis, X-ray absorption near-edge structure (XANES) and high-performance liquid chromatography combined with inductively coupled plasma mass spectrometry (HPLC-ICP-MS).

Soil and pore water samples were collected around the Yoro hot springs, Chiba, Japan, at various depths (0, 3, 6, 9, and 12 cm). Brine water from the hot springs is associated with natural methane gas and contains a large amount of iodine. The sampling sites consisted of (i) soil under flooded conditions with the water layer several centimeters above soil surface and (ii) brine water from the tube well containing iodine as I^- at a concentration of 5.8 mg/L.

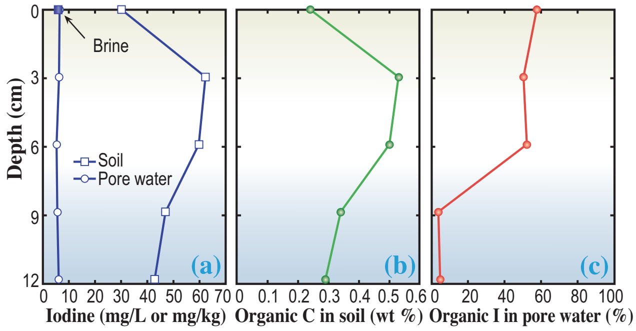

Fig. 1. Vertical profiles of **(a)** iodine concentrations in soil (□), pore water (○) and brine water (■); **(b)** organic carbon contents in soil; **(c)** organic iodine fraction in pore water.

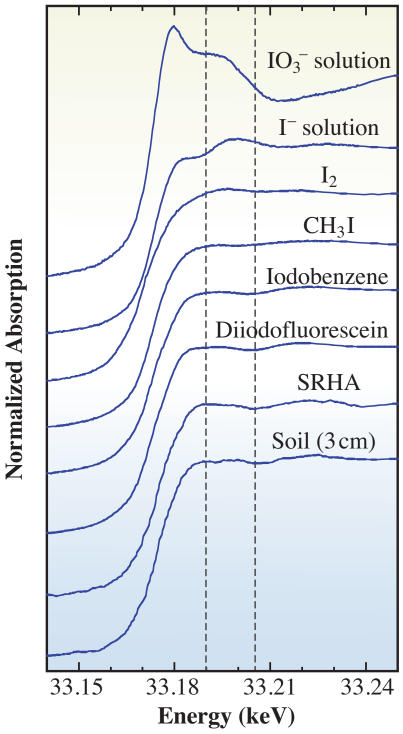

Fig. 2. XANES spectra of standard materials and soil sample collected at 3 cm depth (SRHA: Suwannee River humic acid).

Iodine concentration in soil (Fig. 1(a)) is highly correlated with the organic carbon content (Fig. 1(b)). The correlation coefficients (R^2) of iodine with iron, manganese, and organic carbon are 0.04, 0.01, and 0.95, respectively. Therefore, it is suggested that iodine immobilization in soil is strongly influenced by natural organic matter. Iodine species in soil were determined by iodine *K*-edge XANES, measured at beamline **BL01B1** (Fig. 2) [3]. XANES spectra of iodobenzene, diiodofluorescein, and Suwannee River humic acid (SRHA) showed a concave curve around 33.205 keV and a moderate peak around 33.190 keV. These two structures are useful characteristic features for distinguishing organic iodine from its inorganic forms. According to the fitting of the spectra by the linear combination of organic iodine (humic substances, diiodofluorescein, or iodobenzene) and inorganic iodine (KI or I^- solution), iodine in soil was mainly found to be in organic iodine form.

To describe the host phase for iodine in soil, iodine mapping in soil particles on the micrometer scale was performed by micro-XRF analysis using the iodine $K\alpha$-line (28.6 keV) irradiated at 35 keV, a high X-ray energy region that can be excited by the third-generation synchrotron radiation facility (**BL37XU**). The air-dried soil sample collected at a 3 cm depth was embedded in a high-purity epoxy resin and polished to create a thin section of about 50 μm. X-rays from the undulator were monochromatized using a Si(111) double crystal and focused to 1.5×1.5 μm². Among the various soil particles examined, Fe-rich minerals coated with organic matter and clay minerals contained a large amount of iodine (Fig. 3). A comparison of iodine, Fe, Al, and C mapping results revealed that iodine concentration in organic matter rich areas is higher than that in Fe-rich and clay-rich areas. This result is consistent with the bulk speciation by XANES, illustrating the dominance of organic iodine species.

To determine the chemical reaction of iodine between soil and pore water, iodine speciation in pore water is also necessary. Iodine species in pore water were investigated by HPLC-ICP-MS with anion exchange and size exclusion columns for the separation of (i) I^- and IO_3^-, and (ii) inorganic and organic iodine species, respectively. Pore water collected at a 0–6 cm depth contained 50%–60% of organic iodine bound to dissolved organic matter, with I^- as the other species (Fig. 1(c)). At a 9–12 cm depth, 98% of iodine was in the form of dissolved I^-. According to soil incubation experiments using soil collected at a 3 cm depth, the dissociation of I^- from organic matter occurs under anoxic conditions (data not shown), which is consistent with the observation in the natural soil-water system.

In this study, species of iodine in both soil and pore water were determined. Using these results, the ratios of I^- and organic iodine concentration between soil and pore water (K_d = [iodine in soil]/[iodine in pore water]) was calculated at various depths. Results show that iodide is distributed in the solution more than 10-fold greater than organic iodine species. The transformation of inorganic iodine to organic iodine plays an important role in iodine immobilization, especially in a surface soil-water system (Fig. 4).

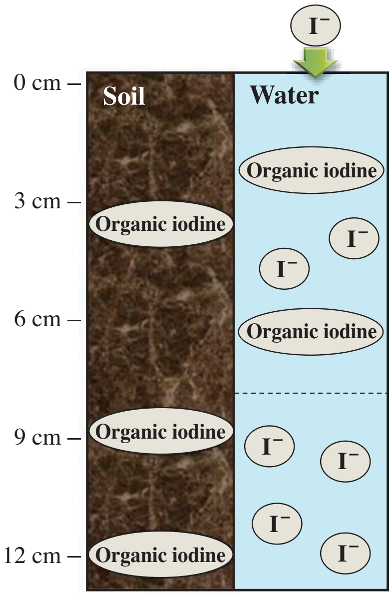

Fig. 4. Schematic of iodine species in soil-water system at Yoro area.

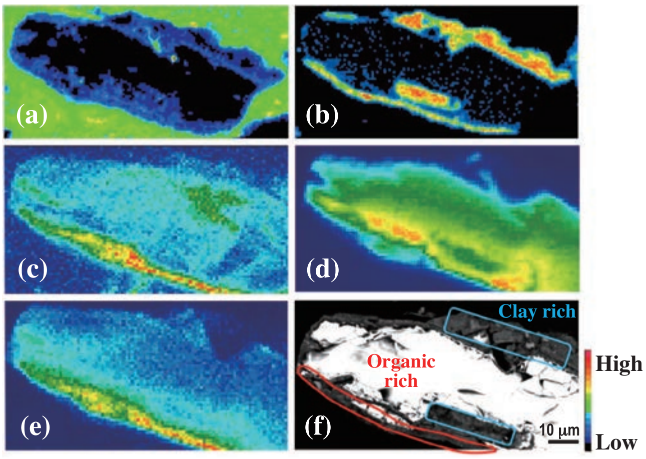

Fig. 3. **(a)** Carbon mapping, **(b)** aluminum mapping, **(c)** iodine mapping, **(d)** iron mapping, **(e)** zinc mapping, and **(f)** backscattered electron image for clay and organic matter-rich areas. **(a)**, **(b)**, **(f)**: obtained by EPMA analysis. **(c)**–**(e)**: obtained by micro-XRF analysis at BL37XU.

Yoko S. Togo[a,*], Yoshio Takahashi[b] and Yasuko Terada[c]

[a] Institute of Geology and Geoinformation, National Institute of Advanced Industrial Science and Technology (AIST)
[b] Department of Earth and Planetary Systems Science, Hiroshima University
[c] SPring-8/JASRI

*E-mail: yoko-togo@aist.go.jp

References

[1] X. Hou *et al*.: Anal. Chim. Acta **632** (2009) 181.
[2] H. Yamada *et al*.: Soil Sci. Plant Nutr. **45** (1999) 563.
[3] Y.S. Shimamoto and Y. Takahashi: Anal. Sci. **24** (2008) 405.
[4] *Y.S. Shimamoto, Y. Takahashi and Y. Terada: Environ. Sci. Technol.* ***45*** *(2011) 2086.*

Chlorinated aromatics in municipal-solid-waste fly ash inhibited by thermochemical zinc behavior

Zinc is a major heavy metal produced anthropogenically in solid-phase compounds such as municipal solid waste (MSW) fly ash. Researchers have reported that the zinc content in fly ash correlated positively with the concentrations of toxic chlorinated aromatic compounds (aromatic-Cls), such as polychlorinated dibenzo-p-dioxins (PCDDs), furans (PCDFs), biphenyls (PCBs), and benzenes (CBzs). During postcombustion, zinc was considered to be generated as zinc chloride ($ZnCl_2$) or an oxidelike compound [1]. Zinc oxide (ZnO) and $ZnCl_2$ showed a weak thermal catalytic activity in aromatic-Cl formation via particulate carbon [2]. However, we cannot conclude that Zn compounds promote aromatic-Cl formation because real systems are more complex than such models. In fact, Hinton and Lane reported data that refuted such a conclusion [3]. They studied the catalytic behavior of zinc using zinc compounds added to real fly ash. When zinc nitrate was added, high concentrations of PCDDs were generated. However, PCDD concentration decreased with the addition of both zinc nitrate and copper nitrate. Their results suggested that zinc nitrate acted as an inhibitor when zinc coexisted with stronger metal promoters in real fly ash. In our previous study [4], to determine whether zinc acts as a promoter, we performed systematic quantitative X-ray spectroscopic experiments under coexistent conditions with $ZnCl_2$ at the temperature of aromatic-Cl formation.

Real fly ash (RFA) samples obtained from municipal solid waste incinerators (MSWIs) were used to determine the major chemical forms and thermal behavior of zinc. We prepared model fly ash (MFA) to understand the thermochemical interaction between zinc and metal chlorides ($CuCl_2$ and $FeCl_3$). Gas chromatography/mass spectrometry (GC/MS) experiments provided quantitative information on aromatic-Cls [2]. The thermochemical states of zinc and chlorine were determined by X-ray absorption fine structure (XAFS) at beamline **BL01B1** in SPring-8 and Photon Factory, respectively. During Zn *K*-edge XAFS measurement, the sample disk was heated from room temperature to 300°C and 400°C in a T-type *in situ* cell [5] under a flow of 10% oxygen/90% nitrogen delivered at 50 mL/min. Surface analysis by X-ray photoelectron spectroscopy (XPS) revealed a characteristic zinc behavior in the solid phase. We discuss the coexistent-specific effects of zinc on the basis of our results.

The nearest-neighbor elements of zinc in RFAs were chlorine or oxygen, according to the peak positions of Zn *K*-edge Fourier-transformed extended XAFS (EXAFS) spectra. We previously reported that ZnO had zero or negative potential to promote the thermochemical formation of aromatic-Cls [2]. In the present study, we used $ZnCl_2$ as a promoter to generate aromatic-Cls. We found that the coexistence of zinc with other trace metals ($CuCl_2$ and $FeCl_3$) was more effective for aromatic-Cl formation than zinc alone. When zinc chloride coexisted with cupric or ferric chloride, the concentrations of ΣCBzs (ΣPCBs) were inhibited to 54% (92%) or 33% (52%), compared with those of MFA added $CuCl_2$ or $FeCl_3$, respectively. T4- and P5-chlorobenzenes showed a higher inhibitory effect, greater than 75% ($ZnCl_2$+$CuCl_2$) and 47% ($ZnCl_2$+$FeCl_3$), than other congeners (Fig. 1(a)). Inhibitory effects greater than 92% and 64% were observed for PCBs from P5 to O8 in the $ZnCl_2$+$CuCl_2$ model and from H6 to O8 in the $ZnCl_2$+$FeCl_3$ model, respectively (Fig. 1(b)). Figure 1 shows visually that zinc chloride inhibited the generation of PCBs (two aromatic rings) at higher rates than CBzs (one ring) owing to coexistence, indicating that the bridged structure of the aromatic ring did not form readily.

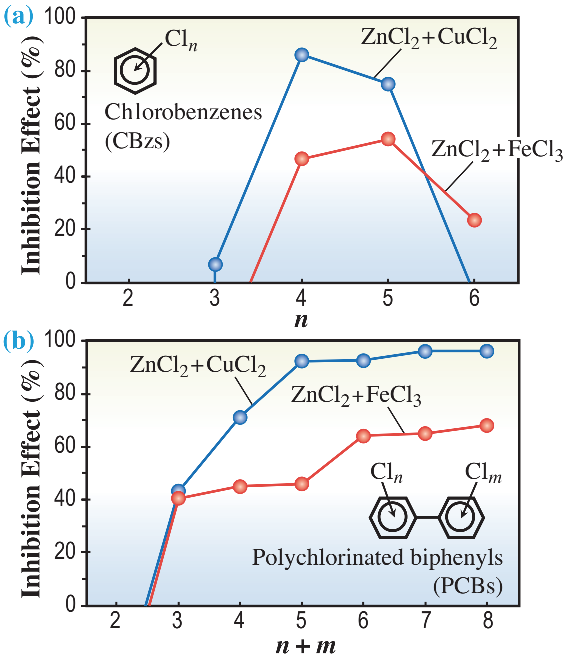

Fig. 1. Inhibition effects of **(a)** chlorobenzenes (CBzs) and **(b)** polychlorinated biphenyls (PCBs) after heating model fly ash at 300°C under coexistent conditions of zinc chloride ($ZnCl_2$) with other metal promoters such as $CuCl_2$ and $FeCl_3$.

We studied the chemical state of zinc chloride at the temperature of aromatic-Cl formation to understand the thermochemical behavior of zinc. Zn *K*-edge EXAFS analysis (Fig. 2) using a model and real fly ash confirmed that the thermochemical state of zinc chloride changed slightly and was thermally stable (i.e., no energy shift of the peak position) at ~300°C, the temperature at which the maximum aromatic-Cl formation occurs in real fly ash. Although Zn-Cl bonding was stable in the complex solid phase, we observed an unstable chlorine behavior with coexisting strong promoters by Cl *K*-edge near-edge XAFS (NEXAFS) analysis. By comparing the spectrum of the $ZnCl_2$+$CuCl_2$ model sample with the theoretical linear combination spectrum Calc($ZnCl_2$+$CuCl_2$), a low-temperature transition of chlorine to the gas phase (low-Cl(g)) with $CuCl_2$ was found to occur (**a**, in Fig. 3(a)) and aromatic-Cl formation was also found to be inhibited at 300°C (**b**, in Fig. 3(a)). In addition, under the coexistent conditions ($ZnCl_2$+$CuCl_2$), XPS analysis results for the near-surface concentrations of Zn (Fig. 3(b)) and Cl (no figure) indicated a weak reactivity between the catalysts and the carbon matrix. $FeCl_3$ also showed a similar behavior to $CuCl_2$ when coexisting with $ZnCl_2$. From these findings, we suggest the importance of studying a "coexistent complex system" to understand the interaction between trace metals and aromatic-Cls in a real thermal solid phase such as MSW fly ash.

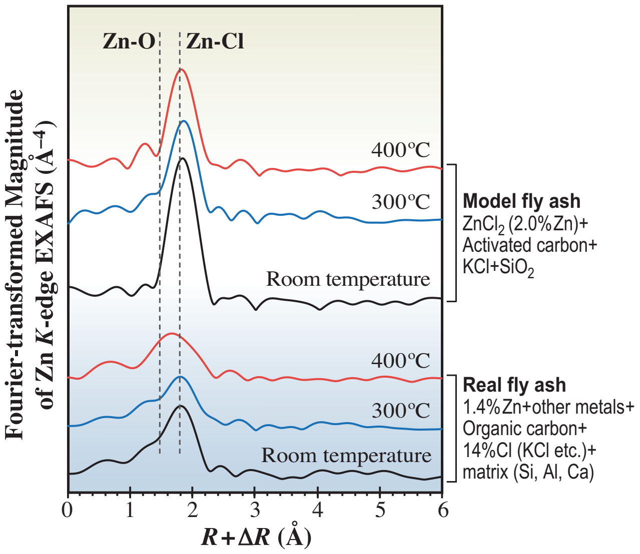

Fig. 2. *In situ* Fourier-transformed k^3-weighted Zn *K*-edge extended X-ray absorption fine structure (EXAFS). Real and model fly ashes admixed with zinc chloride at room temperature, 300°C, and 400°C.

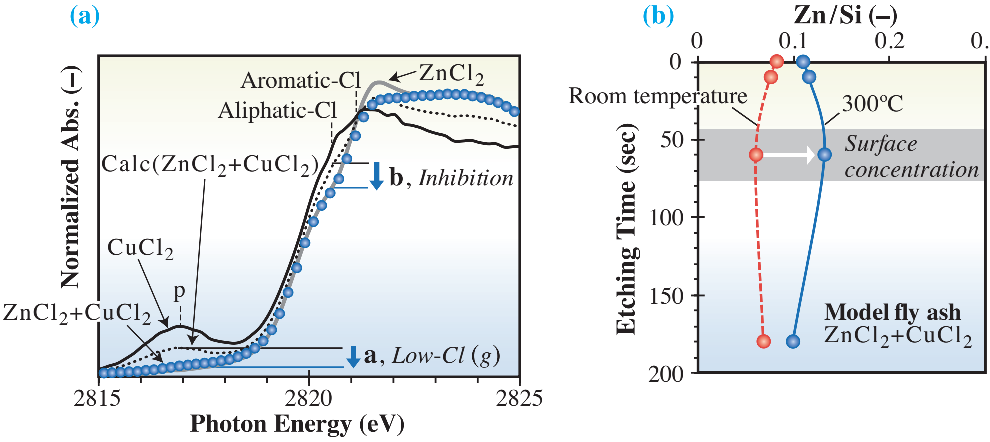

Fig. 3. **(a)** Cl *K*-edge near-edge X-ray absorption fine structure (NEXAFS) for three model fly ashes ($ZnCl_2$, $CuCl_2$, and $ZnCl_2$+$CuCl_2$) after heating at 300°C and theoretical linear combination spectrum of two models ($ZnCl_2$ and $CuCl_2$), Calc($ZnCl_2$+$CuCl_2$). **(b)** Near surface concentration of zinc measured by in-depth X-ray photoelectron spectroscopy (XPS).

Takashi Fujimori[a,b,*] and Masaki Takaoka[a]

[a] Department of Environmental Engineering,
Kyoto University
[b] Center for Material Cycles and Waste Management Res.,
National Institute for Environmental Studies (NIES)

*E-mail: fujimori.takashi.3e@kyoto-u.ac.jp

References

[1] R.P.W. Struis *et al.*: Environ. Sci. Technol. **38** (2004) 3760.
[2] T. Fujimori *et al.*: Environ. Sci. Technol. **43** (2009) 8053.
[3] W.S. Hinton and A.M. Lane: Chemosphere **25** (1992) 811.
[4] *T. Fujimori, Y. Tanino and M. Takaoka: Environ. Sci. Technol.* ***45*** *(2011) 7678.*
[5] M. Takaoka *et al.*: Environ. Sci. Technol. **39** (2005) 5878.

Presence of HgSe (tiemannite) in various tissues of the striped dolphin: evidence obtained by μ-XRF-XRD and XAFS analyses

Marine mammals accumulate mercury (Hg) in their tissues at a high concentration (up to > 10,000 μg/g dry weight) because of their high position in the marine food chain and their long lifespan [1,2]. In spite of the high concentration, no indication of Hg intoxication has been reported for marine mammals, and thus they seem to have the ability to tolerate high Hg concentrations. Many researchers have assumed that methyl Hg taken up from the diet should be demethylated to inorganic Hg and that the resultant inorganic Hg forms an equimolar HgSe compound (mineral name: tiemannite) mainly in the liver of marine mammals. Although Se might detoxify Hg by forming HgSe in tissues other than liver, very few studies have focused on HgSe in tissues other than the liver of marine mammal and no solid evidence as to the presence of HgSe has been reported. Could tiemannite be formed in the tissues of the striped dolphin other than liver? Thus, we explored HgSe granules in various tissues of the striped dolphin and tried to identify their chemical form nondestructively by utilizing a combined analytical system, μ-XRF-XRD and XAFS[3].

Seven tissues (liver, muscle, kidney, brain, lung, pancreas, and spleen) of the striped dolphin (*Stenella coeruleoalba*) were used in the present study. These samples were collected from a male striped dolphin stranded along the coast of Ehime Prefecture, Japan. For μ-XRF-XRD analysis, the tissues were embedded in OCT compound and cut into 25 μm frozen sections using a cryomicrotome.

The SR-μ-XRF-XRD analysis was carried out at beamline **BL37XU**. The monochromatic X-ray beam was focused by Fresnel zone plate (FZP) optics through an order-selecting aperture (OSA) onto a spot of 1.5 (V) × 1.5 (H) μm^2 in the sample. μ-XRD data were collected using the Deby Sherrer mode with an imaging plate (IP) placed behind the sample. The energy of incident X-rays was set to 15 keV (λ = 0.827 Å). The Hg-L_2-XAFS analysis for the non-extractable fraction from the nuclear and mitochondrial fraction of each tissue was also carried out at beamline **BL01B1** in the fluorescence mode by using a 19-element Ge solid state detector. The local structure of Hg was examined by analyzing XAFS data to determine whether Hg is detoxified by forming HgSe in tissues other than the liver of the dolphin.

The 2D elemental maps shown in Fig. 1 were obtained by μ-XRF imaging using an X-ray microbeam (13.4 keV). The normalized X-ray fluorescence intensities are scaled from red (maximum) to blue (minimum). Figure 1 shows the clear positive correlation between the distributions of Hg and Se, and this suggests that Hg forms a compound together with Se in these tissues. It seems that the concentrated points of Hg and Se in the liver and spleen also correspond well to the black granules (5 to 10 μm) in the optical micrograph given on the left side of Fig. 1.

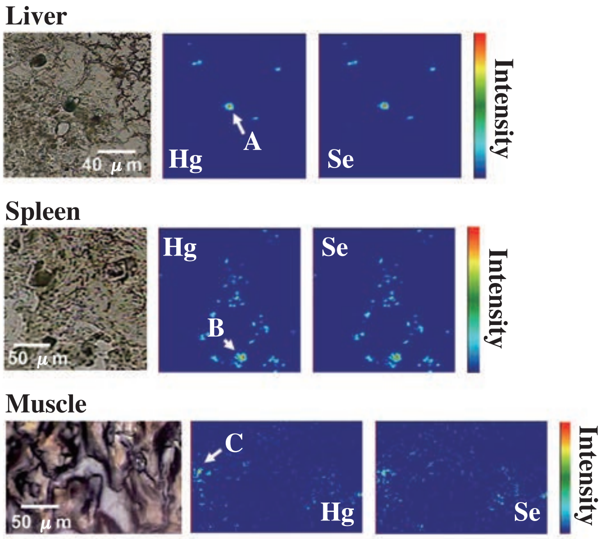

Fig. 1. Micrographs and 2D elemental maps of the liver, spleen and muscle of the striped dolphin. Pixel numbers: 100 (V) × 100 (H), 130 (V) × 130 (H), and 78 (V) × 120 (H) for liver, spleen, and muscle tissues, respectively.

The thin section samples were then subjected to μ-XRD analysis to identify the black granular materials. The XRD patterns were obtained for point A in the liver and point B in the spleen, as shown in Fig. 2. The smooth diffraction rings detected suggest that the biominerals are polycrystalline. The powder diffraction data are shown in Table 1 together with the reference PDF data of tiemannite. The diffraction data measured at points A and B were consistent with those of HgSe (tiemannite), confirming that the granules found in the liver and spleen sections were composed of HgSe

Table 1. A comparison of the diffraction data of point A (liver) and B (spleen) with that of HgSe

Point A (Liver)		Point B (Spleen)		HgSe; tiemannite ^{a}		
d (Å)	*I*	*d* (Å)	*I*	*d* (Å)	*I*	*hkl*
3.46	100	3.51	100	3.51	100	111
3.02	19			3.04	16	200
2.13	54	2.14	46	2.15	50	220
1.82	28	1.83	31	1.84	30	311

Relative intensity (*I*) is given in *hkl*: the indices of reflection.
^{a} PDF file No. 08-0469.

(tiemannite). This is the first clear evidence of the presence of crystalline HgSe (tiemannite) in the spleen other than the liver. These results strongly suggest that Hg is also detoxified by forming HgSe in tissues other than the liver of the striped dolphin.

After the trypsin digestion of the non-extractable fraction from the nuclear and mitochondrial fraction, XAFS analysis was conducted to examine the chemical state of Hg in the seven tissues of the striped dolphin. The Hg L_2-edge XANES spectra of the tissues are shown in Figs. 3(a)–3(g), together with that of the reference samples for mercury compounds. It is found that all of the tissues of the striped dolphin showed similar XANES spectra, suggesting similar local structures around the Hg atoms in these samples. From the chemical shift, Hg was found to be present in the Hg(II) state in these tissues. Also, because of the similarity between the XANES spectra of the dolphin samples and that of the HgSe (tiemannite), the local structures around Hg atoms in the former samples seems to be the most similar to those of HgSe.

We then attempted to obtain the structural parameters for mercury-containing compounds in these tissues by EXAFS analysis. The fitting was conducted for the first strongest peak in the Fourier transform data of the k^3-weighted $\chi(k)$ values for Hg. The coordination numbers and bond lengths for the tissue samples and HgSe were calculated. For all the tissues examined, the Hg-Se bond length and the coordination number were similar (*ca.* 2.6 Å and *ca.* 4, respectively), and these values are consistent with those of tiemannite HgSe (2.63 Å and 4.0, respectively) confirming the presence of crystalline HgSe in the seven tissues.

The present results reinforce the importance of the detoxification role of Se in tissues other than the liver of marine mammals. The biosynthesis and storage of mercury selenide were mainly associated with the liver, but it was not exclusive to the liver. SR-μ-XRF-XRD measurement enables direct analysis of a biomineral at a high spatial resolution. The combination of these techniques would provide information valuable for determining other metal detoxification mechanisms and biomineralization processes in environmental samples [4].

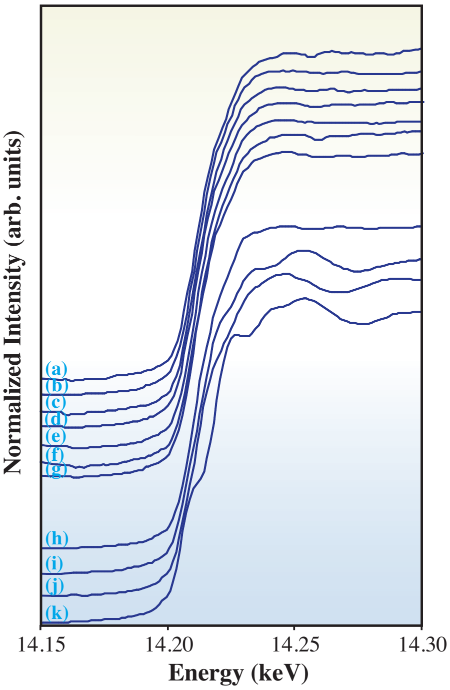

Fig. 3. Normalized Hg L_2-edge XANES spectra of the striped dolphin samples and the reference materials. **(a)** Brain, **(b)** muscle, **(c)** pancreas, **(d)** spleen, **(e)** lung, **(f)** kidney, **(g)** liver, **(h)** HgSe (tiemannite), **(i)** HgS (cinnabar), **(j)** *m*-HgS (metacinnabar), and **(k)** HgO.

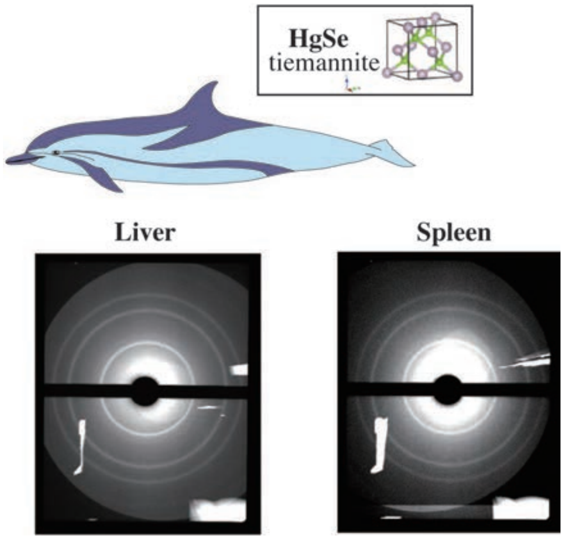

Fig. 2. μ-XRD patterns measured at point A in the liver and point B in the spleen as shown in Fig. 1.

Izumi Nakai[a,*], Yasuko Terada[b] and Akiko Hokura[c]

[a] Department of Applied Chemistry,
Tokyo University of Science
[b] SPring-8/JASRI
[c] Department of Green and Sustainable Chemistry,
Tokyo Denki University

*E-mail: inakai@rs.kagu.tus.ac.jp

References

[1] C. Leonzio *et al.*: Sci. Total Environ. **119** (1992) 77.
[2] T.J. O'Shea: Environmental contaminants and marine mammals. In Biology of Marine Mammals; Eds. By J.E. III. Reynolds, S.A. Rommel, Smithsonian Inst. Press, Washington, 1999; pp 485.
[3] *E. Nakazawa, T. Ikemoto, A. Hokura, Y. Terada, T. Kunito, S. Tanabe and I. Nakai: Metallomics* **3** *(2011) 719.*
[4] S. Endo *et al.*: Environ. Sci. Tech. **42** (2008) 7152.

Identification of wood of archaeological heritages by X-ray micro-CT imaging

The identification of wood of archaeological heritages has provided useful information on the origin of the heritages and sometimes provided a new perspective. Wood identification at the genus level requires the observation of microscopic faces from 3 directions, namely, the transverse, radial, and tangential directions. One method involves using a razor blade for making a thin slice from the wood blocks and then preparing microscopy specimens for the 3 directions. Nevertheless, this method becomes routine after training and experience, but it is not applicable to cases in which only a very small sample is available as is always the case for wood works or artifacts of national heritage class. Furthermore, wood samples are often too brittle to use for microscopy preparations owing to biological attack or degradation. In this study, therefore, synchrotron X-ray micro-tomography, which enables the nondestructive investigation of 3D microstructures was applied [1]. Synchrotron X-ray micro-CT imaging at **BL20XU** provides a resolution of 0.5 μm, which sufficient for visualizing most of the species-specific anatomical features necessary for the identification of wood. We describe an example of applications of this technique to the investigation of a wooden mask below.

In 2008, an old wooden mask shown in Fig. 1 was discovered at Yatsushiro City, Kumamoto Prefecture, Japan. This mask has been handed down from the end of the 16th century; a Japanese soldier brought it from the Korean Peninsula during the war between Japan and Korea in the 16th century.

According to the ancient book named "Higokokushi," written in the middle of the 18th century, a Japanese farmer went to the Korean Peninsula as a soldier with Yukinaga Konishi in the 16th century, and after the war, he brought a large mask to Kumamoto Prefecture. Later, when it was discovered, it was suspected that this mask could be a proof of the historical interaction between Korea and Japan. It is known that the Korean people would hold masquerade parties in ancient times. However, only a few old wooden masks are conserved because masks were allegedly burnt after the ceremony. The most famous masks in Korea are the Hahoe masks: 11 Hahoe masks of the Korai era (around the 14th century) have been conserved in the Hahoe village. They were all registered as national treasures in 1964 and are currently kept by the National Central Museum in Korea. According to Park (2005) [2], all the Hahoe masks were made of Hannoki (*Alnus* sp.), and this wood selection is obviously different from

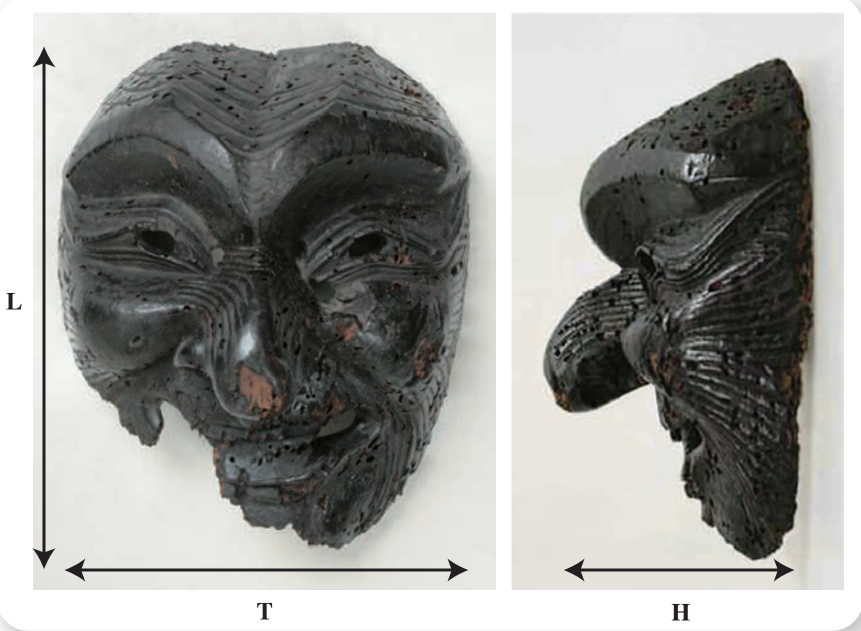

Fig. 1. Old wooden mask discovered at Yatsushiro City, Kumamoto, Japan. It was painted with black lacquer and its size is 25.6(L) × 21.0(T) × 14.0(H) cm^3. The mask has been totally deteriorated by insects and especially the right part of the chin has been damaged seriously. Courtesy of Yatsushiro Municipal Museum.

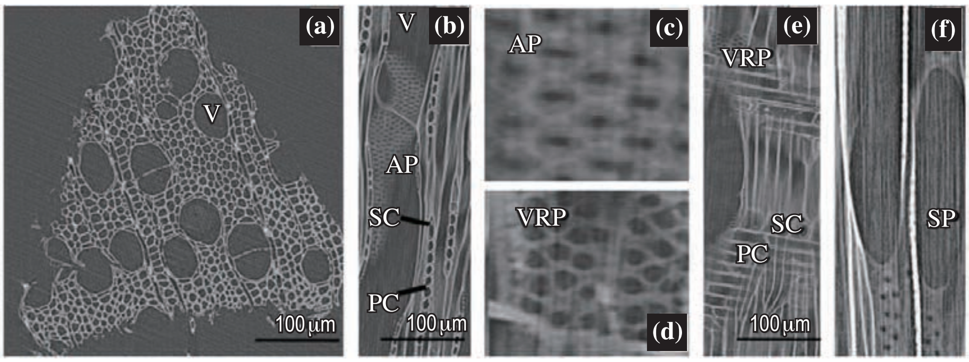

Fig. 2. Pseudo-sections constructed from synchrotron X-ray microtomography dataset of SPring-8: cross section **(a)**, tangential section **(b)**, magnified area of the alternate pitting **(c)**, vessel-ray pitting **(d)**, radial section **(e)**, and simple perforation **(f)**. Note that V: vessel, SC: square cell, SP: simple perforation, PC: procumbent cell, AP: alternate pitting, and VRP: vessel-ray pitting.

the selection for the Japanese wooden masks. The other masks that are not considered as Hahoe masks were also identified as being made of *Alnus* spp. (1969) [3]. There were some concerns that the wooden mask discovered in Kumamoto Prefecture could be one of the Hahoe masks on its basis of the morphological characteristics.

The mask was partly broken and heavily deteriorated by biological attacks. However, in order to understand the history of this mask, the identification of the wood species was requisite. A tiny half-rotted fragment collected during restoration for preservation was used for the analysis. As shown in Figs. 2 and 3, the sample was *Salix* sp., a clearly diffuse porous hardwood characterized by uniseriate heterogeneous ray and simple perforation, and thus the hypothesis that it is one of the Hahoe masks was ruled out. Since wooden masks preserved in Japan are mostly made of Hinoki (*C. obtusa*), Kusunoki (*C. camphora*), Kiri (*P. tomentosa*), and so on, it is unlikely that this mask was made in Japan. Therefore, it remains likely that this old wooden mask is still the oldest in Korea.

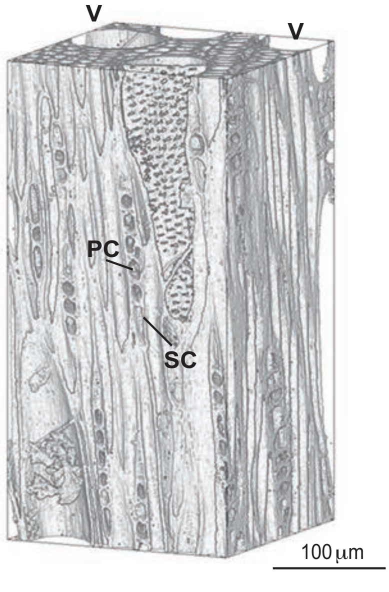

Fig. 3. Typical 3D rendering of *Salix* sp. constructed using synchrotron microtomography dataset. Note that V: vessel, SC: square cell, PC: procumbent cell, and AP: alternate pitting.

Microcomputed tomography methods hold a tremendous amount of potential. Because of their nondestructive character, the identified samples can be used further for chemical analysis such as component analysis. Recent advances in the stable isotope analysis of wood to trace its geographic site would eventually allow us to determine the origin of such wooden artifacts, i.e., to determine where it came from.

Suyako Tazuru-Mizuno and Junji Sugiyama*

Research Institute for Sustainable Humanosphere,
Kyoto University

*E-mail: sugiyama@rish.kyoto-u.ac.jp

References

[1] *S. Mizuno, R. Torizu and J. Sugiyama: J Arch. Sci.* ***37*** *(2010) 2842.*
[2] S.J. Park: Chosen Oukyu no Jumoku (translated and in Japanese), Sekai Syoin (2005) pp. 99.
[3] D. Lee: Korean Mask-Dance Drama (in Korean), Ministry of Culture and Information Republic of Korea (1969) pp. 1-403.

INDUSTRIAL


"Kobushi"- *Magnolia*

APPLICATIONS

In 2010, seven contract beamlines for industrial application were in operation. The cumulative number of company users increased to 3471 from 2436 in 2009, owing to full operation of the Frontier Soft Matter Beamline (FSBL) BL03XU. It is very felicitous that large portion of BL03XU users also participated to experiments at public beamlines. The establishment of a contract beamline for industrial application encourages industrial application of all SPring-8 facilities, including public beamlines.

Industrial applications of SPring-8 in 2009 was strongly influenced by the "Lehman Shock", and the number of proposals by company users at public beamlines drastically declined in 2009. Rapid recovery of the number proposals to the ordinary level occurred in 2010. In particular, the number proprietary proposals largely increased, and the largest number of proprietary proposals was seen in 2010. It is considered that the measurement service of powder diffraction at BL19B2 started in 2010 will play an important role in encouraging proprietary proposals. It seems that proposals by company users is gradually shifting to proprietary proposals from nonproprietary proposals.

In the present issue, five topics are chosen to represent the work carried out in Industrial Applications. We selected these topics taking into considerations XAFS, powder diffraction, CT, and SAXS to introduce diversity in industrial applications of SPring-8 in terms of field of industry and technique, since the last issue mainly introduced topics using X-ray imaging techniques.

The first topic presented by M. Oki is the application of fluorescence XAFS at BL14B2 to establish a quantitative analysis method of hexavalent chromium in pigments of polymers for industrial products, since hexavalent chromium is regulated by the European Union. XAFS measurements proved that linoleic and oleic acids maintained the valence of chromium during the dissolution process of polyethylene, and these acids are suitable solvents for extracting chromium from polymers.

The *in situ* and time-resolved XAFS investigation on catalysis in fuels cell is reported as the second topic. Bimetallic electrocatalysts such as Pt_3Co have been attracting a great deal of attention, since they have demonstrated both higher oxygen reduction activity and improved stability with much smaller amounts of platinum. Dr. Imai found that Pt oxidation of Pt_3Co saturated at around 40 s from the start of the oxidation process, by time-resolved XAFS measurement. He considered that the saturation of Pt oxidation, which indicated the suppression of Pt oxidation, is a key in the higher corrosion resistance of Pt_3Co.

As the third topic, Dr. Itoh discussed the mixed ionic-electronic conduction mechanism in perovskite oxides using precise powder diffraction data at various temperatures, in order to identify some directions of material design for cathodes for solid oxide fuel cells (SOFC). He speculated that a mixture of covalent and ionic bonds is effective for low temperature operation of SOFC, on the basis of electron distributions derived from powder diffraction data.

Both of the fourth and fifth topics concern the output at the contract beamline BL08B2 established and operated by Hyogo prefecture. The former is a SAXS study on polymer emulsion by Dr. Yamamoto, and the latter is CT observation of polymer foam by Dr. Tateishi. I am very happy to present the vigorous activities of industrial application at contract beamlines.

Ichiro Hirosawa

Investigation of the extraction method for hexavalent chromium in plastic samples

Environmental concerns have risen to the top of the global agenda. One consequence is that the design and manufacture of products with minimal impact on humans and the environment is required. The European Union, for example, regulates and limits the use of four heavy metals, namely, lead (Pb), cadmium (Cd), mercury (Hg), and hexavalent chromium (Cr(VI)), and two types of brominated flame retardants (polybrominated biphenyls: PBB, polybrominated diphenyl ethers: PBDE), in electrical and electronic equipment put on the market after July 1, 2006. Directive 2002/95/EC (RoHS directive) governs the restriction on those hazardous substances in European member states; meanwhile, other regions of the world have put similar regulations in place [1]. Owing to these regulations, it is important for the manufacturer to analyze and control certain substances used in products and their materials. Only the oxidation state of the hexavalent species of chromium is regulated in the RoHS directive and therefore its analysis is challenging. Cr(VI) has been used for chromate conversion coatings of metals, pigments of polymers, and other applications in industrial products. However, no reliable determination method for Cr(VI) in polymers has yet been established. One of the reliability problems of Cr(VI) determination is the occurrence of unstable variance during analysis. The valence of chromium is known to be changed easily by the oxidation-reduction reaction. Cr(VI) may change into Cr(III) under acidic conditions, whereas Cr(III) may change into Cr(VI) under alkaline conditions. Therefore, a chemical analysis method that keeps Cr(VI) stable for the extraction process is required. IEC 62321 cites EPA 3060A as a pretreatment method for the quantitative analysis of Cr(VI) in polymer in the Informative Annex [2]. However, when we performed extraction tests of Cr(VI) in polyethylene (PE) powder following the EPA 3060A method, the recovery was very low, about 3%. When thermoplastics are heated, they become soft, changing from a solid state to a liquid state. Moreover, we have found that PE polymer is dissolved by some kinds of fatty acids. Using these properties, we applied liquid/liquid extraction methods for Cr(VI) in PE. We report the effective extraction method of using fatty acid for Cr(VI) in the most difficult polymers such as PE [3]. In particular, it was confirmed whether the valence of Cr changed or not in the extraction process, by XAFS analysis.

XAFS measurement using synchrotron radiation was performed at beamline **BL14B2**. For the fluorescence yield method, a 19-element Ge solid-state detector was used. The intensity was normalized by using the average intensity from 6300 to 6500 eV in which negligible oscillation was observed.

The sample of PE containing Cr(VI) was made by adding lead chromate ($PbCrO_4$) or zinc chromate ($ZnCrO_4$) to PE. The Cr(VI) concentration was set to 1%. Five kinds of fatty acids (oleic acid, linoleic acid, nonanoic acid, octanoic acid and heptanoic acid) were selected as solvent with a boiling point of 200°C and melting point below room temperature. The PE samples containing Cr(VI) were heated with each fatty acid to obtain uniform solutions. These solutions were packed in polyethylene bags for XAFS measurement.

Chromium sulfate ($Cr_2(SO_4)_3$) and potassium dichromate ($K_2Cr_2O_7$) were measured by XAFS as standard materials and the results are shown in Fig. 1. In the case of measuring Cr(VI)-containing samples, a pre-edge peak at 5992 eV was observed. This pre-edge peak corresponds to the electric dipole transition from the 1*s* core state to the *p* component in the *d*-*p* hybridized orbital [4]. We can judge whether chromium is hexavalent or not by confirming the presence of this pre-edge peak. The solutions of PE containing lead chromate dissolved by fatty acids were measured by XAFS. The results are shown in Fig. 2. In the case of using nonanoic acid, octanoic acid and heptanoic acid, the pre-edge peak intensity was lower than the intensity obtained when using oleic acid and linoleic acid. This indicates that the valence change from Cr(VI) to Cr(III) occurred in the dissolving process. The fatty acids have the carboxyl group (-COOH) in the molecular chain end,

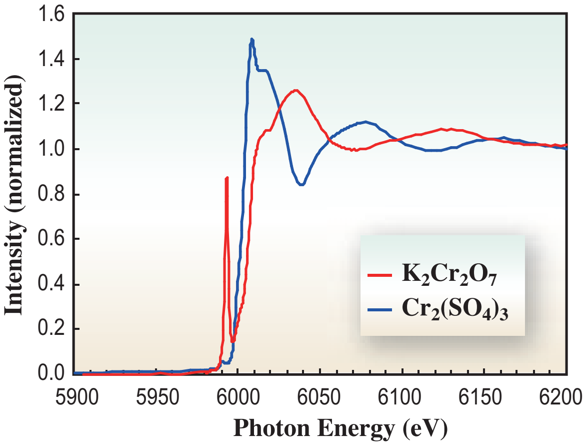

Fig. 1. XAFS spectra of Cr standard materials.

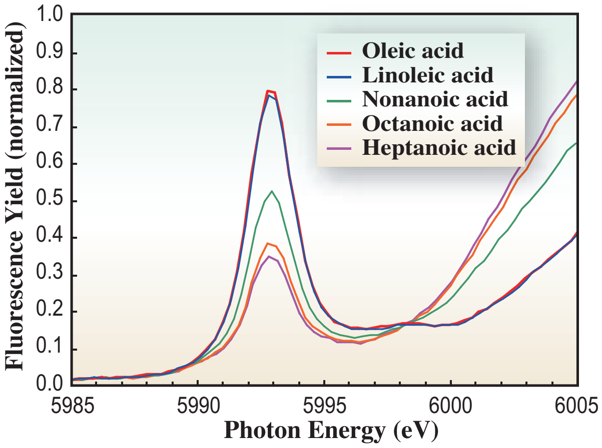

Fig. 2. XAFS spectra of lead chromate containing plastics dissolved by five kinds of fatty acids.

and the carboxyl group is acid. The valence change of Cr(VI) is thought to be attributable to this acid character. For the PE sample containing zinc chromate, the results are shown in Fig. 3. Similarly to the case of lead chromate, the pre-edge peak intensity was low in the cases of dissolution by nonanoic acid, octanoic acid and heptanoic acid. From the above results, it was found that linoleic acid and oleic acid are suitable for dissolving PE without changing the valence of Cr. It is thought that oleic acid and linoleic acids have long carbon chains, and therefore, the valence of Cr is not changed. However, the viscosity of the solution dissolved by oleic acid became higher with lower temperature. Therefore, we investigated the extraction method using only linoleic acid. The PE sample containing lead chromate was dissolved by linoleic acid and then added to KOH solution to extract Cr(VI). The concentration of Cr(VI) in KOH solution was measured by diphenylcarbazide colorimetry. The calculated recovery relative to the amount of added Cr(VI) of about 80% was achieved, which was much higher than the recovery obtained by the EPA 3060A method. This method enables us to determine the concentration of Cr(VI) in polymer samples.

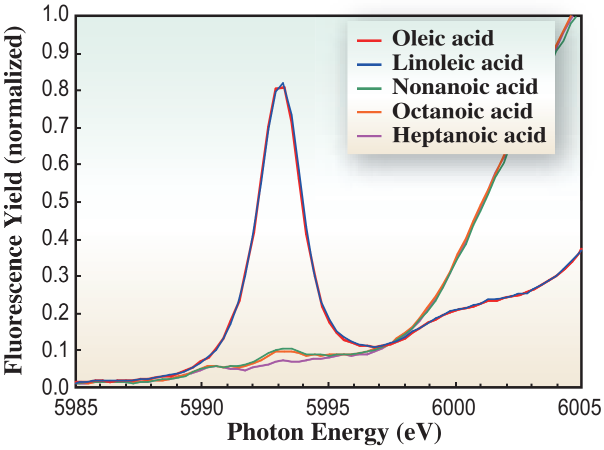

Fig. 3. XAFS spectra of zinc chromate containing plastics dissolved by five kinds of fatty acids.

Mitsuhiro Oki

Corporate Research & Development Center,
Toshiba Corporation

E-mail: mitsuhiro.oki@toshiba.co.jp

References

[1] Directive 2002/95/EC of the European Parliament and of the Council of 27 January 2003 on the restrictions of the use of certain hazardous substances in electrical and electronic equipment.
[2] IEC62321 Ed. 1 (FDIS) Electrotechnical products—Determination of levels of six regulated substances (lead, mercury, cadmium, hexavalent chromium, polybrominated biphenyls, polybrominated diphenyl ethers), (2008).
[3] *M. Muramatsu, M. Oki and M. Takenaka: Anal. Sci. (2012) – in press.*
[4] T. Yamamoto: X-Ray Spectrom. **37** (2008) 572.

In situ analysis of electrochemical reaction inside a fuel cell: Growth limit in behavior of platinum oxides formed on Pt-skin layers on Pt-Co bimetallic electrocatalysts

Fuel cells that convert the chemical energy of hydrogen and oxygen directly into electricity will offer a clean and highly efficient energy conversion system in the near future. Owing to extensive research, the basic performance of such fuel cells is about to reach a level suitable for widespread use. Major car manufacturers will be ready to launch the first commercial fuel-cell vehicles by the end of 2015. The current research interest is shifting to practical issues such as ensuring long-term reliability and reducing the total cost of fuel cells.

The need for platinum electrocatalysts that catalyze the oxygen-reduction reaction at the cathode has been one major obstacle to commercialization because the high cost of platinum and its instability in high-potential regions limit the practical use of fuel cells. Bimetallic electrocatalysts such as Pt_3Co have been attracting a great deal of attention, since they have demonstrated both higher oxygen reduction activity and improved stability with much smaller amounts of platinum. Less-stable transition metals (such as Co) are removed from the surface regions by acid leaching in advance to prevent transition-metal components from dissolving further. This creates platinum-rich surface domains, viz., Pt-skin layers that are responsible for superior catalytic properties (Fig. 1).

Whereas the mechanism responsible for the enhanced catalytic oxygen-reduction activity of Pt-skin layers has been quite well explained by the d-band center shift in the outermost Pt-layers, the factors that increase stability remain elusive. We, therefore, investigated the dynamical oxidation and reduction processes in Pt-skin layers on Pt_3Co bimetallic particles via *in situ* time-resolved X-ray absorption spectroscopy (XAS) combined with electrochemical measurements [1].

The *in situ* and time-resolved X-ray absorption spectroscopy (XAS) measurements were carried out at the Pt L_3 edge on **BL40XU** beamline using a quick-scanning XAS measurement system with quasi-monochromatic undulator radiation (time resolution: 100 ms). The catalysts were mounted onto a thin carbon electrode and the potential step oxidation/reduction was measured using a three-electrode cell in 0.5M H_2SO_4 under N_2 atmosphere.

The oxidation behavior of Pt-skin layers on Pt_3Co differs from that of Pt. Figures 2(a–d) show the results of XAS analyses of Pt and Pt-skin layers on Pt_3Co bimetallic nanoparticles after oxidation/reduction cycles between 0.4 and 1.4 V. Figures 2(a) and 2(c) show plots of the time variations in FT amplitude at around 2.6 Å corresponding to the coordination number (CN) of the first-nearest-neighbor Pt-Pt bond for platinum metal. They thus represent relative changes in the volume of Pt metal. Figures 2(b) and 2(d), on the other hand, show time variations in the white-line intensity in the XANES spectra. The increase in the white-line intensity when oxides are formed on the surface owing to electron transfer from the Pt 5*d*-band to oxygen reflects an increase in the volume of platinum oxide.

Whereas the surface of pure Pt was continuously oxidized and then reduced without any saturation behavior (Figs. 2(a) and 2(b)), the oxidation and reduction of Pt-skin layers of PT_3Co nanoparticles occurred discontinuously with saturation behavior (Figs. 2(c) and 2(d)). Both the FT amplitude and white-line intensity for Pt_3Co exhibit saturation behaviors at around 40 s, indicating that oxidation was suppressed at a certain level of oxidation. The detailed EXAFS analysis revealed that the formation of higher-order platinum oxides such as β-PtO_2 is truly suppressed in the oxidation process of Pt-skin layers on Pt_3Co.

The durable nature of Pt-skin layers may be a result of the existence of a growth limit and particularly

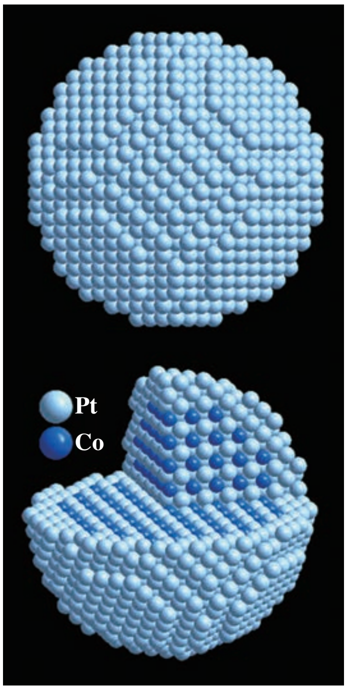

Fig. 1. Average structure of Pt_3Co nanoparticles with Pt-skin layers, determined by Pt-L_3 EXAFS analysis.

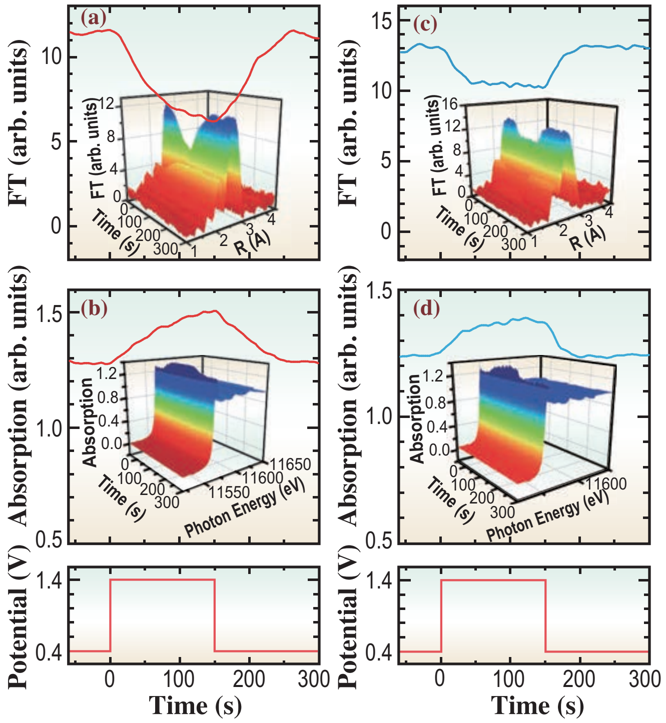

Fig. 2. Time variations in XANES spectra and radial structure functions (FT) during potential-step oxidation/reduction cycle between 0.4 and 1.4 V. Bottom graphs show potential step sequence. **(a)** and **(c)**: Time variations in peak maximum of radial structure functions at 2.6 Å, which correspond to first-nearest-neighbor Pt-Pt bonds for platinum and Pt_3Co. **(b)** and **(d)**: Time variations in XANES spectra (white line intensity at maximum) for pure platinum and Pt_3Co bimetallic particles.

the suppression of higher-order oxides. When higher-order oxides formed by atomic oxygen diffusion into platinum or platinum oxide lattices, there were large platinum atom displacements, particularly at the α- to β-PtO_2 transition. Up to α-PtO_2, oxide can grow almost epitaxially, but for β-PtO_2, half the surface Pt atoms are lift toward surface. In the reduction process to metallic platinum, in turn, platinum atoms move greatly, producing energetically unstable platinum atoms at the solution-oxide interface. This enhances the dissolution of platinum to electrolytes. Thus, Pt-skin layers in which higher-order oxide formation is suppressed could have higher corrosion resistance then that of pure platinum, suppressing the formation of unstable platinum atoms in oxide-reduction processes. Currently, on the basis of the above results, the development of a catalyst with higher corrosion-protection performance is under way.

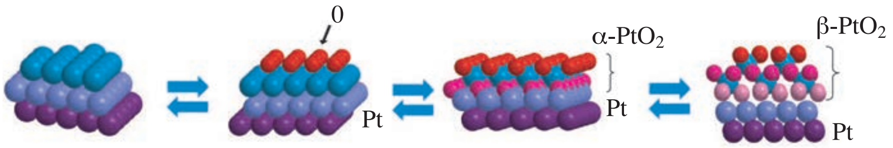

Fig. 3. Schematic drawing of surface oxidation/reduction processes of platinum nanoparticles at 1.4 V.

Hideto Imai[a,b]

[a] Energy-device Analysis Dept., NISSAN ARC Ltd.
[b] Advanced Material Lab., Nissan Research Center, Nissan Mortar. Co., Ltd.

E-mail: imai@nissan-arc.co.jp

References

[1] *H. Imai, M. Matsumoto, T. Miyazaki, K. Kato, H. Tanida, and T. Uruga: Chem. Commun.* ***47*** *(2011) 3538.*
[2] H. Imai *et al*.: J. Am. Chem. Soc. **131** (2009) 6293.

Study of mixed ionic-electronic conduction mechanism in perovskite oxides using Rietveld refinements and the maximum-entropy method analysis of *in situ* synchrotron X-ray diffraction data

Recently, mixed ionic–electronic conductivity (MIEC) in perovskite oxides $ABO_{3-\delta}$ (A indicates an alkaline and/or rare earth metal, while B represents a transition metal) has generated great interest in the development of electrochemical devices such as cathodes for solid oxide fuel cells (SOFCs), oxygen pumps, oxygen sensors, catalysts, and oxygen separation membranes. In particular, SOFCs, which can directly convert chemical energy to electricity, have increasingly attracted worldwide attention owing to their outstanding characteristics such as high efficiency and significantly low emission levels of pollutants. However, an important technical concern present in SOFCs needs to be overcome, namely, the operation temperature of the cells. The operation temperature needs to be reduced to 750–1000 K. To solve this issue, it is indispensable to understand the MIEC mechanism of SOFC cathode materials in detail (Fig. 1). Shao *et al*. have presented $(Ba_{0.5}Sr_{0.5})(Co_{0.8}Fe_{0.2})O_{3-\delta}$ (BSCF) as a promising cathode material for next-generation SOFCs [1]. Extensive studies of BSCF have been conducted on the electrochemical properties, oxygen nonstoichiometry, and crystal structure of perovskite oxides. However, they do not explain why the electrochemical properties of BSCF make it more suited for use in low-temperature-operated SOFCs than other cathode materials.

The maximum-entropy method (MEM) analysis for calculating charge density from X-ray data is a promising approach for studying the bonding state, atomic disorder, and ion conduction in detail [2].

We undertake to discuss the MIEC mechanism in cathode materials of SOFCs by using Rietveld refinements and MEM analysis of *in situ* synchrotron X-ray diffraction (SR-XRD) measurements at 500–900 K for the first time, and compare the temperature dependence of the charge density of $(La_{0.75}Sr_{0.25})MnO_{3-\delta}$ (LSM, SOFC cathode material operating at high temperature) with that of BSCF (SOFC cathode material operating at low temperature). SR-XRD experiments were carried out using a large Debye-Scherre camera installed at **BL19B2**. The Rietveld refinement used the program RIETAN–FP [3] and the MEM analysis used the program PRIMA. The crystal structures and the charge density were visualized using the software package VESTA [4], which is based on VENUS software.

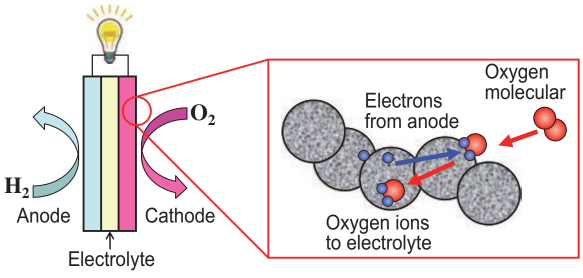

Fig. 1. Role of cathode material in SOFCs.

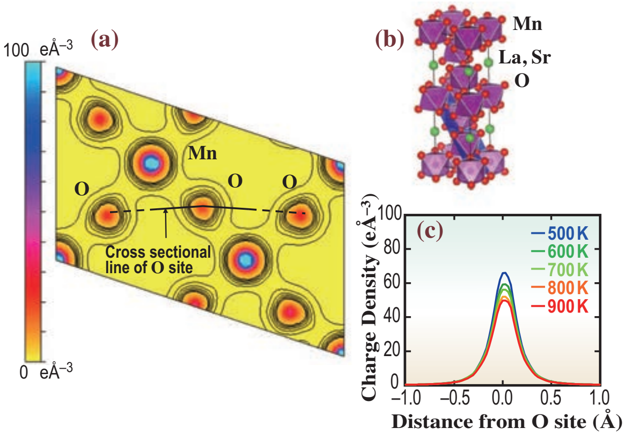

Fig. 2. **(a)** Charge density distribution at 500 K for $R\bar{3}c$ Mn-O $(\bar{1}02)$ plane of LSM, contour line: 0-5 eÅ^{-3}, step: 0.6 eÅ^{-3}. **(b)** Crystal structure for $R\bar{3}c$ Mn-O $(\bar{1}02)$ plane of LSM. **(c)** One-dimensional charge density profile around the O site at 500-900 K for $R\bar{3}c$ along the line in the direction to another O site in the Mn-O plane.

Figure 2(a) shows the charge density distribution of the Mn–O $(\bar{1}02)$ plane at 500 K. This plane possesses isotropic Mn–O bonds, and these bonds show strong covalency in LSM. This result supports the fact that LSM has high electron conductivity. For a strong covalent bond of Mn–O, oxygen ions would be prevented from participating in conduction. In fact, the oxygen ion conductivity of LSM is lower than that of other perovskite oxides that are used as cathode materials for an SOFC. Figure 2(c) shows the one-dimensional charge density profiles around an O site along the line to another O site on the Mn–O plane at 500–900 K. The charge density profiles decrease slightly with an increase in temperature. We speculate that this phenomenon is related to the increase in the atomic isotropic displacement parameter (U_{iso}) and not to the decrease in oxygen site occupancy.

Figure 3(a) shows the charge density distribution (2 0 2) plane of BSCF at 500 K. In Fig. 3(b), the red-colored part of the oxygen site indicates the oxygen site occupancy. We found that the anisotropic bonds in the (Co, Fe)–O1(4*c*) and O2(8*d*) planes in BSCF, and the O1(4*c*) site possess more vacancies than the O2(8*d*) site. The (Co, Fe)–O1(4*c*) bond was less covalent than the (Co, Fe)–O2(8*d*) bond in BSCF. Figures 3(c) and 3(d) show the one-dimensional charge density profile around the O1(4*c*) site along the line to the O2(8*d*) site and the O2(8*d*) sites along the line to the O1(4*c*) site at 500–900 K, respectively. The charge density profiles of the O2(8*d*) site were independent of temperature. It can be speculated that the O2(8*d*) site occupancy does not change with an increase in temperature. On the other hand, the charge density profiles of the O1(4*c*) site dramatically decreased with an increase in temperature. We inferred that the charge density profile expanded to another oxygen site for oxygen ion conduction. The (Co, Fe)–O2(8*d*) plane is involved in conducting electrons for the strong-covalency bond and has a low concentration of oxygen vacancies. In contrast, the (Co, Fe)–O1(4*c*) plane with a high concentration of oxygen vacancies and ionic bonds would be involved in the diffusion of oxygen ions. We understand that the BSCF structure has covalent and ionic bonds; this is different from the case of LSM, which has only strong covalent bonds. We assume that the presence of covalent and ionic bonds is more effective for MIEC in SOFCs operating at low temperatures than the presence of single-type bond suchs as the Mn–O bond in LSM.

Finally, we point out the attention of MEM analysis. MEM analysis possesses several issues in high-temperature diffraction measurement. In particularly, the current MEM analysis does not take account of thermal diffuse scattering (TDS) which increases with an increase in temperature. Therefore, there is a possibility that TDS reduces the accuracy of the charge density at high temperature estimated by MEM analysis. We hope that the consideration of TDS is incorporated into Rietveld refinements and MEM analysis. MEM analysis, however, is very useful and indispensable in discussing the charge density and MIEC mechanism in the crystal structure.

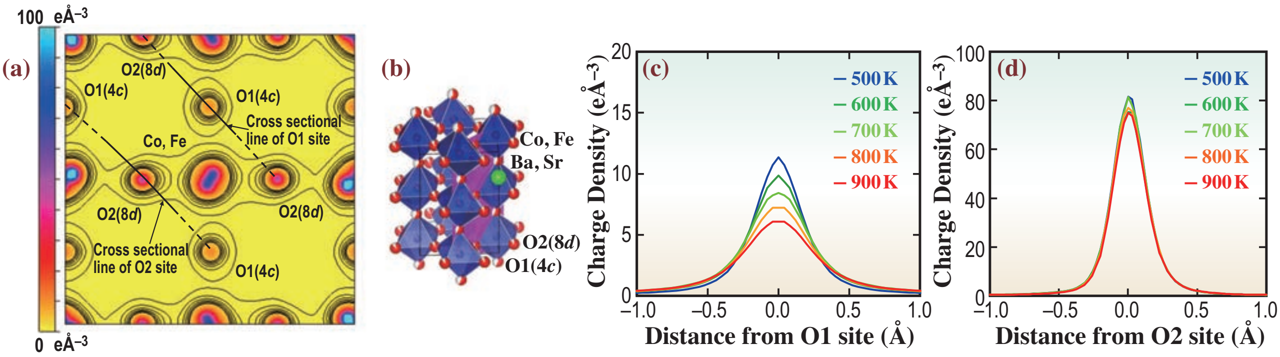

Fig. 3. **(a)** Charge density distribution at 500 K for *Pnma*, (Co, Fe)-O1, O2 (2 0 2) plane of BSCF, contour line: 0-5 eÅ^{-3}, step: 0.6 eÅ^{-3}. **(b)** Crystal structure for *Pnma*, (Co, Fe)-O1, O2 (2 0 2) plane of BSCF. **(c)** One-dimensional charge density profile around the O1 site at 500-900 K for *Pnma* along the line in the direction to another O2 site in the (Co, Fe)-O2 plane. **(d)** One-dimensional charge density profile around the O2 site at 500–900 K for *Pnma* along the line in the direction to another O1 site in the (Ba, Sr)-O1 plane.

Takanori Itoh[a,*], Keiichi Osaka[b] and Ichiro Hirosawa[b]

[a] AGCSeimichemical Co., Ltd.
[b] SPring-8/JASRI

*E-mail: tknitoh@seimichemical.co.jp

References

[1] Z. Shao and S.H. Haile: Nature **431** (2004) 170.
[2] M. Sakata and M. Sato: Acta Crystallogr. A **46** (1990) 263.
[3] F. Izumi and K. Momma: Solid State Phenom. **130** (2007) 15.
[4] K. Momma and F. Izumi: J. Appl. Crystallogr. **44** (2011) 1272.
[5] *T. Itoh, S. Shirasaki, Y. Fujie, N. Kitamura, Y. Idemoto, K. Osaka, H. Ofuchi, S. Hirayama, T. Honma and I. Hirosawa: J. Alloys Comp.* ***491*** *(2010) 527.*

Structure analysis of acrylic emulsion particles and films by small-angle X-ray scattering

An aqueous polymer emulsion, a dispersion of water-insoluble polymer particles with diameters in the range of 50–500 nm stabilized by surfactants, is widely used for coatings and adhesives. The emulsion particles coalesce to form continuous films upon drying after application. It is important to clarify the particle structure and coalescence process that govern the film properties such as mechanical strength. We have characterized polymer dispersion liquids and films by small-angle X-ray scattering (SAXS) at SPring-8.

Three kinds of acrylic polymer emulsions with particles of various diameters at a glass transition temperature (Tg) of –70°C were prepared using surfactants with different structures (Table I). SAXS measurements were performed at beamline **BL08B2** with an X-ray wavelength of 0.15 nm and a camera length of 6050 mm. The size of the primary X-ray beam at the sample position was 0.5 × 0.5 mm^2. The coalescence process during drying of the emulsions at room temperature was monitored in terms of the emulsion concentration. Hydrodynamic particle sizes were also determined by dynamic light scattering (DLS) analysis using NICOMP$^{\text{TM}}$ 380 (Particle Sizing Systems).

Figure 1 shows SAXS profiles of a series of polymer emulsions during a drying process. The plateau appears at q = 0.02 nm^{-1} in 3.13 and 6.25 wt% dilute or semidilute systems, respectively. This is observed as a peak that shifts to higher q with increasing concentration, and finally reaches q = 0.048nm^{-1} for the film (dark gray broken line). This q region is attributed to the close packing structure of the particles. On the other hand, the peaks at around q = 0.079 nm^{-1} are caused by scattering from the particles themselves and shift negligibly (light-gray chain line). From these results, it is found that the film is formed only by mutual contact of the particles without a change in particle size.

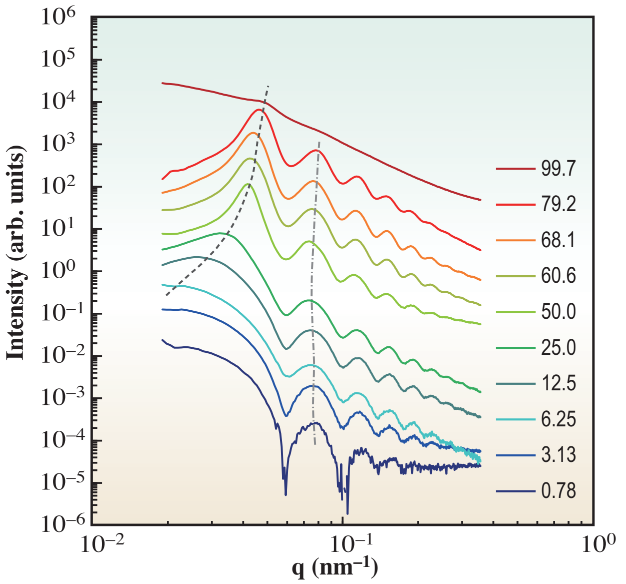

Fig. 1. SAXS profiles at various sample concentrations during dry process. Numerical values in the figure represent nonvolatile content in polymer emulsion. Dark gray broken line and light gray chain line represent the shift of the peaks upon close packing and the position of the peaks by scattering due to the particles themselves, respectively. Curves are vertically shifted.

Figure 2 shows the I•q^2 *vs* q plot of SAXS profiles of the emulsion films with different particle sizes. A value depicted on the curve is the ratio of the peak position for higher order peaks or shoulders to the highest peak (the first peak) position. If the ratio corresponds to $1:\sqrt{3}:\sqrt{4}:\sqrt{7}:\sqrt{9}$... in the SAXS profiles, it means that the particles are packed in the hexagonal structure. All three polymer emulsion films show hexagonal close-packed structures because the ratios agree well with the sequence, though the scattering spectra observed for all the samples are broad.

The spherical emulsion particles are hexagonally packed because of the coalescence in films since Tg of the polymers is lower than room temperature.

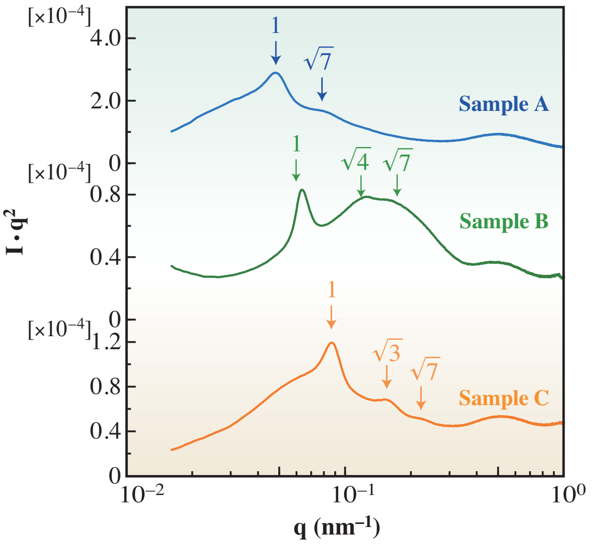

Fig. 2. I•q^2 *vs* q plot of emulsion films. Ratios of position of higher order peaks or shoulders to that of the 1st peak are also indicated.

Table 1. Diameters in emulsion films and solutions obtained from SAXS and DLS results, corona sizes, and the extended molecular lengths of the surfactants

	in solid		in solution				
	Size of hexagonal particles	Size of sphere before coalescence estimated by eq. (1)	Diameter by SAXS	Expected diameter by SAXS	Diameter by DLS	Corona size	Extended molecular length of surfactant
	(nm)	(nm)	(nm)	(nm)	(nm)	(nm)	(nm)
Illustrated structure / Sample code	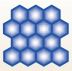	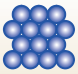					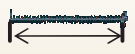
Sample A	130	143	153		174	10.6	9.86
Sample B	99	109	–	119	144	12.3	9.86
Sample C	72	80	–	90	111	10.6	7.72

The distance between the particles estimated from SAXS profiles corresponds to the size of the hexagon, (refer to the second column in Table 1). The diameter of the spherical particles before coalescence can be converted by $\boldsymbol{d} = \mathbf{0.74}^{1/3}\,\boldsymbol{D}$, where d and D are the size of the hexagon and the diameter of the spherical particles before coalescence, respectively. D is shown in the third column in Table 1.

The particle diameter of the 6.25 wt% sample is 153 nm, which is 10 nm larger than that in the film (solid). Because it is reported that poly(methyl methacrylate) has a swelling layer of 10-nm-thick in water [1], it is considered that the diameter of the particles in water becomes about 10 nm larger owing to swelling. Considering this phenomenon, it will be expected that the particle diameters for samples B and C in water may become 10 nm larger when determined from SAXS.

Volume-average diameters measured by DLS become large, as shown in Table 1. SAXS data gives the particle sizes from the difference in electron density between water and particles, whereas DLS yields the hydrodynamic sizes including the extent of surfactant in water. The extent of the surfactant in water, i.e., corona size, is calculated from the difference in sizes obtained from SAXS and DLS data and are listed in Table 1. The corona size for each sample is about 10 nm irrespective of the particle size.

Finally we calculated the extended molecular length of the surfactants for comparison with the corona size (Table 1). The lengths of the surfactants are found to be about 10 nm, and there is a reasonable agreement between the lengths and the corona sizes, being explained by the extension of the molecules in water owing to the repulsion between the ionic head groups of the anionic surfactants. Estimated emulsion particles are schematically shown in Fig. 3.

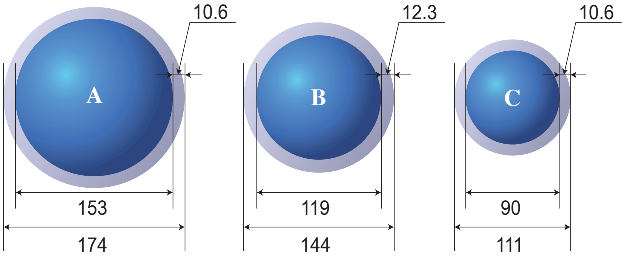

Fig. 3. Schematic models of the emulsion particles with various diameters. Deep and light blue areas indicate the sizes of the core and the corona of the emulsion particles, respectively.

Tomoyuki Yamamoto*, Toshimitsu Inoue and
Kaname Kida

Central Research Laboratory,
The Nippon Synthetic Chemical Industry Co., Ltd.

*E-mail: yamamoto.tomoyuki@mp.nichigo.co.jp

References

[1] K. Tanaka *et. al.*: Langmuir **24** (2008) 296.

Imaging of polymer foam by three-dimensional computed tomography

In the design of footwear soles, one of the most important required functions is the shock-absorbing property for both injury prevention and athletic performance enhancement [1]. Polymer foam has been widely used for footwear soles because of not only its shock-absorbing property but also its flexibility and durability. The excellent shock-absorbing property of polymer foam is due to the microscopic cellular structure. Figure 1(a) shows an SEM image of polymer foam. Polymer foam has a closed cell structure comprising a polymer wall with thickness of 5–10 μm and cell of 50–500 μm in diameter. Figure 1(b) shows the typical stress-strain behaviors obtained from polymer foam and polymer (non-foam) under unidirectional compression. Polymer foam has high nonlinearity in its mechanical property compared with that of polymer (non-foam). The compressive stress-strain behavior of polymer foam can be classified into elastic, plateau, and densification regions. These mechanical behaviors are mainly a result of the cell (cell wall) deformation under compressive load. Since the shock-absorbing property predominantly depends on the amount of deformation energy accumulated in the plateau region, it is very important, for material design, to evaluate the deformation behavior of the cell in this region. In the evaluation of cell deformation behavior, surface observation has been performed by microscopy, but this is not appropriate because the surface is in the singular stress field. Exactly speaking, it is necessary to observe the inner structure to correctly evaluate cell deformation under compression. Three-dimensional X-ray computed tomography (CT) is a useful technique for non-destructively observing the inner structure of material. In the case of applying CT to polymer foam, both a large view field and high spatial resolution are needed. Since polymer foam consists of light elements such as carbon, hydrogen, and air, a high-flux light source is indispensable for polymer foam CT. In order to fulfill the above conditions, it is necessary to perform CT observation using synchrotron radiation. In this study, in order to improve the shock-absorbing property of polymer foam, the deformation behavior of the cell under various compressive stresses is evaluated by the CT technique.

In the experiment, cross-linked EVA (ethylene vinyl acetate) foam generally applied to footwear is used as the specimen. Its porosity is 0.79. EVA foam was fabricated by a one-shot press-molding process. The preformed compounds were composed of organic peroxide as a cross-linking agent, and azodicarbonamide as a chemical bowing agent. The molding conditions were as follows: temperature of 448 K, pressure of 10 MPa, and duration of 30 min. Under these conditions, the cross-linking agent and the bowing agent fully decomposed. The foaming reaction takes place during rapid decompression. The EVA foam specimen is cut to a cuboid shape, with 5 mm length, 5 mm width and 10 mm height. The CT experiment is performed at the Hyogo Prefectural beamline **BL08B2** by the absorption contrast method. In BL08B2, large-view-field and high-spatial-resolution CT measurements are possible. The X-ray energy is adjusted to 12.4 keV. Transmission X-rays are detected using the imager system comprising a P43-type powder phosphor screen, relay lens, and a 4008 × 2672-element cooled CCD camera. The effective pixel size of the detector is 4.28 μm, which is a satisfactory accuracy for observing cell deformation. The EVA foam specimen is inserted into an acryl tube on the rotation stage.

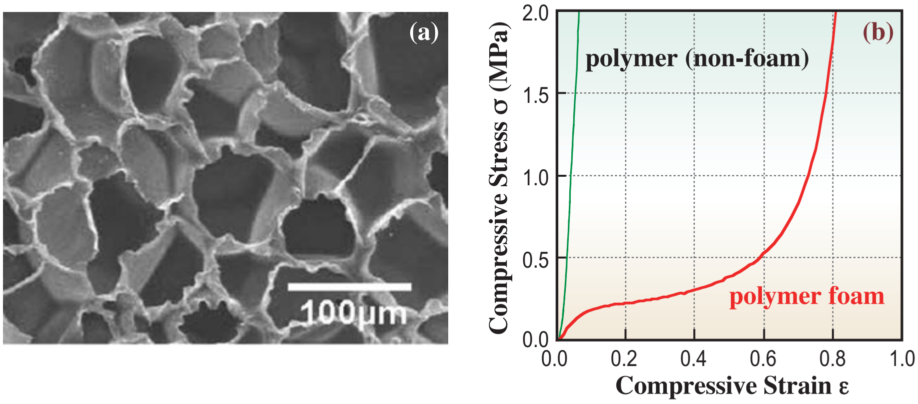

Fig. 1. Typical mechanical properties of polymer foam. **(a)** SEM image. **(b)** Typical stress-strain behavior of polymer foam and polymer (non-foam) under unidirectional compression.

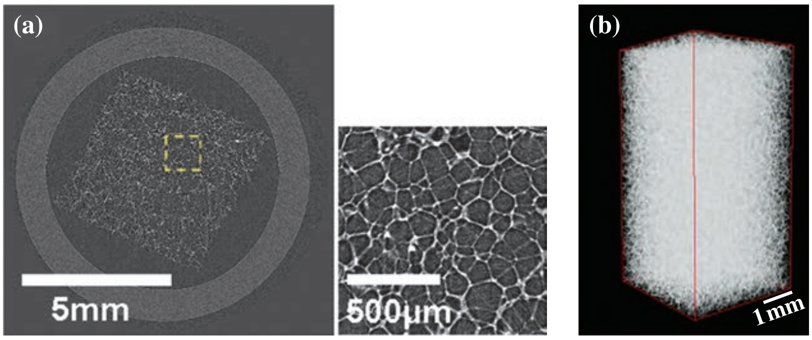

Fig. 2. CT image of polymer foam: **(a)** tomogram and **(b)** volume-rendering view.

The CT images are reconstructed by the back-projection method using 1000 transmission projections imaged through a 180° rotation of the specimen. It took 1.5 hour for the CT measurement.

Figure 2 shows a tomogram and three-dimensional rendering view of an undeformed EVA foam specimen. In Figure 2(a), the cell (dark domain) and cell wall (white linear structure) were clearly depicted, and closed cell structures were revealed. The diameter of the cell ranged from 100 to 300 µm, and the thickness of cell walls ranged from 10 to 20 µm. In Figure 2(b), the three-dimensional rendering view shows that cells were dispersed intricately in three-dimensions with size distributions. Figure 3 shows the stress-strain behavior of the specimen and CT images of the inner layer parallel to the compressive direction. Arrows in the stress-strain curve correspond to these images, and ε in the CT images denote compressive strain. When $\varepsilon = 0$, the uncompressed state, each cell shape is isotropic. When $\varepsilon = 0.1$, the buckling behaviors are induced by the compressive load in some cell walls. In particular, the buckling of thin cell walls is dominant. This strain corresponds to the end of the elastic region. With increasing strain ($\varepsilon = 0.1$–0.6), cell-wall buckling increases and many flat cells appear. Judging from the above results, it is considered that the plateau region is a result of cell wall buckling. Hence, the low-stress increase rate in the plateau region originates from the cell-wall buckling. The buckled cell walls interrupt stress transmission. When $\varepsilon = 0.8$, most cell walls fully buckle and densification occurs. Moreover, buckled cells come into contact with each other, whereby the stress increases rapidly. These results indicate that compressive buckling of a cell is one of the most important design parameters in improving the shock-absorbing property of polymer foam. For the clarification of the shock-absorbing mechanism of polymer foam in detail, it is effective to observe the dynamic deformation by high-speed CT, and to combining CT data with the finite-element method. In the future, CT observation can contribute designing the properties of polymer foam, such as not only the shock-absorbing property but also durability and flexibility.

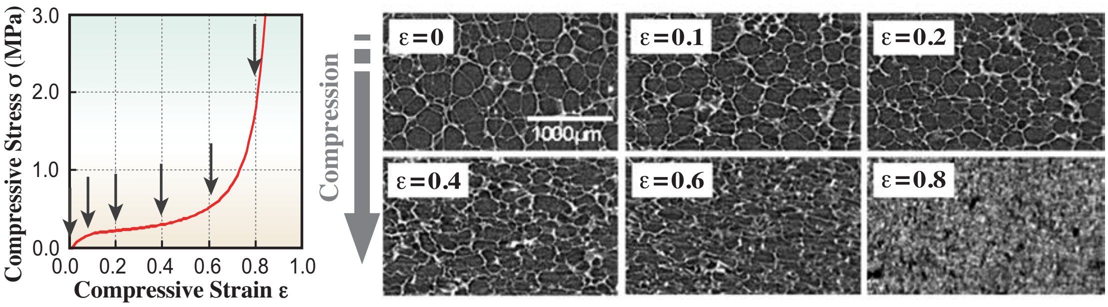

Fig. 3. Stress-strain curve of specimen and CT images of inner layer parallel to compressive direction. Arrows denote strain values corresponding to CT images.

Junichiro Tateishi* and Tsuyoshi Nishiwaki

Institute of Sport Science, ASICS Corporation

*E-mail: tateishi-ju@asics.co.jp

References

[1] T. Nishiwaki: Sports Technology **1** (2008) 76.

NUCLEAR

"Susuki"- *Japanese pampas grass*

PHYSICS

The linearly polarized photon beam is produced by the backward-Compton scattering of laser photons from 8 GeV electrons at BL33LEP. The current LEPS facility studies photo-production of hadrons in the forward angles, where the high linear polarization plays an essential role of decomposing various reaction processes.

The beam polarization is high and can be changed easily by changing the laser polarization. The LEPS covers a photon energy region from 1.5 to 2.9 GeV, which is suitable for studying the creation of excited baryons containing a strange quark or an anti-strange quark near the production thresholds. The production and decay properties of the excited hadrons shed lights on their structure in terms of confined quark.

The first article reports the first exclusive measurement of the $\gamma p \rightarrow K^{*0}\Sigma^{+}$ reaction using linearly polarized photons at beam energies ranging from 1.85 to 2.96 GeV. The angular distributions in the rest frame of the $K^{+}\pi$ system were fitted to extract spin-density matrix elements of the K^{*0} decay. The measured parity spin asymmetry shows that natural-parity exchange is dominant in this reaction, which clearly indicates the need for the t-channel exchange of the $\kappa(800)$ scalar meson.

The second article reports the progress of the LEPS2 project, in which we aim to improve both the beam intensity and the detector acceptance. The construction was started in 2011. The expected performance of the beamline and the research plan with the upgraded LEP beam are presented.

Takashi Nakano
Research Center for Nuclear Physics
Osaka University

Evidence for the κ(800) meson exchange in $\gamma p \rightarrow K^{*0}\Sigma^+$ reaction at $E_\gamma = 1.85–3.0$ GeV

In the simplest quark model, the lightest meson octet has 3 mesons with no strange quark, 4 mesons containing either a strange quark (s) or a strange antiquark ($\bar{s}$), and one meson with a dominant $s\bar{s}$ content. The ground-state pseudoscalar meson octet is well-established, and consists of three pions, four kaons, and an eta-meson. However, for the higher-mass mesons, the assignments are not clear. For example, the Particle Data Group (PDG) states that identification of the scalar mesons is "a long-standing puzzle." In particular, the κ-meson (presumed to be part of the lowest-mass scalar meson octet) with a resonance pole at about 800 MeV is seen in many phenomenological analyses, yet its existence is still controversial.

The quantum numbers of the κ-meson are $J^P = 0^+$ and I = 1/2. The κ is considered to be the scalar partner to the kaon in an analogous way as the σ-meson (also called the $f_0(600)$) is the scalar partner to the η-meson. Definitive evidence for the σ or κ-mesons would provide a significant advance in the understanding of possible multi-quark states. Here, we report on the linear polarization observables for K^* photoproduction measured using a proton target [1]. These observables, the spin-density matrix elements, have been shown to be sensitive to κ-meson exchange. In particular, Ref. [2] predicts that the κ(800) contributes to K^* photoproduction through t-channel exchange, which dominates at forward scattering angles.

The parity spin asymmetry [2], given in terms of the spin density matrix elements by $P_\sigma = 2\rho^1_{1-1} - \rho^1_{00}$, is shown in Ref. [1] to be particularly sensitive to the role of κ-exchange, especially at forward angles. In the case of scalar κ exchange, the parity spin asymmetry is positive, whereas calculations without the κ (with pseudoscalar kaon exchange only) have negative parity spin asymmetry. The present data provide the first-ever reported parity spin asymmetry for K^{*0} photoproduction.

The experiment was carried out using the LEPS detector at beamline **BL33LEP**. The photon beam was produced by the laser backscattering technique [3] using a 275 nm laser, with wavelengths in the deep-UV region, to produce Compton-scattered photons in the range of 1.5 to 2.96 GeV. The laser light was linearly polarized with an average polarization of 98%. The photon beam was incident on a 15 cm liquid hydrogen target, where K^+ and π^- particles were produced and then passed through the LEPS spectrometer [4]. The invariant mass spectrum, calculated from the measured 4-vectors of detected K^+ and π^-, are shown in Fig. 1.

The decay angular distribution can be expressed in terms of nine spin-density matrix elements and linear polarization of the photon beam energy. We extracted the spin-density matrix elements using an unbinned extended maximum likelihood fit (see [5] for details) in the helicity frame and the beam energy region from 1.85 (threshold for $K^*\Sigma$ production) to 2.96 GeV. The K^* production angle $\cos\theta_{K^*}$ ranges from 0.6 to 1.0 and its average value is 0.9115.

Figure 2 shows decay angular distributions for a sum of horizontal and vertical beam polarizations with only a single variable, $\cos\theta_{K^+}$, ϕ_{K^+}, $(\phi - \Phi)_{K^+}$ and Φ_{K^+}, in the helicity frame [6]. Black histograms indicate the estimated Y^* background in the reconstructed Monte Carlo distribution.

The parity spin asymmetry ($P_\sigma = 2\rho^1_{1-1} - \rho^1_{00}$) is estimated to be 0.758±0.123 in the helicity frame over the angular range shown by the horizontal error bar in Fig. 3. The large positive asymmetry shows that the natural parity exchange is the dominant process at forward angles. The dashed (solid) line in Fig. 3 is the result with Model I (Model II) of Ref. [1] at E_γ = 2.5 GeV. The data clearly favors Model II, which includes a substantial contribution from natural-parity κ-exchange. The mass and width of the κ-meson are parameters of the theoretical model, and are not directly measured by the present data.

In summary, the photoproduction of the $\gamma p \rightarrow K^{*0}\Sigma^+$ reaction was measured at the LEPS detector at

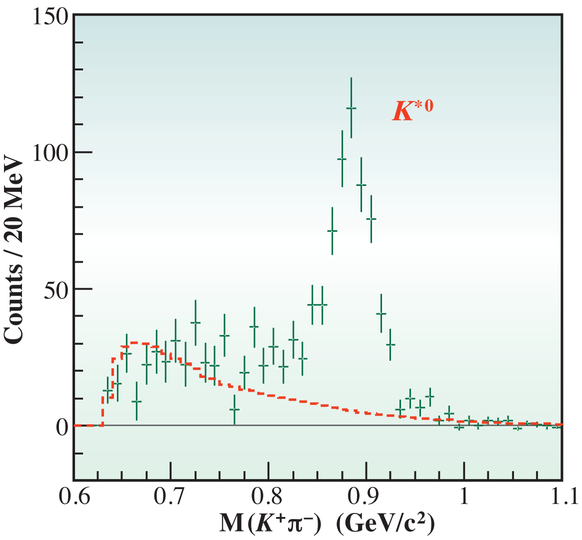

Fig. 1. The invariant mass distribution with a cut on the Σ^+ peak, and the overlaid dashed line shows the estimated Y^* background.

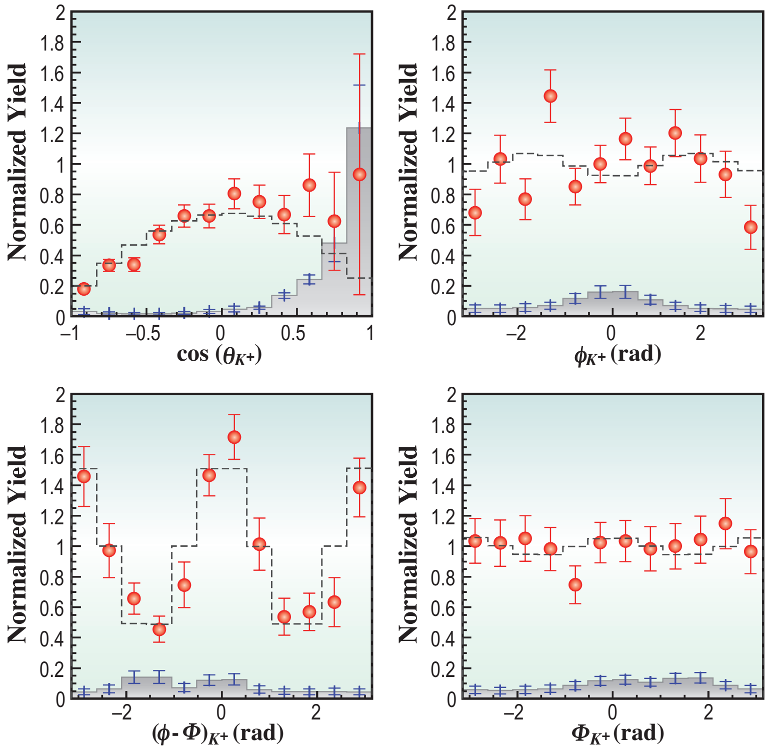

Fig. 2. Decay angular distributions of $\cos\theta_{K^+}$, ϕ_{K^+}, $(\phi - \Phi)_{K^+}$, and Φ_{K^+} in the helicity frame. The dashed line shows Monte-Carlo data using the measured spin-density matrix elements, while the overlaid grey histogram indicates the Y^* background yield from a Monte-Carlo simulation.

forward production angles and energies from 1.85 to 2.96 GeV, using a linearly polarized photon beam at BL33LEP. The parity spin asymmetry ($P_\sigma = 2\rho^1_{1-1} - \rho^1_{00}$) has a large positive value, showing that natural-parity exchange is dominant at forward angles for $K^{*0}\Sigma^+$ photoproduction. A natural explanation for the natural-parity exchange would be t-channel exchange of a scalar meson with strangeness, which is consistent with the κ-meson. The existence of this meson would be a good candidate to complete the lowest-mass scalar meson octet.

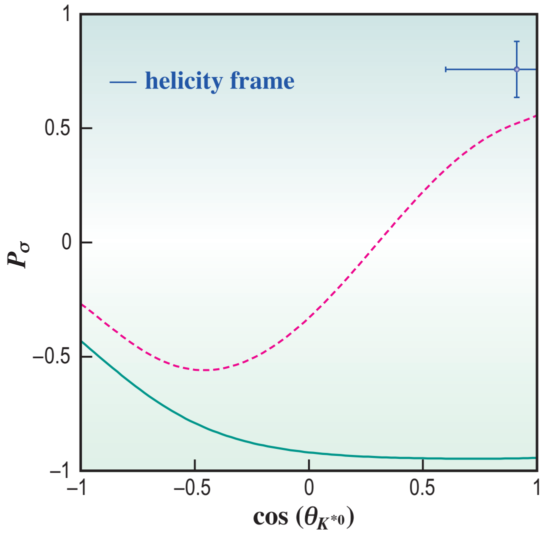

Fig. 3. Parity spin asymmetry ($P_\sigma = 2\rho^1_{1-1} - \rho^1_{00}$) in the helicity frame. The solid (dashed) line is the result of Model I (Model II) of Ref. [1] at $E_\gamma = 2.5$ GeV. Model I has almost no contribution from κ-exchange, whereas Model II includes substantial κ-exchange.

Jung Keun Ahn for the LEPS Collaboration

Dept. of Physics, Pusan National University, Korea

E-mail: ahnjk@pusan.ac.kr

References

[1] *S.H. Hwang, K. Hicks, J.K. Ahn, T. Nakano, D.S. Ahn, W.C. Chang, J.Y. Chen, S. Daté, H. Ejiri, H. Fujimura, M. Fujiwara, S. Fukui, W. Gohn, T. Hotta, K. Imai, T. Ishikawa, K. Joo, Y. Kato, H. Kohri, Y. Kon, H.S. Lee, Y. Maeda, M. Miyabe, T. Mibe, Y. Morino, N. Muramatsu, Y. Nakatsugawa, M. Niiyama, H. Noumi, Y. Oh, Y. Ohashi, T. Ohta, M. Oka, J. Parker, C. Rangacharyulu, S.Y. Ryu, T. Sawada, Y. Sugaya, M. Sumihama, T. Tsunemi, M. Uchida, M. Ungaro and M. Yosoi: Phys. Rev. Lett.* ***108*** *(2012) 092001.*
[2] Y. Oh and H. Kim: Phys. Rev. C **74** (2006) 015208.
[3] I. Hleiqawi *et al.*: Phys. Rev. C **75** (2007) 042201; M. Nanova *et al.*: Eur. Phys. J. A **35** (2008) 333.
[4] T. Nakano *et al.*: Nucl. Phys. A **670** (2000) 332; *ibid*: A **721** (2003) 112.
[5] W.C. Chang *et al.*: Phys. Rev. C **82** (2010) 015205.
[6] T. Mibe *et al.*: Phys. Rev. Lett. **95** (2005) 182001.

LEPS2: the new high-intensity GeV photon beamline BL31LEP

The GeV photon beamline at SPring-8 (LEPS) started the experiments to investigate the sub-atomic and sub-nuclear physics in 2000. The photon beam was produced by means of laser-induced backward Compton scattering from 8 GeV electrons, which was called laser-electron photon (LEP). The photon energies above 1.5 GeV are tagged by detecting recoiled electrons. The beam polarization of LEP is high and nearly 100% at the maximum energy. Polarization observables play an important role to elucidate the photoproduction mechanism. The LEPS experiments have been carried out, mainly using the forward charged-particle spectrometer, and various interesting data on hadron photoproductions, like the pentaquark Θ^+ [1], have been reported. However, the low beam intensity (~10^6/sec) and limited acceptance of the spectrometer have restricted the further investigation, especially for concluding the Θ^+ existence and determining its spin and parity. We need to measure precisely both the photoproduction process and decay process simultaneously.

The construction of a new laser-electron photon beamline, LEPS2, has started at **BL31LEP** in 2010 [2]. Based on the LEPS experience, LEPS2 aims to improve the intensity of the photon beam and to expand the detector acceptance, which requires a much larger space to place the whole detector system. A new LEPS2 experimental building has been constructed outside the experimental hall of the storage ring. By using one of four special beamlines with 30-m straight sections, which have the smallest beam divergence, the LEP beam size will be small within a few cm at the target (150-m downstream of the collision point). A schematic view of the LEPS2 facility is illustrated in Fig. 1 and a picture of the LEPS2 experimental building is shown in Fig. 2.

The high intensity beam enables data collections with high statistics and is the key of the LEPS2 project. Two methods of the laser injection are planned to produce the higher intensity beam. One of the methods is the simultaneous injection of multi-number of lasers into the 8 GeV electron storage ring. In this case the beam intensity is nearly proportional to the number of lasers. We have already tested two-laser injection at the LEPS beamline and successfully used. In LEPS2, we will employ a four-laser injection system, as illustrated in Fig. 3. The new BL31LEP vacuum chambers in the storage ring are designed to expand their apertures for the four-laser injection and the standard vacuum chambers will be replaced with them. A technique of the laser beam shaping is another method. Since the electron beam profile at the collision point is very flat, i.e., horizontally wide, the efficiency of the backward Compton scattering will be increased by an elliptical laser beam. The test of the laser-beam shaping by using a cylindrical lens was succeeded for the visible laser. Twice intensities are expected by the elliptical beam shaping with the optimized design of the optical system. We expect the beam intensity around 10^7/sec for the 355-nm lasers (the maximum LEP energy is 2.4 GeV) and 2×10^6/sec for the 266-nm lasers (the maximum LEP energy is 2.9 GeV), respectively.

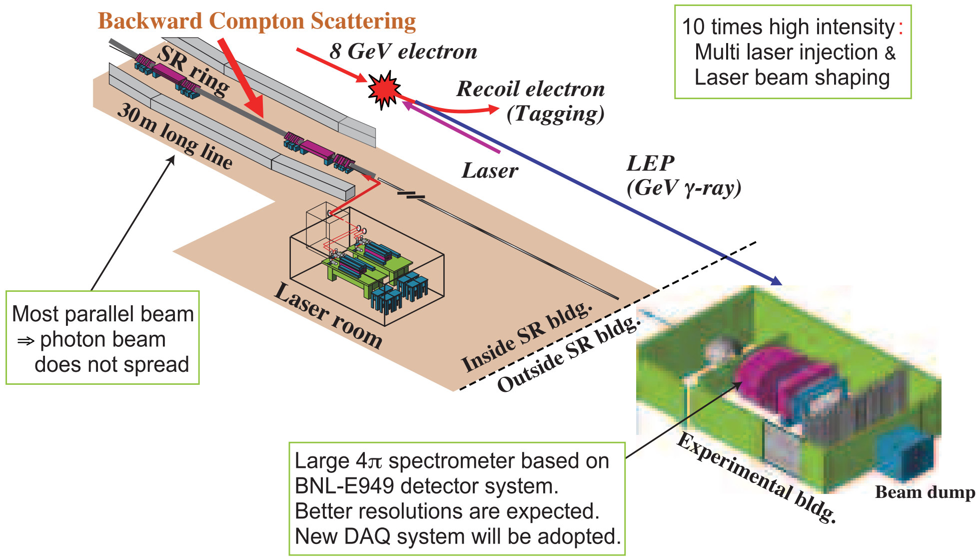

Fig. 1. Schematic view of the LEPS2 facility.

Fig. 2. Photograph of the LEPS2 experimental building. This building was constructed by the support of the RIKEN Nishina Center. A cooling system for the magnet coil is also seen in front of the LEPS2 building.

In order to measure precisely both the photoproduction process and the decay process simultaneously is one of the most important requirements for the LEP2 detector system. Unfortunately, the photoproduction cross section is small and the photon-beam experiment needs much longer beam time than that using hadron beams. Thus, the general-purpose detector with a large solid angle to detect not only charged particles but also neutral particles like photons is desirable. Such a detector, in general, needs a large cost and a long construction time. We have taken a choice to utilize the E949 detector of the Brookhaven National Laboratory (BNL) in the U.S. as such a large solid-angle detector, which was used in the kaon rare-decay experiment. In the E949 experiment, measurements of charged decay products were made in a 1-T magnetic field using an active target, a low-mass central drift chamber and a cylindrical range stack (RS) of scintillating detectors. Photons were detected in a calorimeter consisting of a lead/scintillator sandwich barrel detector surrounding the RS. Although tracking chambers should be modified for the photon-beam experiment, the inner bore size (3-m diameter and 2.2-m length) of the solenoid magnet is sufficiently large for the further optimization of the detector system. According to the simulation results for the LEPS2 experiments using the new detector system consisting of double-sided silicon strip detectors, forward drift chambers, a time projection chambers, and high-resolution time-of-flight counters, etc., we can obtain an invariant mass of Θ^+ with a 3.5 MeV resolution. The E949 magnet and detectors were disassembled and has been transported from BNL to SPring-8. The magnet has just been installed in the LEPS2 experimental building (Fig. 4). The development of detector system is still underway. After the beam commissioning, the physics data-taking will start from 2013.

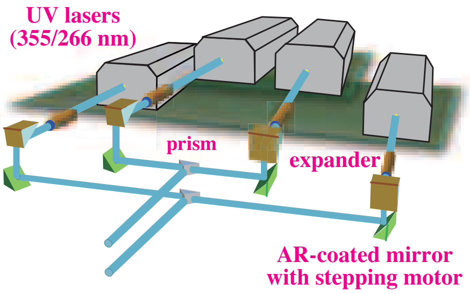

Fig. 3. Setup of the simultaneous injection of four UV Lasers. Each laser output from the beam expander is reflected at the upper mirror and the lower mirror, and then two laser beams with the same height are merged at the prism toward the injection line.

Fig. 4. Photograph of the E949 solenoid magnet installed in the LEPS2 experimental building. The diameter of the magnet yoke is 5 m and the length is 3.5 m. It is placed in the pit with the depth of 1.5 m.

Masaru Yosoi for the LEPS2 Collaboration

Research Center for Nuclear Physics (RCNP),
Osaka University

E-mail: yosoi@rcnp.osaka-u.ac.jp

References

[1] T. Nakano *et al.*: Phys. Rev. C **79** (2009) 025210.
[2] *M. Yosoi (the LEPS2 Collaboration): AIP Conf. Proc.* ***1388*** *(2011) 163.*

Accelerators & Beamlines Frontiers

BEAM PERFORMANCE

Developments and Upgrades of Storage Ring and Booster Synchrotron

Improvement of Coupling Correction

By the precise alignment of the magnets and the appropriate COD correction, at the commissioning phase of the SPring-8 storage ring, we succeeded in achieving the very small coupling of ~0.2% without correction. However, the coupling has increased over the years; thus, recently, we have corrected it and recovered the initial performance. The scheme of the coupling correction at the SPring-8 storage ring is global and is based on the perturbation theory with single resonance approximation [1-5]. The perturbation theory implies that the vertical beam size is proportional to the strength of the coupling resonance. Hence, the strengths of the skew quadrupole magnets for the coupling correction are determined so as to give the minimum of the vertical beam size [6].

After the coupling correction based on the vertical beam size response, we find that there remains the linear coupling mode in the vertical oscillation induced by the horizontal kick by the pulse bump magnets. This is because the vertical beam spread comes from the higher order coupling as well as the linear coupling. The strength of the higher order coupling may vary according to that of the linear coupling; thus, the vertical beam size is not a very suitable measure for the linear coupling correction. Then, we change the way of the coupling correction to correct the linear coupling mode in the vertical oscillation induced by the pulse bump magnet. As a result, we can almost completely eliminate the linear coupling of the beam motion at the storage ring. Figure 1 shows the process of the linear coupling correction, i.e. the change in the strength of the linear coupling mode in the vertical oscillation against the coupling driving term, where the x-axis represents the tune of the vertical oscillation, the y-axis the strength of the coupling driving term, and the z-axis the magnitude of the oscillation mode. By changing the strength of the skew quadrupole magnets appropriately, we can eliminate the linear coupling mode corresponding to the peak at the horizontal betatron tune of 0.15, as shown in Fig. 1.

To further reduce the emittance coupling, we must correct the higher order coupling as implied above. For this end, we are preparing skew sextupole magnets, which generate the higher order coupling.

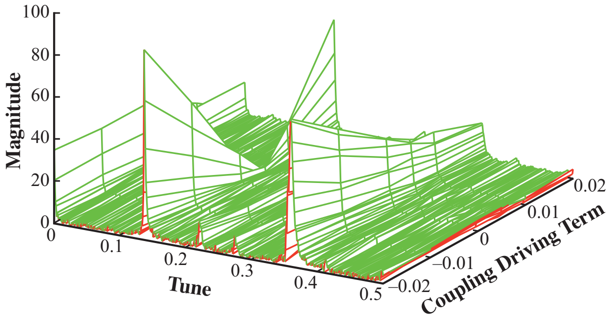

Fig. 1. Spectrum of the vertical oscillation induced by the horizontal kick of the bump magnets with the amplitude of 10 mm against the coupling driving term.

Beam Commissioning of New Lattice for Undulator Installation at LSS

The new beamline BL43LXU has been constructed in one of the long straight sections (LSSs) of the storage ring. In this beamline, small-gap in-vacuum undulators with a short period are used for generating an intense X-ray beam with very high flux and brilliance between 14.4 and 26 keV [7]. To realize a small gap of less than 6 mm, the vertical betatron function was reduced at the center of the undulator, and for this purpose, we installed two sets of quadrupole triplets in the LSS. The LSS was then divided into three subsections and, at the center of each subsection, the vertical betatron function was designed to take the minimum value of 2.5 m. By modifying the storage ring lattice locally, we inevitably lower the symmetry of the ring and this causes degradation of beam stability: the dynamic aperture and momentum acceptance become narrower, and hence the injection efficiency will be lower and the beam lifetime will be shorter. As discussed in Refs. [6,8], however, we can solve this problem and recover the beam stability by combining the schemes of betatron-phase matching, local chromaticity correction and mutual cancellation of nonlinear kicks due to sextupoles. Simulation results show that the dynamic aperture can be kept large even after modifying the lattice.

After installing the quadrupoles in March 2011, we carried out beam tuning of the new lattice and checked its performance. Machine parameters, such as dispersion and betatron functions, beam size, coupling ratio, injection efficiency and beam lifetime, were measured and compared with the design value and/or the value of the original lattice before modification. As examples of measured machine parameters, we show the horizontal and vertical betatron functions in the modified section in Fig. 2.

These were obtained by response matrix analysis, and we see a good agreement between the measured and design values. At present, the overall distortions of the betatron function along the ring are 2.3% in the horizontal direction and 2.4% in the vertical direction. These distortions were corrected with 49 auxiliary power supplies to quadrupoles, and we will soon make further corrections to suppress the distortions to less than 2%.

From the results of beam tests, we concluded that the beam performance of the new lattice is as good as the original one, and from September 2011, the new lattice has been dedicated to user operation. One undulator has been installed in the middle subsection and the other two undulators are planned to be installed within a few years. The minimum gap allowed in the user operation is 5.8 mm, while from a point of view of beam dynamics, the gap of 5.2 mm is the acceptable minimum.

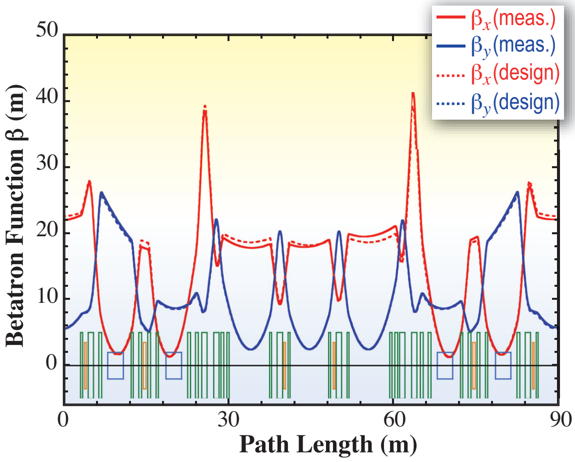

Fig. 2. Betatron function in the modified section including LSS. The solid curves are the horizontal (β_x) and vertical (β_y) betatron functions obtained by response matrix analysis and the dashed curves are the design values. Also shown in the figure is the magnet arrangement (blue: bending magnets, green: quadrupole magnets, orange: sextupole magnets).

Optimization of Lower Emittance Optics for SPring-8 Storage Ring

A design work to modify the present SPring-8 storage ring optics is in progress to provide photon beams with higher brilliance and flux density to current users. The new optics with the lower natural emittance of 2.4 nm·rad than the present optics (3.4 nm·rad) has been designed. It is noted that, in this optics, magnetic positions and polarities are maintained and magnetic fields are optimized within the specifications, so that the optics can easily be changed from the present optics without any shutdown time. The new optics has experimentally been examined at the machine study run. The machine conditions, such as the injection efficiency, the bump orbit for the injection and the vertical dispersion function, have been tuned, and the photon beam performance has been observed by utilizing the accelerator diagnostics beamlines I (BL38B2) and II (BL05SS).

The emittance was determined by measuring the electron beam size with the X-ray beam imager at the diagnostics beamline I, and by using the lattice functions estimated by response matrix analysis. The resulting value of the horizontal emittance shows a good agreement with the design value. The vertical emittance was found to be larger than that of the present optics (present: 12.55 pm·rad, new: 31.46 pm·rad), though the vertical dispersion function and the linear coupling resonance were corrected by the skew quadrupole magnets. From the results of the measurement of the betatron oscillation spectrum, it seems that the vertical emittance growth is caused by the coupling resonance induced by skew sextupole magnetic fields. We will suppress the vertical emittance by optimizing the betatron tunes and by avoiding the resonance.

The flux density of 10 keV photons from the insertion device (ID) was measured at the diagnostics beamline II. The flux density of the new optics was 1.3 times higher than that of the present optics (see Fig. 3), and this result is consistent with the theoretical calculation by SPECTRA [9], in which the above-determined emittances and estimated lattice functions are assumed. This also suggests a possibility that if we operate the ring at a lower energy of 7 GeV to save electric power, we can use the new optics to recover the photon beam performance of ID beamlines to the same level as that of the present optics at 8 GeV.

After optimizing the machine conditions e.g., the vertical emittance, the top-up injection efficiency, and the beam lifetime and verifying the photon beam performance at the beamlines, the new optics will be applied to the user operation.

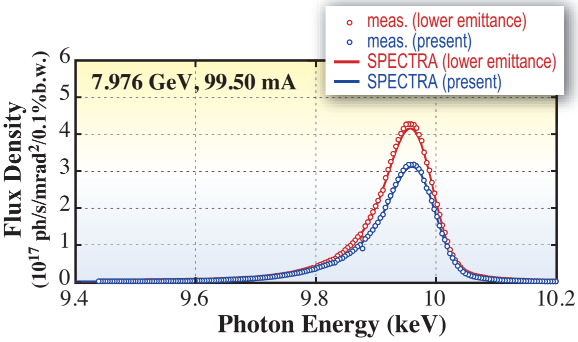

Fig. 3. Flux density of 10 keV photons for ID measured at the diagnostics beamline II (BL05SS).

Short X-ray Pulse Generation with Vertical Kicker

There are a number of requests for a short-pulsed X-ray with a pulse width of around 1 ps for a pump-probe experiment. For these requests, from 2008, we have developed a scheme of short pulsed X-ray generation with a vertical kicker in the storage ring [10,11].

A vertical kick induces a beam head-tail oscillation and finally a vertical beam tilt by synchrotron-betatron coupling due to a non-zero chromaticity [12]. By slitting a radiated X-ray pulse coming from the tilted electron bunch, we can obtain a short-pulsed radiation. Compared with other complex schemes for generating short X-ray pulses, this scheme utilizing a small vertical beam has advantages of the simplest system and the easiest handling; only a small vertical kicker and a trigger timing system are necessary. Although the radiation flux is reduced by light slitting, short-pulsed X-ray can be supplied to all the beamlines by just installing a 30-cm-long vertical kicker.

The following are the two key technical issues in obtaining short X-ray pulses: 1) development of a fast and strong kicker to realize a large tilted electron bunch and 2) understanding the correlation between the storage ring accelerator parameters, such as chromaticity, betatron tune and beam tilt, to obtain a reproducible condition that provides a suitably large beam tilt for slitting.

For the first issue, we have been developing fast-pulsed power supply systems for the vertical kicker. The power of the vertical kicker increased with the progress of high-voltage resistant switching devices: from a 157-A-amplitude, 2.6-μs-width pulse with a test-type kicker system by the year 2009, through a 338 A-amplitude, 2.5-μs-width pulse with a prototype model in 2009-2010, to a 641-A-amplitude, 1.8-μs-width pulse with a developed model, as shown in Table 1. In addition to the amplitude and width improvements, the repetition rate of the pulse increased to 200 Hz.

A high-voltage power supply controls the vertical kick power. The voltage range from 200 to 950 V corresponds to the 0.9 to 4.2 mm vertical oscillation amplitude range. The developed system can generate a maximum vertical kick of about 0.15 mrad and a pulse width as small as 2.4 μs with 200 Hz repetition rate. Figure 4 shows the excitation of the vertical beam oscillation as a function of vertical kicker power. With this system, we successfully observed a longitudinal bunch profile that tilted from 83 to 378 mrad as a function of vertical kick power, as shown in Fig. 5, by a visible-light streak camera measurement. We defined the good tilt (GT) as the bunch center located on the right axis, and the tilt angle was maximum while keeping the bunch shape aligned on a straight line. The bunch shape projected on the s-y plane twisted and deviated from a straight line when the bunch came closer to the maximum tilting angle, where s denotes the beam axis and y the vertical direction.

Table 1. The vertical kicker power progress

Item	Test model ~2009.3	Prototype model 2009.4~2010.3	Developed model 2010.4~
Max. Cur.	157 A/coil/2.9 mT	338 A/coil, 6.9 mT	641 A (2.4 μs), 13.1 mT
Pulse width	2.6 μs	2.5 μs	1.8 μs~3.6 μs
Repetition	1 Hz	1 Hz	200 Hz
No. of FET	2 parallel @ 400 V	4 parallel @ 600 V	6 parallel @ 1 kV

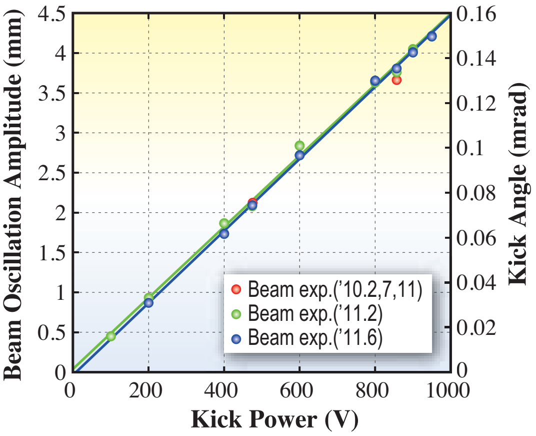

Fig. 4. Excited vertical oscillation amplitude by vertical kicker. The different color marks correspond to the results of experiments performed in different dates.

For the second issue, we have been studying the storage ring parameters to obtain the optimum tilting condition for the short-pulsed radiation by cutting out with vertical slits. By introducing the quantitative evaluation method using the measured data with a visible-light streak camera, we understood the following correlations between the beam tilt and accelerator parameters; the data used for evaluation were the beam tilt angle, the vertical shift from the light axis, and the beam tilt shape. i) The vertical chromaticity should be set to a low value of around 2 to induce the linear beam tilt, ii) there is an optimum turn number at which the linear-shape maximum beam tilt on the light axis depending on the kick power and vertical tune, iii) the reproducibility of the kick power, vertical chromaticity, and vertical tune values were required to be less than 1%, 0.1, and 0.01, respectively.

We confirmed the reproducibility of the above conditions. The X-ray pulse of 675 fs was expected by assuming the absence of emittance growth, with an achieved good tilt angle of 266 mrad (GT) with 800 V kick power, with good reproducibility. The pulse width was estimated from the tilt angle observed in the visible-light streak camera measurement. We will confirm this by a measurement utilizing an X-ray streak camera with the actual cutting out of the radiation by vertical slits.

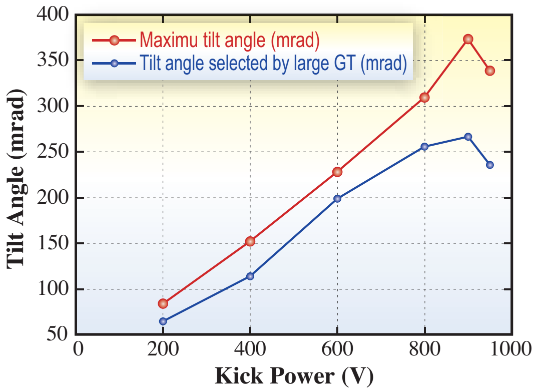

Fig. 5. Induced beam bunch tilts by vertical kicks. The red point shows the maximum tilt angle and the blue point shows the maximum tilt angle when the center of the bunch locates on the light axis keeping the linear bunch shape in the s-y plane.

Development of Bunch-by-Bunch Feedback System

The hybrid filling composed of a high-current singlet bunch with 6 mA/bunch and a bunch train with low bunch current, as shown in Fig. 6, was achieved with the sufficient stability and performance for user operation, and test operations with beamline staff members were performed.

At such filling, the horizontal and vertical beam instabilities for singlets, e.g., mode-coupling single-bunch instability, and for trains, e.g., multi-bunch instabilities by the resistive wall of IDs and cavity higher order modes, are simultaneously successfully suppressed by bunch-by-bunch feedback. The key component that can be used to achieve this is the newly developed bunch current sensitive automatic attenuator [13] placed at the front-end of the feedback [14] (Fig. 7). The feedback detects the position using the signal from the beam position monitor (BPM), calculates the kick necessary to damp the oscillation, and then drives the kicker with it. However, the BPM signal is proportional to the position and current of the bunch; therefore, its level for a high-current singlet, which is ~100 times larger than that of the trains, is so high that it leads the feedback to saturation if the BPM signal is directly fed to the feedback. The automatic attenuator detects the bunch current and controls the attenuators bunch-by-bunch base to reduce the large BPM signal level of the singlets to be controllable. This simultaneous suppression of single-bunch and multi-bunch instabilities under the high contrast of the bunch current is, to the best of knowledge, the first in the world.

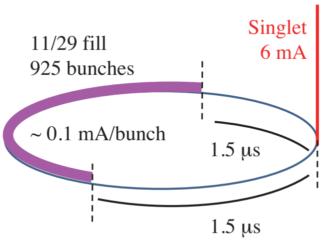

Fig. 6. Hybrid filling with high current singlet.

Also, the very fast growth of the single bunch instability (mode-coupling instability) is suppressed even under the large horizontal oscillation excited by the injection bump formation with the developed high-efficiency horizontal kickers.

Currently, the range of the filling of the trains is limited by the kicker strength, and the bunch current is also assumed to be limited. The installation of the newly developed high-efficiency high-power kicker scheduled in March 2012 is expected to increase the range of the filling and to increase the bunch current to 10 mA/bunch.

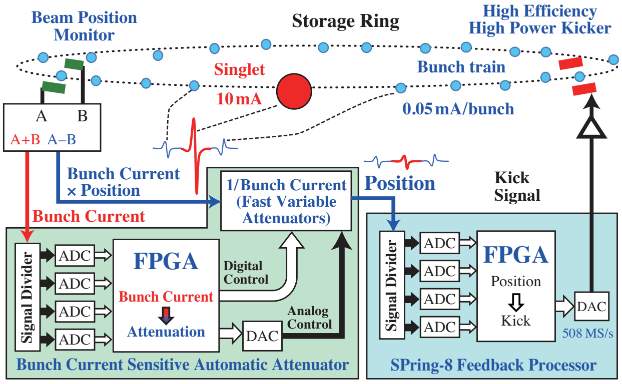

Fig. 7. Bunch-by-bunch feedback with bunch current sensitive automatic attenuator.

Development of Accelerator Diagnostics Beamlines

The fluctuation analysis of the power of the synchrotron radiation pulse [15] is a promising method for the length measurement of sub-ps short bunches. When the radiation pulse has a coherence length comparable to the source bunch length, its pulse-to-pulse intensity fluctuation is sensitive to the bunch length. The required spectral bandwidth to obtain a sufficient small coherence length for sub-ps short bunches is moderate compared with those for long bunches, making the method advantageous the length measurement of short bunches. The feasibility of the fluctuation method was studied at the diagnostics beamline I (BL38B2) by observing visible synchrotron light pulse from a dipole magnet. An interferometric filter with a bandwidth of 1 nm (FWHM) and a silicon avalanche photodiode (APD) module with an embedded amplifier were used. To reduce the number of transverse coherent modes contributing to signal fluctuations, the angular acceptance was limited by a 4-jaw slit in front of the focusing lens to the APD. The detected signals were analyzed using a fast digital oscilloscope. Figure 8 shows an example of a set of intensity histograms for 5000 measurements of a single bunch beam in an experimental 7 GeV operation. The bunch current and RF voltage were 0.2 mA and 18 MV, respectively. The fluctuation ΔI/I was calculated by subtracting the fluctuation of the baseline originating from electronic noise. The bunch length deduced by further taking into account the contributions of photon shot noise and transverse beam emittance was 11.3 ps (r.m.s.), which is consistent with that of 10.8 ps measured simultaneously with a visible light streak camera. The reduction of fluctuation for long bunches obtained by increasing the bunch current was also observed. Further studies of turn-by-turn measurement are planned by using a single-shot visible light monochromator.

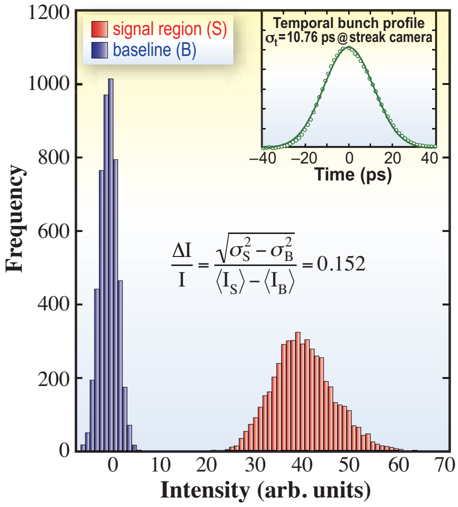

Fig. 8. Example of a set of histograms of intensities in the signal region (red) and the baseline (blue) obtained by integrating oscilloscope traces for 5000 measurements of a single bunch beam. The fluctuation of the detected power of synchrotron radiation pulse ΔI/I is calculated by subtracting the fluctuation of the baseline. The inset shows a temporal bunch profile measured simultaneously with a visible light streak camera (circles) and a fitted Gaussian curve (line).

Increasing Cooling Power of Storage Ring RF Cavities

To increase the beam lifetime, it was desired to apply a higher acceleration voltage to the RF cavities. However, the cooling ability of the cavities was the limiting factor against increasing the acceleration voltage. When the higher acceleration voltage is applied to the cavities, the wall loss of the cavities increases, which requires the increase in the cooling ability of the cavities.

To improve the cooling ability, the heat exchangers with an exchange capacity of 400 kW were replaced with those with an exchange capacity of 600 kW in March 2011. As a result, the acceleration voltage of 19.1 MV became possible, while that of 16 MV was the largest before the replacement. A study was conducted to ensure temperature stability during the 19 MV operation. The acceleration voltage applied to the cavities was gradually increased to 19 MV while observing the temperature change. The cooling water temperatures at the cavity inputs were kept constant within 0.01°C around the 30°C set value up to the 19 MV operation.

As for the configuration of the RF system, there are four RF stations in the storage ring, which are named A, B, C and D stations. In each RF station, a 1 MW klystron delivers the RF power to 8 single cell cavities. The exception is the A station, where 2 klystrons are placed and each supplies the power to 4 cavities. The acceleration voltage is the sum of the voltages evenly supplied by all the four stations. For the 16 MV operation, each station supplies 4 MV, while for the 19.1 MV operation, each station supplies 4.8 MV. If the voltages of three stations are summed, the total voltage is 12 MV before the improvement of the cooling system, while it is 14.4 MV after the improvement. With the 14.4 MV operation, the reduction in beam lifetime is tolerable for the 100 mA user operation. Before the improvement, only about 70 mA could be stored in the storage ring with three-station feeding. Therefore, one of the advantages of increasing the cooling ability is the possibility of maintaining the beam current, even if one of the four RF stations fails. Another advantageous effect of the higher acceleration voltage is a longer Touschek lifetime for the same amount of a single bunch current, or larger single bunch current for the same Touschek lifetime, which can provide a larger number of options in filling patterns in the storage ring.

On the other hand, in spite of the improvement of the higher RF voltage ability, the actual operation has been performed with 16 MV or 14.4 MV acceleration voltage, since the electricity-saving requirement was issued. The cause was the lack of electricity due to from the shutdown of most of the nuclear power plants in Japan after the disastrous earthquake on March 11, 2011 and the successive occurrence of accidents in the Fukushima Dai-ichi nuclear power plant. We expect that the situation of electricity supply will get better and we will have the full benefit of the improvement of the RF cavity cooling system in the near future.

Developments and Upgrades of Linac

Research and Development of Beam Position Monitors for Second-Order Moment Measurement

We are installing new BPMs at the SPring-8 linac, which measure the transverse second-order moments of electron beams, as an enhancement of non-destructive beam diagnosis during top-up injection.

To design the system, we first constructed the comprehensive theory for BPMs [16]. This theory presents an analysis and design method for a stripline-type BPM that detects the multipole moments of a charged particle beam. A numerical analysis based on the finite difference method was also carried out to calculate the electric fields in a BPM.

According to this design method, we have developed six-electrode BPMs with circular (Fig. 9) and quasi-elliptical cross sections for non-dispersive and dispersive sections, respectively. The results of the numerical calculations show that the second-order moment can be detected for beam sizes >0.42 mm (circular) and >0.55 mm (quasi-elliptical). The actual beam sizes are >0.5 mm in the non-dispersive sections and >0.75 mm in the dispersive sections, that is, they are sufficiently large to enable accurate measurements of the second-order moments using these BPMs.

Fig. 9. Six-electrode BPM with circular cross section.

The measurement of a second-order moment requires a good measurement accuracy of about 10^{-4}. Therefore, we developed a low-noise signal processor (Fig. 10) with six channels. The previous signal processor with four channels contained sample-and-hold circuits that generate large sample-and-hold noises. The new signal processor, however, does not employ any sample-and-hold circuit; thus, fast and low-noise analog-to-digital converters (LTC2393, LINEAR TECHNOLOGY) directly acquire signals from the peak-hold circuits. The dynamic range of the signal processor is finally increased to 80 dB, and the maximum signal-to-noise (S/N) ratio is 80 dB.

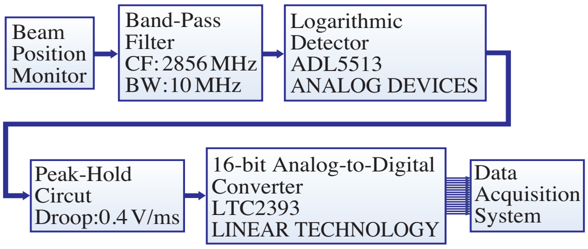

Fig. 10. Block diagram of signal processor (one of six channels).

Haruo Ohkuma, Shigeki Sasaki and Hirofumi Hanaki

SPring-8/JASRI

E-mail: ohkuma@spring8.or.jp

References

[1] G. Guignard: Phys. Rev. E **51** (1995) 6104.
[2] M. Takao: Proc. of EPAC'06, Edinburgh, UK, p.1975.
[3] M. Takao: Phys. Rev. ST Accel. Beams **9** (2006) 084002.
[4] M. Masaki *et al*.: Proc. of EPAC'08, Genoa, Italy, p.3035.
[5] M. Masaki *et al*.: Phys. Rev. ST Accel. Beams **12** (2009) 024002.
[6] SPring-8 Research Frontiers 2009, p.153.
[7] A. Baron: SPring-8 Information **15** (2010) p.14.
[8] K. Soutome *et al*.: Proc. of IPAC'10, Kyoto, Japan, p.4497.
[9] T. Tanaka and H. Kitamura: SPECRA code ver. 9.02 (2012).
[10] C. Mitsuda *et al*.: Proc. of SRI'09, Melbourne, Australia, AIP Conference Proc. 1234, p.193.
[11] C. Mitsuda *et al*.: Proc. of PAC'09, Vancouver, Canada, p.1171.
[12] W. Guo *et al*.: Phys. Rev. ST Accel. Beams **10** (2007) 020701.
[13] K. Kobayashi *et al*.: Proc. of ICALEPCS 2009, Kobe, Japan, p.659.
[14] T. Nakamura *et al*.: Proc. of ICALEPCS 2005, Geneva, Switzerland, PO2.022-2.
[15] M. S. Zolotorev and G. V. Stupakov: SLAC-PUB-7132, March 1996.
[16] K. Yanagida *et al*.: Phys. Rev. ST Accel. Beams **15** (2012) 012801.

NEW APPARATUS, UPGRADES & METHODOLOGY

RISING (Research & Development Initiative for Scientific Innovation of New Generation Batteries) beamline

"Energy" and "environment" become more important for sustainable development in society. Novel developments in the environmental and energy technologies are expected in the next few decades. In a future "smart city", the commodification and dissemination of natural energy into society, such as solar cells and wind power generation, the rejuvenation of infrastructure for transportation due to the commercial deployment of plug-in hybrid vehicles and electric vehicles, and the implementation of smart grid communication in the electrical network will be realized, which will bring us a completely different society. Rechargeable batteries are key components in all these technologies. In other words, a technical leap in rechargeable batteries will play a vital role in green innovation. A lithium-ion battery is typical of the rechargeable batteries.

Japan firstly commercialized lithium-ion batteries in 1990s. Japanese technologies and market share have dominated the world market until early 2000s. In the late 2000s, however, Korea and China have rapidly caught up in the market of compact size rechargeable batteries of portable devices and taken over the first place. In the next decades, Japanese technological predominance in the growing market for large-scale rechargeable batteries for plug-in hybrid vehicles and electric vehicles is being undetermined.

In these unpredictable circumstances, the Research & Development Initiative for Scientific Innovation of New Generation Batteries (RISING) project funded by NEDO (New Energy and Industrial Technology Development Organization) has been started in October 2009. This is the all-Japan project under the robust industry-government-academia collaboration. The final goal of this project is to take back the top share in the global market through the development of post-lithium-ion battery as well as further improvements in the performance of the existing lithium-ion batteries. The following three missions are being focused in the RISING project. They are (1) the innovation of lithium-ion batteries technologies through the strong cooperation among universities, industries and national institutes, (2) the development of truly innovative rechargeable batteries far surpassing the present lithium-ion batteries, and (3) the establishment of a new interdisciplinary community for rechargeable batteries. On the basis of the present project establishments, a new concept for innovative batteries will be introduced and embodied, and also an energy density of 300 Wh/kg will be reached in a laboratory scale by 2015, which will be the obligatory first step in attaining rechargeable batteries with an energy density of 500 Wh/kg in 2030.

Through understanding of the properties in electrodes, electrolyte solutions, and especially the electrode/electrolyte interfaces of rechargeable batteries during battery reactions are indispensable. Thus, the research beamlines specialized for analyses of battery reactions are being built in the most advanced Japanese synchrotron research facility, SPring-8. Using the RISING beamline, we will explore why, under the policy of "Begin with the Basic" as the project leader Prof. Ogumi mentioned.

A typical lithium-ion battery consists of a negative electrode made of graphite, a positive electrode made of a lithium cobalt oxide, a separator diaphragm and an electrolyte containing lithium salt in an organic solvent. Theoretically, lithium ions are extracted from a layered oxide and intercalated into graphite during charge and reversely move from graphite to oxides during discharge. In a working battery, however, the negative and positive electrodes are composed of powders of active materials mixed with a small amount of binder and carbon powder as it is shown in Fig. 1. For example, lithium ions are extracted from graphite and move into the positive electrode through the separator in the discharge process. The migration time of lithium ions from the separator to the aluminum current collector in the positive electrode varies from 10 to 100 s. The time for the insertion of lithium ions into an active material that is controlled by the diffusion rate, a phase transition, and structural

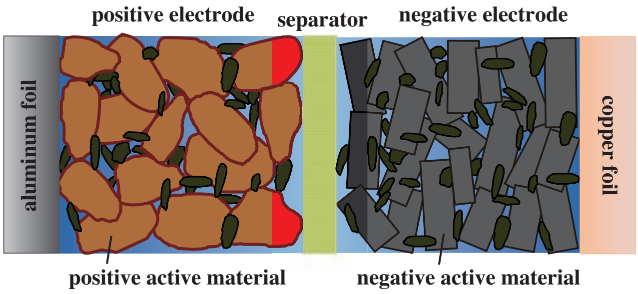

Fig. 1. Schematic drawing of the cross section of a pair of positive and negative electrodes in a commercial lithium-ion battery.

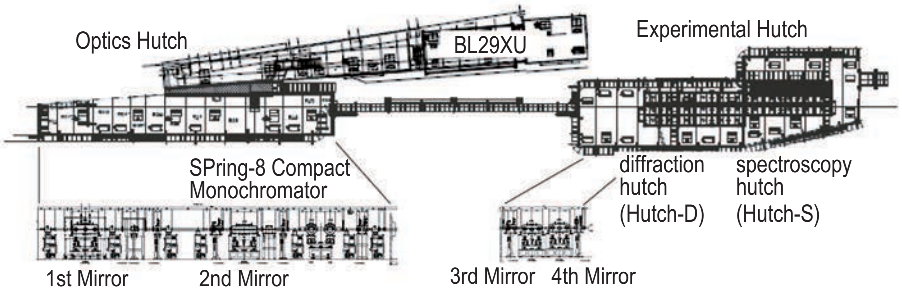
The Kyoto University RISING beamline (BL28XU)

Fig. 2. Floor plan of the RISING beam line (BL28XU) in the SPring-8 experimental hall.

relaxation during lithiation and delithiation, ranges from 10 ms to 1 s. In addition, the migration time through the interface layer between the active material and the electrolyte ranges from 100 μs to 1 ms. Namely, because of this distinctive structure of composite electrodes, the total battery reaction in the composite electrodes in commercial batteries is composed of various elementary reaction processes with different time constants, which induces a time-dependent reaction distribution in a limited space of 100 μm between the two electrodes. This reaction heterogeneity during battery charge/discharge cycles will be thoroughly investigated by special time-resolved experimental techniques for the innovation of the battery performance and the improvement of the cyclic degradation.

Quasi-monochromatic synchrotron beams are obtained from the tapered in-vacuum undulator in the RISING beamline. This beamline consists of one optics hutch and two experimental hutches, as shown in Fig. 2. By using the four mirrors installed for horizontal and vertical focusing processes, and a cut-off of higher harmonics, about 10 to 100 μm^2 focused and very low divergent beams are obtained at the sample in the lower experimental hutch. Either quasi-monochromatic or monochromatic beams from 5 to 30 keV are chosen by the SPring-8 compact monochromator with a Si 111 channel-cut crystal, which is located at the lower side of the second mirror in the optics hutch. In the upper experimental hutch, mainly time-resolved diffraction experiments are carried out during battery reactions. In these diffraction experiments, the anomalous X-ray scattering phenomena will be especially utilized for element- and valence-selective diffraction measurements. Furthermore, the grazing incident X-ray scattering method will also be adopted in order to analyze the structural change at the active material and electrolyte interface during the reaction in a film model battery. In the lower experimental hutch, the spectroscopy experiments by time-resolved XAFS and hard X-ray photoemission spectroscopy (HXPES) measurements are carried out. In addition to the conventional time-resolved XAFS measurements, the quick XAFS, the dispersive XAFS, and the time- and space-resolved XAFS with submicron focused beams by a Kirkpatrick-Baez (KB) mirror will be planned in this spectroscopy hutch. By combining these diffraction and spectroscopy measurements with various measurement times and probe sizes in Fig. 3, we will study complex phenomena in model batteries and commercial ones.

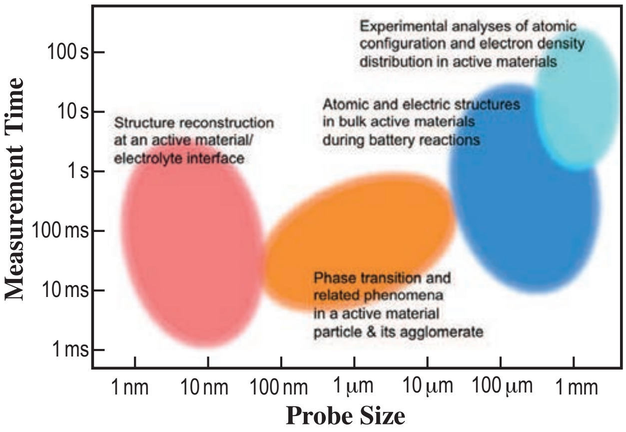

Fig. 3. Mapping of various phenomena in battery materials projected on a graph of measurement times and probe sizes used in the RISING beamline.

Eiichiro Matsubara

Department of Materials Science & Engineering,
Kyoto University

E-mail: matsubara.eiichiro.6z@kyoto-u.ac.jp

A high-flux undulator beamline for high-resolution inelastic X-ray scattering

Non-resonant, high-resolution, hard-X-ray, inelastic scattering is, *in principle*, a nearly ideal tool for the condensed matter scientist. The technique directly probes the electronic density-density correlation function, the dynamic structure factor, $S(\mathbf{Q}, \omega)$, over correlation lengths comparable to unit cell sizes, with resolution that can be at the meV level. These scales are interesting as they are the energy scales of phonons, and low-lying electronic excitations, and also because it is the interplay between low-energy excitations that governs the behavior of many of the most interesting and technologically relevant materials. When one also notes that the brilliance of a third generation synchrotron radiation source allows micron-scale beam sizes to be achieved, one has, again in principle, a very powerful probe of the dynamical behavior of condensed matter systems.

The above optimistic picture, however, lasts only until the count-rate limitations of real experiments are encountered. While modern synchrotron radiation sources provide huge fluxes (~10^{13} or even ~10^{14} hard X-ray photons/s after a typical monochromator), the first thing an IXS experiment does is reduce this flux by several orders of magnitude to achieve the necessary resolution. Thus, while straining to take full advantage of modern third-generation sources, the final flux on the sample in a high-resolution IXS experiment is more characteristic of a first generation source, and the experiments are correspondingly limited. A survey of published data will show that

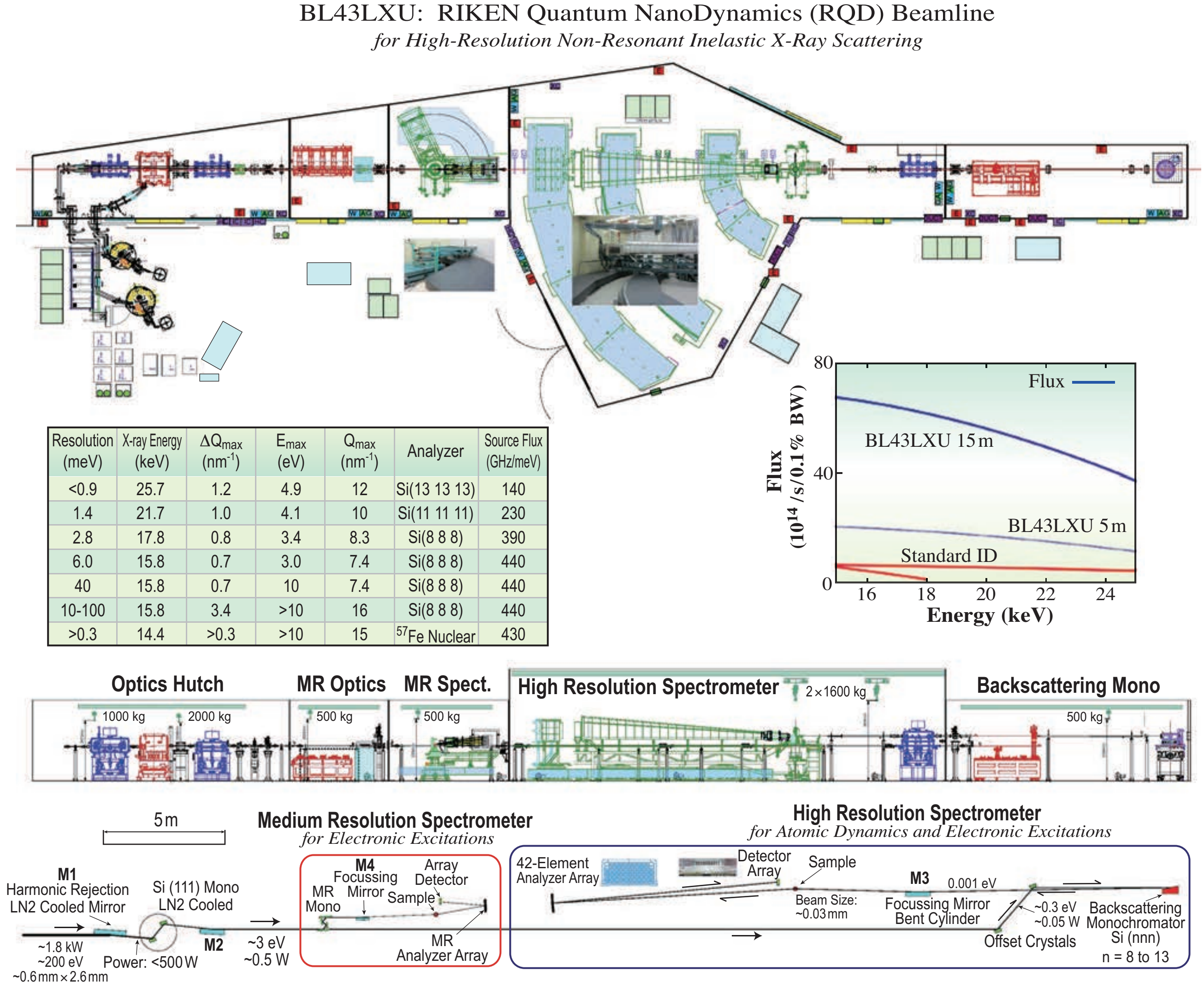

Resolution (meV)	X-ray Energy (keV)	ΔQ_{max} (nm^{-1})	E_{max} (eV)	Q_{max} (nm^{-1})	Analyzer	Source Flux (GHz/meV)
<0.9	25.7	1.2	4.9	12	Si(13 13 13)	140
1.4	21.7	1.0	4.1	10	Si(11 11 11)	230
2.8	17.8	0.8	3.4	8.3	Si(8 8 8)	390
6.0	15.8	0.7	3.0	7.4	Si(8 8 8)	440
40	15.8	0.7	10	7.4	Si(8 8 8)	440
10-100	15.8	3.4	>10	16	Si(8 8 8)	440
>0.3	14.4	>0.3	>10	15	^{57}Fe Nuclear	430

Fig. 1. BL43LXU layout.

essentially all work to date using non-resonant IXS with better than ~100 meV resolution, investigates only the very strongest excitations, phonons, and, even then, experiments are often count-rate limited.

On this basis, discussions began some years ago about creating a very intense beamline for high resolution IXS. The essential idea was to take advantage of SPring-8's strengths – the 8 GeV electron energy, in-vacuum undulator technology and the availability of long straight sections – to make a uniquely powerful beamline, with extremely high flux on the sample. This beamline, the RIKEN Quantum NanoDynamics (RQD) beamline was funded by MEXT, through RIKEN beginning in 2009. In October of 2011, RIKEN allocated funds to largely complete it.

The target of the beamline is the investigation of dynamics with ~1 to ~100 meV energy resolution, with particular emphasis on high-resolution measurement of electronic excitations, and, then, studies of atomic dynamics of difficult systems. The beamline (see the Fig. 1) is expected to provide about 1 order of magnitude more flux onto the sample than a standard ID and will increase parallelization of data collection by about a factor of 3. It will operate at energies between 15 and 25 keV, with resolutions between 1 and 100 meV. A new design for the medium-resolution spectrometer will allow ~20 meV resolution with while a collecting large solid angle and with comfortable space for sample environment.

The RQD is now in the first stages of commissioning. The initial 1/3 of the insertion device has been installed, and, at the end of 2011, the mechanics for the first, high resolution, spectrometer was installed. Commissioning is expected to extend into the spring, with first experiments taking place in the summer. Thanks to the additional funding from RIKEN, the completion of the insertion device is planned for early in 2013. Commissioning of the medium resolution spectrometer will begin late in 2012.

The initial targets for the beamline are, the extension of high-resolution studies into the field of electronic excitations, for example, to investigate the excite states of orbital order, and several problems in atomic dynamics, including phonons in high-temperature superconductors.

Additional details can be found at:
http://user.spring8.or.jp/sp8info/?p=3138

Alfred Q. R. Baron

SPring-8/RIKEN•JASRI

E-mail: baron@spring8.or.jp

The SR nanobeam analysis center for green/nanotechnologies at BL37XU and BL39XU

The recent progress in X-ray focusing mirrors has achieved a 7 nm X-ray beam [1], showing a path towards X-ray analyses at a sub-10 nm resolution. On the way to the ultimate nanobeam applications, to achieve practical uses of a ~100 nm beam is a current issue to meet requirements in the wide fields of scientific and industrial research studies. Under the circumstances, we upgraded two hard X-ray beamlines, BL37XU (Trace Element Analysis) and BL39XU (Magnetic Materials) for nanobeam applications. At the new experimental stations constructed, an X-ray nanoprobe of 100×100 nm^2 size is provided, and X-ray absorption fine structure (XAFS) measurement, X-ray magnetic circular dichroism (XMCD) spectroscopy, and X-ray fluorescence (XRF) analysis at the ~100 nm spatial resolution are routinely available. These nanoscale spectroscopic analyses would meet the strong demands for structural, chemical, electronic, and magnetic characterizations of novel functional materials with the nanostructure, used in fuel cells, rechargeable batteries, nonvolatile data storage devices, solar cells, and biomaterials, which are key devices of green/nanotechnologies.

For the practical use of the X-ray nanoprobe, the position stability and available photon flux of the focused beam were the primary requirements. To achieve this goal, we made a number of technical developments in the X-ray optics and experimental environments [2]: i) dedicated experimental hutches with a precise temperature control system, ii) Si double-crystal monochromators using a liquid-nitrogen cryogenic cooling system with an improved X-ray beam stability, and iii) X-ray focusing mirrors in the Kirkpatrick and Baez (KB) geometry with a large aperture (see Fig. 1).

The BL37XU and BL39XU beamlines were extended to 76 and 74 m from the source, by the outside wall of the experimental hall, where the dedicated experimental hutches were built. X-ray focusing mirrors were placed in the hutches, and the long distance from the source to the mirrors allowed a small focused beam size with a long working distance. The hutches are equipped with thermal shielding walls with heaters and an air-conditioning system for a precise control of the temperature within ±0.02°C a day.

We achieved a marked improvement in the stability of the monochromatic X-ray beam as well as of the focused nanobeam by adopting the newly developed Si double-crystal monochromators with a cryogenic cooling system. A liquid-nitrogen-cycling refrigerator was optimized in terms of several operation parameters such as the rotation frequency and gas pressure so that the vibration of the Si crystals was minimized. We developed a low-vibration tubing for the liquid nitrogen coolant, effective thermal shields between the Si crystals and the positioning stages, and a high-precision temperature control system, and so on. These means have significantly reduced the fluctuation in the intensity of the monochromatic X-ray beam to 1/10 or less than that for the existing cryogenic monochromators.

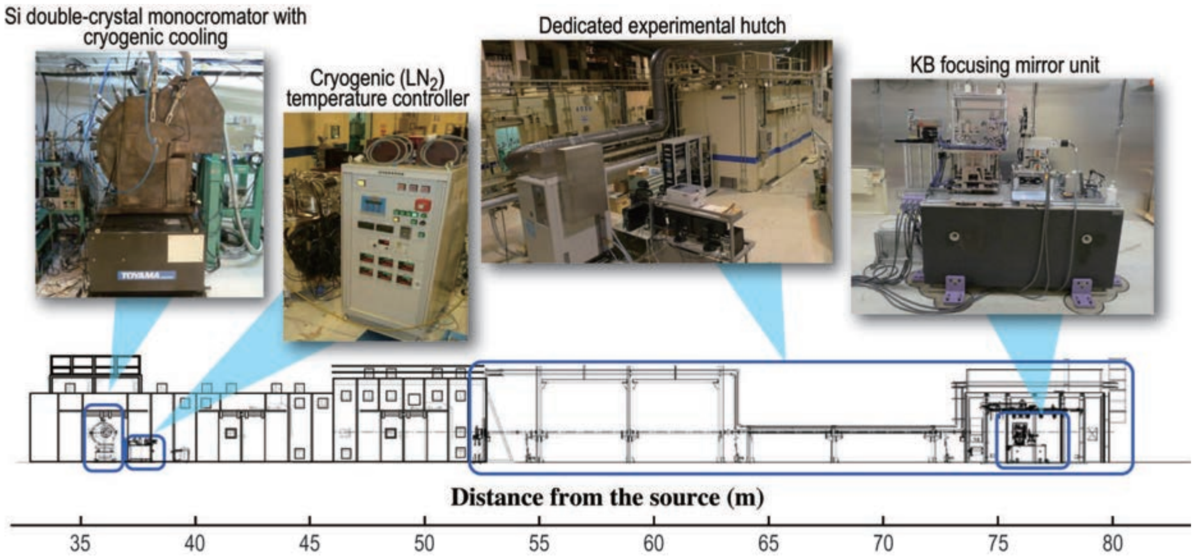

Fig. 1. Upgraded components for the X-ray nanoprobe end station at BL39XU.

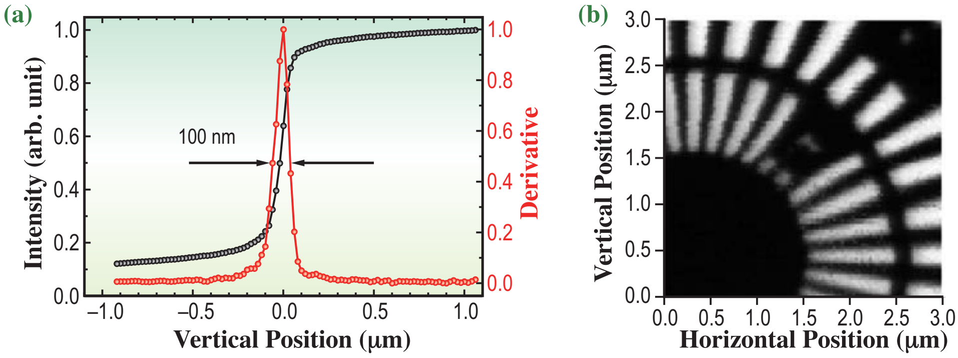

Fig. 2. **(a)** Focused beam profiles in the vertical direction. **(b)** Scanning image of a Ta test chart having the patterns of a 100 nm line and space. The measurement conditions were 100×100 pixels with a 30 nm/pixel step and the acquisition time of 0.1/s pixel.

The KB focusing optics are consists of two elliptical mirrors coated with Rh. The mirrors were fabricated by an elastic emission machining method developed by Osaka University and RIKEN [3]. With the large aperture of 0.76(H)×1.2(V) mm^2, the mirrors can accept almost half of the incoming X-ray flux and focus it into a bright spot on the sample. The mirror units and the sample stages were arranged together on a robust base block made of granite for the isolation of the system from floor vibrations.

Figure 2(a) shows the profiles of a focused X-ray beam in the vertical direction, obtained using the knife-edge method with a gold wire at an X-ray energy of 12.4 keV at BL37XU [2]. The focused beam size of 100(H)×100(V) nm^2 (FWHM) was achieved with the use of the secondary source slits [16(H)×6(V) µm^2] placed just behind the monochromator. The available flux was estimated to be 10^9 photons/s/0.01%bw in the spot. For applications requiring more intense beams, a flux of 10^{12} photons/s/0.01%bw in a 300×300 nm^2 spot can be obtained with the use of the secondary source slit only in the horizontal direction (the vertical slit is open). Figure 2(b) shows a scanning image of a Siemens star test chart, illustrating that our nanoprobe successfully resolves 100 nm line and space patterns. Note that the nearly distortion-free image has proved the high stability of our nanobeam. The apparatus installed in the upgrade, i.e., focusing mirrors, are fully compatible with the X-ray-energy tunability (5–16 keV) and polarization tunability, which are the original useful features of the beamlines.

The X-ray nanoprobe stations were open for public use in May 2011. XAFS measurement at a 100 nm resolution and XMCD experiments at a 300 nm resolution have routinely been carried out. Some preliminary results in several advanced fields have been obtained in the first and second user cycles since the nanoprobe stations opened: Nano-XAFS analysis has revealed the chemical-state distribution inside a single catalyst particle with a size of ~1 µm. The *in situ* observation of the structural transition in submicron-sized phase-change devices by nano-XAFS/EXAFS analysis is ongoing. Bit-patterned magnetic recording media were studied to characterize the elemental, chemical and magnetic states of a single magnetic nanodot using XRF, XAFS, and XMCD techniques, respectively. The magnetization reversal of individual nanodots of perpendicular magnetization was investigated by element-specific XMCD magnetization measurements at external fields up to 1.2 T.

In summary, we have upgraded the two existing beamlines installing the nanobeam capability. Local XAFS/XMCD spectroscopy in a 100 nm region and scanning XAFS/XMCD imaging with a similar resolution will be a powerful tool for the characterization of new functional materials for green/nanotechnologies. Our technical improvements achieved through the upgrade will allow a rapid installation of additional nanoprobe beamlines that will provide different promising applications including nanodiffraction, nanoimaging, and nano-hard-X-ray photoemission spectroscopy in the upcoming years.

Motohiro Suzuki*, Yasuko Terada and Haruhiko Ohashi

SPring-8/JASRI

*E-mail: m-suzuki@spring8.or.jp

References

[1] H. Mimura *et al.*: Nature Phys. **6** (2010) 122.
[2] T. Koyama *et al.*: SPIE Proc. **8139** (2011) 813901.
[3] H. Mimura *et al.*: Appl. Phys. Lett. **90** (2007) 051903.

Cheating the diffraction limit using X-ray nonlinear diffraction

Is there any ingenious method to see finer details than the diffraction limit? In 1878, E. Abbe first pointed out the diffraction limit that the spatial resolution of imaging system is determined ultimately by the half-wavelength, $\lambda/2$ [1]. Nevertheless, scientists have challenged to see smaller structure than $\lambda/2$. Recently a spatial resolution of around $\lambda/10$ was achieved by using the dispersion of Plasmon [2]. Further improvement along this scheme is, however, not feasible due to, for example, the collective nature of Plasmon, that requires a certain volume containing many electrons.

Now we propose a novel method to realize an atomic resolution in the optical region [3]. The unprecedented high resolution unveils the local optical response: how electrons in materials respond to the light. We think that the difficulty in improving the spatial resolution arises from the use of a single wavelength. Instead, we consider using two beams with different wavelengths and separating the spatial resolution from the probing wavelength of interest. However, even if we use two beams, they behave independently without giving any new information. The key piece is X-ray parametric down-conversion (PDC), which makes the two beams cooperate to image the local optical response. Our method does not beat the diffraction limit, but shifts it to X-rays, freeing the probing light from the Abbe's constraint.

X-ray PDC is one of the second order nonlinear optical processes, where an X-ray pump photon decays spontaneously into two photons (signal and idler). We investigate X-ray PDC for the idler photon in the optical region, and find that it is the optical response at the idler frequency that determines the efficiency of X-ray PDC. The underlying mechanism is considered to be the Doppler shift of the pump photon by oscillating electrons driven by the optical idler photon [3,4]. Thus, the X-ray second order nonlinear susceptibility, $\chi^{(2)}$, relates to the optical linear susceptibility, $\chi^{(1)}$, at the idler frequency. In addition, the spatial information obtained by X-ray PDC has the atomic resolution, because it is an X-ray coherent process. When we combine these two features, we expect that we can see the optical response at the idler frequency with the atomic resolution by X-ray PDC.

In fact, X-ray PDC is observed as a nonlinear

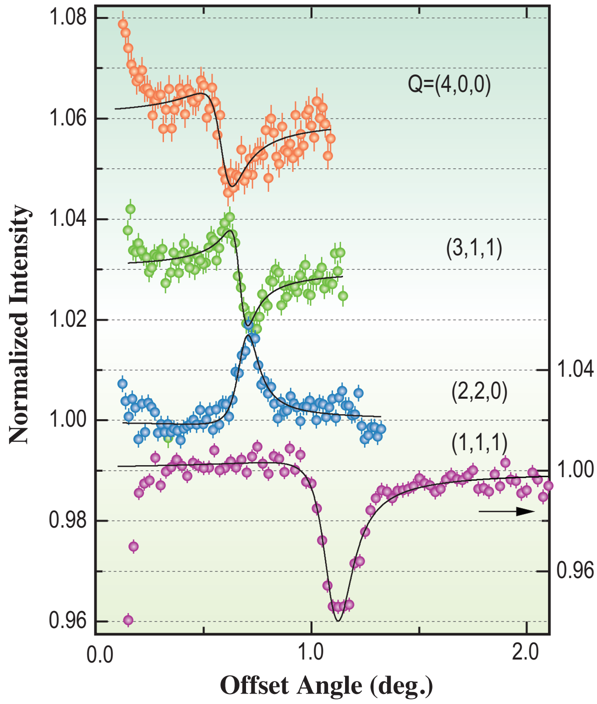

Fig. 1. Rocking curves of nonlinear diffraction measured for the signal wave of X-ray PDC with diamonds. The pump and the idler energies are 11.107 keV and 60 eV. The signal intensity is normalized to the background due to the Compton scattering.

diffraction. Figure 1 shows the rocking curve of the nonlinear diffraction, which is the glancing angle dependence of the intensity of the signal wave. The nonlinear crystal is synthetic type IIa diamonds. The idler photon energy is 60 eV in the extreme-ultraviolet (EUV) region. The asymmetric peaks are due to the Fano effect between X-ray PDC and the background Compton scattering [5]. From the Fano spectra, we estimate, $\chi^{(2)}_{\mathbf{Q}}$ the **Q**th Fourier coefficient of $\chi^{(2)}(\mathbf{r})$ [6]. Then, $\chi^{(2)}_{\mathbf{Q}}$ is converted to $\chi^{(1)}_{\mathbf{Q}}$, the **Q**th Fourier coefficient of $\chi^{(1)}(\mathbf{r})$ [3]. The reconstruction of $\chi^{(1)}(\mathbf{r})$ from $\chi^{(1)}_{\mathbf{Q}}$ follows the standard procedure of X-ray structural analysis.

Figure 2 shows the section of $\chi^{(1)}(\mathbf{r})$ on the (110) plane which contains both the atoms and the covalent bonds. The resolution of the reconstruction, 0.54 Å, is determined by the largest |**Q**| given by the 400 reflection. On the other hand, 203 Å (60 eV) is the idler wavelength at which $\chi^{(1)}(\mathbf{r})$ represents the optical response. As a result, the resolution in the wavelength unit reaches as fine as $\lambda/380$. This is the highest one ever achieved.

The reconstructed $\chi^{(1)}(\mathbf{r})$ reveals the local optical response of diamonds to the EUV light. The core electrons at the atomic site oscillate in phase to the EUV light, whereas the bonding electrons respond in the opposite phase. The opposite sign of oscillation between the atomic and the bonding electrons is due to the different resonance energies, 289 eV and 12 eV, respectively. The contribution from boding electrons is larger than that from the core electrons. So the bonding electrons determine the optical response at 60 eV. We note that these observations are found to be qualitatively consistent with the Lorentz model [3].

The present method opens a new window into the optical property of solids, and adds new structural information to the optical response. Such a microscopic structure cannot be obtained with the conventional spectroscopy, because of the longer wavelength of light than the size of the unit cell. In other words, the charge response at longer wavelengths can be investigated only in the vicinity of the origin in the momentum space. Now, X-ray PDC into optical region can access the local optical response and the charge response over the whole momentum space for better understanding of the optical property of solids.

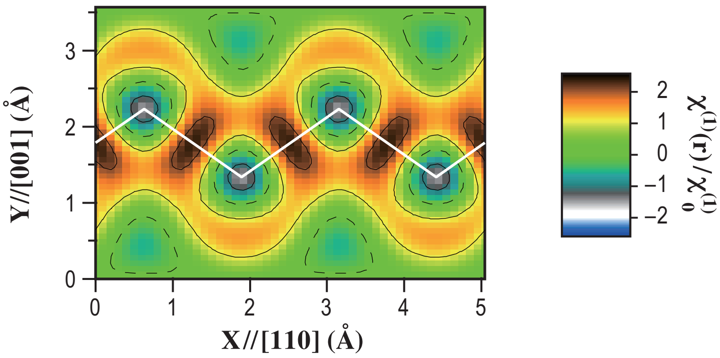

Fig. 2. Reconstructed $\chi^{(1)}(\mathbf{r})$ of diamonds at 203 Å (60 eV) on the (110) plane. The resolution is 0.54 Å, corresponding to $\lambda/380$. The white solid lines indicate the bonds between carbon atoms.

Kenji Tamasaku

SPring-8/RIKEN

E-mail: tamasaku@riken.jp

References

[1] M. Born and E. Wolf: Principles of Optics (Cambridge University Press, 1999).
[2] S. Kawata *et al*.: Nature Photon. **3** (2009) 388.
[3] *K. Tamasaku, K. Sawada, E. Nishibori and T. Ishikawa: Nature Phys. 7 (2011) 705.*
[4] I. Freund and B.F. Levine: Phys. Rev. Lett. **25** (1970) 1241.
[5] K. Tamasaku and T. Ishikawa: Phys. Rev. Lett. **98** (2007) 244801.
[6] K. Tamasaku *et al*.: Phys. Rev. Lett. **103** (2009) 254801.

Direct observation of X-ray induced atomic motion using SR-based STM

The interaction of X-ray photons with materials plays an essential role in various fields such as imaging, diffraction and spectroscopy. As a higher throughput of measurements requires a higher photon density of synchrotron radiation (SR), the strong irradiation effects become an important issue either for applications to the fabrication process [1] or for radiation damage that limits the structural studies [2]. Although the X-ray induced reaction or damage on materials by SR has long been observed under various conditions, the direct observation of the atomic motion induced by hard X-rays in ultrahigh vacuum (UHV) has not yet been reported at an atomic scale, about which we report here the results obtained by scanning tunneling microscopy (STM). Also, we visualized successfully the tracks of the atomic motion [3].

To observe precisely the X-ray induced atomic motion, it is essential to compare the atomic structure on the same surface area before and after X-ray irradiation. The *in situ* SR-based STM (SR-STM) system has already been installed for our past research studies dedicated to a chemical analysis with nanometer resolution assisted by element-selective core-hole excitation using SR (Fig. 1) [4]. To overcome the small efficiency of core excitation by hard X-rays, we installed the STM system at **BL19LXU** having a 27 m long undulator and focused the beam two-dimensionally to increase the photon density. To avoid an excessive heat load by X-rays, small incident beams (ϕ10 μm) were used and controlled with an accuracy of ~1 μm under the total reflection condition that can effectively reduce the X-ray penetration depth.

The Ge(111)c-(2×8) surface is a standard well-defined stable clean surface and BL19LXU can effectively excite the Ge atoms. During X-ray irradiation, the STM tip was under the tunnel-off condition and the sample bias (Vs) was kept at 0 V. Also, the STM observations were performed only under the beam-off condition. Thus, the atomic motion was not produced by the electric field around the STM tip under X-ray irradiation, but solely by X-ray irradiation.

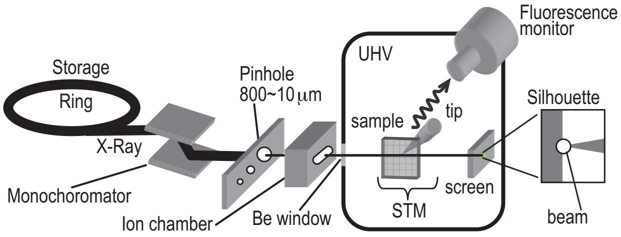

Fig. 1. Schematic view of the SR-STM system.

Figure 2 shows the STM images in the same area on a Ge(111) clean surface before (upper) and after (lower) X-ray irradiation for 3 min (11.119 KeV > Ge *K*-absorption edge, photon density = 2×10^{15} photons/s/mm^2). The low-magnification images (left) show that the X-ray induced atomic motion rate is so low that structural changes are hardly detectable, even by other surface analysis techniques, such as diffraction analysis giving average information. However, the magnified images (right) revealed a clear change in the atomic structures, as indicated by the open circles. The atomic motions are found to occur mainly around defects on the surface, differently from a close-packed 2×8 structure. The origin of the atomic motion is then suggested to be an effect of surface diffusion (the number of atoms does not change after X-ray irradiation), which is different from desorption caused by core excitation [1].

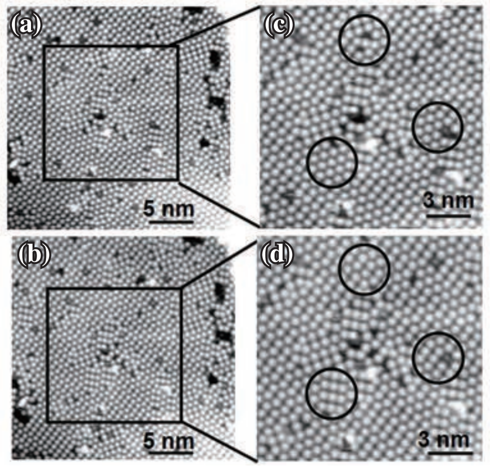

Fig. 2. STM images with different scales within the same area on a Ge(111) clean surface obtained before (**a**, **c**) and after (**b**, **d**) X-ray irradiation (3 min). Open circles indicate the area in which the Ge atomic shift is observed. Vs= 2.0 V and tunneling current It= 0.3 nA.

Next, we developed a technique to recognize atomic motions directly to comprehend their behavior. By merging the STM images obtained before and after X-ray irradiation, the atomic motion track could be newly presented as several continuous lines (Fig. 3), whereas other stable atoms are shown as spheres. The appeared atomic track is the direct evidence and visualized information of the atomic diffusion at an atomic scale.

Using the visualized atomic track, we compared quantitatively dependences of the atomic motion on some parameters to consider the origin of the atomic motion that can be attributed to quantum effect (core-hole excitation) or the thermal effect [1]. For core excitation, in Fig. 3 showing the number of atoms (~1000), the total number of core-hole events is estimated to be ~40 for 3 min of irradiation in one STM image. The observed atomic motion rate (~100 atoms in total track length), for which one core-hole event corresponds to a 2.5 atomic motion, appears very high. The next possibility is then the atomic motion induced by electronic transitions stimulated by impacts of photo-, Auger and secondary electrons generated multiply by one core-excitation event.

For the thermal effect, in which the core excitation is included as the average absorption effect for mass volume, the local increase in temperature (ΔT) on the surface was calculated from the incident heat flux, the specific heat of the sample, and the thermal diffusion rate. The photon density dependence (from 1.2×10^{15} to 4.8×10^{15} photons/s/mm^2 for 11.119 KeV) of the atomic motion rate was found as the moving atomic number increased from 30 to 70 per STM image, where ΔT was estimated to be 23 and 92 K, respectively. (The incident energy dependence of the atomic motion rate was not apparently found owing to a relatively low photon density.) It is worth comparing our results with previous conventional thermal STM observations on the same surface [5], where the atomic motion was found to occur in the form of domain (Fig. 4) and begin at ~220°C. However, our results show the atomic track having a local chain distribution. This locality in diffusion may be attributed to the anisotropy of the surface structure, and probably the origin of atomic motion, to core excitation. In fact, considering ΔT (92 K from RT), our atomic motion rate appears very high in comparison with the past report. Many aspects on the atomic motion still require to be discussed in detail.

The radiation damage by Coulomb explosion has long been an important issue in XFEL. In our experiments, even at a much lower photon density (12~48 photons/s/Å^2 at 11.119 keV) than the conventional barrier derived from the dynamics of damage analyses [2], the surface structure was found to start to break, which has never been observed directly for hard X-rays in UHV at RT. The new feature is probably marginal for the brilliance from the long undulator with focusing. Actually, the photon density lower than 1×10^{14} photons/s/mm^2 scarcely induced the atomic motion. Our observation of the damage barrier has potential importance as an indicator for a damage threshold in the near future for analyzing low-dimensional materials. On the other hand, the dense X-rays are also suggested to have new applications, such as direct X-ray lithography. Also, our results show a new application of the *in situ* SR-STM system. Our method for observing the atomic track will serve to provide new information not only for the effects of the radiation process on various optical devices in new X-ray generators, such as XFEL, but also for basic science by observing photon-matter interactions.

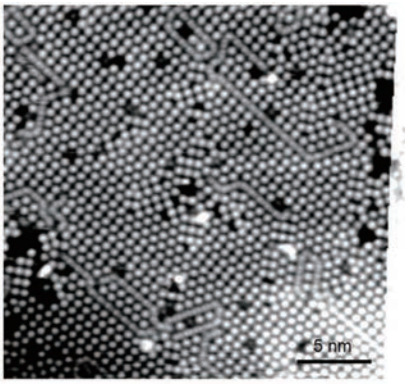

Fig. 3. Merging the STM images before (Fig. 2(**a**)) and after (Fig. 2(**b**)) X-ray irradiation. The atomic motion tracks can be newly presented.

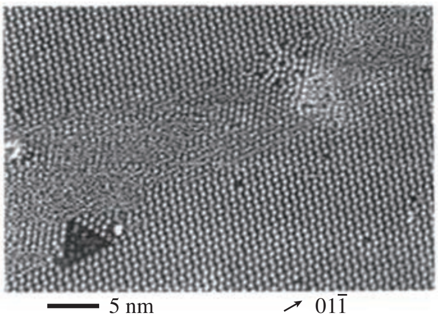

Fig. 4. STM image of the Ge(111) clean surface obtained at 235°C. A band of disordered surface area, located at a domain boundary, extends through the center of the image [5].

A. Saito[a,b,c,*], Y. Kuwahara[a,b] and M. Aono[d]

[a] Dept. of Precision Sci. and Tech., Osaka University
[b] SPring-8/RIKEN
[c] PRESTO, JST
[d] WPI Center, NIMS

*E-mail: saito@prec.eng.osaka-u.ac.jp

References

[1] F. Sato *et al*.: J. Electrochem. Soc. **145** (1998) 3063.
[2] R. Neutze *et al*.: Nature **406** (2000) 752.
[3] *A. Saito, T. Tanaka, Y. Takagi, H. Hosokawa, H. Notsu, G. Ohzeki, Y. Tanaka, Y. Kohmura, M. Akai-Kasaya, T. Ishikawa, Y. Kuwahara, S. Kikuta, and M. Aono: J. Nanosci. Nanotechnol.* ***11*** *(2011) 2873.*
[4] A. Saito *et al*.: J. Synchrotron Rad. **13** (2006) 216.
[5] R.M. Feenstra *et al*.: Phys. Rev. Lett. **66** (1991) 3257.

Two-dimensional approach to fluorescence yield XANES measurement using silicon drift detector

Since the pioneering work by Jaklevic *et al.*, in 1977 [1], fluorescence yield (FY) detection has been widely performed to measure the X-ray absorption near-edge spectroscopy (XANES) spectrum in the hard X-ray region. On the other hand, FY detection is not a mainstream technique in the soft X-ray region because fluorescence decay is a minor channel for low-Z elements. For example, the fluorescence decay probability for an oxygen 1*s* core hole is less than 1%, in which case an electron yield measurement is a common technique used to obtain the XANES spectrum in the soft X-ray region. Although the yield of fluorescence decay is low, FY detection has a notable advantage, that is, a higher signal-to-background ratio than the transmission method and the electron yield detection method [2]. In particular, selective X-ray fluorescence detection using an energy-dispersive detector, which is called partial fluorescence detection (PFY), allows us to obtain XANES spectra for trace elements with concentrations lower than 100 ppm.

A recent progress in the case of soft X-ray detector and the highly brilliant soft X-ray beamline make up for the low fluorescence yield of light elements, and the application of FY is spreading greatly even in the soft X-ray XANES measurement. In the present research, we demonstrated the capabilities of a two-dimensional (2D) fluorescence yield measurement in the X-ray absorption near-edge spectroscopy in the soft X-ray region [3]. The 2D measurement is a correlation plot between the excitation energy and the spectrum obtained by a secondary spectrometer. The noteworthy advantage of 2D data collection is that it allows us to carry out a full survey of XRF spectra and to determine the extracting area after the XANES measurement. In conventional procedures of PFY measurement, the XRF information was lost because the PFY was determined by selecting a region of interest (ROI) prior to the XANES data collection. Only a signal corresponding to the ROI is recorded. This is problematic for the PFY measurement of complex samples in which overlaid peaks obscure the fluorescence. This issue is more serious in the soft X-ray region where absorption edges of different elements are close to each other and where fluorescence lines overlap. In such cases, it is indispensable to store the entire fluorescence spectrum at every single point of the XAFS scan, and to validate the obtained spectrum after the XAFS measurement. In current procedures, the highly brilliant soft X-ray beam and high-count-rate performance of an X-ray detector allow us to collect complete "X-ray fluorescence yield maps" instead of ROI data, even for low-concentration samples of less than 0.1 wt%.

Experiments were carried out at the c-branch of soft X-ray photochemistry beamline **BL27SU**. The XANES spectra were measured by undulator gap scanning as well as monochromator scanning to maintain the maximum intensity of the incident soft X-rays, and by scanning the widths of the entrance and exit slits to maintain a constant resolving power.

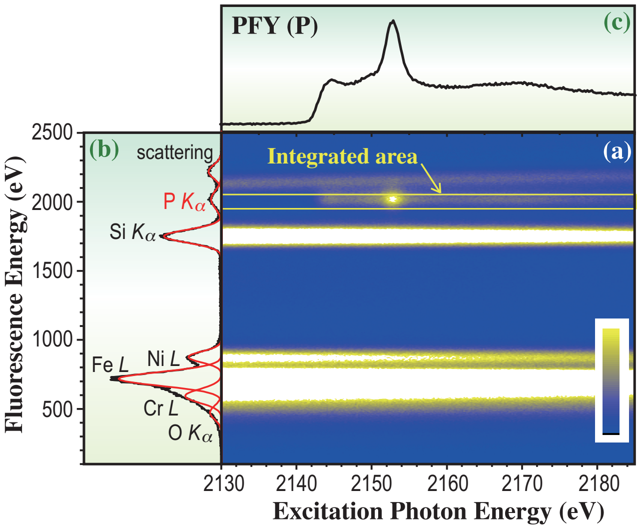

Fig. 1. **(a)** Two-dimensional fluorescence spectrum for SS304 obtained in the P *K*-edge region, **(b)** XRF spectrum obtained at 2190 eV, and **(c)** PFY spectrum of phosphorus extracted from an integration of fluorescence counts in the range of 1940–2020 eV.

The fluorescence signal was detected using a single-element silicon drift detector (SDD). The entrance window mounted in front of the detector is a MOXTEK AP3.3 window consisting of an ultrathin polymer film. The SDD module equipped with the AP3.3 window enables an X-ray transmission to the detector with an energy as low as the B K_α X-ray energy (170 eV), i.e., our detector is applicable to the XANES experiment at a boron *K*-edge.

The XANES spectrum of phosphorus in stainless steel (SS) 304 was measured using the 2D map approach. Generally, in SS304 samples, C (<0.08%), Mn (<2.0%), Si (<1.0%), P (<0.045%), and so forth, are present as minor components, while Cr (18~20%), Ni (8~10.5%) and Fe are present as major components. Figure 1 shows (a) the 2D spectrum, (b) the XRF spectrum obtained at 2190 eV, and (c) the PFY spectrum extracted from the 2D spectrum. The XRF spectrum can be fitted well to seven Gaussian peaks, as indicated by red lines in Fig. 1(b). The four peaks observed in the range of 400–1000 eV originate from the *K*-shell ionization of oxygen and the L_{23}-shell ionization of the main elements, Cr, Fe, and Ni. On the other hand, the fluorescences from Si and P *K*-shell ionizations can be observed at approximately 1720 and 2000 eV, respectively.

The FYs from the main elements and Si form horizontal stripes in Fig. 1(a), because these elements have no absorption edges in this energy region. On the other hand, only the FY of phosphorous changes drastically. Figure 1(c) shows the PFY spectrum extracted from the integration in the range of 1940–2020 eV. The obtained PFY spectrum closely resembles the XANES spectra of iron phosphate. Although the XANES spectrum is clearly observed in the PFY mode, it cannot be found in the TEY spectrum (data not shown). In the TEY mode, the imperceptible signals from the minor components are buried in the higher background signals originating from the excitation of major components, because Auger decay is the dominant decay channel following the *L*-shell ionization of 3*d*-transition metals.

The patterns formed by elastic scattering appear as diagonal stripes in the 2D map. The energy of the phosphorus K_α (2013.7 eV) is about 30 eV lower than the binding energy of the phosphorus 1*s* electron (2045.5 eV). Therefore, the diagonal line does not directly intersect with the phosphorus K_α line in the XANES region. However, elastic scattering contributes to the baseline of the XANES spectrum. Figure 2 shows the PFY spectra extracted from varying integration regions. This procedure corresponds to the PFY measurement with different ROI window selections. In principle, the baseline of the PFY spectrum should be flat in the pre-edge region, because the photon energy is insufficient to excite or ionize the P 1*s* electron and therefore cannot eliminate the K_α fluorescence from phosphorus. However, Fig. 2 indicates that the baseline shape depends on the integrated area owing to the contamination of elastic scattering. The contamination is especially apparent when the higher fluorescence energy region is included in the PFY spectrum extraction as exhibited by its effects on the baseline in the pre-edge region and the tilt of the PFY baseline. This phenomenon could be a significant issue for subtraction of the baseline in the data analysis procedures of the EXAFS measurement. The recording of the full XRF is necessary for a correct data treatment. The present research indicates that the selective fluorescence detection improves sensitivity to the imperceptible signal from phosphorus.

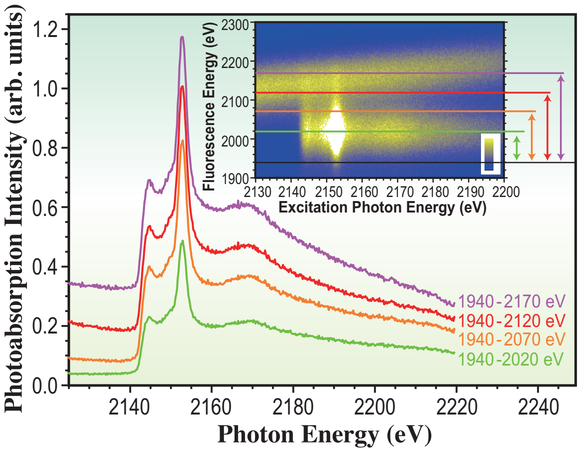

Fig. 2. Extraction region dependence of the PFY spectrum of SS304 in the P *K*-edge region. The inset shows the expanded 2D-XANES spectrum of SS304 in the P *K*-edge region and anintegrated region for each extracted PFY spectrum.

Yusuke Tamenori* and Tetsuya Nakamura

SPring-8/JASRI

*E-mail: tamenori@spring8.or.jp>

References

[1] J. Jaklevic *et al.*: Solid. State. Commun. **23** (1977) 679.
[2] J. Stöhr: NEXAFS Spectroscopy, Springer, Berlin, (1992).
[3] *Y. Tamenori, M. Morita and T. Nakamura: J. Synchrotron Rad.* ***18*** *(2011) 747; Y. Tamenori, M. Morita and T. Nakamura: J. Synchrotron Rad.* ***18*** *(2011) 944.*

Facility Status

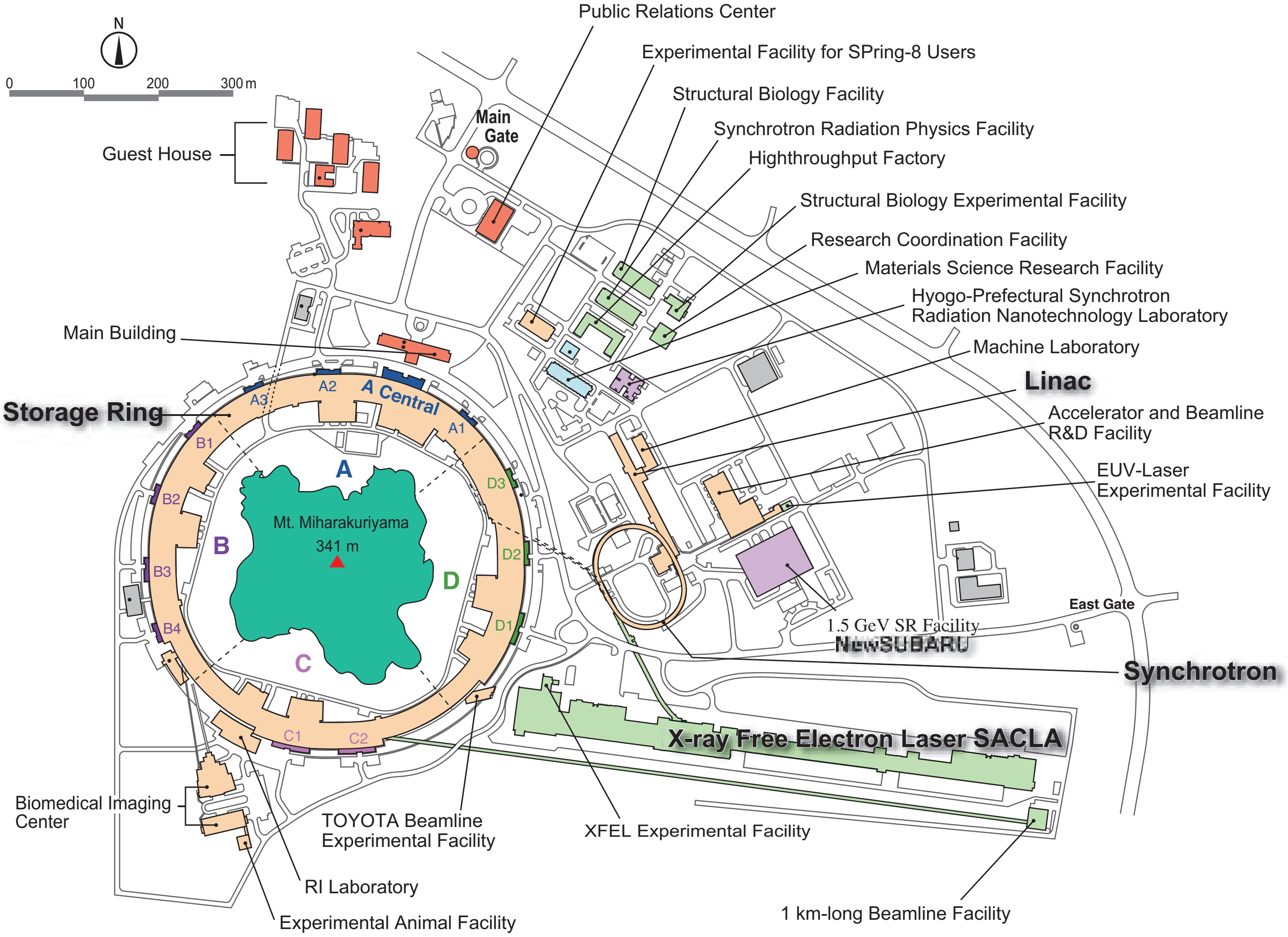

I. Introduction

The Great East Japan Earthquake, which occurred at 2:46 pm on March 11, 2011, devastated those prefectures facing the Pacific Ocean in East Japan and seriously damaged several major scientific research facilities around the area.

Among the facilities affected were the Photon Factory in Tsukuba, J-PARC, and JRR-3 in Tokai. They have been the essential members of Quantum Beam Facilities in Japan. As an immediate assistance, SPring-8 established the Priority Program for Disaster-Affected Quantum Beam Facilities. It was intended to support the users of the Photon Factory facing difficulties to conduct their research proposals. The program, however, kept its door open to the J-PARC and JRR-3 users as well, provided that they could appropriately convert their proposals from neutron-beam-based to X-ray-beam-based. The users from the Photon Factory, J-PARC, and JRR-3 amounted to 297, 4, and 17, respectively, while those facilities were under the recovery process.

It was probably the first incident that the network among the Quantum Beam Facilities in Japan functioned substantially. The experience became a valuable lesson of forming the “Quantum Beam Platform,” which should be a collective research environment in order for science and technology to be a driving force for disaster recovery and reconstruction.

More specifically, science and technology is now strongly required to challenge the energy and environmental problems in light of the current social situation. In this respect, there were three noteworthy events in 2011, symbolizing the proactive stance of SPring-8 on these problems.

Firstly, SPring-8 began acting as a satellite center of the Low-Carbon Research Network funded by the government to promote advanced low-carbon research. Newly installed in 2011A to fulfill this mission were a nanobeam X-ray absorbing spectrum analyzer and a fluorescence analyzer at BL39XU and BL37XU, respectively. When combined with the X-ray nanobeams generated by SPring-8, it is expected that these advanced analyzers will play a central role as advanced tools for atomic and molecular structural/electronic/compositional analysis and control, being essential for the advancement of green/nanotechnologies.

Secondly, in order to further activate the use of SPring-8 towards low carbon and healthcare innovations, the Green/Life Innovation Field has been designated as a new priority field for two years from 2011B. To attract potential users contributing to the innovations, briefing sessions were organized in major cities of Japan.

Lastly, in the direction of the outreach effort, the 3rd SPring-8 Conference was held in Tokyo, November 2011, entitled “Revitalization of Japan driven by leading edge technology and diversity of SPring-8 –towards the solution of the energy problem–.” The conference intensively covered the research projects directly linked to new-generation batteries, solar energy and fuel cells. To clarify the raison d'etre of SPring-8 in the current situation of Japan, the final session was dedicated to a panel discussion, the conclusion of which was that SPring-8 should keep the position as a COE of photon science for academia-industry collaboration by the synergy of cross-disciplinary utilization, especially for overcoming the difficult time of Japan.

In 2011, SPring-8 saw not only the disaster recovery efforts but also another way of making a social contribution. Recently, it has become possible to investigate nanoscale pieces of evidence at the scene of crimes by exploiting the X-ray nanobeam technology at SPring-8. To scientifically uncover the truths, the Japan Synchrotron Radiation Research Institute (JASRI) established the Nano-Forensic Science Group in December 2011. This group is expected to make a large contribution to realize a secure and safe society, not only developing an analysis technology by fully utilizing the nanotechnology applications of SPring-8, such as X-ray fluorescence, X-ray absorption fine structure, and X-ray structural analyses, but also building new databases that help in the identification of evidence materials.

By employing an advanced IT technology, it became possible to virtually generate an experimental environment on a personal computer located far from SPring-8. This Remote Experiment system has been regarded as a promising approach that could further accelerate the utilization of SPring-8, by eliminating the disadvantage of the physical location of SPring-8. In 2011B, the operation of Remote Experiment for public use was commenced domestically, first mainly targeting protein crystallography. Remote Experiment is highly desired, especially in industrial applications, because it enables users to save time and money to travel to/from SPring-8. Carefully considering the needs of users and the safety of the experiments, SPring-8 will gradually extend the application fields of Remote Experiment.

It is highly important for SPring-8 not only to promote its utilization but also to feedback research outcomes to the society. To ensure the feedback process more strictly, the conditions for non-proprietary use were amended from 2011B in such a way that users must publish their research outcomes in refereed journals or equivalents within three years after the end of the research term. In case the users are unable to comply to this condition, they must submit either a SPring-8 research report or a corporate technical journal article refereed at their home institutions. Needless to say, the new condition is not to discourage challenging research at all, but is based on the general knowledge that even unsuccessful/failed experiments could aid other users. More importantly, SPring-8 should strengthen its accountability about the utilization of its valuable X-ray beams for the society through this approach.

As the Registered Institution for Facilities Use Promotion for SPring-8, JASRI organized the 1st International Advisory Committee, July 26-28, 2011, in order to follow its recommendations on the (1) scientific/technological attainments, (2) future plan, (3) balance between academia and industry, (4) interrelationship between academia and industry, (5) manpower shortage, (6) proposal selection system, (7) publication statistics, (8) remote access, (9) beamline portfolio, (10) human resource development, (11) user community, (12) contract beamline, and (13) quantum beam platform. Together with comments regarding overall management structure, the committee deliberately made recommendations and suggestions on each issue, the report of which is open to public at http://www.jasri.jp/ja/enterprise/jiac/pdf/jiac2011_e.pdf.

Also formed in 2011 were two specific review committees for evaluating the Budding Researchers Support Program and the Priority Industrial Application Program. The first program was highly evaluated because it had been playing an essential role of effectively supporting and motivating promising doctoral students. In accordance with the suggestion made by the review committee, the program will expand its applicant eligibility to master students from 2012A, and will offer expert consultation to those students who are less experienced with SPring-8. The second program was also given high marks for an excellent prior consultation by coordinators and for the dedicated experiment support by beamline staff. From 2012A, it will be relaunched as the Priority Industry Creation Program to facilitate industry-academia-government cooperation in technological development.

There was a steady progress in the SPring-8 upgrade plan, which intended to drastically enhance the capabilities of the present SPring-8 and promote the synergetic use with SACLA. The workshop on the SPring-8 upgrade plan was held at SPring-8 in April 2011, especially from the perspective of accelerator and storage ring development. The key concepts of the upgrade plan are (1) an ultimate storage ring in a hard X-ray regime, (2) synergetic use with an X-ray free electron laser, and (3) an energy-efficient facility. In the near future, the utilization of the upgraded SPring-8 will pioneer a whole new science. To realize these concepts and reach the real goal discussed in the previous symposiums and workshops, the working group has intensively worked on the upgrade plan and released a preliminary report for the SPring-8 upgrade plan in January 2012.

II. Machine Operation

The operation statistics for the last five fiscal years are shown in Fig. 1. In FY2011, the total operation time of the accelerator complex was 4918.6 h. The operation time of the storage ring was 4904.2 h, 82.8% of which (4058.5 h) was made available for SR experiments. The downtime resulting from failure accounted for 1.4% (57 h) of the total user time; in November 2011, a great loss of user time was incurred owing to cooling water leak from the cooling pipe to the vacuum vessel of the in-vacuum undulator (ID47); consequently, a user time of 27.15 h was cancelled for the suspension of machine operation. Since FY2004, top-up injection was introduced. Concerning user service operation, a high availability (ratio of net user time to planned user time), e.g., 98.5%, was achieved in FY2011. The total tuning and study time of 803 h was used for machine tuning, to study the linac, booster synchrotron and storage ring, and also for the beamline tuning and study.

Operations in two different filling modes were provided for the following user time: 62.5% in the several-bunch mode, such as the mode of 29 equally spaced trains of 11 bunches, and 37.5% in the hybrid filling mode, such as the mode of 1/14-partially filled multi-bunch with 12-isolated bunches. In FY2011, there was no operation in the multi-bunch mode. The several-bunch mode was the dominant filling mode. The 203-bunch mode and the mode of 29 equally spaced trains of 11 bunches reached 30.3% and 32.2% of the total user time, respectively. For the hybrid filling mode, 1.0, 1.4, 1.6, or 3.0 mA is stored in each isolated bunch. An isolated bunch impurity better than 10^{-10} is routinely maintained in the top-up operation. Table I shows a summary of the useful beam parameters of the storage ring. Table II shows a summary of the beam filling patterns.

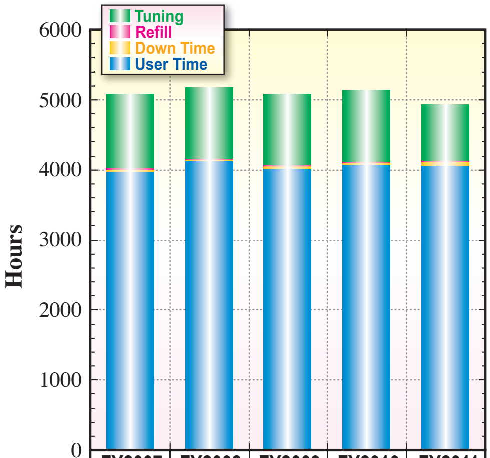

	FY2007	FY2008	FY2009	FY2010	FY2011
Accelerator Operation Time	5063.6	5150.1	5150.1	5125.6	4918.6
Storage Ring Operation Time	5056.3	5133.3	5035.4	5096.3	4904.2
Tuning & Study (Acc. & BL)	1065.0	1008.2	1019.1	1026.6	803
Refill	9.5	10.1	6.3	5.0	4.4
Down Time	29.2	31.0	34.8	27.5	57
Mean Time Between Failures	148.4	143.2	122.9	178.4	117.7
Achieved User Time	3969.3	4110.9	4014.9	4071.6	4058.5
Planning User Time	4008.0	4152.0	4056.0	4104.0	4120.0
Availability (%)	99.0	99.0	99.0	99.2	98.5

Fig. 1. Operation statistics for the last five fiscal years.

Table I. Beam parameters of SPring-8 storage ring

Energy [GeV]	**8**
Number of buckets	**2436**
Tunes (ν_x / ν_y)	**40.14 / 19.35**
Current [mA]:	
single bunch	**12**
multi bunch	**100**
Bunch length (σ) [psec]	**13**
Horizontal emittance [nm·rad]	**3.5 ***
Vertical emittance [pm·rad]	**6.9 ***
Coupling [%]	**0.2**
RF Voltage [MV]	**16**
Momentum acceptance [%]	**±3 (±240 MeV)**
Beam size (σ_x / σ_y)* [μm]	
Long ID section	**297 / 10**
ID section	**303 / 6**
BM1 section	**108 / 13**
BM2 section	**115 / 14**
Beam divergence (σ_x' / σ_y')* [μrad]	
Long ID section	**13 / 0.7**
ID section	**12 / 1.1**
BM1 section	**57 / 0.6**
BM2 section	**74 / 0.6**
Operational chromaticities (ξ_x / ξ_y)	**+1 / +1****
Lifetime [h] :	
100 mA (multi-bunch)	**~200**
1 mA (single bunch)	**~20**
Horizontal dispersion [m]:	
Long ID section	**0.103**
ID section	**0.107**
BM1 section	**0.032**
BM2 section	**0.070**
Fast orbit stability (0.1 – 200 Hz) [μm]:	
horizontal (rms)	**~4**
vertical (rms)	**~1**

* Assuming 0.2% coupling
** With bunch-by-bunch feedback

Table II. Filling patterns

	bunch current (mA)	life time (h)
203 bunches	0.5	25 ~ 30
11 bunch-train × 29	0.3	35 ~ 50
1/7 - filling + 5 single bunches	3.0 (single)	18 ~ 25
1/14 - filling + 12 single bunches	1.6 (single)	18 ~ 25
2/29 - filling + 26 single bunches	1.4 (single)	18 ~ 25
4/58 - filling + 53 single bunches	1.0 (single)	18 ~ 25

III. Beamlines

The SPring-8 storage ring can accommodate up to 62 beamlines: 34 insertion devices, 4 long undulators, and 24 bending magnets. At the time of writing, 54 beamlines are in operation, covering a wide variety of research fields of synchrotron radiation science and technology. The beamlines are classified into the following four types.

(1) Public Beamlines
(2) Contract Beamlines
(3) RIKEN Beamlines
(4) Accelerator Diagnostics Beamlines

There are now 26 public beamlines in full operation. The beamlines that are proposed and constructed by external organizations, such as universities, research institutes, and private companies, are called contract beamlines and exclusively used by the contractors for their own research purposes. At present, 17 contract beamlines are in operation. The contract beamlines include the NSRRC BM (BL12B2) and NSRRC ID (BL12XU) beamlines, which were constructed by the National Synchrotron Radiation Research Center in Taiwan. In 2012A, the operation of RISING beamline (BL28XU) was started. Currently, two contract beamlines are under construction. The beamlines constructed by RIKEN are called RIKEN beamlines, which are used for RIKEN's own research activities. RIKEN is now operating nine RIKEN beamlines and is constructing one beamline. In addition, two accelerator diagnostics beamlines are in operation.

To display the beamline portfolio of SPring-8, the beamline map is shown in Fig. 2 together with the their classification. The research field of each beamline is presented in Table III.

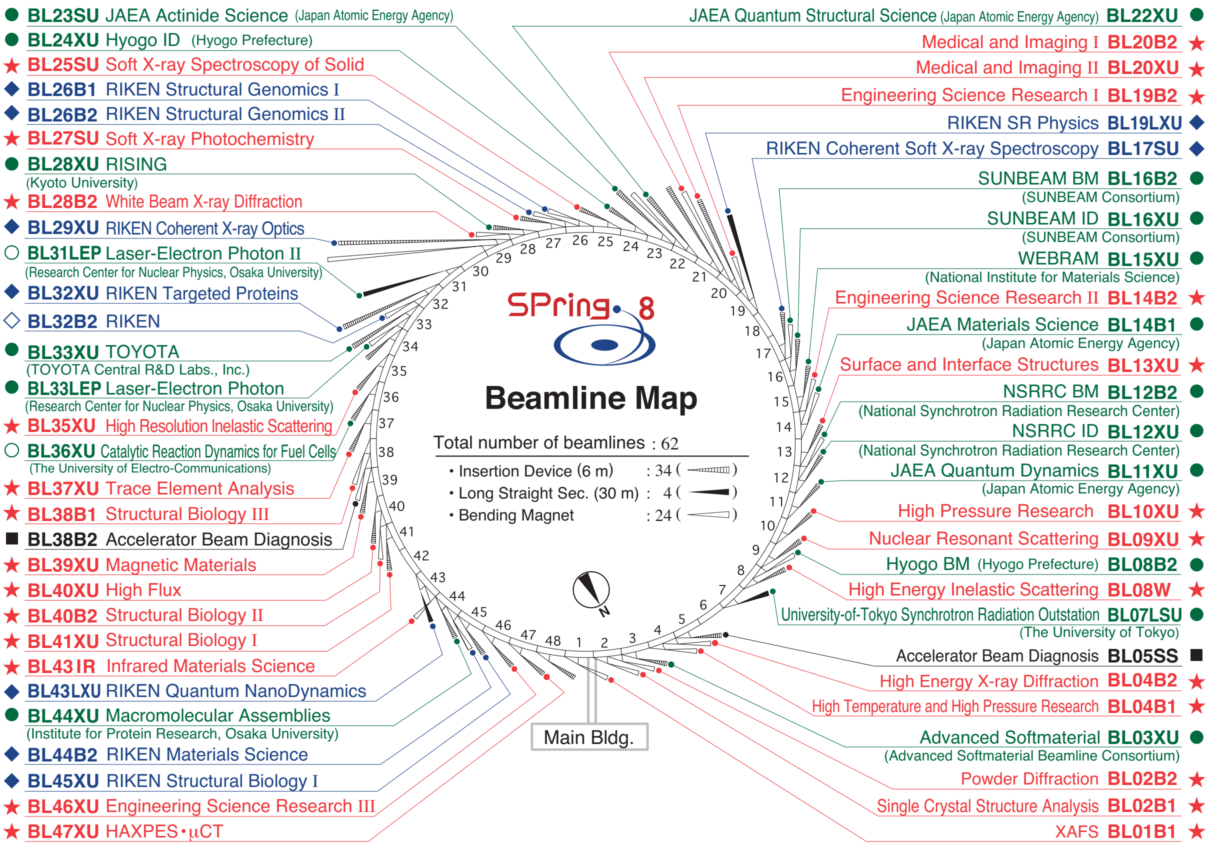

BL: Beamline
B1, B2: Bending Magnets
XU: X-ray Undulator
SU: Soft X-ray Undulator
W: Wiggler

IR: Infrared Radiation
LEP: Laser-Electron Photon
LXU: Long-length X-ray Undulator
LSU: Long-length Soft X-ray Undulator
SS: Straight Section

★ : Public Beamlines
● : Contract Beamlines
◆ : RIKEN Beamlines
■ : Accelerator Diagnostics Beamlines

○ ◇ □ : Planned or Under Construction

WEBRAM: Wide Energy Range Beamline for Research in Advanced Materials
NSRRC: National Synchrotron Radiation Research Center, Taiwan
RISING: Research & Development Initiative for Scientific Innovation of New Generation Batteries
HAXPES•µCT: Hard X-ray Photoelectron Spectroscopy, Micro-Tomography

Fig. 2. Beamline map.

Table III. List of beamlines

BL #	Beamline Name	(Public Use) or (First Beam)	Areas of Research
★ Public Beamlines			
BL01B1	**XAFS**	(Oct. 1997)	XAFS in wide energy region (3.8 to 113 keV). XAFS of dilute systems and thin films. Quick XAFS with a time resolution of seconds to as tenth seconds.
BL02B1	**Single Crystal Structure Analysis**	(Oct. 1997)	Precise crystal structure analysis using high resolution data of single crystal (X-ray energy: 8 – 115 keV). Magnetic resonant X-ray scattering.
BL02B2	**Powder Diffraction**	(Sep. 1999)	Accurate structure analysis of crystalline materials using powder diffraction data by Rietveld refinements and maximum entropy method (MEM).
BL04B1	**High Temperature and High Pressure Research**	(Oct. 1997)	Mineral physics at high temperature and high pressure. Energy-dispersive X-ray diffraction and X-ray radiography using the large-volume press.
BL04B2	**High Energy X-ray Diffraction**	(Sep. 1999)	Structural analysis of glass, liquid, and amorphous materials. X-ray diffraction under ultra high-pressure.
BL08W	**High Energy Inelastic Scattering**	(Oct. 1997)	Magnetic Compton scattering. High-resolution Compton scattering. High-energy Bragg scattering. High-energy fluorescent X-ray analysis.
BL09XU	**Nuclear Resonant Scattering**	(Oct. 1997)	Lattice dynamics using nuclear inelastic scattering. Time domain Mössbauer spectroscopy, especially under the extreme conditions. Nuclear excitation by electron transition (NEET).
BL10XU	**High Pressure Research**	(Oct. 1997)	Structure analysis and phase transitions under ultra high pressure (DAC experiment). Earth and planetary science.
BL13XU	**Surface and Interface Structures**	(Sep. 2001)	Atomic-scale structural analysis of surfaces and interfaces of crystalline materials, ultra-thin films, and nanostructures. Surface X-ray diffraction (SXRD). Microbeam diffraction.
BL14B2	**Engineering Science Research II**	(Sep. 2007)	XAFS in wide energy region (3.8 to 72 keV). XAFS of dilute systems and thin films.
BL19B2	**Engineering Science Research I**	(Nov. 2001)	Residual stress measurement. Structural analysis of thin film, surface, interface. Powder diffraction. X-ray imaging, X-ray topography. Ultra-small angle X-ray scattering.
BL20XU	**Medical and Imaging II**	(Sep. 2001)	Microimaging. Hard X-ray microbeam/scanning microscopy, imaging microscopy, microtomography, phase-contrast microtomography with Bonse-Hart interferometer, X-ray holography, coherent X-ray optics, and other experiments on X-ray optics and developments of optical elements. Medical application. Microangiography, refraction-enhanced imaging, radiation therapy, phase-contrast CT using interferometer. Ultra-small angle scattering.
BL20B2	**Medical and Imaging I**	(Sep. 1999)	Microimaging: microtomography, phase-contrast microtomography with Bonse-Hart interferometer and grating interferometer for biological specimen and other kinds of specimen. Evaluation and development of various kinds of optical elements for novel imaging techniques. Large field X-ray topography.
BL25SU	**Soft X-ray Spectroscopy of Solid**	(Apr. 1998)	Observation of electronic structures by photoemission spectroscopy (PES). Observation of electronic band structures by angle resolved photoemission spectroscopy (ARPES). Magnetic state study by magnetic circular dichroism (MCD) of soft X-ray absorption. Element-specific magnetization curve measurements by MCD analysis of atomic arrangements by photoelectron diffraction (PED). Observation of magnetic domains by photoelectron emission microscope (PEEM).
BL27SU	**Soft X-ray Photochemistry**	(May 1998)	Ambient atmospheric pressure Soft X-ray photoabsorption spectroscopy. Chemical state analysis of light elements in dilute samples (NEXAFS). High resolution atomic and molecular electron spectroscopy. Dissociation dynamics of inner-shell excited molecules. (Molecular science) Photoemission and soft-X-ray emission spectroscopy for solids. (Solid state and surface physics)
BL28B2	**White Beam X-ray Diffraction**	(Sep. 1999)	White X-ray diffraction and topography. Time-resolved energy-dispersive XAFS (DXAFS) for studies of chemical and/or physical reaction process. Biomedical imaging and radiation biology studies.
BL35XU	**High Resolution Inelastic Scattering**	(Sep. 2001)	Material dynamics on ~meV energy scales using inelastic X-ray scattering (IXS) and, sometimes, nuclear resonant scattering (NRS).
BL37XU	**Trace Element Analysis**	(Nov. 2002)	X-ray microbeam spectrochemical analysis. Ultra trace element analysis. High energy X-ray fluorescence analysis.
BL38B1	**Structural Biology III**	(Oct. 2000)	Structural biology. Macromolecular crystallography. Automatic data collection.
BL39XU	**Magnetic Materials**	(Oct. 1997)	X-ray magnetic circular dichroism (XMCD) spectroscopy and element-specific magnetometry under multiple-extreme conditions. XMCD/XAS using a sub-micron X-ray beam. X-ray emission spectroscopy. Resonant X-ray magnetic scattering.
BL40XU	**High Flux**	(Apr. 2000)	Time-resolved diffraction and scattering experiments. Microbeam X-ray diffraction and scattering experiments. X-ray photon correlation spectroscopy. Fluorescence analysis. Quick XAFS.
BL40B2	**Structural Biology II**	(Sep. 1999)	Noncrystalline small and wide angle X-ray scattering.
BL41XU	**Structural Biology I**	(Oct. 1997)	Structural biology. Macromolecular crystallography. Data collection from small crystals and large unicell crystals. Ultra-high resolution data collection.
BL43IR	**Infrared Materials Science**	(Apr. 2000)	Infrared microspectroscopy. Magneto-optical spectroscopy.
BL46XU	**Engineering Science Research III**	(Nov. 2000)	Structural characterization of thin films by X-ray diffraction and X-ray reflectivity measurement. Residual stress measurement. Time resolved X-ray diffraction measurement. Hard X-ray photoemission spectroscopy.
BL47XU	**HAXPES·μCT**	(Oct. 1997)	Hard X-ray photoelectron spectroscopy (HAXPES). Depth analysis of angle resolved HAXPES with wide acceptance lens. Projection type microtomography. Imaging type microtomography. Hard X-ray microbeam/scanning microscopy.

BL #	Beamline Name	(Public Use) or (First Beam)	Areas of Research
● Contract Beamlines			
BL03XU	**Advanced Softmaterial** (Advanced Softmaterial Beamline Consortium)	(Nov. 2009)	Structural characterization of softmaterials using small- and wide-angle X-ray scattering. Grazing-incidence small- and wide-angle X-ray scattering for thin films. X-ray diffraction and reflectivity measurements for softmaterials.
BL07LSU	**University-of-Tokyo Synchrotron Radiation Outstation** (The University of Tokyo)	(Oct.2009)	Time-resolved soft X-ray spectroscopy, nano-beam photoemission spectroscopy, ultra high-resolution soft X-ray emission spectroscopy, and any methods requiring the highly brilliant soft X-ray beam.
BL08B2	**Hyogo BM** (Hyogo Prefecture)	(Jun. 2005)	XAFS in a wide energy region. Small angle X-ray scattering for structural analyses of polymer and nanocomposite materials. X-ray topography. Imaging. Powder diffraction with a high angular-resolution.
BL24XU	**Hyogo ID** (Hyogo Prefecture)	(May. 1998)	Surface/interface analysis by fluorescent X-ray analysis, strain measurements and grazing incidence X-ray diffraction. Microbeam formation studies for materials and life sciences. Micro-SAXS for local long-range structure analysis.
BL12XU	**NSRRC ID** (National Synchrotron Rad. Res. Center, Taiwan)	(Dec. 2001)	High resolution non-resonant or resonant inelastic X-ray scattering. High resolution near-edge X-ray Raman scattering. Phase transitions under high-pressure, low and high temperatures. High-resolution X-ray absorption and emission spectroscopy. X-ray physics and optics.
BL12B2	**NSRRC BM** (National Synchrotron Rad. Res. Center, Taiwan)	(Oct. 2000)	X-ray absorption spectroscopy. Powder X-ray diffraction. High resolution X-ray scattering. Protein crystallography.
BL15XU	**WEBRAM** (National Institute for Materials Science)	(Jan. 2000)	Hard X-ray photoelectron spectroscopy. High-precision X-ray powder diffraction.
BL16XU	**SUNBEAM ID** (Consortium)	(Oct. 1998)	Characterization of semiconductor materials, secondary batteries, fuel cells, catalysts, electrical display related materials, and structural materials by X-ray diffraction, X-ray microbeam based evaluation technique (including X-ray magnetic circular dichroism), and fluorescence X-ray analysis.
BL16B2	**SUNBEAM BM** (Consortium)	(Oct. 1998)	Characterization of secondary battery related materials, semiconductors, fuel cells, catalysts, and several industrial materials by X-ray absorption fine structure measurements, X-ray diffraction (including X-ray reflectivity technique) and X-ray topography.
BL28XU	**Research & Development Initiative for Scientific Innovation of New Generation Batteries (RISING)** (Kyoto University)	(Apr. 2012)	Analysis of rechargeable batteries. Time-resolved X-ray diffraction and XAFS with microbeam. XAFS of dilute systems and thin films. Dispersive XAFS. Hard X-ray photoelectron spectroscopy.
BL33XU	**TOYOTA** (TOYOTA Central R&D Labs., Inc.)	(Apr. 2009)	Time-resolved XAFS. Characterization of industrial materials, such as catalysts, secondary batteries, fuel cells.
BL33LEP	**Laser-Electron Photon** (RCNP, Osaka University)	(Jun. 1999)	Meson photoproduction from nucleon and nucleus. Photoexcitation of hyperons, nucleon resonances, and other exotic states. Photonuclear reactions. Beam diagnoses. Test and calibration of detectors with GeV photon beam.
BL44XU	**Macromolecular Assemblies** (IPR, Osaka University)	(May 1999)	Crystal structure analysis of biological macromolecular assemblies (e.g. membrane complexes, protein complexes, protein-nucleic acid complexes, and viruses).
BL11XU	**JAEA Quantum Dynamics**	(Oct. 1998)	Nuclear scattering. Surface and interface structure analysis with MBE. Inelastic X-ray scattering. XAFS.
BL14B1	**JAEA Materials Science**	(Dec. 1997)	Materials science under high-temperature. *In situ* study on catalysis using dispersive XAFS. X-ray diffraction for structure physics.
BL22XU	**JAEA Quantum Structural Science**	(May 2002)	Materials science under high-pressure. Resonant X-ray scattering. Speckle scattering. Residual stress/strain distribution analysis.
BL23SU	**JAEA Actinide Science**	(Feb. 1998)	Surface chemistry with supersonic molecular beam. Biophysical spectroscopy. Photoelectron spectroscopy. Magnetic circular dichroism.
◆ RIKEN Beamlines			
BL17SU	**RIKEN Coherent Soft X-ray Spectroscopy**	(Sep. 2003)	High resolution photoemission spectroscopy. Soft X-ray emission spectroscopy for liquid and biological samples. Soft X-ray diffraction spectroscopy. Surface science.
BL19LXU	**RIKEN SR Physics**	(Oct. 2000)	SR science with highly brilliant X-ray beam.
BL26B1	**RIKEN Structural Genomics I**	(Apr. 2002)	Structural genomics research based on single crystal X-ray diffraction.
BL26B2	**RIKEN Structural Genomics II**	(Apr. 2002)	Structural genomics research based on single crystal X-ray diffraction.
BL29XU	**RIKEN Coherent X-ray Optics**	(Dec. 1998)	X-ray optics, especially coherent X-ray optics.
BL32XU	**RIKEN Targeted Proteins**	(Oct. 2009)	Protein micro-crystallography.
BL43LXU	**RIKEN Quantum NanoDynamics**	(Oct. 2011)	High resolution inelastic X-ray scattering for investigating atomic and electronic dynamics.
BL44B2	**RIKEN Materials Science**	(Feb. 1998)	Structural materials science research using powder X-ray diffraction.
BL45XU	**RIKEN Structural Biology I**	(Jul. 1997)	Time-resolved and static structures of non-crystalline biological materials using small-angle scattering and diffraction techniques.
■ Accelerator Diagnostics Beamlines			
BL05SS	**Accelerator Beam Diagnosis**	(Mar. 2004)	Accelerator beam diagnosis. R&D of accelerator components.
BL38B2	**Accelerator Beam Diagnosis**	(Sep. 1999)	Accelerator beam diagnosis. R&D of accelerator components.

IV. User Program and Statistics

JASRI calls for public use proposals twice a year. The submitted proposals are reviewed by the Proposal Review Committee (PRC). As for General Proposals, 464 proposals out of the 673 submitted proposals were approved in the research term 2010B, and 414 out of the 597 submitted proposals were approved in 2011A. Since the start of the Long-term Program in 2000B, 34 Long-term Proposals have been implemented, that is, 11 and 12 proposals were carried out in 2010B and 2011A, which include 1 and 3 proposals newly approved. As for Priority Field Proposals, Nanotechnology Support Proposals and Industrial Application Proposals were called for in 2010B and 2011A. Out of the 217 submitted proposals, 148 proposals were approved in 2010B, and 119 out of the 194 submitted proposals were approved in 2011A. The proposal statistics are shown in Table IV for the period from 1997B to 2011A; Power User Proposals and JASRI Proposals are excluded. During the period from 2003B to 2011A, 18 user groups were designated as Power User groups (PUs), which include 8 PUs active in 2011A. To date, a total of 4122 shifts have been used by PUs, 729 shifts of which were spent from 2010B to 2011A. In particular, 104 proposals were approved as the "Affected Facilities Support Proposals" in 2011A.

SPring-8 consistently provided 2,094 hours of user beamtime in 2010B and 2,131 hours in 2011A. Since the start of operation in 1997, SPring-8 has succeeded in providing users with a total beamtime of 53,214 hours. In 2010B, 1,069 experiments were conducted by 7,684 users at public and contract beamlines, and 1,049 experiments by 7,413 users in 2011A. From the start of operation in 1997 to 2011A, a total of 19,440 experiments were conducted by 132,132 users.

The beamtime available to the users, the number of experiments conducted, and the number of user visits at the public and contract beamlines are summarized in Table V and in Fig. 3.

Figure 4 shows the breakdown of the approved proposals sorted by user affiliation and of the number of experiments conducted at the public and contract beamlines from 1997B to 2011A. The percentages of experiments conducted by users from abroad were 5.8% in 2010B and 6.7% in 2011A.

For the promotion of Industrial Application at SPring-8, the Industrial Application Division was established in 2005. With consultation support for new users given by the division's coordinators, currently, Industrial Application Proposals account for approximately 20% of the total number of proposals conducted at the public beamlines. In addition, the Measurement Service has been introduced since 2007B, in which the personnel of the Industrial Application Division carries out XAFS measurements on behalf of users at BL14B2. SPring-8 has also launched the Mail-in Protein Crystallography Data Collection at BL38B1 and the powder X-ray diffraction Measurement Service at BL19B2 since 2009B.

Table IV. Numbers of submitted proposals and approved proposals by research term

Research Term	Beamtime (shifts)	Deadline	Submitted proposals	Approved proposals
1997B: 1997.10 - 1998.03	168	1997.1.10	198	134
1998A: 1998.04 - 1998.10	204	1998.1.6	305	229
1999A: 1998.11 - 1999.06	250	1998.7.12	392	258
1999B: 1999.09 - 1999.12	140	1999.6.19	431	246
2000A: 2000.02 - 2000.06	204	1999.10.16	424	326
2000B: 2000.10 - 2001.01	156	2000.6.17	582	380
2001A: 2001.02 - 2001.06	238	2000.10.21	502	409
2001B: 2001.09 - 2002.02	190	2001.5.26	619	457
2002A: 2002.02 - 2002.07	226	2001.10.27	643	520
2002B: 2002.09 - 2003.02	190	2002.6.3	751	472
2003A: 2003.02 - 2003.07	228	2002.10.28	733	563
2003B: 2003.09 - 2004.02	202	2003.6.16	938	621
2004A: 2004.02 - 2004.07	211	2003.11.4	772	595
2004B: 2004.09 - 2004.12	203	2004.6.9	886	562
2005A: 2005.04 - 2005.08	188	2005.1.5	878	547
2005B: 2005.09 - 2005.12	182	2005.6.7	973	624
2006A: 2006.03 - 2006.07	220	2005.11.15	916	699
2006B: 2006.09 - 2006.12	159	2006.5.25	867	555
2007A: 2007.03 - 2007.07	246	2006.11.16	1099	761
2007B: 2007.09 - 2008.02	216	2007.6.7	1007	721
2008A: 2008.04 - 2008.07	225	2007.12.13	1009	749
2008B: 2008.10 - 2009.03	189	2008.6.26	1163	659
2009A: 2009.04 - 2009.07	195	2008.12.11	979	654
2009B: 2009.10 - 2010.02	210	2009.6.25	1076	709
2010A: 2010.04 - 2010.07	201	2009.12.17	919	665
2010B: 2010.10 - 2011.02	210	2010.7.1	1022	728
2011A: 2011.04 - 2011.07	215	2010.12.9	1024	731

Notes
1997B-2006B: The number of proposals are indicated as of submission deadline.
After 2007A: The total number of proposals are indicated.
The number of long-term proposals are counted by beamline, that is, if the project leader uses two beamlines, it is counted as two proposals.

Table V. Numbers of experiments and users at public and contract beamlines (by research term)

Research Term	User time (hours)	Public BL		Contract BL	
		Experiments	Users	Experiments	Users
1997B: 1997.10 - 1998.03	1,286	94	681	–	–
1998A: 1998.04 - 1998.10	1,702	234	1,252	7	–
1999A: 1998.11 - 1999.06	2,585	274	1,542	33	467
1999B: 1999.09 - 1999.12	1,371	242	1,631	65	427
2000A: 2000.02 - 2000.06	2,051	365	2,486	100	794
2000B: 2000.10 - 2001.01	1,522	383	2,370	88	620
2001A: 2001.02 - 2001.06	2,313	474	2,915	102	766
2001B: 2001.09 - 2002.02	1,867	488	3,277	114	977
2002A: 2002.02 - 2002.07	2,093	545	3,246	110	1,043
2002B: 2002.09 - 2003.02	1,867	540	3,508	142	1,046
2003A: 2003.02 - 2003.07	2,246	634	3,777	164	1,347
2003B: 2003.09 - 2004.02	1,844	549	3,428	154	1,264
2004A: 2004.02 - 2004.07	2,095	569	3,756	161	1,269
2004B: 2004.09 - 2004.12	1,971	555	3,546	146	1,154
2005A: 2005.04 - 2005.08	1,880	560	3,741	146	1,185
2005B: 2005.09 - 2005.12	1,818	620	4,032	187	1,379
2006A: 2006.03 - 2006.07	2,202	724	4,809	226	1,831
2006B: 2006.09 - 2006.12	1,587	550	3,513	199	1,487
2007A: 2007.03 - 2007.07	2,448	781	4,999	260	2,282
2007B: 2007.09 - 2008.02	2,140	739	4,814	226	1,938
2008A: 2008.04 - 2008.07	2,231	769	4,840	232	1,891
2008B: 2008.10 - 2009.03	1,879	672	4,325	217	1,630
2009A: 2009.04 - 2009.07	1,927	669	4,240	238	1,761
2009B: 2009.10 - 2010.02	2,087	722	4,793	275	2,144
2010A: 2010.04 - 2010.07	1,977	685	4,329	293	2,483
2010B: 2010.10 - 2011.02	2,094	744	4,872	325	2,812
2011A: 2011.04 - 2011.07	2,131	740	4,640	309	2,773
	53,214	14,921	95,362	4,519	36,770

Notes
The number of long-term proposals are counted by beamline, that is, if two beamlines were used for one experiment, those are counted as two experiments.

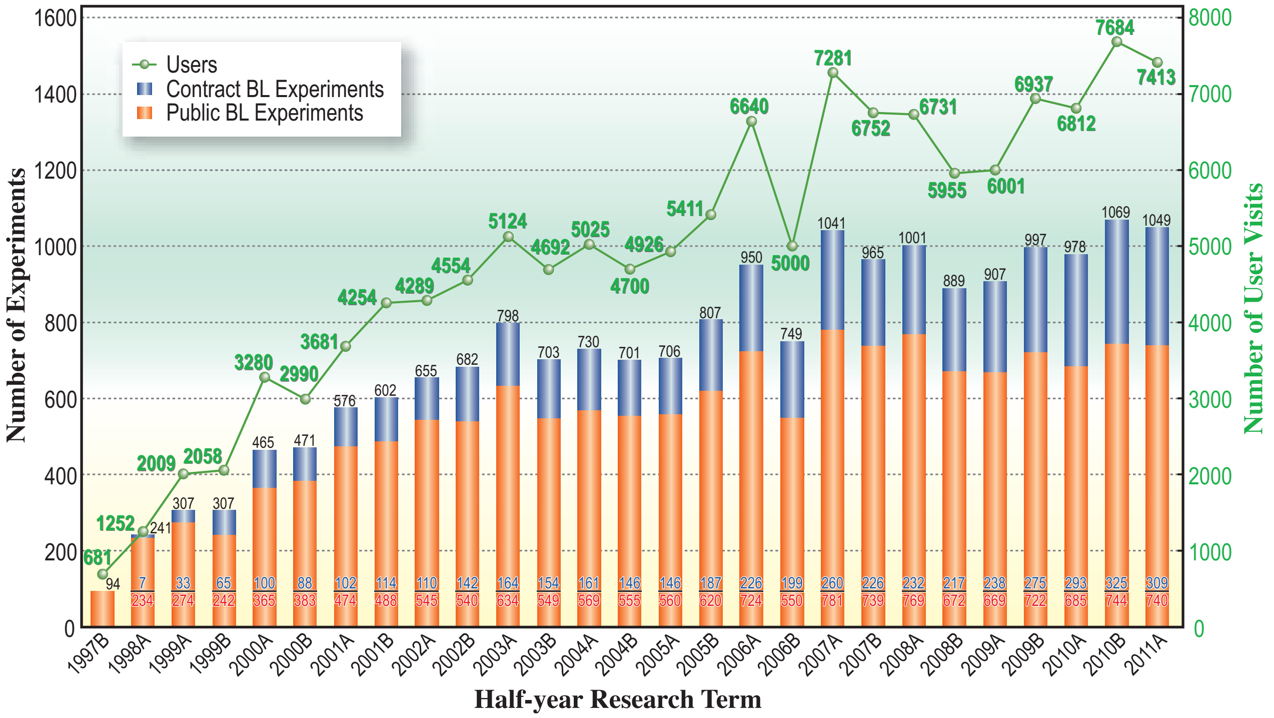

Fig. 3. Numbers of user visits and conducted experiments.

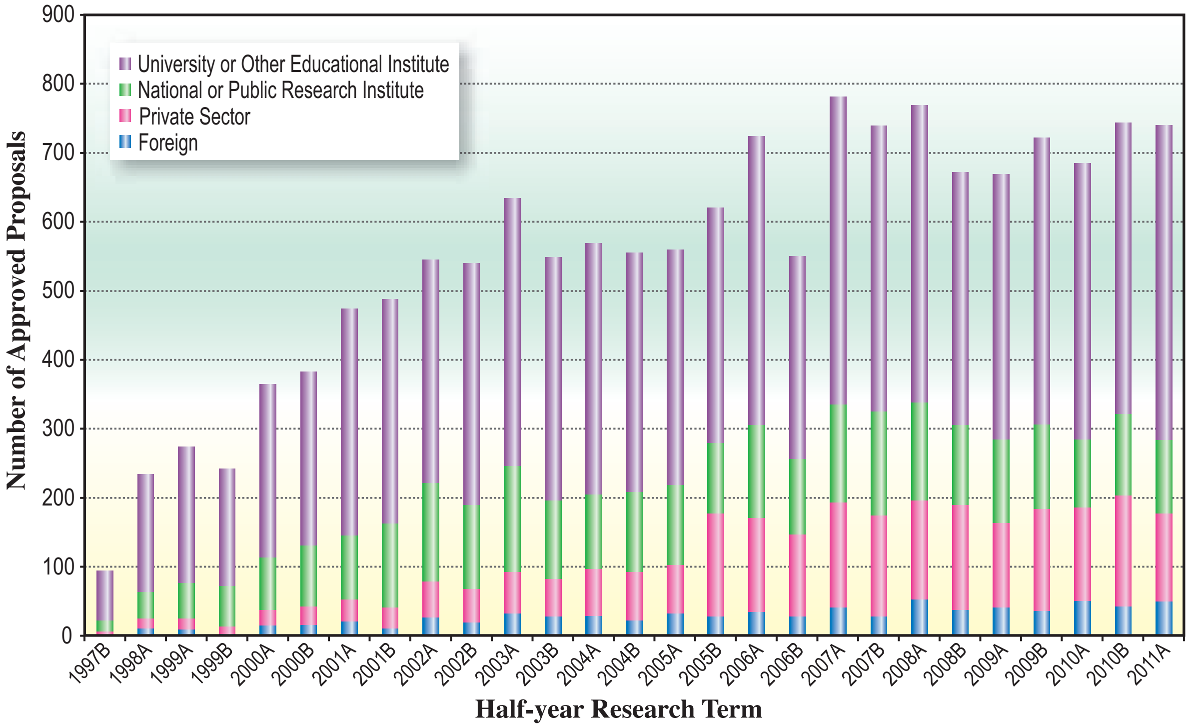

Fig. 4. Number of approved proposals by affiliation of applicants (public beamlines).

V. Research Outcome

When users conduct non-proprietary experiments, they are required to submit an experiment summary report within 60 days of the completion of their experiments. From 2011B, the users are strongly required to publish their research results in refereed journals or equivalent, and to register the published works with the Publications Database within three years after the end of the research term. In case of being unable to comply with this requirement, the users are required to submit a SPring-8 Research Report (tentative) or, for industrial application, a technical report. Figure 5 shows the annual statistics of the refereed papers. As of March 2011, the number of registered refereed papers is 7,210, out of which 5,875 papers resulted from the use of public beamlines, 1,272 papers from that of contract beamlines, 844 papers from that of RIKEN beamlines, and 414 papers from that of hardware/software R&D. The papers resulting from the use of two or more beamlines are counted at each beamline.

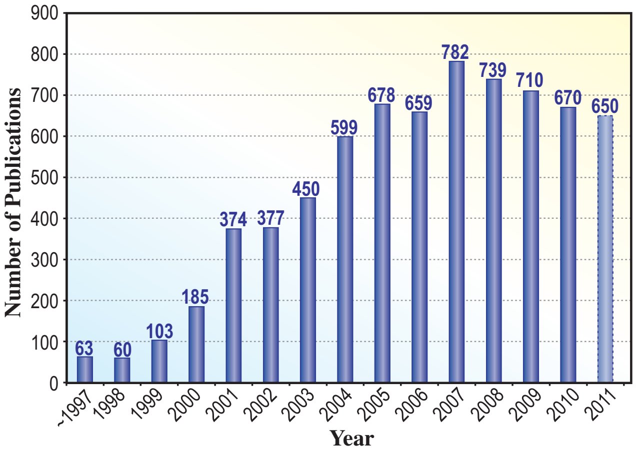

Fig. 5. Number of refereed publications as of March 2012.

VI. Budget and Personnel

Since the start of operation in 1997, SPring-8 had been jointly managed by RIKEN, JAERI (JAEA, as it is known today), and JASRI. Since JAERI withdrew from the management of SPring-8 on September 30, 2005, SPring-8 has been administered by RIKEN and JASRI in a collaborative manner.

Figure 6 shows the annual budget allocated to the operation, maintenance, and promotion of the use of SPring-8 from FY1997 to date. The budget for FY2011 is 8.39 billion yen. The total number of staff members of RIKEN and JASRI is 1,333 as of October 2011, as shown in Fig. 7.

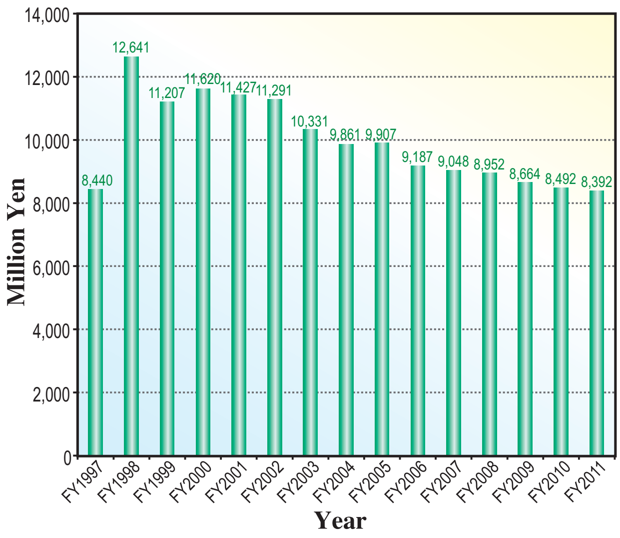

Fig. 6. SPring-8 budget.

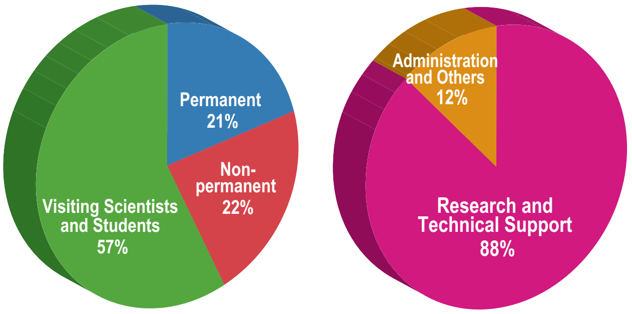

	by Type			by Field	
	Permanent	Non-permanent	Visiting Scientists and Students	Research and Technical Support	Administration and Others
RIKEN	47	157	619	783	40
JASRI	235	137	138	387	123

Including double counts.

Fig. 7. Personnel at SPring-8: JASRI and RIKEN.

VII. Research Complex

The facilities of SPring-8, SACLA and NewSUBARU form a center of excellence at the SPring-8 campus, where JASRI, public beamline users, contractors of contract beamlines, RIKEN, and the University of Hyogo work in close cooperation to form a research complex by playing their own roles to deliver high-quality results in the field of synchrotron radiation science and technology. Figure 8 shows the SPring-8 research complex and the operation and management of each research facility. The organizational charts of RIKEN and JASRI, which form the kernel of this research complex, are shown in Figs. 9 and 10, respectively.

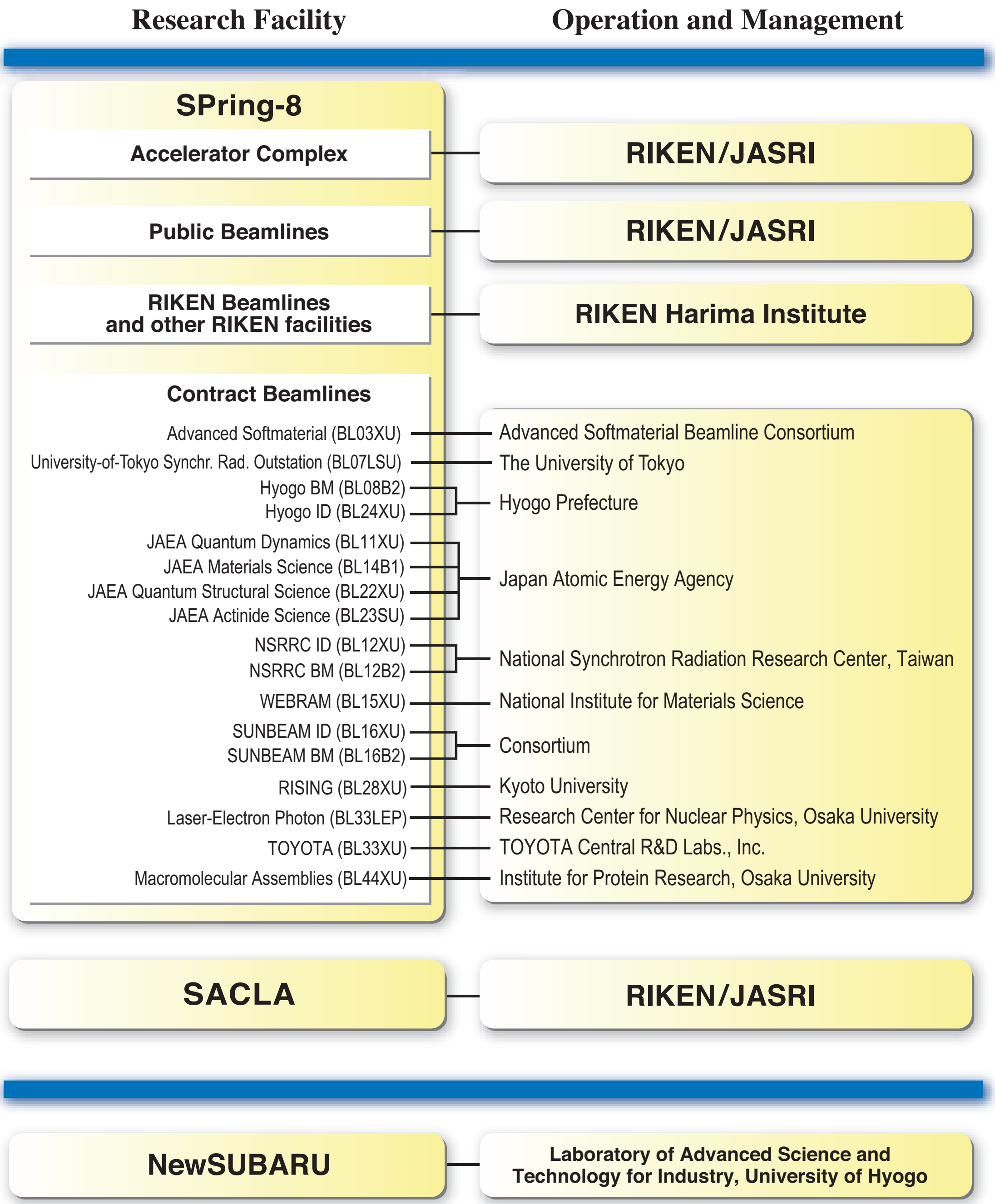

Fig. 8. SPring-8 research complex as of April 2012.

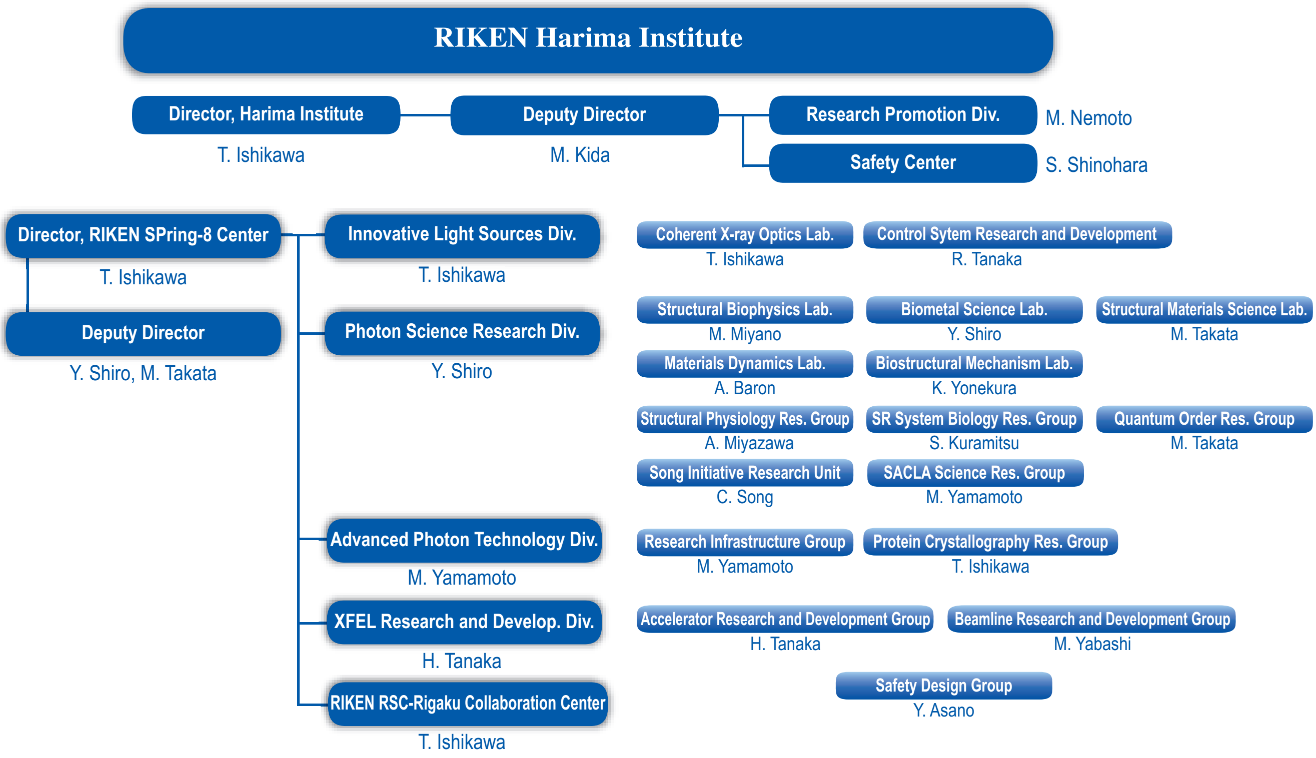

Fig. 9. RIKEN Harima chart as of April 2012.

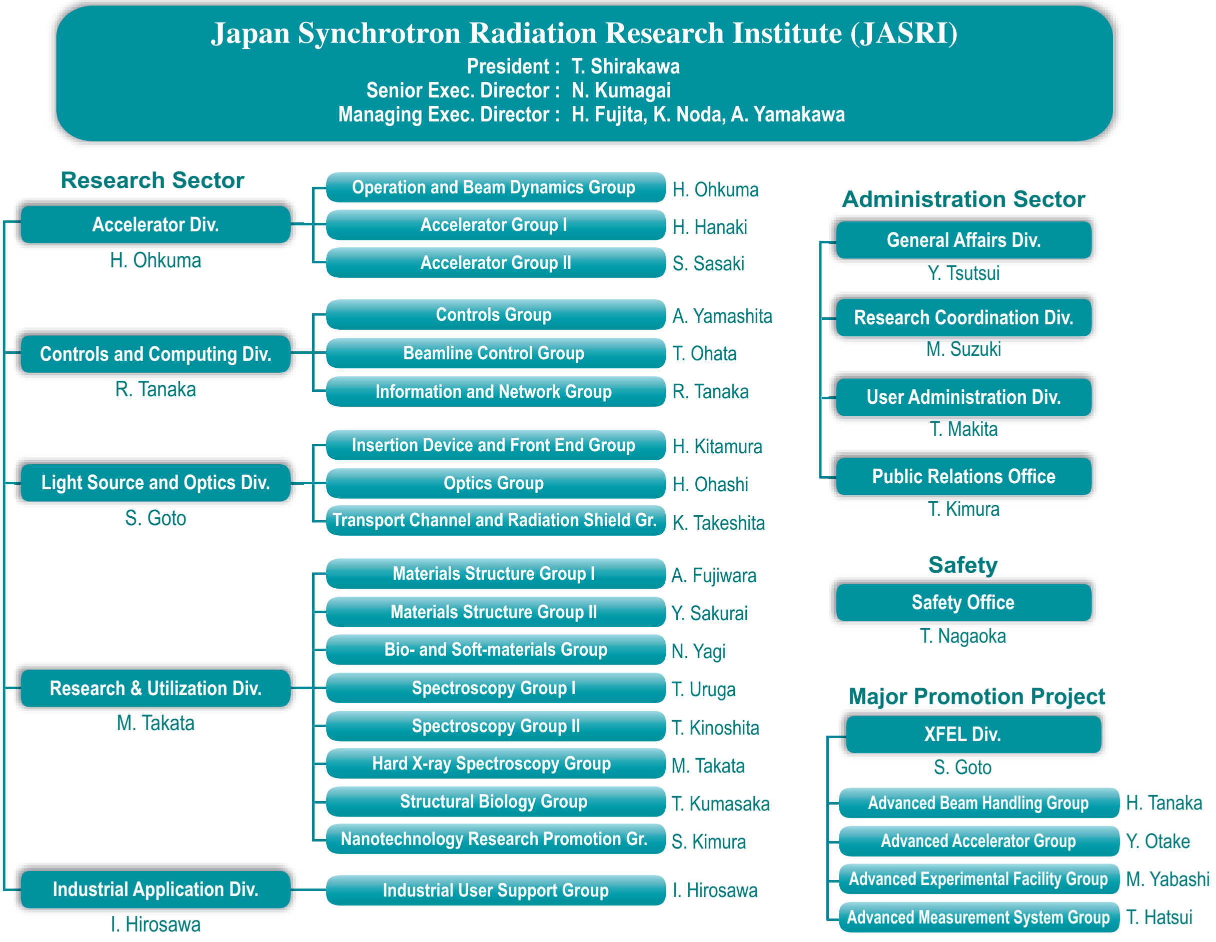

Fig. 10. JASRI chart as of April 2012.

VIII. Users Societies, Conferences and Other Activities

Users Society

The **SPring-8 Users Society** was organized in May 1993, when SPring-8 did not exist, to discuss the construction of and the scientific research studies at SPring-8. During the construction and development phases of SPring-8, the SPring-8 Users Society made enormous contributions in helping construct the beamlines and promoting the utilization of SPring-8 through discussions among users and between users and facility staff. However, the number of members of the SPring-8 Users Society remained to be about 1,200, while the number of SPring-8 users reached 9,000 at present. This situation necessitates the SPring-8 Users Society to be reformed so that it could organize all users of SPring-8 and could continue to make contribution in the promotion of the utilization and upgrade of SPring-8 at a mature phase of SPring-8.

In April of 2012, a new organization, SPring-8 Users Community (SPRUC), was formed; it includes not only all users but also potential users who are interested in using SPring-8. In terms of its organization, SPRUC has a remarkable feature, that is, the representatives of about thirty institutes (principal universities and national research institutes), to which quite a few users belong, participate in SPRUC to discuss further promotion of the utilization of SPring-8 from strategic and bird's-eye viewpoints. As a kick-off of SPRUC, SPRUC will organize a SPring-8 users symposium in August 2012 at Osaka University.

The **Industrial Users Society of SPring-8** was established by the members of various companies in September 1990 to promote the use of SPring-8 and develop the SPring-8 user program. Several research groups focused on various fields of applications have been organized; at present, eight are active. The main purpose of the society is not only to provide information on the trends of the synchrotron radiation facilities in Japan and abroad, and their latest research achievements, but also to enhance communication among the industrial sector, JASRI, and MEXT. As a result, the percentage of industrial applications has increased to 20% in terms of the number of proposals approved. The society consists of 78 companies and one organization as of December 31, 2011.

Users Meeting

The meeting for users jointly organized by the SPring-8 Users Society and/or the Industrial User Society of SPring-8, and JASRI and RIKEN is listed below.

- The 8th Report Meeting on SPring-8 Industrial Application
  September 8–9, 2011 - Translational Research Informatics Centre, Kobe

Conferences and Workshops

The conferences and workshops organized, sponsored, or hosted by RIKEN, JASRI, or both in 2011 are listed below.

- 24th Annual Meeting of Japanese Society for Synchrotron Radiation Research
January 7–10, 2011 - Tsukuba International Congress Centre, Ibaraki
- 6th Workshop on Speciation, Techniques, and Facilities for Radioactive Materials at Synchrotron Light Sources and Other Quantum Beam Sources
March 2–4, 2011 - Public Relations Center and "Houkou-kan", SPring-8
- The Report Meeting of SPring-8 Industrial Application Proposals in FY2010
March 2, 2011 - Convention Room AP Shinagawa, Tokyo
- The Symposium on X-ray Free Electron Laser
April 21, 2011 - PACIFICO Yokohama
- The Workshop on SPring-8 Upgrade Plan
April 25–26, 2011 - Public Relations Center, SPring-8
- The 1st Annual Meeting for Whole-Organism Science Society / Joint Meeting with The 10th Annual Meeting of Whole Cell Project of *Thermus thermophilus* HB8
August 19–21, 2011 - Public Relations Center, SPring-8
- The 3rd Workshop on the Basis of Synchrotron Radiation
September 6–7, 2011 - Kwansei Gakuin University, Osaka
- The 4th Workshop on the SPring-8 Budding Researchers Support Program
October 12, 2011 - Campus Innovation Centre, Tokyo
- The FEL 3-site Meeting
October 31–November 3, 2011 - RIKEN SPring-8 Center and Hotel Wakamizu,Takarazuka, Hyogo
- SPring-8 Conference
November 1–2, 2011 - Tokyo Station Conference, Tokyo
- The 1st Activity Report Meeting of Advanced Softmaterial Beamline Consortium
November 8, 2011 - Osaka International Convention Centre, Osaka
- The Workshop on Phase-Change Materials and Disordered Materials-Towards New Functional Materials
November 11–12, 2011 - Osaka Science & Technology Center, Osaka
- The 1st Workshop on the Utilization of SACLA
November 24, 2011 - XFEL Experimental Facility, SACLA, SPring-8
- The 1st SACLA Symposium
December 3, 2011 - Marunouchi MY PLAZA Hall, Tokyo
- The Annual Meeting of SPring-8 Priority Nanotechnology Support Program FY2010/2011
December 20, 2011 - Shinagawa Hotel U-Port, Tokyo

Other Activities

- The 2nd Open Lecture for Citizens
March 26, 2011 - Himeji City Cultural Center, Hyogo
- The 19th SPring-8 Open House
April 30, 2011
- The 11th SPring-8 Summer School 2011
July 10–13, 2011 - Public Relations Center, SPring-8
- The 5th AOFSRR School - Cheiron School 2011
September 26–October 5, 2011 - Public Relations Center, SPring-8

SACLA

We are pleased to inform you of the dedication of the XFEL facility in March 2011. It was almost on time and within budget, which is exceptional for a project of this scale, although the delivery of a small portion of the hardware was delayed because of the big earthquake and tsunami on 11th March. The facility was named SACLA, after 'SPring-8 Angstrom Compact free electron LAser'. We decided to start the user operation of SACLA from March 2012. Preparation toward user operation started accordingly. The RIKEN-JASRI joint project team for XFEL construction dissolved when the construction was completed. The management and commissioning tasks were decided to be taken by a new XFEL division set up in the RIKEN SPring-8 Center. Since the technical phase of the facility was not very much matured and needed much R&D works for several years in contrast to SPring-8, RIKEN decided to operate the facility by itself in order to find out possible improvement effectively.

Electron beam commissioning went smoothly. By the end of March 2011, we reached the design operation energy 8 GeV, and recorded the spontaneous radiation from undulators with the 8 GeV electron beam. With the help of the X-ray image detectors and double-crystal monochromator already installed in the photon beamline and waiting for the beams, we were able to measure the undulator spectrum and observe the circular off-resonance monochromatic radiation patterns from each undulator module to determine precisely the magnetic field parameter. We have developed a new method of beam-based alignment toward the SASE lasing using the monochromatic undulator radiation pattern to adjust the magnetic field of each of the 18 undulator modules independently. We observed the first SASE laser amplification at 0.12 nm on 7th June 2011, which was the world equal record of the shortest laser wavelength at that time attained at LCLS. The following tuning process of the accelerator and undulator made it possible to observe the lasing at 0.063 nm at the end of October 2011.

In addition to the development of the SASE FEL light source, photon beamlines and end-station equipment were developed to meet various users' needs from different application fields. Ultrafast optical lasers were prepared in the experimental hall for pump-probe measurements. Octal-module X-ray CCD detectors with 60 Hz read-out capability were equipped to make coherent X-ray diffraction imaging and other imaging experiments. A Kirkpatrick-Baez X-ray focusing mirror was installed and produced the focused beam with a focal size of 1 μm × 1 μm. A number of end-station instruments have been developed in collaboration with outside researchers all over Japan. These include AMO, Pump-Probe, and Imaging instruments. Commissioning of these end-station instruments has been carried out after September 2011 by teams sometimes including foreign collaborators. One example is the Tohoku-Kyoto-MPI collaboration team for AMO instruments. Another example is the AIST-DESY-PTB-RIKEN collaboration team for pulse energy measurement, producing three types of inter-calibrated detectors using an AIST calorimeter as a standard.

The prototype EUV-FEL has been used by many users. It should be noted that this facility recorded the world's first seeded operation of SASE EUV-FEL by using HHG. We are planning to deliver seeded SASE-FEL to general users in the near future.

Last but not least, our accelerator designer, Dr. Tsumoru Shintake, moved to Okinawa Institute for Science and Technology (OIST) in September 2011. We miss him a lot and wish him to open another new world.

Tetsuya Ishikawa

1. Status of SACLA Construction

In February 2011, the manufacture of all the components for SACLA and the high power conditioning of all the RF components were completed. The beam commissioning started on 21st February, and the spontaneous emission at a wavelength of 0.08 nm was observed with the electron beam energy of 7.8 GeV at the end of March 2011. Thus, this five-year construction project for an 8 GeV XFEL facility was completed successfully in March 2011.

In April, the SASE tuning started and, on 7th June 2011, the first SASE laser amplification was successfully observed at a wavelength of 0.12 nm. By this observation, we confirmed that all the components of SACLA have excellent performance as designed.

2. Status of SACLA Operation

2-1. Beam Commissioning

SACLA accelerator commissioning started in February 2011, and the first SASE-FEL light was successfully obtained in June 2011. Figure 1 shows the measured spectrum and transverse profile of XFEL light together with the spontaneous radiation spectrum. During beam commissioning, a beam diagnostic system and a control system were also tested and improved to enable fine tuning of the machine.

Beam tuning was started from the injector section, where the electron beam is compressed by a factor of 20 by velocity bunching. Considering stability and ease of maintenance, a 500-kV pulsed gun with a thermal cathode is used as an electron source in SACLA. The RF phases of the injector cavities were determined by detecting the phase of the self-induced electromagnetic fields of the electron bunch. Since the beam current from the thermionic gun is about 1 A, a bunch compression factor of 3000 is necessary to obtain lasing, which is roughly one order higher than that of a photocathode system. After the velocity bunching in the injector, the electron beam is further compressed by a three-stage magnetic bunch compressor (BC1~3). The final peak current, more than 3 kA, was confirmed by a C-band deflector cavity installed downstream of BC3.

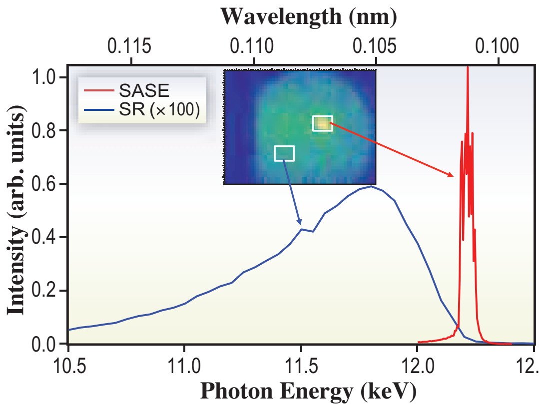

Fig. 1. Measured spectrum of XFEL light (red) and spontaneous radiation (blue). The inset shows the transverse profile of XFEL light.

After fixing the RF parameters, the transverse envelope of the electron beam was adjusted along the accelerator to match the FODO-like magnet lattice of the undulator section. For beam envelope calculation, a linear accelerator model based on a normalized emittance was developed, which is a method commonly used for analyzing the beam dynamics in a storage ring. Since the measurement of a transverse beam profile after BC3 was found to be difficult owing to the intense coherent OTR, several OTR screens were replaced with YAG screens with a spatial mask to remove the coherent OTR.

The electron beam orbit at the undulator section was aligned by monitoring the overlap of the radiation axes of 18 undulators using a monochromator and a CCD, which were located 90 m downstream from the exit of the undulator.

The pulse energy of XFEL light, which was initially about 30 μJ after the first lasing, was increased to 120 μJ at 0.12 nm in autumn by improving the projected emittance and nonlinear correction in the multi-stage bunch compressor. In December 2011, the CeB_6 cathode of the electron gun was replaced with a new one to prepare for the public user operation starting in March 2012.

2-2. Instrumentation Tuning of the Accelerator

The unique characteristics of the SACLA accelerator include high-gradient acceleration with more than 35 MV/m for a compact machine. High precision and reliability are required for achieving a stable X-ray lasing process. To realize these characteristics, the conditioning by high-power RF sources using 50 MW C-band pulsed klystrons was continued throughout almost the whole year of 2011. We finally achieved an acceleration gradient of more than 35 MV/m, as shown in Fig. 2 [1], which is necessary for achieving an electron beam energy of up to 8.3 GeV. To tune electron beams for a stable lasing, well-calibrated beam monitors were important. Therefore, we calibrated a beam position monitor (BPM) and a differential current transformer (DCT) by using the accelerated electron beams. The

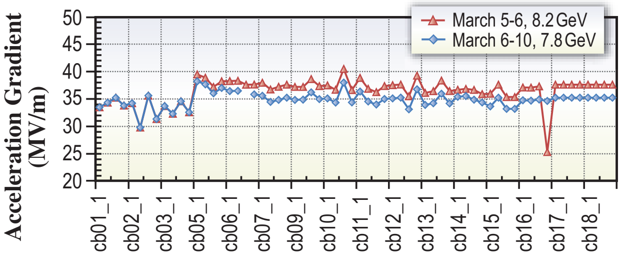

Fig. 2. Acceleration gradient of the C-band accelerator.

calibration data of the BPM and DCT were obtained while changing the beam positions and charges [2,3], as shown in Fig. 3(a) and 3(b). These sensitivities are about 35 μm/0.1 V and 0.05 nC/0.1 V, respectively, which were sufficient for the fine beam tuning of the SACLA accelerator. By using the well-conditioned accelerator, the high-precision beam monitors and the very stable RF system, we realized X-ray lasing with acceptable stability.

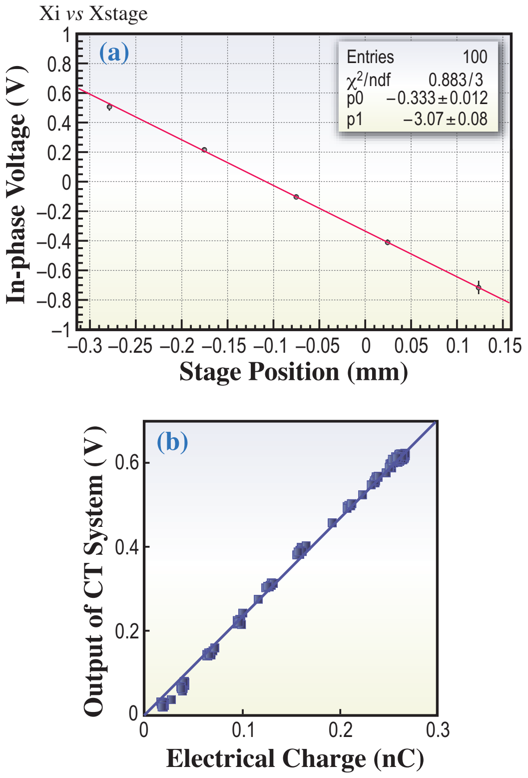

Fig. 3. **(a)** Calibration of the BPM X-axis. **(b)** Calibration of DCT charge dependence.

2-3. Undulator Fine Tuning

Undulator fine tuning is a process used to optimize the parameters related to the undulator operation, which is the final step toward the realization of lasing. We have carried out 5 steps for undulator tuning: fine gap adjustment, undulator height alignment, trajectory correction, phase matching, and undulator taper optimization.

The fine gap adjustment and height alignment are important to ensure that all the undulator segments have the same K value. To carry out these tuning schemes, we measured the spectrum of the spontaneous radiation from a target undulator segment. On the basis of data analysis results together with the theory of undulator radiation, we optimized the undulator gap and adjusted the undulator height. The achieved resolution for each tuning was found to be better than 1 μm for the gap and 50 μm for the height, which were sufficiently good for achieving FEL saturation.

Next, we attempted the trajectory correction based on the spatial profile measurement of the spontaneous radiation from a target undulator segment. After averaging over 10 shots, we deduced the electron beam angle of injection, which was then corrected by a steering magnet installed just in front of the target segment. The most important feature of this correction scheme is the pointing stability of the electron beam, which has been found to be higher than 1 μrad, being sufficiently good for satisfying the criterion for trajectory correction.

After the above tuning based on the characterization of spontaneous radiation, we tried two more tuning schemes to enhance the FEL output based on the characterization of SASE radiation. One is the phase matching between undulator segments by tuning the gap of the phase shifter, a magnetic device to create a bump electron orbit in the drift section. The other is the undulator tapering to compensate the energy loss of the electron due to the resistive wake field and FEL interaction. Both optimizations were carried out to maximize the FEL pulse energy measured by the FEL intensity monitor, which is described later.

2-4. Beamline and Experimental Stations

We introduced the first spontaneous radiation (λ = 0.08 nm) into the optics hutch in March 2011. We started precise tuning of the undulator section by using the beamline components in April, and first observed a lasing at a wavelength of 0.12 nm on 7th June. We continued commissioning of the beamline components in the optics hutch and the experimental stations, and performed test experiments with several collaborative research groups.

Figure 4 shows a layout of the beamline in the experimental hall. In the optics hutch, we installed

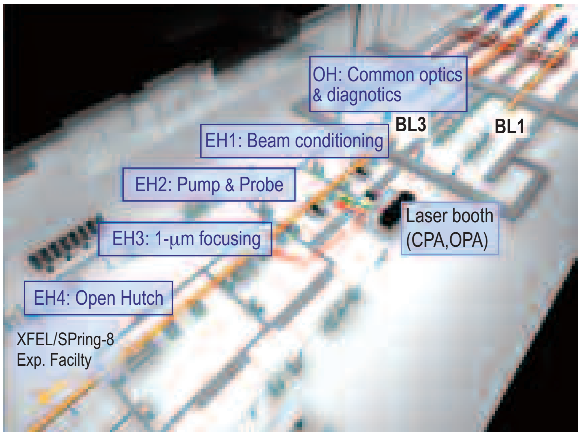

Fig. 4. Beamline layout.

basic optical components (i.e., a double-crystal monochromator (DCM) and a total-reflection mirror system) and key diagnostic devices (i.e., intensity monitors, profile monitors, and a wavelength monitor). We performed precise tuning and calibration of these devices, and confirmed operation as designed.

Figure 5 shows the spatial profile of XFEL light after monochromatization with the DCM, measured 110 m from the exit of the final undulator. We found a stable round-shaped profile with a small angular divergence of ~2 μrad, which is consistent with a design value. We measured the intensity of XFEL radiation to be ~150 μJ/pulse at 0.12 nm using a thin-foil intensity monitor [4]. Furthermore, we performed absolute-intensity measurement in collaboration with DESY, PTB, and AIST groups.

For experimental stations, we started commissioning of key devices. In particular, we tuned a focusing mirror system [5] developed by Osaka University, and obtained a small, intense spot of X-rays with a diameter of 1 μm. We also performed single-shot measurement of XFEL spectra, and found interesting dependence of the profile on the bunch duration. A preliminary test of the pump-probe scheme combined with an optical laser was performed.

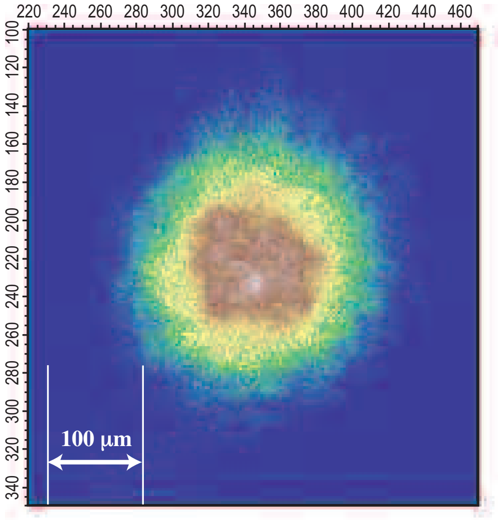

Fig. 5. Spatial profile of XFEL light.

2-5. Detector System

X-ray two-dimensional (2D) detectors optimized for XFEL applications are required to explore the full potential of the XFEL source. As the standard X-ray 2D detector of the SACLA facility, we started to develop a multiport CCD (MPCCD) detector in March 2009. In 2011, two types of MPCCD detector, namely, single- and octal-sensor detectors, were developed. These detectors have been utilized for the commissioning of the accelerator and user experiments. The detector together with a data acquisition system enabled operation stable enough to conduct the user experiments. Advanced 2D sensor development based on silicon-on-insulator sensor technology was carried out. In 2011, the design of a large imaging area of 66 mm × 30 mm was finalized using the results obtained from a feasibility study of smaller sensor chips. The sensor will provide a higher dynamic range required for the coherent X-ray imaging of samples with sizes of sub-micrometers or larger.

2-6. Control System

The control system was completed on schedule. After the completion of the accelerator control, we modified the system to achieve a higher stability in the summer of 2011. For high power RF and vacuum systems, we increased the number of CPUs to ease the CPU heavy load. Because of the severe timing control of the magnet system, we replaced a VME CPU board with Intel Corei7 and used a busy wait mode for a precise timing. The beamline control system was built on the basis of the "standardization concept" for quick start up. We installed three VME systems for the BL3 control. One was used for the front-end components and transport channel, and the others for the beamline interlock system. As a beamline operation console, SuSE Linux Enterprise 11 with a Xen virtual machine was adopted.

A data acquisition system for the experiments was constructed to handle the 2D X-ray detector (MPCCD), commercial cameras and waveform digitizers, and beamline apparatus in the hutches. The data can be recorded shot-by-shot in synchronization with X-ray pulses up to 60 Hz. All the data have beam tag numbers as record labels. The data flow up to 5 Gbps from the ten MPCCD sensors has been transferred by the 10 GbE transfer backbone and stored in a high-speed storage since October 2011.

The installation of the interlock systems for the accelerator, BL3, and BL1 was completed in February 2011. An electron beam that deviates from the nominal route may generate unwanted radiations. Therefore, we integrated the beam route monitor and a fast signal transmission system to stop the electron gun. We separated the interlock system into the personnel safety and the machine protection units for sake of simplicity. We developed the interlock status monitoring system by using the FL net that records the operation history onto the database.

3. Operation Status of the SCSS Test Accelerator

At the SCSS test accelerator, research using intense extreme ultraviolet (EUV) light is carried out in a wide variety of disciplines, including technical research in preparation for XFEL experiments, atomic and molecular physics, coherent diffraction imaging methods, studies of damage of optics, materials science such as advanced scintillators, and nonlinear X-ray devices. Fourteen papers were published in 2011 [6-19].

Here, we introduce a result reported by a group led by Professor A. Hishikawa [6]. They observed a new nonlinear photoabsorption pathway in the EUV region involving the joint excitation of two electrons by shot-by-shot photoelectron spectroscopy. They found that the nonlinear process is the three-photon double excitation of He in the intense EUV-FEL fields, and showed that three-photon double excitation is enhanced by intermediate Rydberg states below the first ionization threshold, giving a greater contribution to the total photoionization yield than the two-photon process by more than 1 order of magnitude. Another result is described in Research Frontiers 2011, page 80 and Ref. [9].

References

[1] T. Inagaki *et al*.: Proc. IPAC11 (2011) 104.
[2] H. Maesaka *et al*.: Proc. FEL11, THPA29 (2011).
[3] S. Matsubara *et al*.: Proc. IPAC11 (2011) 1227.
[4] K. Tono *et al*.: Rev. Sci. Instrum. **82** (2011) 023108.
[5] H. Mimura *et al*.: Rev. Sci. Instrum. **79** (2008) 083104.
[6] A. Hishikawa *et al*.: Phys. Rev. Lett. **107** (2011) 243003.
[7] E. V. Gryzlova *et al*.: Phys. Rev. A **84** (2011) 063405.
[8] T. Sako *et al*.: Phys. Rev. A **84** (2011) 053419.
[9] M. Nagasono *et al*.: Phys. Rev. Lett. **107** (2011) 193603.
[10] R. Moshammer *et al*.: Opt. Express **19** (2011) 21698.
[11] H. Ohashi *et al*.: Nucl. Instrum. and Meth. Phys. Res. A **649** (2011) 163.
[12] T. Sato *et al*.: J. Phys. B : At. Mol. Opt. Phys. **44** (2011) 161001.
[13] N.A. Inogamov *et al*.: J. Opt. Technol. **78** (2011) 473.
[14] R. Bachelard *et al*.: Phys. Rev. Lett. **106** (2011) 234801.
[15] N.A. Inogamov *et al*.: Contrib. Plasma Phys. **51** (2011) 419.
[16] T. Shimizu *et al*.: Appl. Phys. Express **4** (2011) 062701.
[17] M. Yao *et al*.: Eur. Phys. J. Special Topics **196** (2011) 175.
[18] N. Miyauchi *et al*.: J. Phys. B: At. Mol. Opt. Phys. **44** (2011) 071001.
[19] T. Togashi *et al*.: Opt. Express **19** (2011) 317.

NewSUBARU

A 1.5 GeV synchrotron radiation ring named NewSUBARU is the main facility of the Laboratory of Advanced Science and Technology for Industry (LASTI) at the University of Hyogo. NewSUBARU is at the site of SPring-8 campus and can provide light beams from IR to soft X-ray. We have achieved storing 500 mA at 1 GeV and 200 mA at 1.5 GeV. At present, NewSUBARU has six bending section beamlines (BL2, BL3, BL5, BL6, BL10, and BL11), a short undulator beamline (BL7), a long undulator beamline (BL9), and an optical-klystron beamline (BL1), as shown in Fig. 1.

Topics of the NewSUBARU research activities in this year are as follows. The first is the basic characteristic research of the NewSUBARU electron storage ring and photonuclear reaction with laser Compton scattering γ-ray. The second is extreme ultraviolet (EUV) activities that include mask observation using a coherent EUV scattering microscope, nanostructure pattern replication using an EUV interference lithography system, and the development of *in situ* contamination measurement in the EUV resist outgassing environment. BL9C beamline was branched from BL9B beamline for use of EUV interference lithography for the evaluation of the exposure characteristics of EUV resist. The third concerns micro- and nanodevices, such as a three-dimensional lab-on-CD and an X-ray grating for the X-ray Talbot interferometer. The fourth is on the materials science of various materials such as Si-containing DLC, BN and GaN. Furthermore, the performance of the material analysis beamline BL5 for industrial purposes was evaluated by NEXAFS spectra measurements using the standard samples of h-BN, CaF_2, and Ni.

Most of our research activities are conducted in collaboration with industries, government research institutes, and other universities. We will continue to respond to the community's demand by offering new science and technologies.

Shinji Matsui
Director of LASTI, University of Hyogo

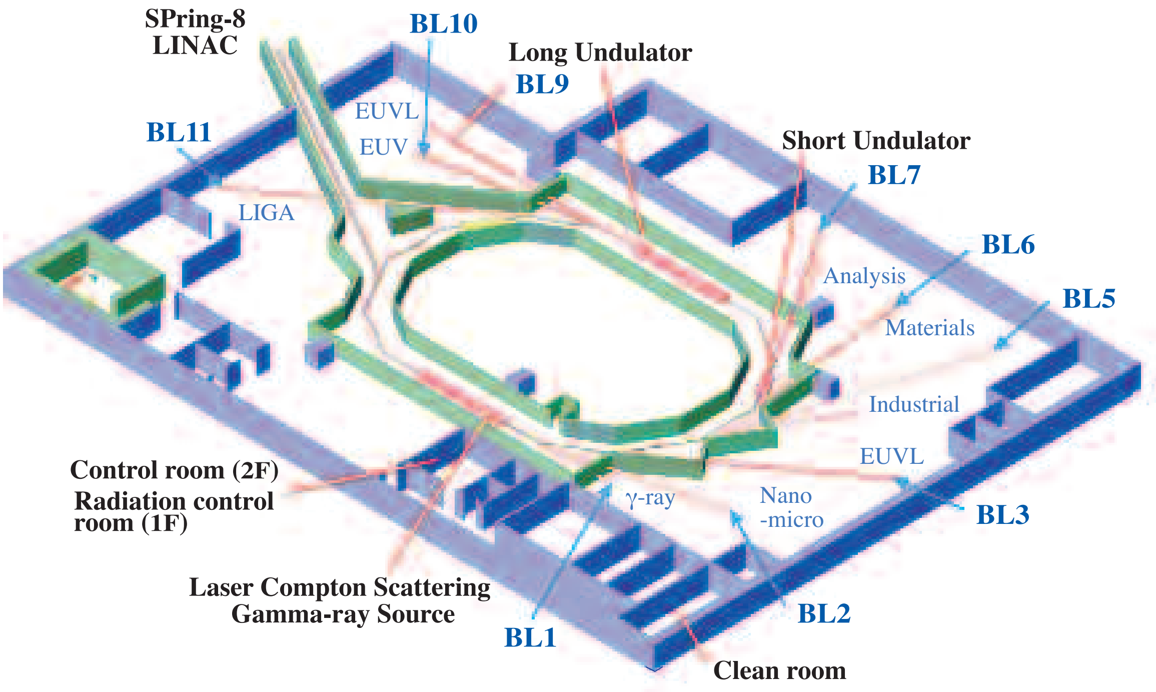

Fig. 1. Beamline arrangement in NewSUBARU.

Major Activity of NewSUBARU

1. Photonuclear reaction of iodine-129 with laser-Compton scattering γ-ray

The photonuclear reaction cross section of iodine-129 was measured using a polarized laser-Compton scattering γ-ray beam in an energy range from 13.9 to 19.7 MeV. The maximum cross section was evaluated to be 220 mb ± 50% at a photon energy of 15.9 MeV ± 4%. We did not observe any appreciable difference in the cross sections for linearly and circularly polarized γ-ray beams, within the limits of experimental error.

Figure 2 shows photonuclear reaction cross section σ_R derived by assuming the value of σ_s proposed by Berger *et al.* [1] in an energy range from 13.9 to 19.7 MeV for both linear (crossed) and circular (circled) polarizations of incident γ-rays. The γ-ray photon energy was scanned by changing the energy of the electron beam from 890 to 1060 MeV. The probability distribution of the signal intensity against the count rate was assumed to be a Poisson distribution. From the standard deviation, the error bars in Fig. 2 were calculated to be 12% at respective γ-ray energy. The error in the absolute value of the cross section was evaluated to be ±50% by taking into account the errors due to the alignment accuracy between the γ-ray beam and the target axes; this accuracy was a major factor compared with the errors in the number of iodine-129 atoms (< ±1%), the flux of the γ-rays (±2%), their energy spread (–3%), and the peak detection efficiency of the Ge detector (±10%).

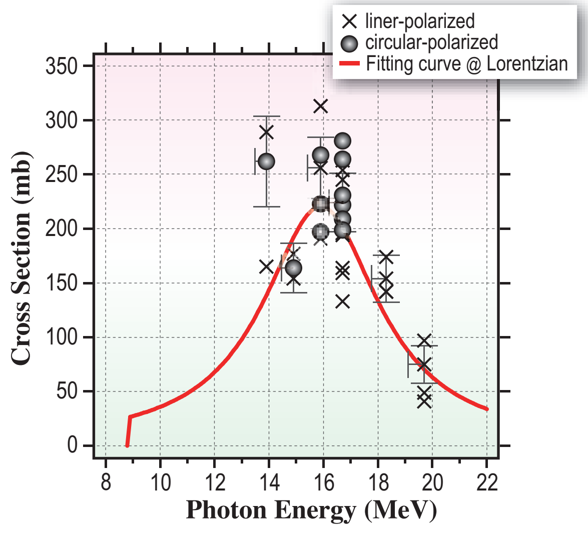

Fig. 2. Dependence of photonuclear reaction cross section of iodine-129 on energy and polarization of γ-ray photons.

2. EUV interference lithography

EUV interference lithographic system that can evaluate the resists for half pitch (hp) 22 nm, hp 16 nm, and hp 11 nm nodes has been developed. Since a replicated resist pattern with high accuracy and high resolution can be obtained by EUV interference lithography using light diffraction and interference, the resolution and line edge roughness (LWR) of resist itself can be evaluated without other factors. This EUV-IL exposure system is installed at beamline BL9. Since the 10.8-m-long undulator (LU) is employed as a light source, spatial coherence is large and a fine pattern can be replicated over the entire exposure area. Up to now, a 60-nm-pitch transmission grating pattern, which corresponds to hp 15 nm resist pattern on a wafer, has been fabricated.

The intensity of the light produced from the LU is 1,000 times higher than that from the bending magnet. In addition, a highly coherent light is produced from the LU. By Young's interference experiment, it was confirmed that the spatial coherence length is longer than 1 mm. EUV-IL two window transmission gratings were used. When the EUV light is irradiated to one grating window, the light diffracts into 0th, –1st, and +1st orders. With two window gratings, –1st-order light from one window grating and +1st-order light from another window grating interfere to produce the interference fringes on a wafer. Consequently, a resist pattern with a half the pitch size of the transparent grating is replicated on the wafer. The transmission grating is fabricated at the EUVL R&D center. Figure 3 shows the replicated resist pattern of the commercial resist ZEP-520A for electrons utilizing EUV-IL. SEM photographs of hp 22.5 nm, hp 20 nm, and hp 15 nm resist patterns are shown in this figure. We obtained resist patterns with high contrast.

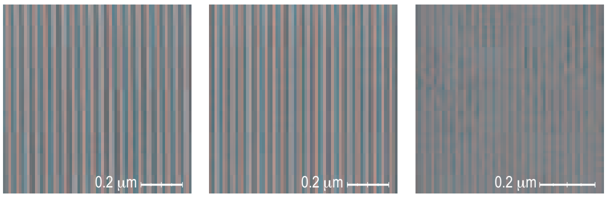

(a) hp 22.5 nm (b) hp 20 nm (c) hp 15 nm

Fig. 3. Exposure results obtained by EUV-IL.

3. High-sensitivity detection of Polychlorinated Biphenyl on three-dimensional lab-on-a-CD

This presents high-sensitivity detection of polychlorinated biphenyl (PCB) in a three-dimensional lab-on-a-CD, which consists of multiple disks with three-dimensional microchannel networks. To perform the automatic sequencing of the competitive protocol, capillary-barrier-type passive valves with vertically embedded capillary valves were designed and fabricated. We successfully demonstrated the detection of polychlorinated biphenyl.

Figure 4 shows the photographs of planar microchannel disks of polydimethylsiloxane (PDMS) and through-hole poly(methyl methacrylate) (PMMA) disks fabricated by standard rapid prototyping and deep X-ray lithography. A bundle-like capillary structure of square capillaries (75 µm in diameter) are formed on the PMMA disks for the effective immobilization of antibody. To demonstrate the detection of PCB, the bundle-like capillary structure is immobilized with anti-PCB antibody and blocked with BSA by off-chip immobilization. Then the disk is reversibly bonded with PDMS (also blocked) to construct the 3D lab-on-a-CD. We observed a strong effect of the micromachining accuracy of the bundle-like capillary structure on the reproducibility of the assay.

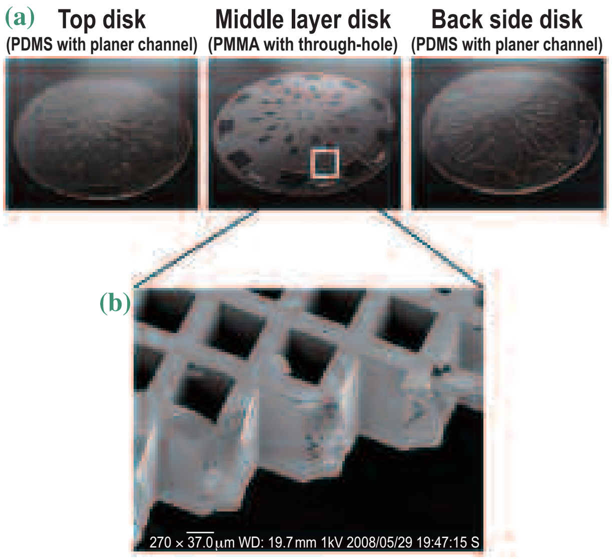

Fig. 4. **(a)** Photographs of fabricated disks of 3D lab-on-a-CD. **(b)** SEM image of bundle-like capillary structure for antibody immobilization.

4. Present Status of Material Analysis Beamline at BL5 for Industrial Enterprises

A material analysis beamline for industrial enterprises' use was completed at BL5 in March 2008. BL5 consists of two branch lines: a double-crystal monochromator beamline (BL5A) for use in the higher-energy region (1300-4000 eV) and a varied-line-spacing plane grating (VLSPG) monochromator beamline (BL5B) for use in the lower-energy region (50-1300 eV). These two branch lines can be operated simultaneously. The entire range of useful energy of the BL5 is the soft X-ray region from 50 to 4000 eV. The X-ray absorption fine structure (XAFS) measurements of the total electron yield (TEY) and fluorescence yield (FLY) can be performed at BL5A and BL5B. In addition, the X-ray photoelectron spectra (XPS) can be measured at BL5B.

We readjusted of the optical mirror and measured standard samples by the TEY method in BL5B. Figure 5 shows the near-edge X-ray absorption fine structure (NEXAFS) spectra of calcium fluoride (CaF_2) powder obtained using a grating with 400 lines/mm and calcium $L_{3,2}$-edge. The spectra were normalized to I_0 and the linear pre-edge background was removed. After optical adjustment (slit width: 50 µm), the improvement of resolution was verified by comparison with that before optical adjustment (slit width: 200 µm). The calcium $L_{3,2}$-edge spectral shape of CaF_2 almost corresponds to the spectrum reported by Naftel *et al.* [2].

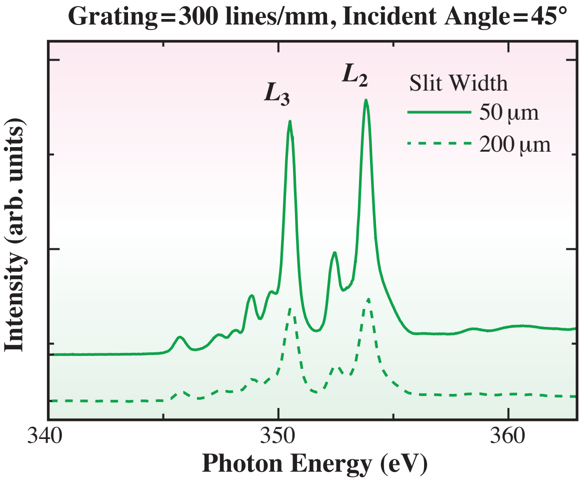

Fig. 5. CaF_2 Ca $L_{3,2}$-edge NEXAFS spectra.

References

[1] M.J. Berger *et al.*: "XCOM: Photon Cross Sections Database," <http://www.nist.gov/pml/data/xcom/index.cfm>
[2] S.J. Naftel *et al.*: J. Synchrotron Rad. **8** (2001) 255.

Editor
Hideo Ohno
SPring-8 / JASRI

Editing, Design & Layout
Marcia M. Obuti-Daté
SPring-8 / JASRI

Printing
ROKKO Publishing & Sale Co.

JASRI
Library and Information
Users Administration Division

1-1-1 Kouto, Sayo-cho, Sayo-gun
Hyogo 679-5198 • JAPAN
Tel. +81-(0)791 58-2797   Fax. +81-(0)791 58-1869

frontiers@spring8.or.jp
http://www.spring8.or.jp/

Japan Synchrotron Radiation Research Institute
1-1-1 Kouto, Sayo-cho, Sayo-gun, Hyogo 679-5198 JAPAN

http://www.spring8.or.jp